



Universidad de Oviedo
Universidá d'Uviéu
University of Oviedo

Programa de Doctorado en Materiales

NANOPARTÍCULAS BIOFUNCIONALES PARA INMUNOENSAYOS
MAGNÉTICOS: APLICACIÓN A LA DETECCIÓN DE
NEUMOLISINA PARA EL DIAGNÓSTICO RÁPIDO DE NEUMONÍA
NEUMOCÓCICA

BIOFUNCTIONAL NANOPARTICLES FOR MAGNETIC
IMMUNOASSAYS: APPLICATION TO THE DETECTION OF
PNEUMOLYSIN FOR THE RAPID DIAGNOSIS OF
PNEUMOCOCCAL PNEUMONIA

TESIS DOCTORAL

María Salvador Fernández

Diciembre 2021



Universidad de Oviedo
Universidá d'Uviéu
University of Oviedo

Programa de Doctorado en Materiales

NANOPARTÍCULAS BIOFUNCIONALES PARA INMUNOENSAYOS
MAGNÉTICOS: APLICACIÓN A LA DETECCIÓN DE
NEUMOLISINA PARA EL DIAGNÓSTICO RÁPIDO DE NEUMONÍA
NEUMOCÓCICA

BIOFUNCTIONAL NANOPARTICLES FOR MAGNETIC
IMMUNOASSAYS: APPLICATION TO THE DETECTION OF
PNEUMOLYSIN FOR THE RAPID DIAGNOSIS OF
PNEUMOCOCCAL PNEUMONIA

TESIS DOCTORAL

Directores de tesis

Dra. Dña. Montserrat Rivas Ardisana (Universidad de Oviedo)

Dr. D. José Carlos Martínez García (Universidad de Oviedo)

Dr. D. Davide Peddis (University of Genova)

Dr. D. Fabio Bruni (Università degli Studi Roma Tre)



RESUMEN DEL CONTENIDO DE TESIS DOCTORAL

1.- Título de la Tesis	
Español: Nanopartículas biofuncionales para inmunoensayos magnéticos: aplicación a la detección de neumolisina para el diagnóstico rápido de neumonía neumocócica.	Inglés: Biofunctional nanoparticles for magnetic immunoassays: application to the detection of pneumolysin for the rapid diagnosis of pneumococcal pneumonia.
2.- Autora	
Nombre: María Salvador Fernández	DNI:
Programa de Doctorado: Programa de Doctorado en Materiales	
Órgano responsable: Comisión Académica Programa Doctorado en Materiales	

RESUMEN (en español)

El desarrollo de la humanidad conlleva nuevos problemas: la sobrepoblación y su envejecimiento, la globalización, el calentamiento global y la contaminación ponen en jaque a las administraciones cada día. Así, hoy el cáncer es la enfermedad que más muertes causa, un virus se propaga de una zona del mundo a su opuesta en un abrir y cerrar de ojos, las bacterias resistentes a los antibióticos no paran de crecer y tenemos un alto riesgo de contaminación en nuestra comida por residuos farmacéuticos o agrícolas. Para abordar estos problemas de forma rápida y eficaz se necesitan herramientas de detección que permitan, *in situ*, obtener resultados fiables de modo sencillo y en el menor tiempo posible. Este tipo de dispositivos, denominados *point-of-care*, no dependen de equipos sofisticados o personal cualificado, siendo de gran utilidad especialmente en áreas de difícil acceso y países en desarrollo.

En la actualidad, los inmunoensayos de flujo lateral son los test *point-of-care* más utilizados. El test de embarazo casero o los test rápidos de antígenos utilizados durante la pandemia del COVID-19 son los ejemplos más relevantes. Sin embargo, algunas mejoras como el aumento de su sensibilidad o la posibilidad de cuantificación del analito permitirían que su uso fuese más extensivo. El uso de nanopartículas magnéticas como marcas de detección permitiría alcanzar ambos propósitos. El objetivo general de esta tesis es el estudio y caracterización de nanopartículas magnéticas para su aplicación en inmunoensayos de flujo lateral que permitan detectar y cuantificar biomoléculas de interés, mediante un sensor inductivo y optimizando su sensibilidad.

Las aplicaciones biomédicas de las nanopartículas magnéticas son múltiples. El primer capítulo describe unas nanopartículas de magnetita con una doble capa de ácidos grasos diferentes: se caracterizan fisicoquímica, estructural y magnéticamente y se aplican en resonancia magnética nuclear, hipertermia magnética y ensayos de biodetección. Los resultados demostraron que dichas nanopartículas (1) superan el rendimiento del agente comercial de contraste de referencia; (2) presentan una excelente capacidad de calentamiento, y (3) pudieron ser utilizadas como marcas en ensayos cuantitativos mediante el modelo de afinidad biotina-neutravidina.

El segundo capítulo describe la búsqueda de nanopartículas de magnetita con las propiedades óptimas para su uso en el sensor inductivo. Para ello se sintetizaron diferentes muestras de magnetita por descomposición térmica, concluyéndose que la susceptibilidad magnética inicial es un parámetro esencial para una buena detección, siempre que estas se encuentren dentro del régimen superparamagnético. También se estudió su respuesta en los ensayos de flujo mediante el modelo de afinidad biotina-neutravidina, constatándose que la producción de aglomerados anterior o durante el proceso de bioconjugación aumenta la señal por unidad de biomolécula a detectar, amplificando la señal.

En los dos últimos capítulos se describe el uso de las nanopartículas de magnetita con características óptimas en dos aplicaciones de interés clínico real: la detección de los anticuerpos generados por SARS-CoV-2 y la cuantificación de neumolisina. Esta última es una proteína cuya presencia en la orina indica neumonía neumocócica. Las pruebas de diagnóstico actuales requieren tomas invasivas y no son concluyentes, por lo que muchas veces se



prescriben antibióticos indiscriminadamente. El test desarrollado supone una herramienta útil para la detección de neumolisina que además aprovecha las propiedades magnéticas de los clústeres de nanopartículas para preconcentrar muestras cuyas concentraciones están fuera del límite de detección y aumentar la señal del test gracias a la recolocación magnética. Por último, también se detectaron anticuerpos de SARS-CoV-2 en las concentraciones de interés clínico, lo que permitiría monitorizar la respuesta inmune de la población, tanto durante la infección como tras su vacunación.

RESUMEN (en Inglés)

Humanity faces new problems as it evolves: overpopulation and aging, globalization, global warming, and pollution put administrations in check almost every day. Today, cancer is the disease that causes the most deaths, a virus spreads from one region of the world to its opposite in the blink of an eye antibiotic-resistant bacteria do not stop growing, and there is a high risk of contamination of our food chain by pharmaceutical or agricultural wastes. To address these problems quickly and effectively, detection tools that allow the obtention *in situ* of reliable results easily and in the shortest possible time are needed. These devices, called *point-of-care*, do not depend on sophisticated equipment or qualified personnel, being very useful, especially in remote areas and developing countries.

Currently, lateral flow immunoassays are the most widely used *point-of-care* tests. The home pregnancy test or the rapid antigen tests used during the COVID-19 pandemic are the most relevant examples. However, some improvements such as increasing its sensitivity or the possibility of quantifying the analyte would allow a more extensive use. The use of magnetic nanoparticles as detection labels would allow both purposes. This thesis' general objective is to study and characterize magnetic nanoparticles for their application in lateral flow immunoassays that allow the detection and quantification of biomolecules of interest, using an inductive sensor and optimizing their sensitivity.

The biomedical applications of magnetic nanoparticles are multiple. The first chapter describes magnetite nanoparticles with a double layer of three different fatty acids: Their physicochemical, structural, and magnetic characterization, and performance in nuclear magnetic resonance imaging, magnetic hyperthermia, and biosensing tests are shown. The results showed that such nanoparticles (1) increase the contrast between the tissues, exceeding the commercial reference agent; (2) they have an excellent heating capacity; and (3) they could be used as labels in quantitative assays using the biotin-neutravidin affinity model.

The second chapter describes the search for optimal properties of magnetite nanoparticles in inductive biosensing. Different samples of magnetite were synthesized by thermal decomposition and characterized structurally, physicochemically, and magnetically as well as in the inductive sensor. In this way, the initial magnetic susceptibility was determined as an essential parameter for good detection within the superparamagnetic threshold. The particles' response in flow tests was also studied using the biotin-neutravidin model, verifying that both the initial aggregates or the ones produced during the bioconjugation process increase the magnetic mass per unit of the biomolecule. This aggregation amplifies the signal.

The last two chapters describe how magnetic clusters with the optimal characteristics were used in two applications of real interest: Detecting antibodies generated by SARS-CoV-2 and quantifying pneumolysin. The latter is a protein that indicates pneumococcal pneumonia when detected in the urine. Pneumococcal pneumonia diagnosis currently involves taking challenging and invasive samples, which are not decisive, and often resolved with indiscriminate antibiotic prescriptions. The test developed is a helpful tool for detecting pneumolysin. It also takes advantage of the magnetic properties of nanoparticle clusters to pre-concentrate samples whose concentrations are outside the detection limit and increase the test signal thanks to magnetic relocation. Finally, SARS-CoV-2 antibodies were also detected at concentrations of clinical interest. Thus, they might monitor the population's immune response during infection and after vaccination.

A mis abuelos, Mario y Paulina, y mi tía Felisa,
por labrar mi camino.

Few subjects in science are more difficult to understand than magnetism.

Encyclopaedia Britannica. 15th Edition, 1989

“Life is not easy for any of us, but what of that? We must have perseverance and above all confidence in ourselves. We must believe that we are gifted in something, and that this thing, at whatever cost, must be attained.”

— Marie Curie

“Done is better than perfect because perfect gets never done.”

— Benjamin Franklin

INDEX

Thesis outline.....	1
Esquema de la tesis.....	2
Schema della tesi.....	3
Summary.....	5
Resumen.....	9
Sommario.....	13
Graphical abstract.....	17
Glossary.....	19
List of abbreviations.....	19
Nomenclature.....	22
Index of tables and figures.....	25
PART A.....	29
Motivation.....	31
General introduction.....	35
I. Background and state of the art.....	37
1. Biosensors and <i>point-of-care</i> testing.....	37
2. Lateral flow assays: The basics.....	40
2.1. Lateral flow assays: Construction.....	41
2.2. Lateral flow assays: Design.....	43
2.3. Lateral flow assays: How to search.....	46
2.4. Lateral flow assays: How to find.....	49
2.5. Lateral flow assays: From qualitative to quantitative.....	50
II. Objectives.....	57
PART B.....	59
Section I: Magnetic nanoparticles in biomedicine.....	61
I. The nanoscale.....	63
II. Magnetism at the nanoscale.....	63
III. Magnetic nanoparticles.....	69
1. Superparamagnetism.....	71
2. Dynamic magnetic properties.....	76
3. Magnetic interactions.....	77

4. Synthesis of magnetic nanoparticles.....	79
5. Characterization of magnetic nanoparticles.....	85
5.1. Size, shape, and structure.....	85
5.2. Composition and surface properties.....	90
5.3. Magnetic properties.....	93
6. Application of magnetic nanoparticles.....	96
6.1. Magnetic nanoparticles in biomedicine: A marriage of convenience.....	96
Chapter 1 – Biological and medical applications of magnetic nanoparticles	
Introduction and motivation.....	109
<i>Book chapter</i>	115
Section II: Magnetic nanoparticles as labels.....	165
I. Magnetic nanoparticles as labels.....	167
1. Bioconjugation processes: "There is strength in numbers".....	167
2. Magnetic detection by inductive biosensing.....	170
Chapter 1 – Synthesis of superparamagnetic iron oxide nanoparticles: SWOT analysis towards their conjugation to biomolecules for molecular recognition applications	
Introduction and motivation.....	177
<i>Literature review</i>	183
Section III: Results.....	229
Chapter 1 – Double-layer fatty acid nanoparticles as multiplatform for diagnostics and therapy	
Introduction and motivation.....	231
<i>Scientific article</i>	237
Chapter 2 – Improved magnetic lateral flow assays with optimized nanotags for point-of-use inductive biosensing	
Introduction and motivation.....	271
<i>Scientific article</i>	277
Chapter 3 – Magnetic nanoclusters increase the sensitivity of lateral flow immunoassays for protein detection: Application to pneumolysin in urine as a biomarker for <i>Streptococcus Pneumoniae</i>	
Introduction and motivation.....	303

<i>Scientific article</i>	309
Chapter 4 – MagCOVID: development of a rapid magnetic serological test for COVID-19	
Introduction and motivation.....	333
<i>Unpublished results</i>	339
Section IV: Conclusions and future perspectives	347
I. Conclusions.....	349
II. Conclusiones.....	353
III. Conclusioni.....	359
IV. Future perspectives.....	365
SCIENTIFIC PRODUCTION	367
LITERATURE	377

Thesis Outline

This thesis is structured into two main parts.

First, the reader will find the summary (in English, Spanish and Italian), a list of abbreviations and nomenclature, and a list with tables and figures (except those found in the articles).

Part A of the report consists of the motivation, the general introduction describing the necessary background to orient the reader, and the thesis's objectives.

Part B has four sections. Section I includes a bibliographic review that introduces magnetic nanoparticles, their main characteristics, how to obtain and characterize them, and their applications in biomedicine. Section II goes deeper into the application of magnetic nanoparticles as detection labels. It includes a description of the bioconjugation processes and the inductive sensor used during the development of the thesis. Section III collects the experimental results in four chapters, following the line established by sections I and II: from general bioapplications to magnetic nanolabeling. Finally, section IV presents the conclusions and perspectives for future works.

At the very end, the reader will find the scientific production (articles, conferences, and courses), and the references cited in parts A and B, except for those of the experimental results chapters in section III, which are at the end of each one.

I hope you enjoy your reading.

Esquema de la tesis

La memoria de esta tesis se estructura en dos partes principales.

En primer lugar, el lector podrá encontrar los resúmenes, la lista de abreviaturas y nomenclatura, y la lista con tablas y figuras (excepto las que se encuentran en los artículos).

La parte A del informe consta de la motivación, la introducción general, que describe los antecedentes necesarios para situar al lector en el campo en el que se desarrolla la tesis, y los objetivos de la misma.

La parte B incluye cuatro secciones diferentes. En la sección I se incluye una revisión bibliográfica que introduce las nanopartículas magnéticas, sus características principales, cómo obtenerlas y caracterizarlas y sus aplicaciones en biomedicina. La Sección II describe la aplicación de nanopartículas magnéticas como etiquetas de detección. Incluye una descripción de los procesos de bioconjugación y del sensor inductivo que se utilizaron durante el desarrollo de la tesis. La Sección III recoge los resultados experimentales en cuatro capítulos, siguiendo la línea establecida por las secciones I y II: desde las bioaplicaciones generales hasta el nanoetiquetado magnético. Finalmente, la sección IV recoge las conclusiones y las perspectivas que han de considerarse en trabajos futuros.

Al final, el lector encontrará la producción científica (artículos, conferencias y cursos) y las referencias bibliográficas citadas en las partes A y B, excepto las de los capítulos de resultados experimentales de la sección III, que se encuentran al final de cada uno.

Espero que disfrute de su lectura.

Schema della tesi

La memoria di questa tesi è strutturata in due parti principali.

In primo luogo, il lettore potrà trovare il sommario (in inglese, spagnolo e italiano), l'elenco delle abbreviazioni e della nomenclatura, e l'elenco con le tabelle e figure (tranne quelle che si trovano negli articoli).

La parte A del documento è costituita dalla motivazione, dall'introduzione generale che descrive lo sfondo necessario per collocare il lettore e gli obiettivi della tesi.

La parte B comprende quattro diverse sezioni. La Sezione I comprende una rassegna bibliografica che introduce le nanoparticelle magnetiche, le loro principali caratteristiche, come si ottengono e si caratterizzano, e le loro applicazioni in biomedicina. La Sezione II approfondisce l'applicazione delle nanoparticelle magnetiche come etichette di rilevamento. Include una descrizione dei processi di bioconiugazione e del sensore induttivo utilizzato durante lo sviluppo della tesi. La Sezione III raccoglie i risultati sperimentali in quattro capitoli, seguendo la linea stabilita dalle sezioni I e II: dalle bioapplicazioni generali alla nanoetichettatura magnetica. Infine, la sezione IV raccoglie le conclusioni e le prospettive per i lavori futuri.

Alla fine, il lettore troverà la produzione scientifica (articoli, convegni e seminari o corsi) e i riferimenti citati nelle parti A e B, ad eccezione di quelli dei capitoli dei risultati sperimentali nella sezione III, che sono alla fine di ciascuno.

Spero che il lettore apprezzi la lettura.

SUMMARY

Humanity, as it develops, must face new problems derived from population growth and aging, globalization, and pollution: A viral infection spreads from one part of the world to the opposite in the blink of an eye. Cancer is the disease that causes the most deaths. The number of bacteria resistant to antibiotics is growing. And there is a high risk that contaminants such as pharmaceutical or agricultural residues are present in our food. Detection tools to address these problems quickly and effectively are needed. They must allow reliable results to be obtained easily in the shortest time at the point of application. These devices are called *point-of-care*, and they do not rely on sophisticated equipment or qualified personnel. In this way, they allow screening of many samples and be used in places far from well-equipped laboratories. Thus, their implementation is advantageous in rural health centers, industrial plants, in-field applications, or developing countries.

The most widely used point-of-care tests are lateral flow immunoassays, such as the home pregnancy test or the rapid antigen test used during the coronavirus disease 2019 (COVID-19) pandemic. However, they have limitations that prevent their use from being more extensive. On the one hand, it is necessary to increase its sensitivity by reducing the number of false negatives. On the other hand, it is necessary to add quantifying capacity in many applications (currently, they can be associated with devices that give a semi-quantitative result). With these two purposes, magnetic nanoparticles can act as detection marks in this type of immunoassay.

This **thesis's general objective** is to **study and characterize magnetic nanoparticles for lateral flow immunoassays that allow the detection and quantification of biomolecules** by inductive methods and optimize their sensitivity.

The **first chapter** describes magnetite nanoparticles synthesized by coprecipitation covered with a double layer of three different fatty acids. Its physicochemical, structural and magnetic characterization are described. The biomedical applications of magnetic nanoparticles go

beyond their use as labels in immunoassays. In this work, their potential in nuclear magnetic resonance imaging and magnetic hyperthermia, in addition to biosensing assays, has been studied. The results demonstrate that these particles outperform commercial contrast agents and have an excellent heating ability. Back to the main objective of the thesis, these nanoparticles were evaluated as labels in quantitative assays using the biotin-neutravidin affinity model. It revealed the enormous importance of clustering before and during bioconjugation. A moderate degree of agglomeration favors detection.

The **second chapter** describes the synthesis of different magnetite particles by thermal decomposition and their structural, physical-chemical, and magnetic characterization. Its properties were related to its response in the inductive sensor to optimize them. In this way, we concluded that the initial magnetic susceptibility is an essential parameter to obtain a good response in the sensor. Since it increases with size, its limit is at the superparamagnetic critical value. The nanoparticle response was also studied using the biotin-neutravidin affinity model in the flow assays. We confirmed the importance of the agglomeration to increase the number of particles per biomolecule, which amplifies the signal. Therefore, initial susceptibility and the retained magnetic mass in the test line are essential to increase sensitivity in lateral flow magnetic immunoassays.

These conclusions led us to study particles with high initial susceptibility and controlled agglomeration: Nanoclusters in which magnetite particles are organized in spherical structures of optimum size and very homogeneous. In the last two chapters, these nanoclusters were applied to detect two molecular markers of great interest: Pneumolysin (**third chapter**) and the severe acute respiratory syndrome coronavirus 2 (SARS-CoV-2) IgG antibody (**fourth chapter**). Pneumolysin is a new protein marker that allows the diagnosis of pneumococcal pneumonia in a simple urine sample. Nowadays, this diagnosis of pneumonia is made in centralized laboratories on samples that are difficult to obtain (sputum or lung tissues) or, otherwise, the test results are not conclusive, which frequently leads to the indiscriminate prescription of antibiotics. In this work, magnetic nanoclusters were used to preconcentrate the analyte and relocate the particles in the test line. Additionally, they allowed the quantification of pneumolysin itself. The first two techniques significantly increased the sensitivity of the method. All in all, the developed

pneumolysin test is ideal for the rapid and decentralized diagnosis of pneumococcal pneumonia. In the last part of this thesis, magnetic immunoassays were used to monitor the population immune response during a SARS-CoV-2 infection and after vaccination. Nanoclusters were successfully applied to lateral flow magnetic immunoassay to detect SARS-CoV-2 antibodies at concentrations in the range of clinical interest.

RESUMEN

La humanidad, a medida que se desarrolla, debe enfrentar nuevos problemas derivados del aumento de la población y su envejecimiento, la globalización, y la contaminación: una infección vírica se expande de una parte del mundo a la opuesta en un abrir y cerrar de ojos; el cáncer es la enfermedad que más muertes causa; crece el número de bacterias resistentes a los antibióticos y existe un riesgo alto de que contaminantes como residuos farmacéuticos o agrícolas estén presentes en nuestra comida. Para abordar estos problemas de forma rápida y eficaz se necesitan herramientas de detección que permitan obtener resultados fiables de una manera sencilla, en el menor tiempo posible y en el punto de aplicación. Estos dispositivos se denominan *point-of-care*, y no dependen de equipos sofisticados o personal cualificado. De esta forma, permiten realizar cribados a gran cantidad de muestras y su aplicación en lugares alejados de laboratorios bien equipados, por lo que su implementación es de gran utilidad en centros de salud rurales, plantas industriales, aplicaciones de campo, o países en desarrollo.

En la actualidad, los tests *point-of-care* más utilizados son los inmunoensayos de flujo lateral, como por ejemplo los tests de embarazo o los tests rápidos de antígenos utilizados durante la pandemia por coronavirus de 2019 (COVID-19). Sin embargo, tienen algunas limitaciones que impiden que su uso sea más extensivo. Por un lado, es necesario aumentar su sensibilidad reduciendo el número de falsos negativos. Por otro, en muchas aplicaciones es necesario añadir su capacidad cuantificadora (actualmente se pueden asociar a dispositivos que den un resultado semicuantitativo). Con estos dos propósitos, se propone utilizar las nanopartículas magnéticas como marcas de detección en este tipo de inmunoensayos.

El **objetivo general** de esta tesis es el estudio y **caracterización de nanopartículas magnéticas para inmunoensayos de flujo lateral que permitan detectar y cuantificar biomoléculas** mediante métodos inductivos y optimizar su sensibilidad.

El **primer capítulo** describe nanopartículas de magnetita sintetizadas

por coprecipitación y con doble capa de tres ácidos grasos diferentes. Se describe su caracterización fisicoquímica, estructural y magnética. Las aplicaciones biomédicas de las nanopartículas magnéticas son muchas más que su uso como etiquetas en los inmunoensayos, y en este trabajo se ha estudiado su potencial para aplicación en resonancia magnética nuclear e hipertermia magnética además de los ensayos de biodetección. Los resultados demostraron que estas partículas superan el rendimiento de los agentes comerciales de contraste de referencia y tienen una excelente capacidad de calentamiento. Volviendo al objetivo central de la tesis, se evaluaron estas nanopartículas como marca en ensayos cuantitativos mediante el modelo de afinidad biotina-neutravidina. Este nos descubrió la enorme importancia de la formación de clústeres antes y durante la bioconjugación. Un grado de aglomeración moderado favorece la detección.

En el **segundo capítulo** se describe la síntesis de diferentes partículas de magnetita por descomposición térmica y su caracterizaron estructural, fisico-química y magnética. Sus propiedades se relacionaron con su respuesta en el sensor inductivo para determinar las propiedades óptimas. De esta forma, se concluyó que la susceptibilidad magnética inicial es un parámetro esencial para obtener una buena respuesta en el sensor. Dado que esta aumenta con el tamaño, su límite se encuentra en el valor crítico superparamagnético. También se estudió su respuesta en los ensayos de flujo mediante el modelo de afinidad biotina-neutravidina. Confirmamos la importancia de la aglomeración para favorecer la unión de la biomolécula a un número elevado de nanopartículas y, con ello, amplificar la señal. Por tanto, la susceptibilidad inicial y la masa magnética retenida en la línea de test son esenciales para aumentar la sensibilidad en los inmunoensayos magnéticos de flujo lateral.

Estas conclusiones nos llevaron a estudiar para esta aplicación partículas con elevada susceptibilidad inicial y aglomeración controlada: nanoclústeres en los que las partículas de magnetita están organizadas en estructuras esféricas de tamaño óptimo y muy homogéneo. En los dos últimos capítulos estos nanoclústeres se aplicaron a la detección de dos marcadores moleculares de enorme interés: la neumolisina (**tercer capítulo**) y el anticuerpo IgG del coronavirus de tipo 2 causante del síndrome respiratorio agudo severo (SARS-CoV-2) (**cuarto capítulo**). La neumolisina es un nuevo marcador proteico que permite el diagnóstico de neumonía neumocócica en una simple muestra de orina. Actualmente

este diagnóstico se realiza en laboratorios centralizados sobre muestras de difícil obtención (esputo o tejido pulmonar) o, en caso contrario, sus resultados no son concluyentes lo que frecuentemente lleva a una prescripción indiscriminada de antibióticos. En este trabajo se aprovechó el carácter magnético de los nanoclústeres para realizar preconcentración del analito y recolocación de las partículas en la línea de test además de la propia cuantificación de la neumolisina. Las dos primeras técnicas aumentaron significativamente la sensibilidad del método. Con todo, el test de neumolisina desarrollado resulta ideal para el diagnóstico rápido y descentralizado de neumonía neumocócica. En la última parte de esta tesis, se exploró la posibilidad de utilizar los inmunoensayos magnéticos para monitorizar la respuesta inmune de la población tanto durante una infección de SARS-CoV-2 como tras la vacunación. Los nanoclústeres se aplicaron con éxito al inmunoensayo magnético de flujo lateral para detección de anticuerpos de SARS-CoV-2 en concentraciones del rango de interés clínico.

SOMMARIO

L'umanità, nella sua evoluzione, ha affrontato e deve affrontare nuovi problemi derivanti dalla crescita e dall'invecchiamento della popolazione, dalla globalizzazione e dall'inquinamento: un'infezione virale si diffonde da una parte all'altra del mondo in un batter d'occhio; Il cancro è la malattia che causa più morti; Il numero di batteri resistenti agli antibiotici classici è in crescita e c'è un alto rischio che contaminanti come residui farmaceutici o agricoli siano presenti nei nostri alimenti. Sono necessari strumenti di rilevamento per affrontare questi problemi in modo rapido ed efficace. Devono consentire di ottenere facilmente risultati affidabili, nel più breve tempo possibile e nel punto di applicazione. Questi dispositivi sono noti come point-of-care e non si basano su apparecchiature sofisticate o personale qualificato. Queste caratteristiche consentono lo screening di molti campioni e anche in condizioni in cui sono assenti laboratori ben attrezzati. Pertanto, la loro implementazione è particolarmente vantaggiosa nei centri sanitari rurali, negli impianti industriali, nelle applicazioni sul campo o nei paesi in via di sviluppo.

I test point-of-care più utilizzati sono i test immunologici a flusso laterale, come il test di gravidanza domiciliare o il test rapidi dell'antigene utilizzato durante la pandemia di coronavirus 2019 (COVID-19). Tuttavia, ci sono limitazioni che ne impediscono un uso più esteso. Da un lato, è necessario aumentarne la sensibilità riducendo il numero di falsi negativi. D'altra parte, è importante migliorare la sensibilità in molte applicazioni (attualmente possono essere associate a dispositivi che danno un risultato semi-quantitativo). Con questi due scopi, le nanoparticelle magnetiche rappresentano degli ottimi marcatori di rilevamento in questo tipo di test immunologico. **L'obiettivo generale** di questa tesi è quello di **studiare e caratterizzare nanoparticelle magnetiche per saggi immunologici a flusso laterale che consentano il rilevamento e la quantificazione di biomolecole** con metodi induttivi e ottimizzandone la sensibilità.

Il **primo capitolo** è focalizzato su nanoparticelle di magnetite sintetizzate per coprecipitazione e ricoperte da un doppio strato di tre

diversi acidi grassi. Viene descritta la sua caratterizzazione fisico-chimica, strutturale e magnetica. Le applicazioni biomediche delle nanoparticelle magnetiche vanno oltre il loro uso come marcatori nei test immunologici. In questo lavoro, oltre ai saggi di biorilevamento, è stato studiato il loro potenziale nella risonanza magnetica nucleare e nell'ipertermia magnetica. I risultati hanno dimostrato che queste particelle hanno prestazioni superiori agli agenti di contrasto commerciali e hanno un'eccellente capacità di riscaldamento. Tornando all'obiettivo principale della tesi, queste nanoparticelle sono state valutate come etichette in saggi quantitativi utilizzando il modello di affinità biotina-neutravidina, rilevando l'enorme importanza del raggruppamento prima e durante la bioconiugazione. Un moderato grado di agglomerazione favorisce il rilevamento.

Il **secondo capitolo** descrive la sintesi di diverse particelle di magnetite per decomposizione termica e la loro caratterizzazione strutturale, chimico-fisica e magnetica. Questo studio ha evidenziato come la suscettività magnetica iniziale sia un parametro essenziale per ottenere una buona risposta nel sensore induttivo. Poiché la suscettività aumenta con le dimensioni, il suo limite è al valore critico superparamagnetico. La risposta delle nanoparticelle è stata studiata anche utilizzando il modello di affinità biotina-neutravidina nei saggi di flusso. È stata anche confermata l'importanza dei fenomeni di aggregazione per aumentare il numero di particelle per biomolecola, amplificando il segnale rilevato dal sensore induttivo. Pertanto, la suscettibilità iniziale e la massa magnetica trattenuta nella linea del test sono essenziali per aumentare la sensibilità nei test immunologici magnetici a flusso laterale.

Queste conclusioni ci hanno portato a studiare particelle con elevata suscettibilità iniziale e agglomerazione controllata: Nanocluster in cui le particelle di magnetite sono organizzate in strutture sferiche di dimensioni ottimali e molto omogenee. Negli ultimi due capitoli, questi nanocluster sono stati applicati per rilevare due marcatori molecolari di grande interesse: la pneumolisina (**terzo capitolo**) e l'anticorpo dal sindrome respiratoria acuta grave da coronavirus 2 (SARS-CoV-2) IgG (**quarto capitolo**). La pneumolisina è un nuovo marker proteico che consente la diagnosi di polmonite pneumococcica in un semplice campione di urina. Oggigiorno questa diagnosi viene fatta in laboratori centralizzati su campioni di difficile reperibilità (espettorato o tessuti polmonari) o, con risultati che non consentono una diagnosi certa, spesso

inducendo ad una prescrizione indiscriminata di antibiotici. In questo lavoro, la natura magnetica del nanocluster è stata utilizzata per preconcentrare l'analita e riposizionare le particelle nella linea di test. Inoltre, è stato possibile quantificare la pneumolisina. Le prime due tecniche hanno aumentato significativamente la sensibilità del metodo. Tutto sommato, il test della pneumolisina sviluppato è l'ideale per la diagnosi rapida e decentralizzata della polmonite pneumococcica. Nell'ultima parte di questa tesi, sono stati utilizzati saggi immunologici magnetici per monitorare la risposta immunitaria della popolazione durante un'infezione da SARS-CoV-2 e dopo la vaccinazione. I nanocluster sono stati applicati con successo al test immunologico magnetico a flusso laterale per rilevare la SARS- CoV-2 a concentrazioni nell'intervallo di interesse clinico.

Medical diagnosis
Food safety
Environmental control

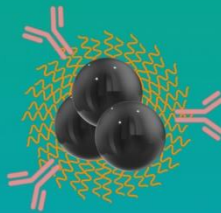
Semi-quantitative
Moderate sensitivity



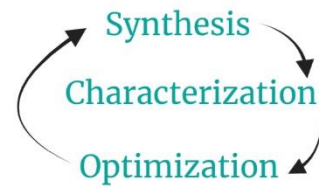
Lateral flow assays



Magnetic nanoparticles



Bioconjugation



Magnetic concentration and relocation



Pneumococcal pneumonia
SARS-CoV-2 immune response

Rapid, portable and highly sensitive diagnostic tests

GLOSSARY

LIST OF ABBREVIATIONS

μ MRS	Micro-nuclear magnetic resonance
AC	Alternating current
AuNPs	Gold nanoparticles
CNPs	Carbon nanoparticles
COVID-19	Coronavirus disease 2019
DC	Direct current
DCD	Direct current demagnetization
DLS	Dynamic light scattering
DSC	Differential scanning calorimeter
EDC	1-ethyl-3-(3-dimethylaminopropyl) carbodiimide hydrochloride
EDX	Energy-dispersive X-ray
ELISA	Enzyme-linked immunosorbent assays
EU	European Union
FC	Field cooling
FDA	Food and drug administration
FFP	Field-free point
FTIR	Fourier transform infrared
GMR	Giant magnetoresistance
hCG	Human chorionic gonadotropin
HRTEM	High resolution transmission electron microscopy
ICP	Inductively coupled plasma
ICP	Inductive coupled plasma
IRM	Isothermal remanent magnetization
LFAs	Lateral flow assays
LFIA	Lateral flow immunoassays
MH	Magnetic hyperthermia

MLFAs	Magnetic lateral flow assays
MNPs	Magnetic nanoparticles
MPI	Magnetic particle imaging
MRI	Magnetic resonance imaging
MRS	Magnetic relaxation switch sensors
MS	Mass spectroscopy
NALF	Nucleic acid lateral flow
NALFIA	Nucleic acid lateral flow immunoassay
NHS	N', N'-dicyclohexyl carbodiimide
NMR	Nuclear magnetic resonance
NPs	Nanoparticles
PCR	Polymerase chain reaction
PDI	Polydispersity index
PHE	Planar Hall effect
POCT	Point-of-care testing
QDs	Quantum dots
RF	Radio frequency
RNA	Ribonucleic acid
SAR	Specific absorption rate
SARS-CoV-2	Severe acute respiratory syndrome coronavirus 2
SEM	Scanning electron microscopy
SERS	Surface-enhanced Raman scattering
SI	International system of units
SLP	Specific loss power
SPM	Superparamagnetism
SQUID	Superconducting quantum interference device
TEM	Transmission electron microscopy
TGA	Thermogravimetric analysis
TMR	Tunnel magnetoresistance
UCNPs	Up-converting nanoparticles
USA	United States of America
VSM	Vibrating sample magnetometer

W/O	Water in oil
WHO	World Health Organization
XPS	X-ray photoelectron spectroscopy
XRD	X-ray diffraction
ZFC	Zero-field cooling

NOMENCLATURE

μ	Magnetic moment
C_S	Sample specific heat capacity
C_{dm}	Dispersion media specific heat capacity
C_m	Magnetic phase specific heat capacity
D_{hkl}	Mean diameter of the crystal
E_B	Energy barrier
E_{EX}	Exchange energy
E_K	Anisotropy energy
E_{MS}	Dipole or magnetostatic energy
E_{Tot}	Total energy
E_Z	Zeeman energy
$E_{thermal}$	Thermal energy
H_C	Coercive field
H_{SW}	Switching field
H_d	Demagnetizing field
K_S	Surface anisotropy constant
K_{eff}	Effective anisotropy
K_{eff}	Effective anisotropy constant
K_B	Bulk anisotropy constant
K_S	Crystallite shape factor
M_{FC}	Field cooling magnetization
M_S	Saturation magnetization
M_{ZFC}	Zero-field cooling magnetization
M_r	Remanent magnetization
T_B	Blocking temperature
T_N	Néel temperature
T_C	Curie temperature
T_{IRR}	Irreversibility temperature
T_{MAX}	Maximum temperature
T_1	Longitudinal relaxation time
T_2	Transverse relaxation time
V_H	Hydrodynamic volume

V_{act}	Activation volume
d_P	Diameter
d_{SPM}	Superparamagnetic diameter
d_H	Hydrodynamic diameter
k_B	Boltzmann constant
m_r^{DCD}	Remanent DCD magnetization
m_r^{IRM}	Remanent IRM magnetization
M_{FC}	FC magnetization
M_{ZFC}	ZFC magnetization
r_C	Critical radii for monodomain
r_1	Longitudinal relaxivity
r_2	Transverse relaxivity
μ_r	Relative permeability
σ_{noise}	Sensor noise
τ_B	Brownian relaxation time
τ_M	Magnetic relaxation measuring time
τ_N	Néel relaxation time
τ_0	Attempt measuring time
χ_0	DC magnetic susceptibility (volume)
μ_0	Permeability of vacuum
μ_B	Bohr magneton
A	Exchange stiffness
B	Magnetic induction
f	Frequency
M	Volume magnetization
T	Temperature
V	Volume
R	Sensor resolution
$R(v)$	Electrical resistance
S	Inductive sensor signal
w	Width of the line containing magnetic mass
D	Translational diffusion coefficient.
F	Force

H	Magnetic field
K	Anisotropy constant
L	Self-inductance
$L(x)$	Langevin function
Z	Electric impedance
d	Interplanar distance
hkl	Miller's indexes of the crystalline planes
m	Mass
z	Ionic charge
Σ	Sensor sensitivity
ν	Frequency
β	Full-width at half-maximum
η	Fluid viscosity
λ	Wavelength
ρ	Fluid density
χ	Magnetic susceptibility (volume)
χ'	Real magnetic susceptibility
χ''	Imaginary magnetic susceptibility
ψ	Mass correction factor
ω	Angular frequency

Index of tables and figures

Tables

Table 1. Summary of the methods for the synthesis of magnetic nanoparticles.

Table 2. Summary of the experimental techniques used during research for this thesis for the MNPs characterization.

Figures

Figure 1. A) Schematic drawing of a typical biosensor consisting of the analyte, the biorecognition element, the transducer, and the final signal obtained. B) Different types of analytes, biorecognition elements, and transducer principles to get the signal. C) Main fields of applications for biosensors.

Figure 2. Schematic drawing of the most common paper-based POCT devices A) dipsticks, B) lateral flow assays, C) flow-through tests, and D) μ PADs. Adapted from [9].

Figure 3. A) Schematic view of the different components that make up LFAs. B) Schematic view of assembled LFAs showing the flow direction. C) Schematic view of negative (left) and positive (right) LFAs in a cassette for better handling.

Figure 4. Schematic view of a sandwich-type LFA. If there is an analyte in the sample, it will be captured, and the test line will be visible. When there is no analyte, only the control line will appear. The signal is directly proportional to the amount of analyte in the sample within the linear range.

Figure 5. Schematic view of a competitive LFA. If there is no analyte in the sample, the labeled capture antibodies will get trapped at the test line, making it visible. When there is an analyte, it will compete for the detection antibodies, and they will not be able to bind to the test line. The signal is inversely proportional to the amount of analyte in the sample within the linear range.

Figure 6. A) Structure of an IgG antibody consisting of two light and two heavy chains, each composed of constant (C_L , C_{H1} , C_{H2} , C_{H3}) and variable (V_L , V_H) regions. B) Structure of the immunoglobulin isotypes.

Figure 7. Schematic illustration of POCT devices according to their size and operational complexity together with the detection strategy based on the nanotag.

Figure 8. A) Comparison of the contribution of AuNPs labels in optical and MNPs in magnetic detections. B) Comparison of LFAs for histamine detection in wine using MNPs (left) and AuNPs (right) as labels. Obtained from [65]. C) Schematic illustration of a magnetic pre-enrichment protocol.

Figure 9. Summary of the magnetic behavior of materials.

Figure 10. Schematic of a hysteresis curve showing the relationship between the magnetization (M) and the applied magnetic field (H) in ferromagnetic (orange) and superparamagnetic (green) materials. The dashed orange line represents the initial magnetization curve.

Figure 11. Representation of the domain structure and coercivity of a magnetic nanoparticle as a function of size.

Figure 12. A) Definition of the usual axis system for a uniaxial nanoparticle under an external magnetic field. B) Representation of the switching of the magnetization of a uniaxial magnetic nanoparticle as a function of its direction. The height of the energy barrier E_B is given by the magnetic anisotropic constant and the particle volume.

Figure 13. ZFC-FC curves for A) monodisperse MNP sample B) MNPs with a log-normal distribution. The difference in the blocking temperature (T_B), maximum temperature (T_{MAX}), and irreversibility temperature (T_{IRR}) are shown. Adapted from [78].

Figure 14. A) Scheme of the two approaches to obtain MNPs. B) Classical LaMer model for the formation mechanism of monodisperse particles in solution.

Figure 15. Schematic view of the characteristic sizes to consider in MNPs for biological applications.

Figure 16. A) Sample preparation for TEM measurements. B) Schematic representation of a TEM instrument.

Figure 17. Schematic representation of Bragg's equation.

Figure 18. Schematic representation of the scattered light from MNPs with different sizes. Obtained from [100] without further modification.

Figure 19. A) Schematic representation of a typical mass spectrometry instrument. B) Data output in an MS to detect qualitatively and quantitatively the elements in the sample by their respective m/z .

Figure 20. Schematic representation of the photoelectric effect.

Figure 21. A) Schematic representation of a VSM. From [103]. B) Schematic illustration of the sensing element of the SQUID, where H_{ext} is the applied external magnetic field. The difference of voltage U_{sig} is detected by the magnetic field-induced imbalance of the current I_{mod} flowing through two semiconducting loops (1) and the two Josephson junctions (2) of the sensing ring. From [104].

Figure 22. Schematic representation of the differences in the relaxation times for an NMR sensor.

Figure 23. A) Schematic illustration of the magnetic hyperthermia process. B) Relaxation mechanisms for MNPs: Néel relaxation is the rotation of the magnetic moment inside the particle, while Brown relaxation process is the rotation of the particle itself.

Figure 24. A) In an external magnetic field, spins align parallel or antiparallel and precess at the Larmor frequency. When the RF pulses, the magnetization of the spins changes, and when it is turned off, the excited spins undergo both T_1 and T_2 relaxation processes to return to their normal orientation. B) Shortening of T_1 (left) and T_2 (right) signals using contrast agents. The relaxation enhancement results in brighter contrast in T_1 and darker contrast in T_2 . B) Influence of the r^2/r_1 ratio on the image contrast. High values are characteristic of T_2 contrast agents, making organs appear darker in the image. Low values of r^2/r_1 define T_1 contrast agents, making organs clearer and brighter. Adapted from [148].

Figure 25. Schematic representation of different approaches for drug delivery. A) Polymeric NP with both the drug and the MNPs entrapped in the polymeric matrix. B) Porous MNPs with the drug within its internal structure. C) Hollow MNP with the drug entrapped in its nucleus. D) Magneto-liposome with both the drug and the MNPs entrapped in the inner aqueous compartment.

Figure 26. Schematic representation of the different superficial stabilizations for MNPs (clockwise direction): Bare precipitated MNPs with hydroxyl groups, polymer attached via a polymer end group, polymer

grafted or covalently bound to a pre-existing coating, and electrostatic interactions among coatings.

Figure 27. Schematic representation of the A) EDC/NHS and B) biotin/neutravidin bioconjugation processes.

Figure 28. A) Schematic representation of the sensing system showing the impedance analyzer, the micro-positioner, and the personal computer used to control both. B) Image of the sensing device, which comprises the planar inductor, the LFAs holder, and the micro-positioner. C) Photography of the micro-positioner. Images provided by José Luis Marqués-Fernández.

Figure 29. A) Detailed image of the planar inductor printed in the insulating substrate. B) Plan of the planar coils specifically designed to encompass the entire width of the MNPs and LFAs samples, respectively. Images provided by José Luis Marqués-Fernández.

Figure 30. Calibration curve of the sensor signal with different MNPs masses.

Figure 31. Schematic representation of a cross-section of the test line and the planar coil to show the auto-inductive sensing principle: A RF current flows through the Cu-based conductor. The RF field generated excites the MNPs, which in turn, increases the impedance of the planar coil. Only one MNPs has been represented for the sake of simplicity.

Figure 32. Sensor signal for two consecutive scans in opposite directions for a sample of A) MNPs and B) LFAs.

Part A

Motivation

Now more than ever, the world is aware of the need for fast and accessible biosensing techniques. No one in any corner of the world has been oblivious of the tremendous crisis that severe acute respiratory syndrome coronavirus 2 (SARS-CoV-2) has caused. This pandemic has completely changed our lives. Of all the messages from the authorities, the World Health Organization (WHO) director-general, Tedros Adhanom, highlighted a simple one: we need to test, test, and test. In this case, breaking the chain of transmission was the most effective way to prevent infections and save lives. In fact, in addition to clinical diagnosis and monitoring, testing can avoid many other critical situations.

Foodborne illnesses are usually infectious or toxic and caused by bacteria, viruses, parasites, or chemical substances entering the body through contaminated food or water. Their effects on human and animal health are generally not yet well understood, but they are known to be potentially dangerous. According to the numbers, contaminated food caused more than 600 million cases of foodborne diseases, out of which more than 400 000 were fatal. For example, in 2011, a novel bacteria strain of *Escherichia coli* affected more than 4000 people across Europe, of whom 53 died. Another example caused by *Listeria monocytogenes* bacteria happened in 2017. The most severe listeria crisis caused more than 200 deaths in South Africa, due to contaminated processed meat.

In addition, water pollution is an increasing global concern that damages economic growth and the health of billions of people. Agrochemicals, drug residues, heavy metals, and all kinds of toxins (including mycotoxins, algal toxins, bacterial toxins, and plant toxins) are present in our water supplies. Of particular interest is the increasing concentration of antibiotics. Their presence can contribute to and spread the worrying antimicrobial resistance; so much so that the WHO has declared it one of the top 10 threats to global public health facing humanity.

In addition to the deaths caused, all these crises involve significant economic costs, especially in the form of health costs and financial challenges for those impacted, possibly leading to diplomatic tensions among countries.

Monitoring of all these biomolecules or microorganisms has been done traditionally by techniques such as chromatography and spectrometry analysis, enzyme-linked immunosorbent assays (ELISA), and polymerase chain reaction (PCR). These sophisticated methods are sensitive enough to detect up to femtomolar concentrations. However, in most cases, is this the point? To achieve these sensitivities, these methods are very complex, and hence, require specialized laboratories and personnel. They have high acquisition and operational costs, which means they could be accessible in developed countries but cost-prohibitive in many others.

Moreover, their results usually take considerable time, which may not be available in critical situations when decisions need to keep pace with emergencies. Scientists from many disciplinary fields are hoping to design and develop bioanalytical tools that overcome these disadvantages.

Point-of-care testing (POCT) is an *in vitro* detection method that obtains quasi-immediate results on-site: in a hospital or emergency room, at home, or in a remote village or plant. There is no standard definition of what a POCT is, but it must have certain characteristics. POCT devices provide at least qualitative and at best quantitative results when they are read on easy-to-use portable devices. Their ease of use allows tests to be carried out in decentralized environments by non-specialists. In addition, their quickness allows almost immediate results, reducing to a minimum the protocols for obtaining the sample, which can be a drop of blood, saliva, or urine, and for performing the test. These POCT devices are generally low-cost, disposable electrodes or strips that provide the necessary sensitivity and specificity. The best known are the glucometer and the home pregnancy test. The first allows people with metabolic problems to monitor their glucose through a drop of blood. The device consists of an electrode and a portable reader that fits in a bag. In this way, immediate measurement can be performed anywhere, anytime, and the appropriate insulin injected if necessary. As for the home pregnancy test, a paper strip provides an optical signal in pregnancy using urine. It only takes a few minutes to know the result.

The WHO gathered these characteristics for an ideal POCT, which must adhere to the REASSURED criteria [1]:

- Real-time
- Ease of specimen collection

- Affordable
- Sensitive (few false negatives)
- Specific (few false positives)
- User-friendly
- Rapid and robust
- Equipment-free/environmentally friendly
- Deliverable to end-users

These characteristics make them ideal for tackling situations of concern, related, for instance, to food safety, animal welfare, and environmental control wherever they occur. However, their principal uses are in the health field. Nowadays, diseases not detected on time or misdiagnosed and not adequately monitored are still the leading causes of death. These include ischemic heart disease, respiratory and bacterial infection, and cancer. Lately, advances in molecular techniques have made it possible to obtain molecules that indicate the early presence of these diseases. Therefore, implementing quick and easy-to-use control and analysis tools that correctly detect and timely administer the proper treatment would reduce deaths, morbidity, and economic expense.

Lateral flow assays (LFAs) are probably the quintessential POCT devices. Their use ranges from the medical field to detect biomarkers, to food safety to detect pathogens and toxins, to environmental control to detect pesticide or antibiotic residues. Simple as a paper-like strip, they work thanks to microfluidics and biorecognition. Traditionally they have been used qualitatively, where it was necessary to know only the presence or absence of the molecule of interest. This applies, for example, to the home pregnancy test or the detection of coronavirus disease 2019 (COVID-19) via rapid diagnostic tests. However, many other cases require quantification, that is, a test that provides the amount of analyte present. For example, in medicine, the severity of certain diseases and their treatment is related to the amount of the biomarker present. Similarly, knowing the amount of toxins or hazardous waste in food safety or environmental control allows compliance with legislation when the limits are regulated.

The quantification of these molecules is achieved thanks to their labeling with particles of similar size. Nanometric particles provide many advantages in biosensing applications. For example, they have a large surface-to-volume ratio so that they can interact with many biomolecules

per particle. In addition, their size gives them unique properties that are not found in bulk materials. Thus, nanoparticles (NPs) have become the most widely used transducer in biosensors: They are responsible for converting the biorecognition event into a measurable signal. Traditionally, these NPs have been latex or gold. However, parameters such as ambient light, humidity, and the nature of the sample matrix may interfere when these LFAs rely on optical methods for quantification. Hence, they provide only a semi-quantitative measurement.

Magnetic nanoparticles (MNPs) are similar in size to most biomolecules of interest. Moreover, thanks to their magnetism, they add possibilities such as remote manipulation, both to pre-concentrate samples or to accumulate them in specific places, the generation of heat in response to alternating magnetic fields, or their use as contrast agents in magnetic resonance imaging. MNPs can also act as signal reporters. When MNPs are used in LFAs for this purpose, they can provide a dual signal: in addition to their magnetization, MNPs also provide intense color. Advances in the production and characterization of MNPs currently allow fine control of their size, morphology, crystalline quality, and surface and magnetic properties. Thus, the design of new bio-functional nanoparticles that enables hybrid applications is emerging.

The motivation for this doctoral thesis is to study and characterize magnetic nanoparticles used as tags in LFAs. The goal is to optimize the quantification of biomolecules of interest. For this purpose, this thesis combines the study of different magnetic nanoparticles' structural, surface, and magnetic properties, with their response in an inductive sensor developed in the research group's laboratory.

Nanoparticles with optimal properties for their quantification were used as labels to detect pneumococcal pneumonia. This respiratory tract disease caused by the bacterium *Streptococcus pneumoniae* is the leading cause of global deaths due to infectious diseases, especially in developing countries. Accurate diagnoses and correct treatments could prevent most of these deaths and alleviate the growing and worrying resistance to antibiotics. With all this, the aim is to develop a POCT device that allows a quick response with an easy and cheap technology for use in biomedical diagnostic applications transferable to food and environmental safety and control applications.

GENERAL INTRODUCTION

I. Background and state of the art

1. Biosensors and *point-of-care* testing

Many of the aspects of our daily lives are governed by the interactions we have with our environment. Most of our actions are carried out thanks to the help of sensors. A sensor is defined as an instrument capable of detecting a change in a variable and of turning it into a signal that can be detected and analyzed. Biosensors are sensors that integrate a biological element with an electronic component to monitor a process and generate a signal [2,3]. This signal's information is either qualitative (the presence of something) or quantitative (the amount of this something). A typical biosensor comprises an analyte to detect, a biorecognition element, a transducer to convert the event into a measurable signal, and the electronics to generate the latter (see Figure 1).

Analytes are substances of interest classified as organic (such as proteins, cells, viruses, or pesticide and drug residues) and inorganic (such as heavy metals, or phosphates, and nitrates). Bio-recognition elements, such as enzymes, antibodies and aptamers, nucleic acids, and even cells, will identify the analyte and produce an event that the transducer will recognize. Different operational principles like optical, gravimetric, magnetic, electrochemical, or thermometric convert this event into a measurable signal. Bio-recognition elements and transducers are the key elements of biosensors, and they will be primarily responsible for their selectivity and sensitivity. With suitable electronics, the signal produced will be visualized and analyzed.

The remarkable development of the last decades in POCT biosensors is mainly due to the combination of several factors. For one, the incredible advance in molecular biology has made it possible to sequence and use new biomarkers and new bio-recognition molecules. For another, miniaturization and manufacturing technologies made possible new insights into microfluidics and the production and characterization of new nanomaterials. The latter is having a tremendous impact on our society today. For example, in biosensors, it is at the nanoscale level at which most biological events occur. Hence, nanoparticles have the ideal size to interact with the different analytes. Thanks to their large surface-to-volume ratio, they are increasingly being used as carriers for immobilizing the biorecognition elements. More importantly, thanks to

fundamental properties specific to their nanometric size, they are also being used as labels for signal generation, transduction, and amplification.

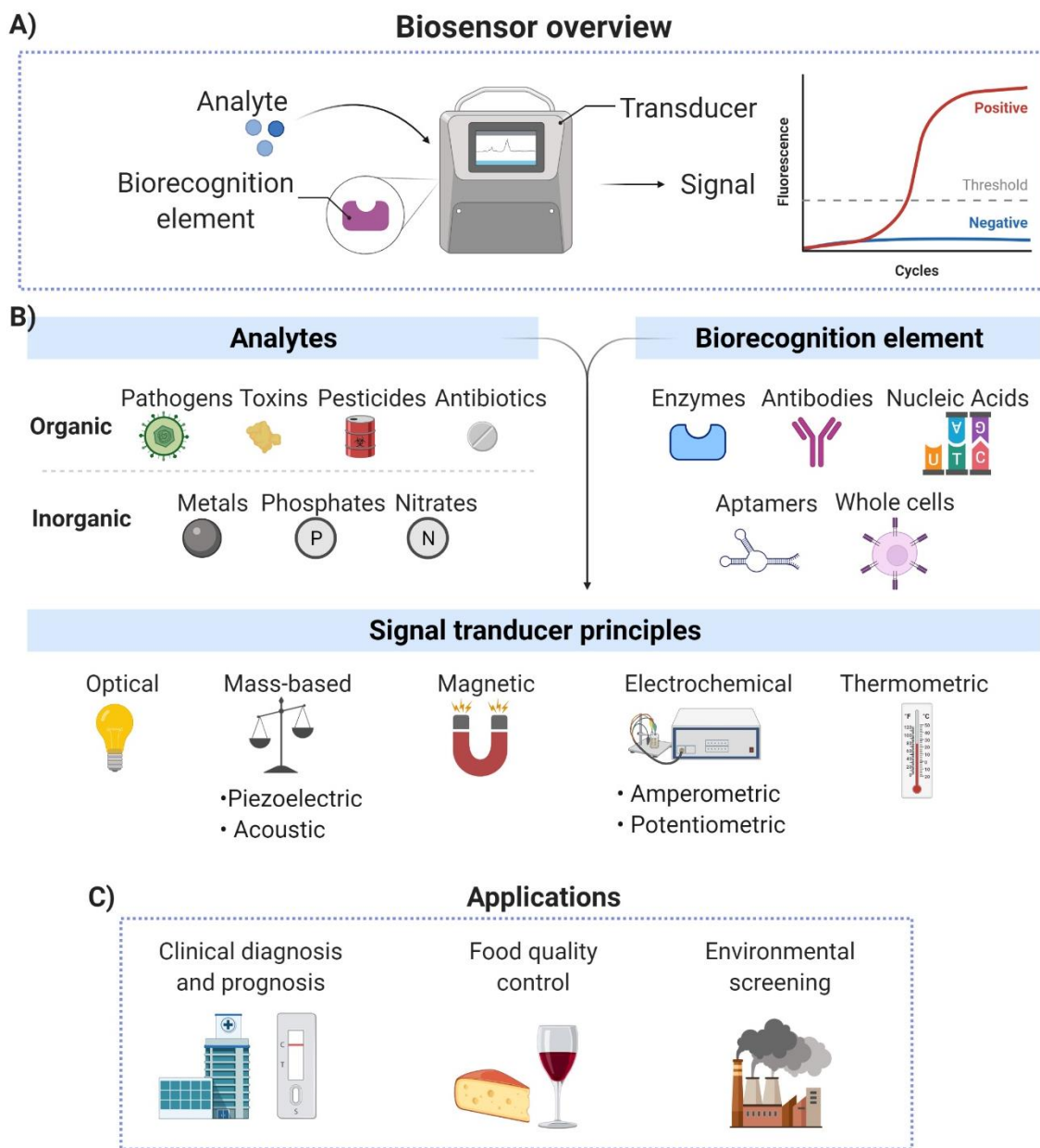


Figure 1. A) Schematic drawing of a typical biosensor consisting of the analyte, the biorecognition element, the transducer, and the final signal obtained. B) Different types of analytes, biorecognition elements, and transducer principles to get the signal. C) Main fields of applications for biosensors.

It is straightforward: biosensors can significantly benefit society, not only in crises such as the current pandemic we are experiencing. Growing populations lead to a parallel rise of diseases and infections, notably impacting people's quality of life and the associated health expenditures.

Early detection saves lives and costs [4], and therefore many disease prevention programs have been created in healthcare systems today. This population growth causes a growing demand for products, be they textiles, medicines, or food. Quality control of the final products and surveillance of the possible residues generated are mandatory to avoid toxins and pathogens in food, or pesticide and drug residues in water supplies. This will maintain a safe food chain and a sustainable environment.

Many analytical techniques have been developed to detect these analytes. Most of them are very specific and sensitive but labor-intensive. They are usually placed in centralized laboratories requiring specialized personnel to handle the sample acquisition and preparation, and to operate the sophisticated equipment. However, the current reality demands these techniques to be transferred to the point where they are needed, literally. Thus, POCT are “on-site” devices that can perform fast and accurate analyses easily and cost-effectively. They try to avoid the tedious workflow and waiting. These features bring POCT technology closer to remote areas and low-income countries, where, unfortunately, even basic infrastructures are not always available [5].

Currently, there are several POCT devices on the market [6,7]. The two main types are printed electrodes [8] and paper-based devices [9], of which the most representative examples are the glucose sensor and the home pregnancy test, respectively.

Paper-based devices use paper, or its technological derivatives (i.e., nitrocellulose), for their construction. This makes them ideal for POCT due to their low cost, availability, and recyclability. Moreover, the paper allows for functions such as filtering or sample moving due to capillarity (no need for external pumping) with a wide variety of biological samples [10]. Most paper-based POCT devices can be classified into four categories (see Figure 2):

- Dipstick assays: The strips contain dried reagents that react with the sample to produce color changes. To determine the results of the test, the strips are compared to a chart [11].
- Lateral flow assays (LFAs): They are made of several overlapping components. Their function is based on microfluidics and biorecognition. The bio-recognition elements, which are usually

antibodies, are printed onto the membrane, and the sample flows parallel to the paper's surface.

- Vertical lateral flow or flow-through tests: The sample is applied vertically to the surface of the membrane. The tests can have a single layer or a combination of several layers, which allows the detection of several analytes at the same time when the liquid diffuses from the bottom to the top layers [12,13].
- Microfluidic paper-based assay devices (μ PADs): Here, a hydrophobic reagent defines the paper's hydrophilic flow channels. They will direct the sample to a defined location for its analysis [14,15].

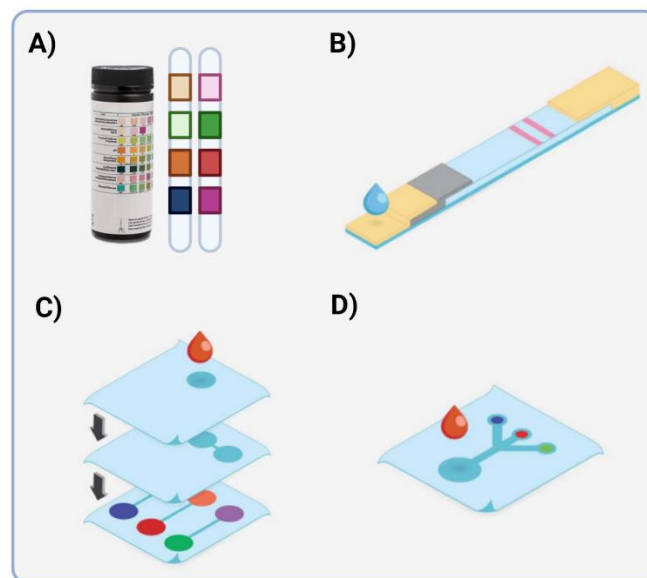


Figure 2. Schematic drawing of the most common paper-based POCT devices A) dipsticks, B) lateral flow assays, C) flow-through tests, and D) μ PADs. Adapted from [9].

2. Lateral flow assays: The basics

Lateral flow assays (LFAs) first emerged in the late 1960s to monitor serum proteins, but the main application driving their development was the human pregnancy test, which became the first commercial success of LFAs in the 1970s [16]. The test is based on the specific interaction of an antigen, the human chorionic gonadotropin (hCG), and an antibody, anti-hCG [17]. It was the result of enormous advances in immunology. Since then, other improvements mentioned above, such as miniaturization, new manufacturing technologies, and biology, have allowed LFAs to evolve. Now, LFAs are a mature, off-the-shelf, technology widely used to detect various molecules of interest in different fields of application.

2.1. Lateral flow assays: Construction

LFAs are based on the same foundation as ELISA: The specific antigen-antibody interaction. Briefly, ELISA involves the immobilization of a reactant (an antibody or antigen) onto a solid surface. Then, enzymes or fluorescence probes are used as markers for the presence and abundance of this specific antigen-antibody interaction [18]. On the other hand, LFAs are designed to perform the entire test in a single step and in a few minutes, avoiding all the intermediate steps required in ELISA. Biorecognition elements, mainly antibodies and aptamers or nucleic acids, are immobilized on a nitrocellulose membrane. This membrane promotes the flow of the sample by capillary action and facilitates the separation, capture, and detection of the analyte.

A conventional lateral flow strip is made up of several zones, each one with a specific function, and typically created by segments made of different materials (see Figure 3A and B):

- **Sample pad:** It is usually made of cellulose acetate, glass fiber, or rayon. Its primary function is to allow a uniform and continuous transfer of the sample to the other components of the strip. Not all LFAs carry a sample pad. If so, they may be used to pre-treat the sample, either to eliminate undesired compounds that may interfere or because specific reagents are added to facilitate interaction with the system (e.g., buffer salts or surfactants).
- **Conjugate pad:** It is made of fiberglass, cellulose, or polyester. In most cases, its primary function is to hold the detection reagent until the test is performed. However, not all tests have their labels immobilized on the conjugate pad. The capture of the analyte is often performed out of the strip, in a microtube, before making the sample flow like a dipstick. In this kind of LFA, the sample pad is not needed.
- **Membrane:** It is made with nitrocellulose, and is probably the most crucial part of the LFA [19]. Although nitrocellulose is hydrophobic in nature, it is made hydrophilic with rewetting agents such as surfactants. Its characteristics are a high protein-binding capacity, relative ease of handling, and a great variety of porosity, which mainly affect the wicking rates and sample volume, and therefore, the test's sensitivity. It is in the membrane where the analytical areas of the test are delimited. The test and control lines are where

molecular recognition reactions take place. The recognition elements in these lines are automatically dispensed. Their retention in the membrane is firstly produced due to electrostatic attraction. Long-term bonding is then accomplished by combining hydrophobic interactions, hydrogen bonds, and van der Waals forces between the membrane's residual chemical groups and the recognition molecules. However, there are certain disadvantages inherent to the use of porous membranes: Their life span, their alteration due to particular environmental conditions such as humidity, or their manufacturing variability. The latter causes the membrane's pores to be inhomogeneous. The structure is actually sponge-like, and therefore, membranes cannot be characterized by their pore size but instead by their flow speed or "wicking rate." This parameter has been defined as the time it takes for a standard sample to travel four centimeters through the membrane. The choice of this parameter is crucial, as it determines the speed and kinetics of the assay's development, and therefore, it will affect assay performance and sensitivity.

- **Absorbent:** It is considered the test's engine, made with high-density cellulose. The absorbent is designed to pull all the samples up and not release them back, avoiding false positives. Its choice influences the improvement of sensitivity by being able to increase the volume of the sample.

The construction of the LFAs is a relatively simple procedure performed by overlapping these parts onto one another on a backing card. The cards are typically polystyrene or other plastic materials coated with a pressure-sensitive adhesive. This way, LFAs acquire structural rigidity and ease handling. Since the components of the strips come in large rolls, the membrane is usually mounted on the backing card first. The immobilization of the biorecognition elements is carried out subsequently. Then, the sample and conjugate pads and the absorbent are overlapped by about 2 mm. Finally, the LFAs are obtained by cutting strips approximately 5 mm wide using a guillotine. Some commercial LFAs add a more rigid cassette to protect the strip and guide the final user to perform the test and read the results (see Figure 3C).

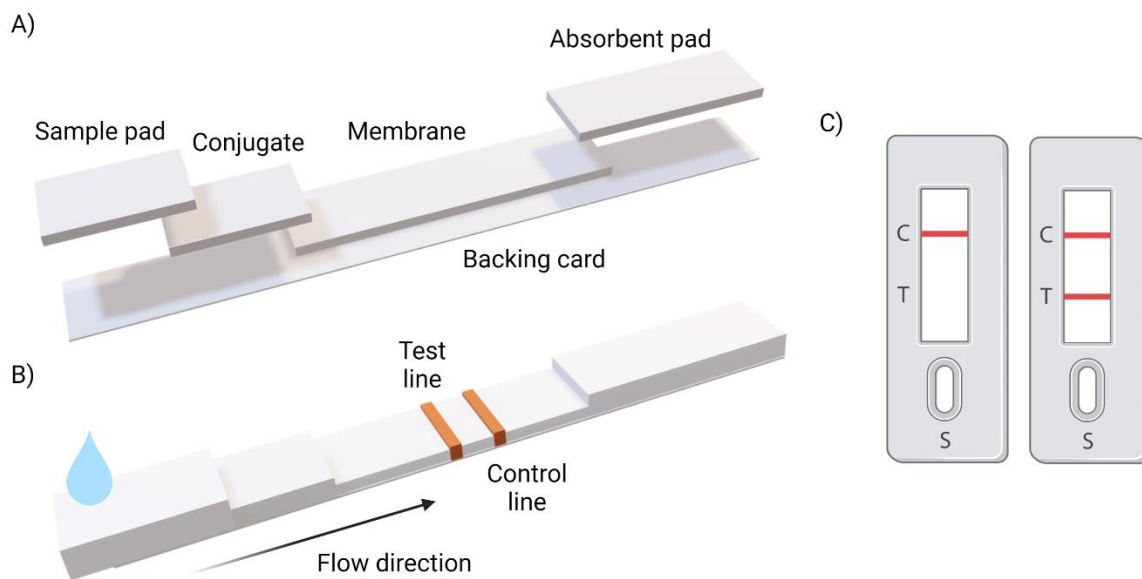


Figure 3. A) Schematic view of the different components that make up LFAs. B) Schematic view of assembled LFAs showing the flow direction. C) Schematic view of negative (left) and positive (right) LFAs in a cassette for better handling.

2.2. Lateral flow assays: Design

Once the strip is built, to perform the test, one simply adds the liquid sample to the sample pad (or inserts the strip into the microtube in the dipstick format), and it begins to flow by capillary action toward the absorbent, passing through each of the components described above. This is microfluidics: One of the two working principles of LFAs. The other is biorecognition. The first recognition element is the detection element, and its function to identify the analyte in the sample matrix. However, to be detected, it must be tagged by some label. These tags will later act as transducers to obtain the signal. Thus, the tagged analyte flows toward the membrane, reaching the analytical zone. It will meet two other biorecognition elements that were previously immobilized to form the test and control lines. What happens in this area depends mainly on the test format, which can be a sandwich-type or a competitive format. Typically, the choice is determined by the size of the analyte. Sandwich assays are used for large analytes, where several recognition sites allow the binding of various detection elements. However, the competitive format is used for small molecules due to insufficient dimensions for the presence of several epitopes or because these would cause steric impediments. The most important details of each one detailed below.

- **Sandwich-type format:** This is probably the most used format. Its name arises because the target molecule is trapped by two different elements: the detection and the capture bioreceptor (see Figure 4). Therefore, if there is an analyte in the sample, it will first form a complex with the detection antibody, which will be retained on the test line by the capture antibody. In this way, the test line will become visible, indicating a positive test. If there is no analyte, all the detection antibodies will bypass this zone to the control line. There, a third antibody is immobilized against the detection antibody. The interaction between these two antibodies always must be present, indicating that the sample has risen entirely and, therefore, validates the test. The intensity of the test line corresponds to the signal, which in this format is directly proportional to the amount of target in the sample (see Figure 4).

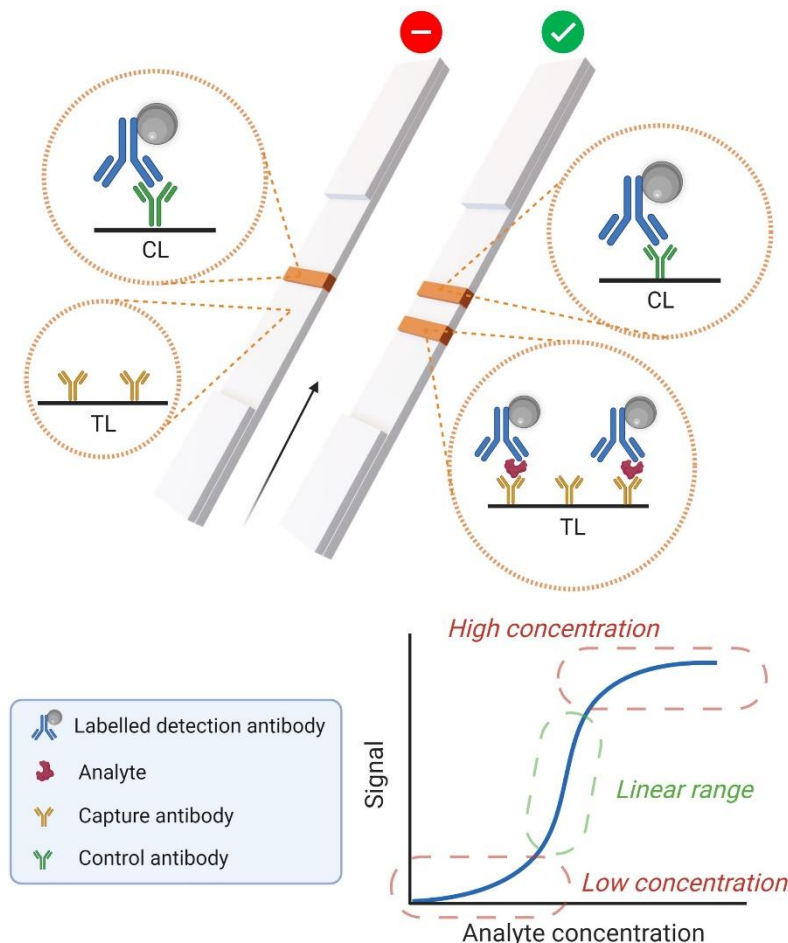


Figure 4. Schematic view of a sandwich-type LFA. If there is an analyte in the sample, it will be captured, and the test line will be visible. When there is no analyte, only the control line will appear. The signal is directly proportional to the amount of analyte in the sample within the linear range.

- Competitive format: In this case, synthetic analytes are immobilized in the test line. When no real analyte is present, the labeled detection antibodies recognize the synthetic analytes and are retained on the test line, making it visible. On the contrary, if there is real analyte in the sample, there is a competition between them and the immobilized synthetic analytes in the test line for the labeled detection antibodies. Suppose there is a lot of analyte present. In that case, the labeled antibodies will be blocked entirely and will not be trapped at all in the test line. Visually, nothing appears in the test line. The labeled antibodies continue to flow towards the absorbent, passing the control line, which is also present to validate the test. Thus, the signal obtained in competitive tests is inversely proportional to the analyte present in the sample (see Figure 5).

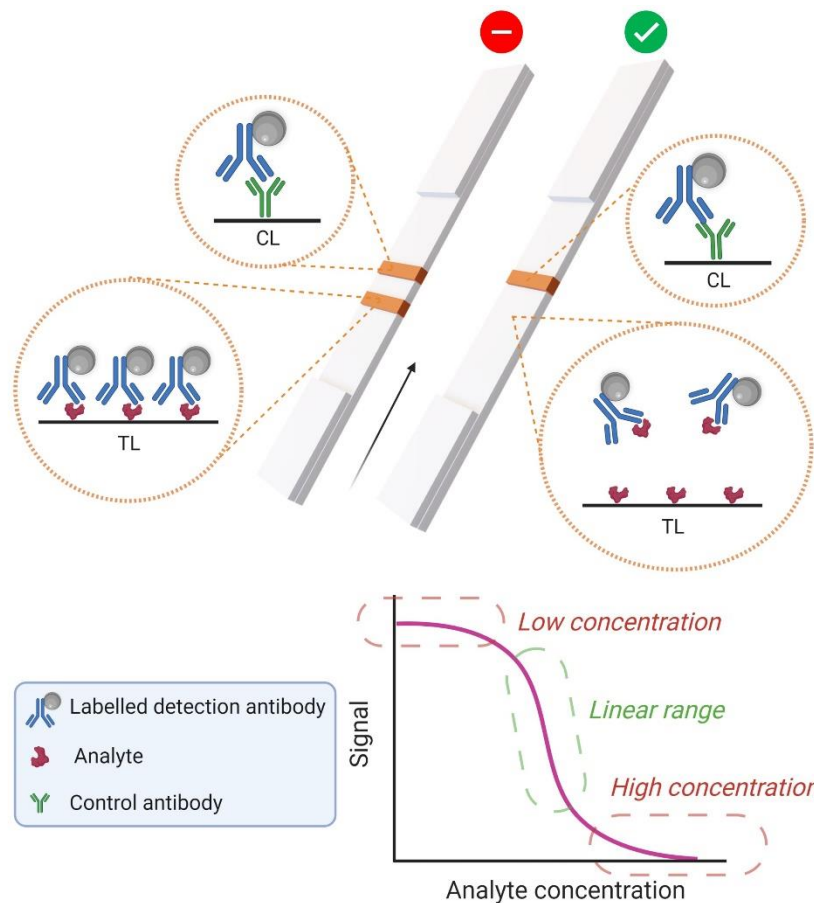


Figure 5. Schematic view of a competitive LFA. If there is no analyte in the sample, the labeled capture antibodies will get trapped at the test line, making it visible. When there is an analyte, it will compete for the detection antibodies, and they will not be able to bind to the test line. The signal is inversely proportional to the amount of analyte in the sample within the linear range.

These two formats of LFAs allow the detection of a single analyte. However, different combinations have been designed to detect several analytes simultaneously in what is known as multiplex assays [20]. In the clinical field, adding the possibility of detecting different analytes easily and quickly is very promising. Generally, several biomarkers may determine the disease prognosis and evolution and/or the patient response to treatment.

There are different multiplex combinations. The best known are those in which several test lines are printed in the same strip. Each of these lines has specific antibodies for each of the analytes. Examples of this format are the detection of periprosthetic joint infection through the detection of alpha-defensin and C-reactive protein [21] or the detection of multiplex cardiac biomarkers for the quick diagnosis of acute myocardial infarction [22]. This approach, however, is limited by the length of the strip. Although the length could be incremented, it cannot be done indefinitely since this would require an increase in the required sample and test time. As a solution, individual strips are arranged so that a unique sample flows through all of them, in parallel, in each strip, and there is no interference between them. For example, Zhao and colleagues developed a star-like multiplex assay to detect 10 foodborne pathogens simultaneously [23]. Other more advanced settings have been described [24,25].

2.3. Lateral flow assays: How to search

The specificity of the LFAs is achieved through the recognition elements. Their function is to “search and recognize” only the desired analyte, avoiding other molecules in the sample (false positives). Therefore, it is always necessary to carry out a careful analysis and selection of the recognition elements. The latter will entirely depend on the target analyte, seeking the highest possible affinity and stability of the complex. There are different elements of biorecognition, among which antibodies and nucleic acid-based molecules stand out.

- Antibodies: Most LFAs use antibodies as biorecognition elements. In this case, LFAs are known as lateral flow immunoassays (LFIAs). Antibodies, also called immunoglobulins (Ig), are proteins generated by B lymphocyte cells in the immune system in response to the presence of foreign molecules in the organism [26,27]. These molecules are called antigens, which can be virtually any known

molecular structure, whether biological such as proteins, bacteria, viruses or synthetic, such as small organic compounds.

Most antibodies are derived from the active immunization of laboratory animals with an immunogen responsible for eliciting an immune response. The antigen, for its part, is capable of binding to an antibody but not necessarily eliciting an immune response. The sites to which both immunogen and antigen can bind the antibodies are called epitopes or antigenic determinants. The part of the antibody that recognizes and binds to the immunogen or antigen is called paratope. The estimated molecular size of antibodies is 15 nm x 7 nm x 4 nm, although immunoglobulins are highly variable [28]. The basic structure of an Ig antibody consists of two identical heavy polypeptide chains paired with two identical shorter light chains, forming a Y shape (see Figure 6A). Joined by a variable number of disulfide bonds, both types of chains are, in turn, composed of constant (C) and variable (V) regions. Chemically, these regions are divided into Fc, Fab, and Fv. The former is the constant heavy region at the tail of the antibody, which plays a role in modulating immune cell activity. The Fab fragment is the antigen recognition zone. This fragment is further divided into the Fv fragment, the smallest part that retains the antigen-binding capacity.

The excellent specificity that antibodies have for a particular antigen makes them ideal bio-recognition elements for LFIA. Ideally, this interaction must happen quickly to optimize the time they remain in contact, both in the sample and when passing through the analytical zones of the membrane.

There are five classes of immunoglobulins: IgG, IgD, IgE, IgA, and IgM, which are determined by their heavy chain, their activity, and when they appear during the immune response (see Figure 6B).

IgG antibodies are the most widely used, and depending on their production, can be polyclonal or monoclonal [29]. The former is a heterogeneous mixture of antibodies that recognize different epitopes of a single antigen. Their production is simple and does not require much time, but they may have reproducibility problems because they are derived from live animals. Monoclonal antibodies, by contrast, come from a hybridoma: A single, immortal B lymphocyte. Thus, they recognize a single epitope of the antigen and can be made available in limitless quantities. However, their production time is longer since it requires intermediate purification stages. For their use in LFAs, both

monoclonal and polyclonal antibodies have their advantages and disadvantages. Each LFA case requires particular study [30]. Monoclonal antibodies, due to their lower variability and greater specificity, are preferred as detection elements. However, the recognition of several epitopes may be helpful for capture elements in test lines. Nevertheless, the nature of their production makes them a manufacturing challenge.

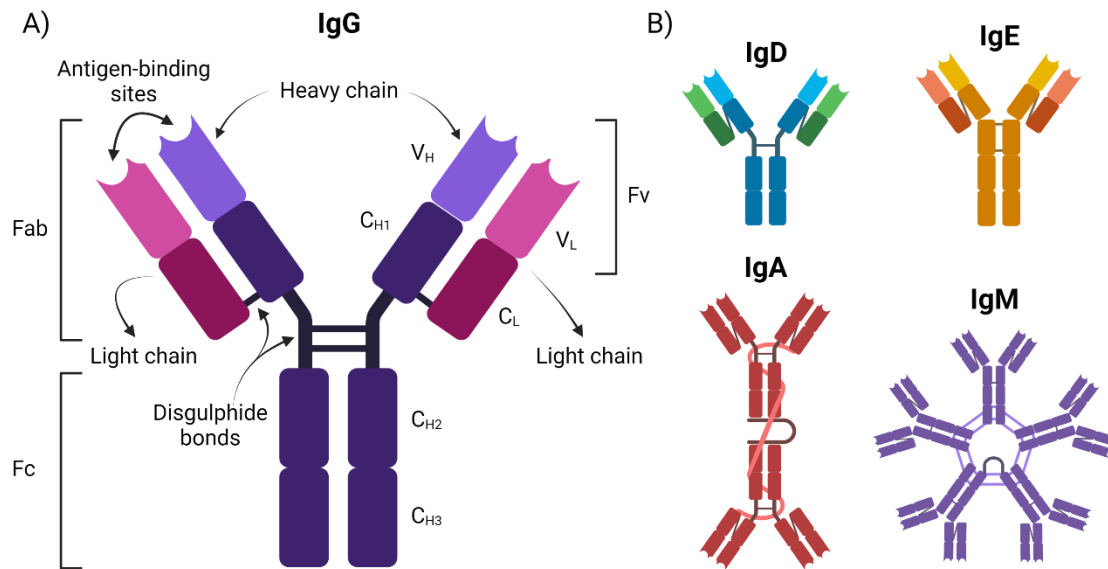


Figure 6. A) Structure of an IgG antibody consisting of two light and two heavy chains, each composed of constant (C_L, C_{H1}, C_{H2}, C_{H3}) and variable (V_L, V_H) regions. B) Structure of the immunoglobulin isotypes.

Currently, there is a particular effort in engineered antibodies, known as recombinant, to get a faster production, reproducibility, and facility to fine-tune the affinities and specificities without the need to immunize living animals [31].

- Nucleic-acid-based recognition elements: These are ideal for pathogens identification. Two main groups stand out: nucleic acids and aptamers [32]. The former allows the detection of genetic material with the advantages of using the LFA method, displacing expensive and time-consuming PCR. There are two main types of lateral flow nucleic acid tests. First, nucleic acid lateral flow (NALF) directly detects DNA, exploiting capture and labeled reporter oligonucleotide probes [33,34]. Secondly, nucleic acid lateral flow immunoassay (NALFIA) detects hapten-labeled DNA using capture and labeled reporter antibodies or streptavidin [35,36].

Aptamers are engineered artificial oligonucleotides that can bind to a wide range of targets, from small molecules to proteins and even cells, with high affinity [37]. They are also known as “chemical or synthetic” antibodies because they exert an extraordinary analyte binding efficiency that is comparable to that of antigen-antibody interactions. They can be relatively easily synthesized through an iterative *in vitro* evolution process called systematic evolution of ligands by exponential enrichment (SELEX) [38]. This is also its most significant advantage over the use of conventional antibodies in LFAs since they can be synthesized at a large scale without compromising their quality [39].

2.4. Lateral flow assays: How to find

Being able to recognize the analyte through the biorecognition elements does not imply its detection. It must be labeled or tagged by an element that we can detect somehow. The most widely used labels are nanoparticles. They have a similar size to biological elements and have a large surface-to-volume ratio. Therefore, they can act as cargo for the biorecognition elements. Most importantly, they have specific properties that are used as generators of a signal.

The ideal label or tag for LFAs should have the following characteristics [40,41]:

- It can be detected by multiple methods or technologies in a very large and helpful dynamic range.
- It has colloidal stability in solution under various chemical conditions and temperatures.
- It can be used for the detection of multiple analytes.
- The attachment of the biorecognition elements during the conjugation process must be easy, efficient, and reproducible. It should also not interfere with the chemical and biological activity of the analyte.
- It should be commercially available at low cost.

There exists no nanometric label that has all these characteristics. However, many have been used to develop LFAs: gold, silver, latex, luminescent and chemiluminescent, carbon, and magnetic nanoparticles. For each of them, there are different strategies to read and interpret the signal generated in the LFAs.

2.5. Lateral flow assays: From qualitative to quantitative

LFAs provide an immediate qualitative response through visual inspection of the test and control lines [42]. The presence or absence of the analyte does not require external devices, and even an estimated value (semi-quantitative) can be given if the strip is compared with color standards. However, this qualitative response can lead to errors in its reading due to the operators' subjectivity [43]. But above all, visual inspection is insufficient in many cases, where immediate actions must be taken depending on the concentration of the analyte.

Quantitative detection in LFAs is achieved depending on the label used. The most employed devices can be classified as optical, electrochemical, and magnetic [44,45]. However, all of them must be consistent with the LFA technique's simplicity, speed, low cost, and portability. This means that although there are benchtop devices to analyze the strips, the current trend is to develop handheld devices and even incorporate this technology into smart devices, such as smartphones or smart wearable devices (see Figure 7) [46]. These would be ideal for data processing: they are portable, accept open-source applications, have abundant sensors and wireless communication, and are ubiquitous. These characteristics will provide tremendous opportunities for remote expert advice and supervision of on-site measurements, crucial in developing countries or in emergencies and remote locations. They will allow the development of "cloud" databases and simple and effective statistical analysis of large-scale screening results for healthcare programs [47,48]. However, even with all these advantages, they must be used with caution to yield trustworthy results. For example, mobile-phone cameras used for optical analysis must be standardized and use consistent lighting.

Optical reading is the most widespread detection method. It is used in colorimetric, fluorescence, and surface-enhanced Raman scattering (SERS) LFAs.

Colorimetric assays are based on converting the color density of the test strip into optical density, which is correlated with the analyte concentration. There are commercial devices based on reflectance or fluorescence measurements, which operate by scanning the strips. However, a simple scan or the mobile-phone camera can also take a photo of the tests and analyze the intensity using different programs, such as Image J. Its most significant asset is its speed and portability.

Nevertheless, they have low reproducibility, usually because of their strong dependence on ambient light conditions. So far, gold nanoparticles (AuNPs) are the most widely adopted reporters for a quantitative colorimetric LFA [49]. AuNPs are straightforward to obtain and bioconjugate. For example, antibodies strongly bind to their surface through non-covalent interactions [50]. This allows a simple protocol that does not influence the antibodies' or, the bio-recognition capability. Other labels that base their detection on their color are latex and carbon particles (CNPs). Their darker colors, especially the black of the CNPs, offer better contrast with the white membrane than AuNPs. Linares et al. compared these three tags, and the results showed that CNPs deliver remarkably higher sensitivity [51].

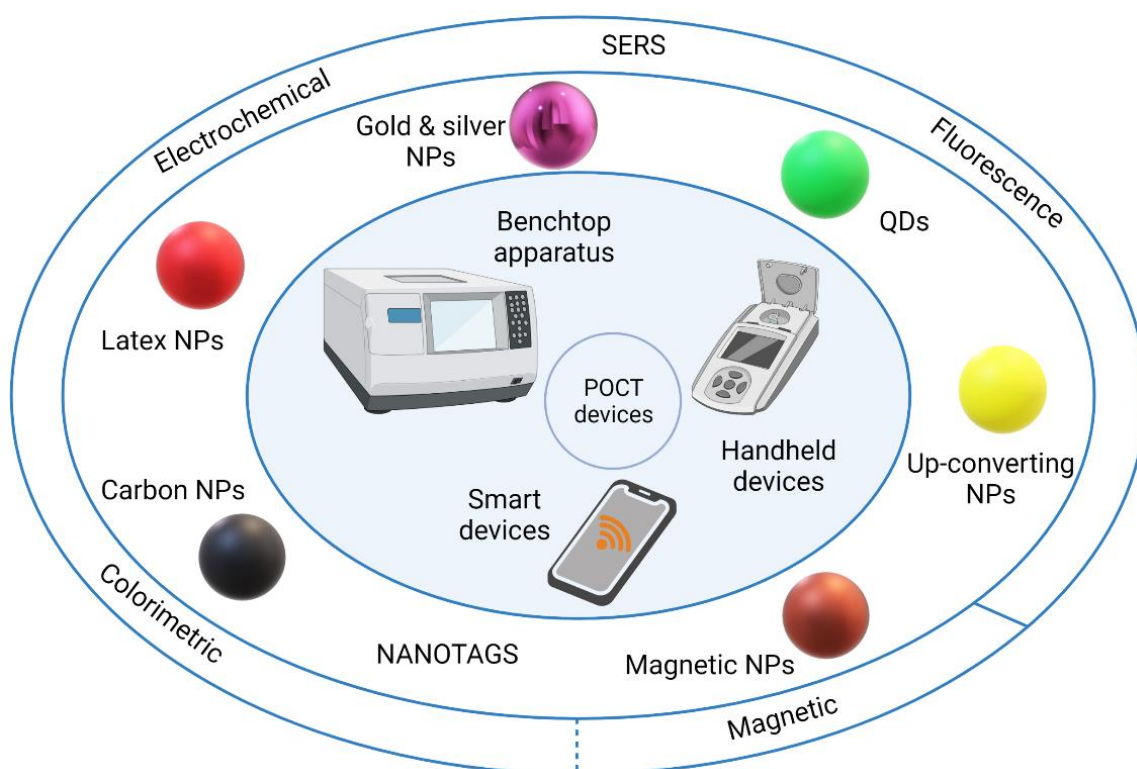


Figure 7. Schematic illustration of POCT devices according to their size and operational complexity together with the detection strategy based on the nanotag.

Improving sensitivity is achieved by using luminescent nanoparticles, mainly because these particles offer measurements with a higher signal-to-noise ratio. Quantum dots (QDs) are semiconductor nanocrystals with fluorescent properties [52]. Their emissions can be quantifiable and have high absorption coefficients. Their use in multiplex assays is auspicious, as they greatly simplify the analysis. When excited, QDs with different sizes provide non-overlapping signals, allowing each of these to be related

to a different analyte [53].

However, the union between the recognition elements and the QDs is not direct, involving more steps for their biofunctionalization [54]. They also present some limitations in their chemical and colloidal stability in biological environments, which is solved by their coating or encapsulation. Up-converting nanoparticles (UCNPs) are inorganic crystalline nanomaterials that convert near-infrared excitation light into visible and ultraviolet emission light [55]. Compared to QDs, UCNPs can enhance sensitivity by eliminating the autofluorescence background measurement of the sample matrix or the device components [56]. The naked eye cannot directly detect either of QDs or UCNPs. Hence, these tags require the development of devices for their quantitative analysis. Unlike in colorimetric readers, the detectors for these particles need high-power light sources, such as lasers and emission filters. This is a disadvantage as it makes their construction more complicated and expensive.

Thanks to SERS, metallic nanoparticles, such as silver and AuNPs, can be detected [57]. In this technique, when molecules are adsorbed onto corrugated metal surfaces, their inelastic light scattering is greatly enhanced by a factor reported to be as large as 10^{10} to 10^{11} . These magnitudes imply that the SERS-based sensors could detect even a single molecule [58], making them one of the most sensitive LFA detection methods. Nevertheless, reading out the samples takes time. It also needs a laser with high power and narrow spectral bandwidth and a Raman spectrometer, making it very expensive and keeping it from establishing itself as a POCT [59].

Another way to quantify LFAs is by electrochemistry. This approach uses redox tracers that can be quantitatively measured. To do so, it exploits electron transfer processes that occur at the interface of dedicated electrodes on the membrane [60]. The parameters that are recorded can be changes in current, voltage, or resistance. These systems are referred to as amperometric, potentiometric, or conductometric systems, respectively. The attractions of this technology are its simplicity, its great sensitivity, and the rapid generation of a signal. Moreover, it is cost-effective, and its mass production is already implemented thanks to the commercial glucose sensor. However, this methodology still suffers from limited applicability due to design complications: it involves adding specific agents and requires the assay to be performed in solution. Most

importantly, the integration of electrochemical transducers still requires complicated fabrication methods [61].

Lastly, magnetic nanoparticles have been postulated as an exciting alternative to traditional colorimetric labels, such as AuNPs. There are several situations where MNPs stand out and allow obtaining substantial increases in LFA sensitivity. The first is the very nature of biological samples since they do not contain magnetic substances per se. This avoids any background signal or possible interferences even with the most complex matrices. Second, MNPs' quantification is obtained thanks to the magnetic fields they generate when excited. This magnetic effect is independent of both visual and mechanical contact and is spatially distributed. When the nanoparticles are retained in the test line of the LFAs, they are distributed throughout the volume of the membrane, whose thickness is around 100 μm . Optical methods quantify the signal only from the surface of the strip, which is only about 10% of the cross-sectional volume. More than 90% of the labeled analyte is, therefore, undetected [42]. However, magnetic signals from the entire strip volume can be detected, thus considerably increasing the sensitivity of the assays (see Figure 8A).

Additionally, the magnetic signal is much less dependent on the environmental conditions in which the measurements are taken compared to optical methods. This facilitates the interpretation of the results and their reproducibility. Furthermore, the magnetic signal has greater stability since it is not affected by aging, darkening, or staining of the membrane. Also, there are complex samples in which optical methods must be discarded: they might give false results due to colorimetric interferences (see Figure 8B). What is more, MNPs offer a dual detection mode, meaning they can also be used as visual markers thanks to their color, which offers greater contrast with the membrane, thus increasing the signal-to-noise ratio for optical detection.

The magnetic properties of these NPs allow additional means to improve sensitivity. In this aspect, there are mainly two approaches. The first takes place before performing the test: magnetic pre-concentration [62]. Often, the samples to be analyzed are in very complex matrices with other components that could interfere with the performance of the LFAs. Other times, the samples may be so diluted that the signal would be undetectable. In both cases, pre-concentration improves sensitivity by

enriching in the component of interest the portion of the sample to be analyzed. The procedure is simple and does not require additional sophisticated instruments, such as separation columns or different chromatographs. In this case, the MNPs are biofunctionalized with the analyte-specific antibody and mixed with the sample. After the immunorecognition reaction occurs, a magnet is placed in proximity. Its field collects the MNPs, with the advantage that they will carry the analyte with them. The supernatant then can be removed and the sample resuspended. Now, the sample contains the analyte in higher proportions (see Figure 8C).

The second sensitivity improvement approach occurs while the test is being performed. One of the parameters that most influences analyte-antibody (or aptamer) recognition is time allowed for the reaction to occur. An increase in reaction time can increase the number of captured labels in the test, and therefore, the signal [63]. Although there are options such as adding cotton threads into the membrane to slow the flow rate, the ideal would be something that could be activated and deactivated when needed. In this sense, the magnetic character of the MNPs can be used to retain them in the area of the test line by just placing a magnet beneath the strips. In this way, the interaction time between magnetic probe-labeled targets and the capture antibody is increased. When the magnet is removed, normal flow is reestablished. This method has achieved great improvement in sensitivity compared to that of conventional LFAs [64].

As mentioned before, there is still no ideal label, but MNPs come very close. MNP synthesis in the laboratory is achieved through different methods, allowing fine control and tuning of their structural and magnetic properties. Its colloidal stability is obtained through different approaches, such as coating with different polymers or liposome encapsulation. The superficial chemical groups of the latter fulfill the function of acting as a link to the biorecognition elements through relatively simple protocols. To be quantified, several magnetic readers can be attached to the strips, relying on different principles, including Hall-effect, magnetoresistance, and induction.

Therefore, magnetic lateral flow assays (MLFAs) can overcome the limited analytical sensitivity and low quantitative capability of conventional LFAs. They already comply with the REASSURED (real-time, ease of collection, affordable, sensitive, specific, user-friendly,

rapid/robust, equipment-free, and deliverable to end-users) guidelines stipulated by the WHO. Now, suppose they demonstrate high-performance testing. In that case, the MLFAs could be established as the most common biosensing platforms in healthcare, food testing, and environmental control.

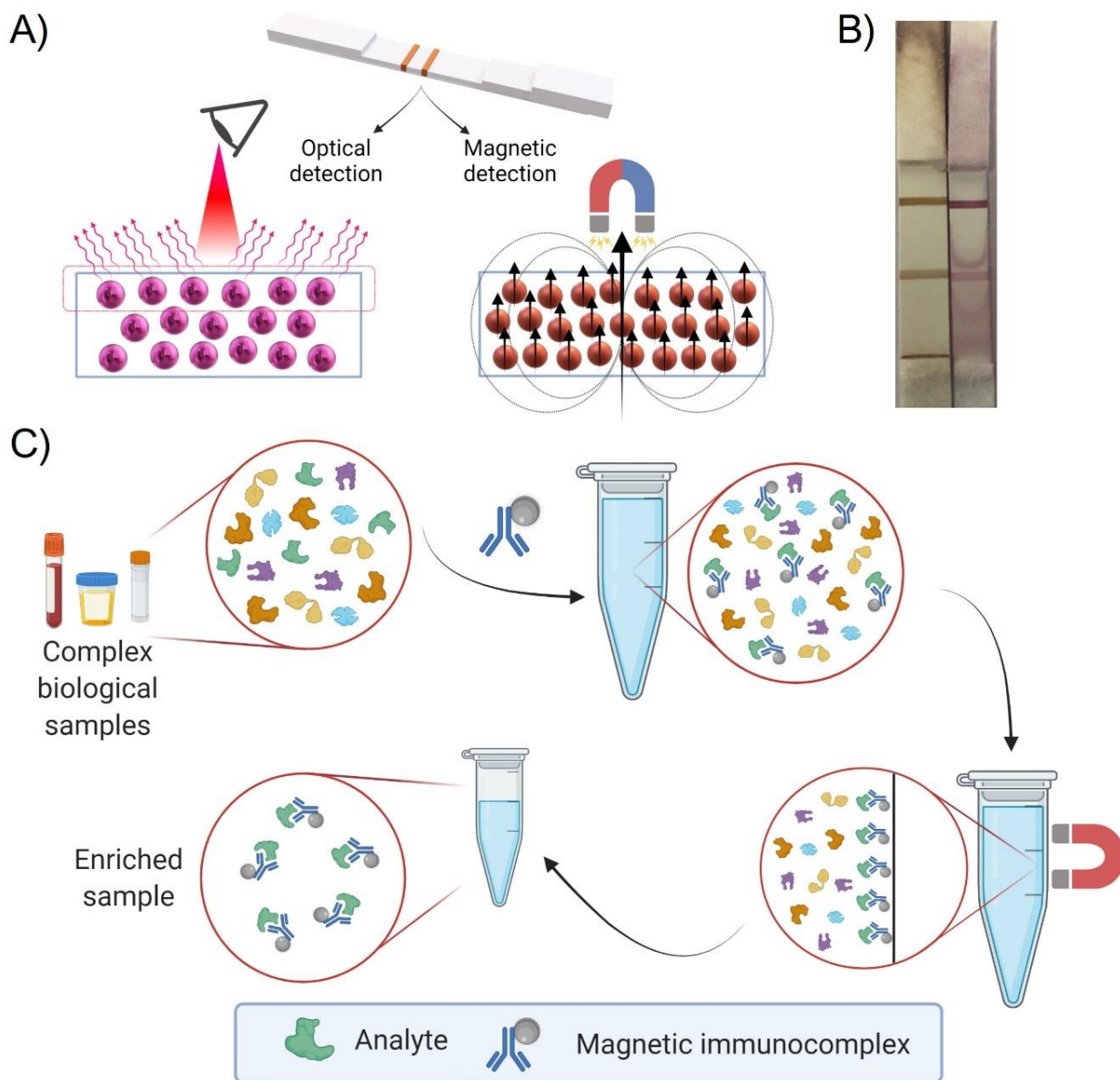


Figure 8. A) Comparison of the contribution of AuNPs labels in optical and MNPs in magnetic detections. B) Comparison of LFAs for histamine detection in wine using MNPs (left) and AuNPs (right) as labels. Obtained from [65]. C) Schematic illustration of a magnetic pre-enrichment protocol.

That is to say, MNPs' characteristics have aroused a fierce interest in their application in bioanalysis and modern biomedicine over the past 30 years. Different scientists have shown how MNPs can be used to

develop diagnostic tools, prevent, and treat diseases, selectively target tissues and organs, or regenerate them. This has sparked the interest of hundreds of scientists from different fields to join forces in fundamental studies of MNPs. With a wide catalog of applications, MNPs are well worth analyzing, studying, and understanding.

II. Objectives

Health care, environmental control and food safety are social challenges that require new technologies to improve the current diagnostic tests. The rapid, cost-effective, and sensitive detection of biomolecules can prevent the spread of infectious diseases, prematurely diagnose pathologies, monitor their treatment, and control food quality. Lateral flow strips have proven to be effective and portable tools capable of detecting the presence or absence of many compounds, usually in less than 30 minutes. However, their reliable quantification is still a challenge that brings together physicists, chemists, biologists, engineers, and material scientists. Magnetism can contribute to increasing their sensitivity and quantifying performance.

This research thesis aims at analyzing the potential of magnetic nanoparticles and their ideal characteristics for application in rapid diagnostic tests for biomolecule quantification. For this purpose, several specific objectives have been defined:

- Review the state of the art of MNP synthesis and characterization techniques with a particular focus on their use in biomedical applications.
- Test various MNPs for bioapplication in magnetic resonance imaging, magnetic hyperthermia, and, especially, magnetic quantification in biosensing. The requirements of the particles for lateral flow immunoassays deserve special attention.
- Correlate the signal given by the MNPs in a radio frequency inductive sensor with properties like their initial magnetic susceptibility, magnetic moment, size, and clustering degree.
- Investigate the optimal bioconjugation conditions to apply the selected MNPs for pneumolysin detection and design and fabrication of a lateral flow immunoassay, including a magnetic immuno-concentration step. Calibration of the detection curves and calculation of the limits of detection for optical presence/absence and magnetic quantitative biosensing.
- Design and develop a rapid magnetic serological test to detect the presence of antibodies against severe acute respiratory syndrome coronavirus 2 (SARS-CoV-2).

Part B

SECTION I

MAGNETIC
NANOPARTICLES IN
BIOMEDICINE

I. The nanoscale

Mankind has always been fascinated by big things. Planets, galaxies, and the universe, in general, have always amazed humanity. However, until recently, we did not ask ourselves about the “staggeringly small world below.” The great physicist Richard Feynman is considered the father of nanotechnology, catalyzing its development with his lecture at the annual American Physical Society meeting in 1959. The development of nanotechnology has been driven by the information revolution, which has allowed the progress in computer systems and the Internet. The parallel evolution of technology associated with this revolution, such as the development of integrated circuits, has allowed us to enter this nanometric world and begin to discover all its possibilities.

Nanotechnology is defined as the understanding, manipulating, and controlling matter at dimensions between 1 nm and 100 nm. At these scales, materials present unique phenomena and characteristics that are very different from those of bulk materials, enabling novel applications.

Today, nanotechnology impacts human life every day. Remarkable applications in different fields spark even greater the interest in the scientific community. Biomedicine is one of them in which nanotechnology presents a huge potential for diagnosis, prognosis, and specific treatment. Remarkably, there are a plethora of medically related products containing nanomaterials on the market. For example, the tremendous success of coronavirus disease 2019 (COVID-19) vaccines is worth noting. They would not have been possible without the nanomaterials in which they are encapsulated. The great interest caused by nanoparticles (NPs) is mainly due to their size: they are very similar to most biological entities, such as cells, proteins, or viruses. They also have a large specific surface, which allows the attachment of many molecules, either as bio-recognition elements or cargo. Furthermore, biomedicine can take advantage of different and peculiar properties or states the NPs have at these scales.

II. Magnetism at the nanoscale

Magnetism has to do with orbital and spin angular momentum of electrons and how their spins interact with one another. As all matter is made up of atoms, all matter is magnetic at some level. The question is

whether or not there is a collective long-range interaction between atomic magnetic moments.

When a magnetic field (H) is applied to any material, the individual atomic moments contribute to the overall magnetic induction (B) of the material following equation (1):

$$B = \mu_0(H + M) \quad (1)$$

where μ_0 is the permeability of vacuum, and M is the magnetization (magnetic moment per unit of volume). To some extent, all materials respond to a magnetic field. One way to classify them is, in turn, based on their volumetric magnetic susceptibility (χ). As its name suggests, it quantifies how susceptible the material is to being magnetized by a magnetic field H . Susceptibility χ is dimensionless in the International System of Units (SI) and correlates the induced magnetization M to the field H :

$$M = \chi H \quad (2)$$

In this way, we can classify matter into diamagnetic, paramagnetic, antiferromagnetic, and ferromagnetic, according to its response to an applied magnetic field (see Figure 9.) Diamagnetism is usually very weak. The atoms within these materials have no net magnetic moment, and when exposed to a magnetic field, a slight repulsion is produced. This means that the magnetization has the opposite direction to that of the applied field. In diamagnetic materials, χ is negative, with values around 10^{-6} , and independent of the temperature. Some examples of these materials are water, most organic compounds (oil and plastics), biological compounds (proteins, DNA, etc.), and metals such as Hg or Au.

Paramagnetism is the tendency of certain materials to become slightly magnetized in the direction of the applied field. Paramagnetic substances have unpaired electrons that, in the absence of external magnetic fields, have their fluctuating atomic magnetic moments randomly oriented. Therefore, they do not present a net magnetization. When a magnet field is applied, there are different theories to explain the paramagnetic behavior depending on the specific material. When they have non-interacting localized electrons, the Langevin model states that this random orientation of the magnetic moments results from thermal agitation. The application of a magnetic field creates a slight alignment.

As the temperature increases, the latter will be harder to obtain due to the thermal agitation opposing it. Hence, the χ of the material is inversely proportional to the temperature. This behavior is known as the Curie law. The Pauli model applies to materials where the electrons are free and interact to form a conduction band. Under an applied field, there is an imbalance between electrons with opposite spins leading to a low magnetization in the same direction as the field. In this case, χ is positive and independent of temperature.

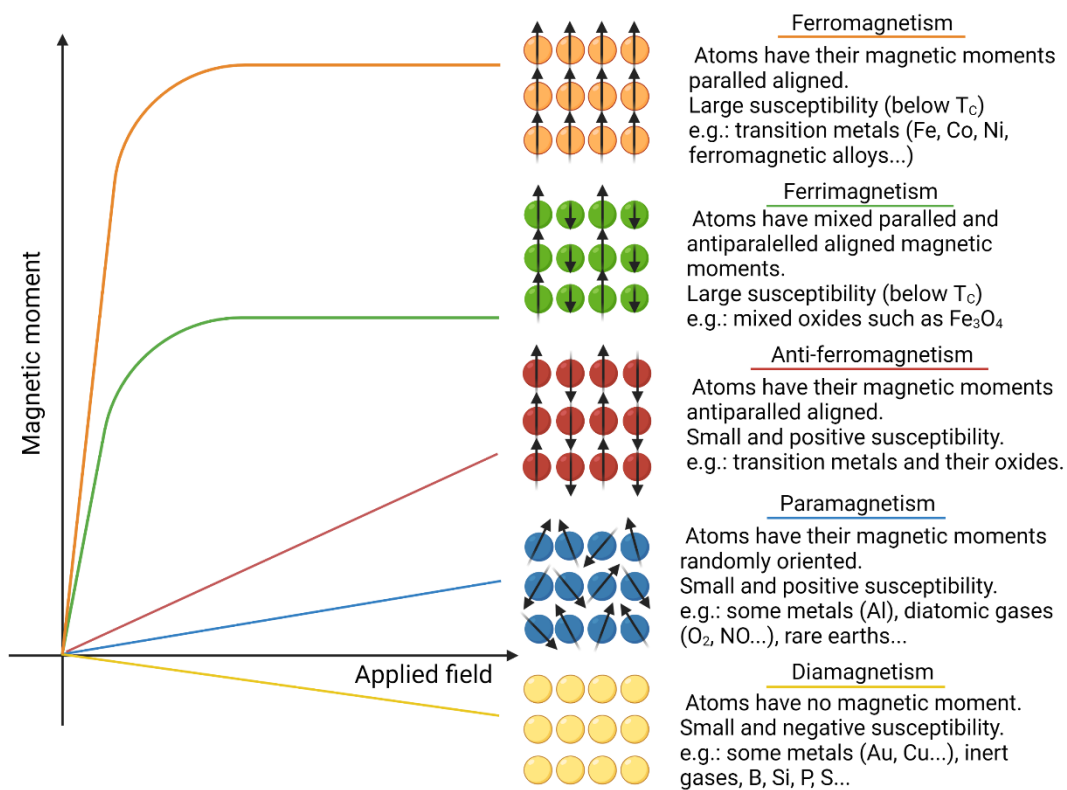


Figure 9. Summary of the magnetic behavior of materials.

Antiferromagnetic materials align in a regular pattern alternating the directions of the neighboring spins. Macroscopically, it is similar to paramagnetism, where the antiparallel alignment results in a zero net moment at zero field. When a field is applied, a total moment is obtained. Antiferromagnetic order may exist at temperatures lower than the Néel temperature (T_N) above which it vanishes, and the material behaves as a paramagnet. So, their susceptibility is small but positive and reaches a maximum at T_N . Examples of antiferromagnetic materials include metals such as Cr, alloys such as iron manganese (FeMn), and oxides such as nickel oxide (NiO) or hematite (α - Fe_2O_3).

Lastly, ferromagnetic and ferrimagnetic materials are those that are classified as “magnetic” because they have a net magnetic moment in zero field. Moreover, they are strongly attracted to a magnetic field. In ferromagnetic materials, the atomic magnetic moments can interact to be aligned parallel to each other due to the strong interaction between neighboring spins, known as the exchange interaction. This results in a positive and significant susceptibility (around $10^3 - 10^6$), and, in small particles, and a non-zero magnetic moment even when no field is applied. This nonvanishing magnetization is usually known as spontaneous magnetization. Of the 3d transition metals, only Fe, Co, and Ni are strictly ferromagnetic up to a critical temperature, called Curie temperature (T_C). The thermal agitation above T_C destroys their magnetically ordered arrangement and turns the materials into paramagnetic.

In the case of ferrimagnetic materials, some of the magnetic moments are aligned antiparallel, reducing the net magnetic moment. Still, it never becomes zero (as in the case of antiferromagnetic materials) except at a compensation temperature. Usually, exchange interactions of the different ions in the crystalline structure of ferrimagnetic materials lead to parallel alignment in sublattices A and B, which are aligned antiparallel to each other.

The magnetism in ferrimagnetic and ferromagnetic materials is similar. Their susceptibilities can have similar values, but ferrimagnetic materials commonly exhibit lower saturation magnetizations. They are also temperature-dependent and become paramagnetic above T_C . Typical ferrimagnetic substances are ferrites, including spinel-type ferrites, with a general formula $M^{2+}Fe_2^{3+}O_4$, where M^{2+} can be any divalent metal (Fe^{2+} , Co^{2+} , Mn^{2+} , Zn^{2+} , Ni^{2+} , etc.) Among them, iron ferrites are the workhorse in biomedicine applications since the human body can easily metabolize iron [66,67].

In addition to possessing a net atomic magnetic moment ($\vec{\mu}$), all magnetic materials have other characteristics when exposed to an external magnetic field (H), which are captured in the hysteresis loops (see Figure 10). If the material has never been magnetized, its magnetization will follow the dashed line up to saturation (point A), which represents the magnetic saturation (M_S). At this point, all the magnetic moments within the material are aligned parallel to the direction of the external field. When H is reduced to zero, the curve will move to point B,

where there is still some residual magnetization. This is known as remanent magnetization (M_r). When the field is reversed, the magnetization will move to point C, where the coercive field or coercivity (H_c) means there is no magnetization within the material. The switching field (H_{sw}) is a more appropriate term to describe the necessary magnetic field to reverse the moment orientation of a magnetic material. However, both terms are commonly used interchangeably. Continuing with the hysteresis curve, if the field applied continues to increase in the negative direction, the material will reach saturation in the negative direction (point D). When reducing H to zero, the curve will get to point E, having a remanent magnetization in the negative direction. Then, when point F is reached, the coercivity is in opposed direction. If the field is increased even more, the curve reaches point A again, closing the loop. Notice that the curve does not return to the initial magnetization curve. To do so, it would be necessary to demagnetize the material to remove the remanent magnetization.

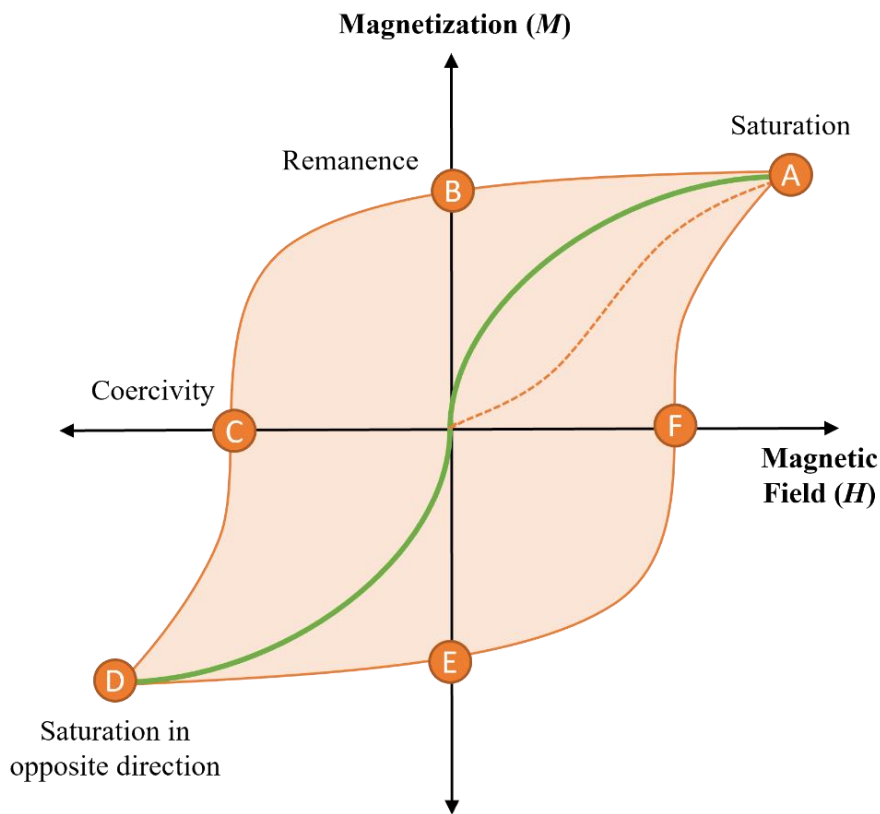


Figure 10. Schematic of a hysteresis curve showing the relationship between the magnetization (M) and the applied magnetic field (H) in ferromagnetic (orange) and superparamagnetic (green) materials. The dashed orange line represents the initial magnetization curve.

Beyond these magnetic features, there is another critical parameter to consider in magnetic materials, which becomes crucial at the nanoscale. In single-crystalline magnetic materials, the magnetization depends on the magnitude and direction of the external magnetic field with respect to the crystallographic axes. As the symmetry is reduced within a crystal lattice, it creates easy and hard directions of magnetization. The total magnetization of a system with no applied field will prefer to lie along an easy axis. Hence, the magnetization is determined by the anisotropy of the system (K). The energy required to reverse the direction of the magnetization is the anisotropy energy. The anisotropy net energy density balances the energies coming from crystalline lattice effects (structure, shape, volume, or defects) and the collective magnetic interactions (exchange or interparticle interactions). This means that contributions to K are complex and depend on the unique features of the material under study. There are different sources of anisotropy in a material, which significantly influence the overall magnetic behavior. However, in real systems, all the contributions are considered as an effective anisotropy (K_{eff}).

- Magnetocrystalline anisotropy forces a magnetic moment to stay in certain preferred orientations that match the crystallographic axes thanks to spin-orbit coupling.
- Surface anisotropy comes from the symmetry break of the surface atoms and their different interactions with their neighbors in the core. It has great importance in small particles because of their large surface-to-volume ratio.
- Shape anisotropy favors the magnetization depending on the major or minor sample axes thanks to the energy minimization of the magnetostatic fields. There is a demagnetizing field (H_d) that opposes the magnetization and tends to demagnetize the sample. H_d is larger along a short axis than along a long axis, causing magnetization to align with the long axis of a nanowire or within the plane of a thin film.
- Colloidal anisotropy: Higher-order structures such as chains can be formed when NPs are in a liquid. This will create a preferred orientation of the magnetic moments.
- Strain anisotropy comes from mechanical stress when the crystal lattice is deformed.

III. Magnetic nanoparticles

Magnetic nanoparticles (MNPs) are solids of mainly quasi-spherical shape made of a magnetic material with sizes below 100 nm. The total energy of bulk magnetic materials is the sum of contributions from the exchange (E_{ex}), magnetostatic or dipole (E_{ms}), anisotropy (E_{K}), and Zeeman (E_{Z}) energies:

$$E_{\text{tot}} = E_{\text{ex}} + E_{\text{ms}} + E_{\text{K}} + E_{\text{Z}} \quad (3)$$

The thermal energy ($E_{\text{thermal}} = k_{\text{B}}T$) is particularly important because it sets the scale by which all the other energies are compared. All these energies accumulate and balance within the materials. To minimize this overall value, magnetic materials spontaneously arrange themselves into magnetic domains. They are regions containing magnetic moments coupled in the same direction and separated by domain walls. Here, a smooth change from one domain's moment direction to another takes place. When the material size is reduced, like in a system of small particles, the energetic stability achieved through these domains' formation decreases, and it adopts a single-domain configuration (see Figure 11). A magnetic monodomain particle has a magnetic moment ($\vec{\mu}$) proportional to its volume (V) and its saturation magnetization (M_{S}) as $\vec{\mu} = M_{\text{S}} \times V$. It is usually represented as a “superspin” as it rotates coherently as a single giant magnetic moment (since there are no domain walls to move) when an external field is applied. Depending on the size and the material, the magnetic moments of single-domain particles can be around 10^3 to 10^5 Bohr magnetons (μ_{B}). The critical radius (r_{C}) below which a particle acts as a monodomain can be roughly approximated as follows:

$$r_{\text{C}} \approx 9 \frac{\sqrt{AK}}{\mu_0 M_{\text{S}}^2} \quad (4)$$

where A and K are the exchange stiffness and the anisotropy constants, respectively, μ_0 is the vacuum permeability and M_{S} the saturation magnetization. Typical values for MNPs are in the order of 5 nm to 1000 nm, specifically, ca. 8 nm for Fe, ca. 50 nm for CoFe_2O_4 , ca. 64 nm for Fe_3O_4 , and ca. 375 nm for SmCo_5 .

The energy associated with a monodomain particle with uniaxial anisotropy depends on the anisotropy constant K , the volume of the

particle V , and the angle between the easy axis of magnetization and the magnetization direction θ (see Figure 12A). As an approximation, this energy barrier can be written as:

$$E(\theta) = KV \sin^2 \theta \quad (5)$$

When a magnetic field is applied, equation (5) must be subsequently modified considering the field angle (α) with respect to the anisotropy axis (see Figure 12A), as expressed in equation (6):

$$E(\theta) = KV \sin^2 \theta - \mu_0 H M_S V \cos(\theta - \alpha) \quad (6)$$

When no magnetic field is applied, there are two energy minima at $\theta = 0^\circ$ and $\theta = 180^\circ$ separated by an energy barrier (E_B) with a height equal to KV , so both magnetization states are equally probable (see Figure 12B). However, when a magnetic field is applied upwards or downwards, the state with the same orientation will become energetically favorable. The system will subsequently switch to that configuration.

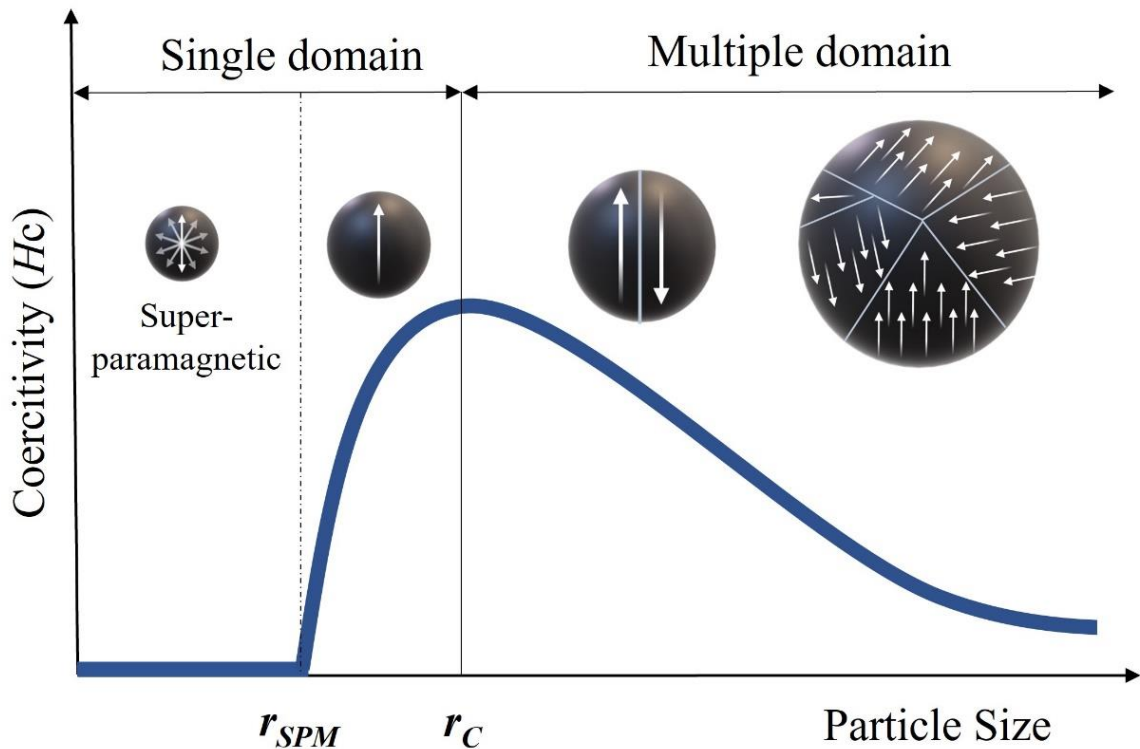


Figure 11. Representation of the domain structure and coercivity of a magnetic nanoparticle as a function of size.

1. Superparamagnetism

When the size of a single monodomain particle is further reduced and in the absence of a magnetic field, there will be a critical size (r_{SPM} , see Figure 11) below which the thermal energy itself ($E_{\text{thermal}} = k_B T$) will be able to overcome the anisotropy energy barrier ($E_B = K_{\text{eff}} V$). Then, the magnetization will spontaneously fluctuate from one direction to the other, as depicted in the middle of Figure 12B. This regime was named superparamagnetism (SPM) by Bean and Livingston in 1959, because it resembled the one for paramagnets but with magnetic moments and susceptibilities several orders of magnitude larger [68].

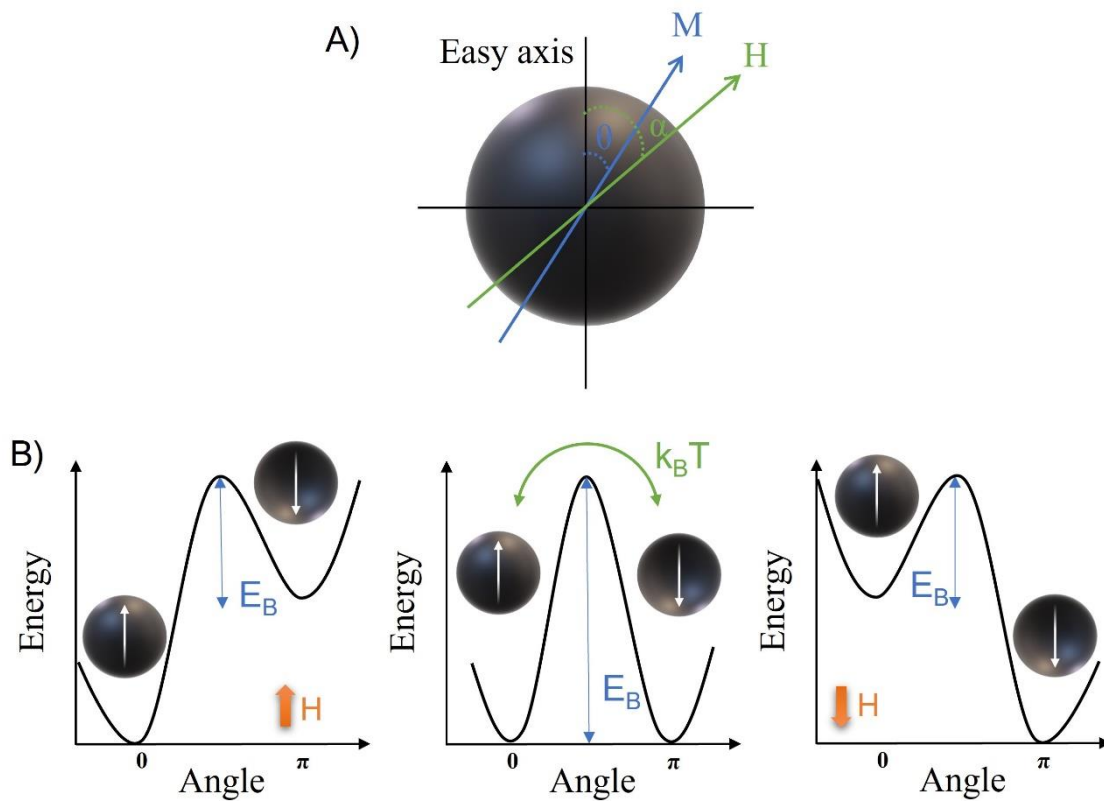


Figure 12. A) Definition of the usual axis system for a uniaxial nanoparticle under an external magnetic field. B) Representation of the switching of the magnetization of a uniaxial magnetic nanoparticle as a function of its direction. The height of the energy barrier E_B is given by the magnetic anisotropic constant and the particle volume.

The Néel-Brown model describes the superspin dynamics in superparamagnetic nanoparticles when no field is applied. For non-interacting particles with uniaxial anisotropy, there is a characteristic time, known as the Néel relaxation time (τ_N) for the magnetization reversal

due to the thermal fluctuations.

$$\tau_N = \tau_0 \exp\left(\frac{E_B}{k_B T}\right) \quad (7)$$

where k_B is the Boltzmann constant (1.381×10^{-23} J/K) and τ_0 is the attempt time, which depends on several parameters. However, it is assumed to be constant with values around 10^{-9} to 10^{-13} s. From equation (7), τ_N is an exponential function of the particle size that ranges from nanoseconds for NPs to years in bulk materials. The process to reverse the magnetization by Néel relaxation is the moment rotation within the particle. However, when MNPs are dispersed in a solution (usually called ferrofluids), there is another relaxation process known as Brownian relaxation. It implies the rotation of the whole particle and is given as:

$$\tau_B = \frac{3\eta V_H}{k_B T} \quad (8)$$

where η is the fluid viscosity and V_H is the hydrodynamic volume of the MNPs.

The measured magnetic behavior of a magnetic nanoparticle will depend on the timescale of the measurement (τ_M). For macroscopic techniques such as vibrating sample magnetometer (VSM) or superconducting quantum interference device (SQUID) magnetometer, τ_M is 1 s and 100 s, respectively. However, for microscopic techniques, such as Mössbauer spectroscopy, nuclear magnetic resonance (NMR), or neutron scattering, the timescale is much shorter, in the range of nanoseconds or less (10^{-12} s to 10^{-7} s). Then, there will be two possibilities: If the measurement time τ_M is longer than the relaxation time τ_0 , the measured magnetization is averaged to zero, and the particle is in the SPM regime. The reversal happens faster than the measurement. If τ_M is smaller than τ_0 , the particle is in the blocked regime, meaning all the atomic magnetic moments within the particle seem to be frozen, and a nonzero magnetization is measured. The blocking temperature (T_B) separates these two regimes, and it depends on the τ_M . The blocking temperature T_B is related to the energy barrier $K_{\text{eff}}V$, so it increases with the volume of the particles. This means that the larger the particle, the higher the T_B , so the more difficult to enter the superparamagnetic regime. The value for T_B can be calculated by:

$$T_B = \frac{K_{\text{eff}}V}{\ln(\tau_M/\tau_0) k_B} \quad (9)$$

Considering a spherical nanoparticle, the diameter at which the superparamagnetic regime appears at a given T_B is:

$$d_{\text{SPM}} = \left[\frac{6k_B T_B \ln(\tau_M/\tau_0)}{\pi K_{\text{eff}}} \right]^{1/3} \quad (10)$$

This means that T_B and d_{SPM} depend on the measurement time. Thus, T_B is not a critical temperature as is T_C , and d_{SPM} is not governed by energy balance arguments as is the monodomain size. For typical values of $\tau_M = 100$ s and $\tau_0 = 10^{-9}$ s in equations (9) and (10), the T_B and d_{SPM} can be calculated following the well-known equations (11) and (12), respectively.

$$T_B = \frac{K_{\text{eff}}V}{25k_B} \quad (11)$$

$$d_{\text{SPM}} = \left[\frac{6k_B T_B 25}{\pi K_{\text{eff}}} \right]^{1/3} \quad (12)$$

The magnetization of MNPs in SPM regime is averaged to zero when no field is applied, as their magnetic moment flips several times during the measurements (providing that $T > T_B$ and $\tau_M > \tau_N$). When a field is applied, the MNPs' magnetic moments tend to align with the field direction. Therefore, a net magnetization appears. This average magnetization of an ensemble of non-interacting nanoparticles can be described by the Langevin equation as follows:

$$M = M_S L(x) = M_S \left[\coth(x) - \frac{1}{x} \right] \quad (13)$$

where $x = \mu_0 M_S V H / k_B T$. This relationship is identical to that of atomic paramagnetic magnetization but with extremely large magnetic moments and susceptibilities. Magnetization curves show no hysteresis, meaning they do not have coercivity and remanence (see Figure 10). Moreover, when these anhysteretic magnetization curves are plotted as a function of H/T , they superimpose on a single universal curve for all fields and temperature ranges. Therefore, the Langevin equation allows the average

magnetic moment per particle to be obtained, and consequently, the average particle size from the experimental isothermal magnetization curves. It is important to remark that the Langevin equation does not consider the anisotropy and the magnetic interactions [69]. Additionally, any sample size distribution must be considered because real MNPs samples will probably not be an ensemble of identical, monodisperse MNPs. Usually, the overall sizes can be described by a log-normal distribution [70]. Then, equation (13) must be adjusted for a volume or diameter weighted log-normal distribution [71,72].

The diameter obtained by fitting the Langevin equation has been found to be smaller (even by a few nanometers) than the physical diameter obtained by electron microscopy (see Figure 15). This result suggests the existence of a magnetically dead layer on the surface of the MNPs, where spin canting and other phenomena may lead to disorder of the magnetic dipoles, thus, decreasing their magnetization [73]. These surface effects cannot be neglected at the nanoscale. When a material is reduced in size, the fraction of atoms at the surface is considerable. For example, in a 3 nm particle, about the 80% of the atoms lie on its surface, which is structurally and magnetically disordered [74]. Therefore, the image of a perfect single-domain particle, in which all spins point in the same direction, and which coherently relaxes, is a dream. The magnetic diameter obtained from the Langevin equation suggests a core-shell structure for the particles, with a highly ordered core that can be described by the Stoner-Wohlfarth model [75], and a disordered shell of spins. A phenomenological expression has been used to include the effect of the surface anisotropy on the effective anisotropy. For a spherical nanoparticle it is as follows:

$$K_{\text{eff}} = K_b + \frac{6}{d_p} K_s \quad (14)$$

where K_b is the bulk anisotropy, K_s is the surface energy density, and d_p is the particle diameter. The results show that the surface anisotropy is two to three orders of magnitude greater than the bulk magneto-crystalline anisotropy [76]. Therefore, K_s plays a major role in the total anisotropy in nanoparticulate systems.

In addition to magnetization curves, zero-field cooling (ZFC) and field cooling (FC) measurements are recorded to characterize MNP ensembles.

These protocols allow the extraction of information about the above-described parameters such as the average blocking temperature, size distribution, or effective magnetic anisotropy. Starting with samples with no previous magnetic history, ZFC and FC curves are obtained as follows. ZFC (M_{ZFC}) starts by cooling the sample without field from room temperature, a DC field is applied, and the magnetization measured while warming the sample. What happens is that when the MNPs are cooled in zero field, their moments are randomly oriented when frozen. Then, a field is applied, but there is almost no magnetization because the moments are frozen. As the sample starts to warm, the magnetization will increase as more MNPs become unblocked due to the thermal energy. There will be a temperature at which the magnetization starts to decrease because more particles are in the superparamagnetic state. FC (M_{FC}) is obtained similarly, but this time, cooling the sample in the same applied field. Now, the moments are frozen in the direction of the applied field, so the starting measurements at low temperatures show non-zero magnetization values. However, the magnetization starts decreasing as the sample is warmed, and the thermal energy allows the moments to relax. This behavior can be different when magnetic interactions are present, as the magnetic moments are not so easy to align with the external field [77].

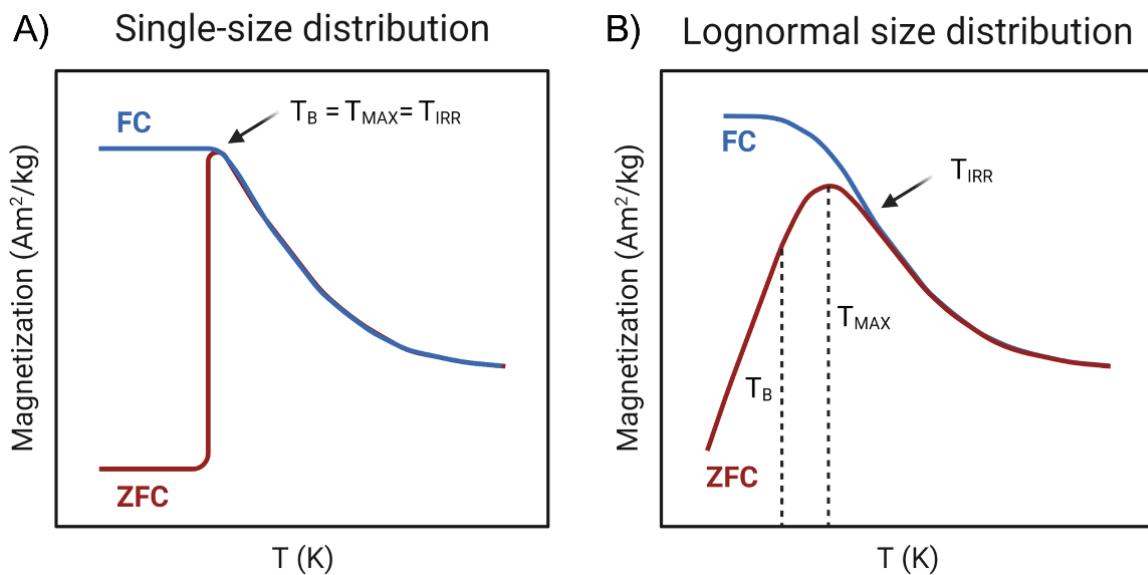


Figure 13. ZFC-FC curves for A) monodisperse MNP sample B) MNPs with a log-normal distribution. The difference in the blocking temperature (T_B), maximum temperature (T_{MAX}), and irreversibility temperature (T_{IRR}) are shown. Adapted from [78].

The blocking temperature T_B can be obtained from the transition between the blocked and the superparamagnetic states. For

monodisperse MNPs samples, T_B is given by the M_{ZFC} maximum (T_{MAX}). However, for real samples, T_B should be calculated from the temperature derivative of the difference of $M_{ZFC} - M_{FC}$. This difference gives information about the distribution of energy barriers, and thus, about the size distribution of the MNPs. The splitting point of the ZFC and FC curves is usually called the irreversibility temperature (T_{IRR}). For monodisperse samples, T_{IRR} should coincide with T_B . Otherwise, the polydispersity degree of the MNPs can be quantified by the difference between T_{MAX} and T_{IRR} (see Figure 13). Once T_B is determined, K_{eff} can be calculated from equation (11).

2. Dynamic magnetic properties

AC measurements can be applied to get information about the dynamic magnetic properties of MNPs. To do so, a small amplitude alternating magnetic field $H(t) = H_0 \cos \omega t$ is superimposed on the DC field, inducing a time-varying magnetization $M(t)$. At low frequencies ($f = \omega/2\pi$), the result is just the initial magnetic susceptibility χ (see equation 2) [79]. However, when f is increased, the magnetic moments in the sample lag $H(t)$, resulting in a complex susceptibility χ . Thus, AC magnetic measurements allow the real χ' (in phase with the field) and the imaginary χ'' (out of phase with the field) parts of the magnetic susceptibility to be obtained as a function of frequency [79,80]:

$$\begin{aligned}\chi'(\omega) &= \frac{\chi_0}{1 + (\omega\tau)^2} \\ \chi''(\omega) &= \frac{\chi_0\omega\tau}{1 + (\omega\tau)^2}\end{aligned}\tag{15}$$

where χ_0 is the DC susceptibility ($\chi_0 = (M_s V)^2 / 3k_B T$) and τ is the effective characteristic relaxation time. MNPs can relax their magnetic moments by two mechanisms [80]: Brownian relaxation (τ_B), which involves the rotation of the whole particle, and Néel relaxation (τ_N), in which it is the magnetic moment that relaxes within the NP. Whether MNPs relaxes by Brownian or Néel relaxations depend on parameters such as the size, the magnetic anisotropy, the viscosity of the medium, the magnetic interactions, and the excitation frequencies. In any case, both mechanisms can contribute, and therefore, an effective characteristic relaxation time can be estimated as [81]:

$$\tau = \frac{\tau_B \tau_N}{\tau_B + \tau_N} \quad (16)$$

3. Magnetic interactions

Magnetic interactions play an important role in real MNPs samples, greatly affecting their macroscopic magnetic properties [82]. There are different types of magnetic interactions: dipolar or magnetostatic interactions, exchange interactions, and Ruderman-Kittel-Kasuya-Yosida (RKKY) interactions. Magnetostatic and exchange interactions both apply in cases of agglomeration (formation of reversible and alterable magnetic groups) or aggregation (formation of magnetic groups that remain permanently together) [83]. These two processes usually lead to a mix of clusters in MNP samples. Oscillatory RKKY interactions may occur when the MNPs are metallic and dispersed in a conductor.

Magnetostatic or dipolar interactions are long-range interactions whose strength depends on interparticle distances. The energy of this interaction for a system of randomly distributed MNPs with an average magnetic moment μ and an average distance d can be approximated as [84]:

$$E_d \approx \frac{\mu_0 \mu^2}{4\pi d^3} \quad (17)$$

When there is agglomeration/aggregation, the distance among the MNPs decreases, and the dipolar interactions increase, favoring a collective behavior. Therefore, magnetization and ZFC curves can change significantly. For example, there is a shift in the maximum temperature of the ZFC curve towards higher temperatures compared to non-interacting materials. In the FC curve, the interactions can result in a temperature-independent magnetization below this maximum temperature [85]. To avoid this type of interaction, MNPs are usually stabilized with polymers or diluted; both approaches ensure adequate separation.

Short-range exchange interactions involve the coupling of the magnetic moments of neighboring atoms. This coupling forces their magnetic moments to align. Exchange interactions applied within MNPs and may occur at the interfaces of aggregated MNPs [83].

For core-shell MNPs, there is also an important magnetic interaction at the core-shell interface. The exchange bias effect is attributed to an interfacial exchange anisotropy at the intersection between a ferromagnetic and antiferromagnetic phase. This shifts the hysteresis loop along the magnetic field axis after field cooling [86].

Different experimental approaches can assess the nature and strength of magnetic interactions. One of the most accepted ones is the remanent magnetization technique. It is based on the comparison of the isothermal remanent magnetization (IRM) and the direct current demagnetization (DCD) curves [84,87,88]. The IRM curve starts from a totally demagnetized state. Then, the remanence magnetization (m_r^{IRM}) is measured after the application and removal of an increasing field as many times as necessary until the sample reaches saturation. On the contrary, the DCD curve starts from negative saturation, to which a field in the opposite direction is applied and removed. The m_r^{DCD} is measured, and the experiment repeated increasing the field until the saturation in the opposite direction is reached. In an ideal non-interacting system of monodomain particles, both IRM and DCD curves are related via the Wohlfarth relationship as follows [89,90]:

$$\delta M(H) = m_r^{\text{DCD}}(H) - (1 - 2m_r^{\text{IRM}}(H)) = 0 \quad (18)$$

A non-zero value of δM suggests the presence of interactions. For positive δM values, the nature of the interactions promotes the magnetization state (exchange), whereas negative δM values promote magnetostatic interactions (dipolar). Henkel plots are another way to represent the information in equation (18). It consists of a graph of m_r^{DCD} versus m_r^{IRM} . For non-interacting MNPs it is a straight line with a slope of -2. Magnetic interactions cause deviations from this linearity.

It is important to remark that δM and Henkel plots show the predominant interaction in a system. There is always a balance between exchange and dipolar interactions, which are both present, but contribute oppositely in Henkel plots. For a thorough insight into the nature of magnetic interactions, the activation volume (V_{act}) can be obtained by relaxation measurements [84,91]. The V_{act} is the smallest unit that reverses its magnetization. This technique compares the physical and activation volumes to provide information about the interactions.

4. Synthesis of magnetic nanoparticles

Many different routes have been proposed to synthesize MNPs during the last 20 years, either for their fundamental scientific interest or for their many possible technological applications. In fact, it is each application that determines the preferred method to obtain the particles. For example, in data storage, MNPs must be stable and not influenced by temperature fluctuations. In biomedicine, especially for *in vivo* applications, there are quite a few more requirements. In general, MNPs with a superparamagnetic behavior at room temperature are ideal: they can be used to target any part of the human body under the influence of a magnetic field. Once this is removed, the SPM particles retain no remanent magnetism, and therefore, they are unlikely to agglomerate. This characteristic is very important because there is a reduced danger of thrombosis or blockage of blood capillaries. This means precise control of the particles' size and its size distribution. MNPs also need biocompatibility and stability in aqueous environments. The former is accomplished via their elemental composition or by a polymeric layer or encapsulation procedure. Different compositions have been proposed, such as single metal nanoparticles or different ferrites. However, the iron oxides magnetite (Fe_3O_4) and maghemite ($\gamma\text{-Fe}_2\text{O}_3$) are the most relevant since the body easily metabolizes iron [67]. Because of this, iron oxides have been approved for their use in human by the Food and Drug Administration (FDA) in the USA and the European Commission in the EU [92].

Stability is achieved thanks to the steric and coulombic repulsions of the coating chemical residual groups. These also will allow binding of biorecognition elements or drugs by entrapment, adsorption, or covalent attachment. There is still no golden standard route to produce MNPs that satisfy all the demands for their biomedical applications. Among the key parameters are the control of the composition, size and size distribution, shape, crystallinity, surface effects, collective interactions, and magnetic properties. All of them are determined by each other and the synthesis conditions, which stir a challenging interplay difficult to control.

The synthesis of the MNPs can be addressed by two different approaches: top-down or bottom-up [93]. In the former, bulk materials are broken down into nanometer sizes. In the latter, the atoms composing the final MNPs are nucleated and grow into coordinated nanostructures

(see Figure 14A). These approaches can also be classified into three groups: physical (milling or grinding, gas-phase deposition, and electron beam lithography), wet chemical (co-precipitation, thermal decomposition, solvothermal, microwave-assisted synthesis, microemulsions, and polyol), and biological methods [94]. So far, there is a better understanding and control of the particle formation mechanism in the wet chemical methods, making them preferable for the synthesis of MNPs for biomedical applications. Table 1 gathers the most common synthesis routes for each group, remarking some of their advantages and disadvantages.

The formation of monodisperse colloidal particles was described by LaMer and colleagues in the 1940s, with two main factors governing the process: nucleation and growth. The separation in time of these two stages will lead to monodispersity. According to LaMer's work [95], the whole process can be divided into three phases (see Figure 14B). In the first one, the concentration of the solute's monomers increases gradually until it reaches supersaturation (C_{\min}). If there are no "seeds" in the medium homogenous nucleation will take place (otherwise, it will be a heterogenous one) at the maximum concentration (C_{\max}). In the second phase, nuclei are simultaneously formed, and the concentration of monomers drastically drops. Theoretically, no more nucleation will be possible from now on. Finally, in the third phase, nuclei will ideally grow through diffusion. However, other processes such as aggregating and Ostwald ripening have also been proposed [96].

It is important to remark that the large atoms at the MNPs surface led to an extremely high driving force of these particles to minimize the surface energy, which, consequently, results in uncontrolled growth and particle agglomeration. To avoid this drawback, different surfactant molecules are used to separate the nuclei formed and stabilize even the smallest particles. These molecules are usually long hydrophobic hydrocarbons or polymers that attach to the surface of the MNPs and leave functional groups at their endings (phosphines, amines, thiols, carboxylates).

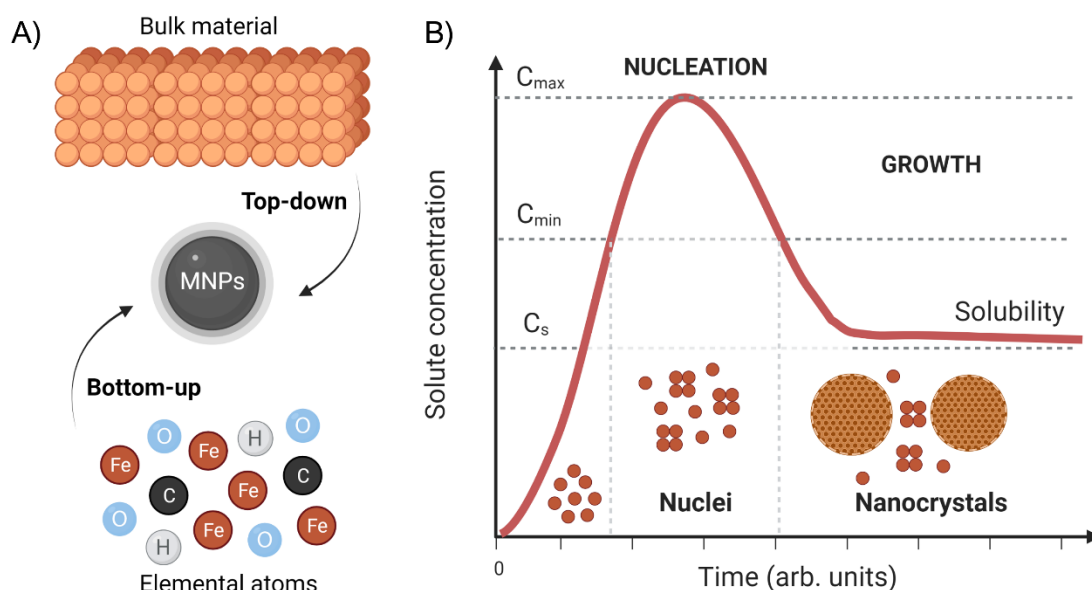
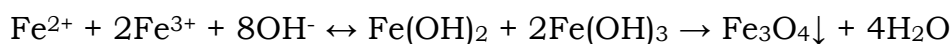


Figure 14. A) Scheme of the two approaches to obtain MNPs. B) Classical LaMer model for the formation mechanism of monodisperse particles in solution.

- **Co-precipitation**

Aqueous co-precipitation is the most extended route to obtain MNPs, especially iron oxide. The process is straightforward and consists of the dissolution of the metal precursors Fe^{2+} and Fe^{3+} (or other ionic metals) to mix them with a basic reagent to precipitate the spinel form. It was developed by Massart [97]. Since then, many changes have been introduced. One of the most important is the addition of capping agents in the reaction media that allow the obtention of stable colloidal suspensions. Additionally, they protect magnetite (Fe_3O_4) from being oxidized into maghemite ($\gamma\text{-Fe}_2\text{O}_3$) by the presence of oxygen. Two steps are proposed for the synthesis reaction:



However, more recent studies suggest much more complex mechanisms that have an enormous influence on the final precipitated product, with even the appearance of non-magnetic phases.

This procedure yields reasonable amounts of MNPs (gram-scale), allowing partial control over the size and shape of the particles by adjusting parameters such as the ionic strength, temperature, pH, or reagents concentration.

- **Thermal decomposition**

Metal-organic precursors (e.g., iron (III) acetylacetonate $\text{Fe}(\text{acac})_3$, iron (III) decanoate ($\text{Fe}(\text{decanoate})_3$, or iron (0) pentacarbonyl ($\text{Fe}(\text{CO})_5$)) are decomposed or reduced in high-boiling non-polar solvents (e.g., octyl ether, benzyl ether, or octadecene) in the presence of organic surfactant molecules (e.g., oleylamine or oleic acid). This method allows fine control over the size and distribution thanks to separating the nucleation and the growth phases. These and other characteristics such as shape and crystallinity can be controlled by basic parameters of the reactions, namely temperature, heating time and rate, and precursor-to-surfactant ratios. However, the yield of this method is poor (milligram-scale), requires large amounts of time and energy because of the high temperatures of the solvents. Unfortunately, the latter are usually toxic and non-environmentally friendly. Additionally, further steps are required to transfer MNPs to biocompatible solutions that also allow biofunctionalization. Different approaches such as ligand exchange or extra coating layers can be used for this purpose.

- **Microwave-assisted synthesis**

Microwave synthesis is a variation of the thermal decomposition method that reduces the reaction time, has higher MNPs quality and yield, and excellent reproducibility. A more efficient and homogeneous internal heating due to the use of microwaves is responsible for these advantages. However, the equipment needed is still expensive, and there are doubts about the possibility of scaling it up.

- **Microemulsions**

Microemulsions are thermodynamically stable dispersions of two immiscible liquids that are stabilized by surfactant molecules. In reverse microemulsion, also called water-in-oil (W/O) microemulsions, water nanodroplets called micelles are dispersed in a continuous organic phase stabilized by both surfactant and cosurfactant molecules. The nucleation and growth of the MNPs occur inside these water droplets, acting as a nanoreactors, for more uniform and controlled sizes. This is the main advantage of the W/O method, allowing better control of the size distribution while different compositions and microstructures can be obtained.

- **Solvothermal/Hydrothermal**

High pressures and temperatures (supercritical conditions) produce

highly crystalline and monodisperse MNPs via solvothermal and hydrothermal methods. In the former, the solvents used are organic, while in the latter, it is water. Under the hydrothermal process, hydrolysis and oxidation reaction takes place to produce the MNPs. Different surfactant molecules are used in both. The sophisticated equipment and the difficult scale-up make this method still challenging to implement.

- **Polyol**

In the polyol synthesis, salt metals are mixed with polyalcohols or ether glycols, which act both as a solvent, surfactant, and reducing agent. This way, they reduce the metal salts to metal nuclei that then nucleate to form the MNPs. Moreover, the amphiphilic character of polyols allows the obtention of already hydrophilic suspensions for bio-applications. Like thermal decomposition, size, crystallinity, and agglomeration can be well controlled while reducing the precursor materials' cost and toxicity.

- **Biological synthesis**

Biological methods of MNPs preparation include the use of microorganisms, enzymes, or plants and their extracts [98]. Among them, MNPs coming from magnetotactic bacteria are one of the most interesting. These MNPs are naturally covered with a membrane made of phospholipids and proteins that makes them highly biocompatible. Moreover, they are single-domain, show good crystallinity and close-to-bulk magnetization. However, there is still limited knowledge, their production yields a low amount of MNPs and requires elaborate work in microbial culture.

This thesis has followed different methodologies to synthesize MNPs, namely, co-precipitation, thermal decomposition, polyol, and microemulsion.

Table 1. Summary of the chemical methods for the synthesis of magnetic nanoparticles.

	Synthesis method	Advantages	Disadvantages
Chemical methods	Co-precipitation	Simple, aqueous solution, high yield.	Difficult control of nanoparticle properties, especially size distribution. Aggregation, poor crystallinity.
	Hydrothermal	Highly crystalline nanoparticles, aqueous solution.	High temperature and pressure, difficult to scale-up.
	Microwave-assisted	Short reaction time, good reproducibility.	Low yield, difficult to scale-up.
	Microemulsion	Control of size and size distribution, shape.	Not very efficient, problems to scale-up, purification methods for separation of surfactants.
	Polyol	Good control of the properties of the nanoparticles.	Expensive reagents, high temperature, inconsistency in scaling up, formation of undesirable subproducts.
	Solvothermal	Well control of growth dynamics, highly crystalline nanoparticles.	High temperature and pressure, difficult to scale-up.
	Thermal decomposition	Fine control of size and size distribution, and shape. Highly crystalline nanoparticles.	Organic solvents at high temperature, hydrophobic solutions, time-consuming reactions.
Physical methods	Ball milling	Large-scale production.	Difficult control of nanoparticle properties.
	Electron beam lithography	Small particle size, narrow distribution.	Expensive, complex process.
	Laser ablation	Ultrapure particles, liquid suspensions.	Expensive, low yield.
	Aerosol spray pyrolysis	Cost-effective, scalable.	Control of particles' structure.
Biological methods	Magnetotactic bacteria	Homogeneous nanoparticles, good magnetic properties, biocompatible.	Low yield, control of bacteria growth.

5. Characterization of magnetic nanoparticles

Characterization of MNPs is a fundamental step to understand their properties better and, therefore, control their behavior in their final applications. Each technique provides essential parameters such as size, morphology, composition, and surface and magnetic properties. However, correctly characterizing MNPS is not a simple task, and several problems may arise. One of them is the lack of universal materials or protocols, which might facilitate performing the techniques in a similar way. Then, the results could be compared without any risk of misinterpretation. In addition, results are strongly influenced by the preparation of the sample. This makes the preliminary steps crucial for reliable results and easier interpretation. In any case, none of the existing methods can provide complete information about the NPs. Therefore, it is always recommended to employ different techniques to compare the results and have a more precise understanding of the sample.

The following lines contain the basic concepts of the techniques used during research for this thesis. They have been classified by the principal information they provide, but it is not unique or exclusive. Table 2 summarizes all the information each of these techniques provides.

5.1. Size, shape, and structure

Size is one of the main parameters that modify the properties of the MNPs when compared with their bulk counterparts. Different techniques allow estimation of size. However, it is essential to remark that different sizes are defined for MNPs, each important for further correlation with other properties or applications. For example, the magnetic core determines the transition to the superparamagnetic regime. The magnetic diameter is related to the active magnetic part of the particle, while different other sizes can be obtained when additional layers are added (see Figure 15). The latter are essential for bioconjugation protocols.

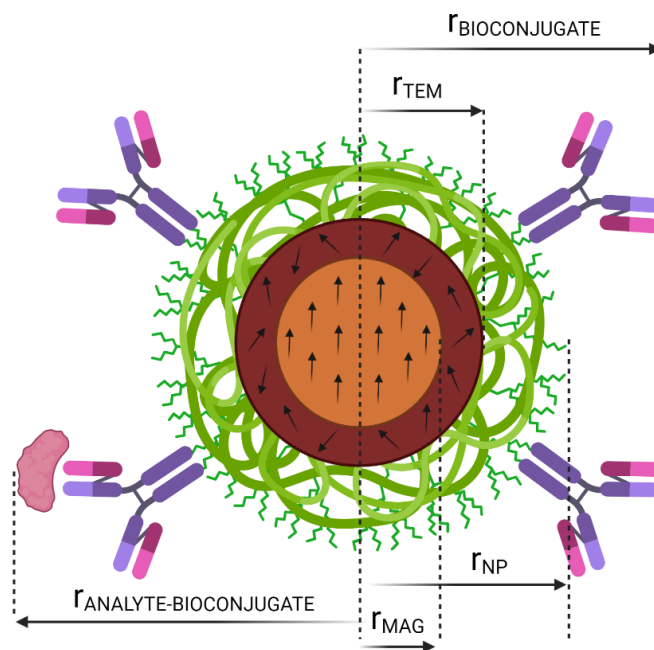


Figure 15. Schematic view of the characteristic sizes to consider in MNPs for biological applications.

Shape and crystalline structure are also important properties because they can introduce magnetic coupling and a strong anisotropy in the system, modifying the magnetic properties.

Transmission electron microscopy

Transmission electron microscopy (TEM) uses a beam of accelerated electrons (about 60 keV to 150 keV) to provide magnified bidimensional images in extremely thin specimens. A tungsten filament emits electrons that are focused by electromagnetic lens and travel through the microscope's vacuum tube. When passing through the sample, the electrons either scatter or hit a fluorescent screen at the bottom of the microscope (see Figure 16). The images obtained show gray intensities as a function of the un-scattered electrons density. In high-resolution TEM (HRTEM), the image contrast is formed by combining the electrons transmitted and diffracted. Thanks to resolutions of 0.05 nm, HRTEM allows the direct imaging of the sample atomic structure, thickness of disordered surface, and the observation of dislocations or point defects [99].

Both TEM and HRTEM have become the most common technique to get information about the core size, shape, and crystallinity of MNPs. However, they have some limitations. Sample preparation needs to be

done carefully to avoid aggregation or any damage to the sample. If there is an organic compound, selective stain to enhance the contrast may be needed. Additionally, the region studied could be insignificant and hence not representative of the sample [100,101].

Scanning electron microscopy

Scanning electron microscopy (SEM) scans the surface of the sample with an incident electron beam. The reflected electrons (the secondary ones are the most common mode) are detected and generate information about the surface's atomic composition and topographic details. The image produced is in black and white format, in which the larger number of electrons detected corresponds to whiter zones. Therefore, SEM is a common technique to obtain size, structure, porosity and superficial morphology with a resolution of about 1 nm [102].

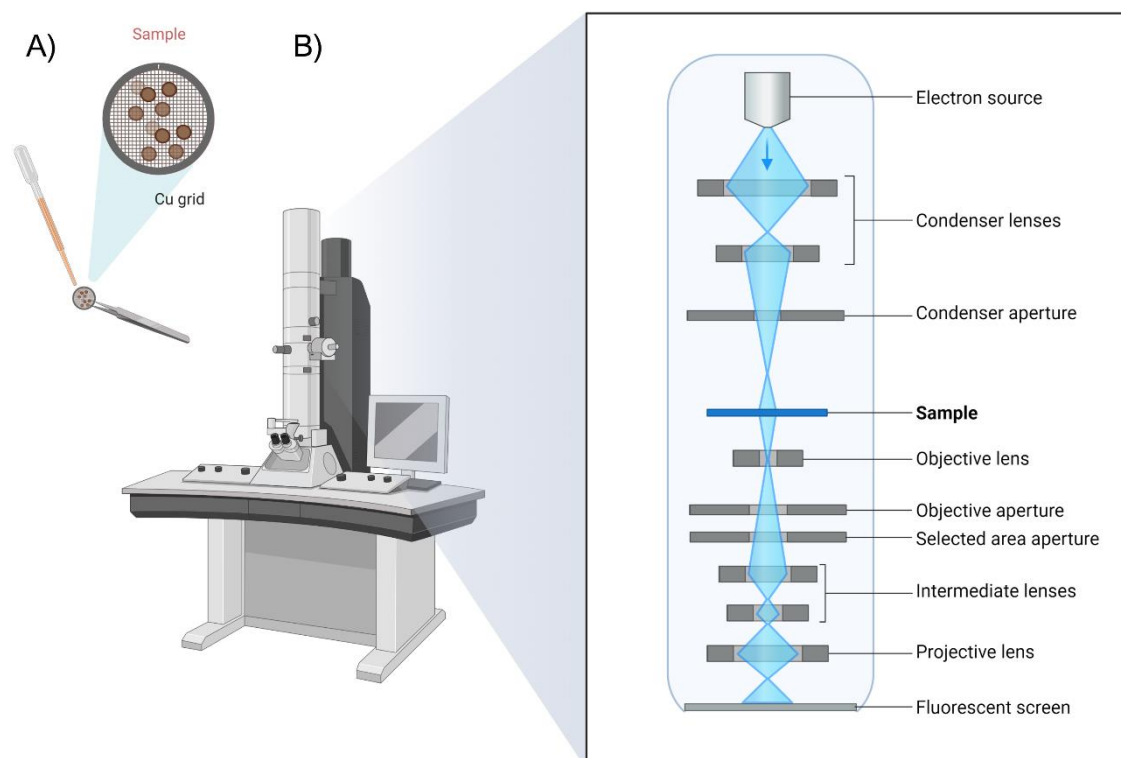


Figure 16. A) Sample preparation for TEM measurements. B) Schematic representation of a TEM instrument.

X-ray diffraction

Diffraction occurs when a beam of X-rays with a wavelength comparable to interatomic distances interacts with the periodic array of molecules in

a crystal. X-ray diffraction (XRD) allows characterizing crystalline materials, providing information on their structure, phases, and preferred orientations. Some structural parameters such as average grain size, strain, and crystal defects can be obtained.

XRD is based on the constructive interferences of monochromatic X-ray and the crystalline sample. The constructive interferences indicate the waves are in phase, which happens when an integer multiple (n) of the wavelength (λ) equals the path the diffracted X-rays travel. This path only depends on the distance between the crystal planes d and the incident angle θ . Everything is summarized in Bragg's law (see Figure 17):

$$n\lambda = 2d \sin \theta \quad (19)$$

The raw data obtained is called a diffractogram and consists of a record of the intensity of the measured photons as a function of the diffraction angle (2θ). The position of the peaks determines the symmetry and lattice parameters. In contrast, the peak width is related to intrinsic sample properties (grain size, microstrain, etc.) and the angular resolution of the instrument. The analysis of the data and its comparison with databases allows determining the present phases in the sample. Unfortunately, magnetite (Fe_3O_4) and maghemite ($\gamma\text{-Fe}_2\text{O}_3$) are nearly identical spinel structures. Therefore, an XRD pattern is not the most recommended technique to discern between them [103].

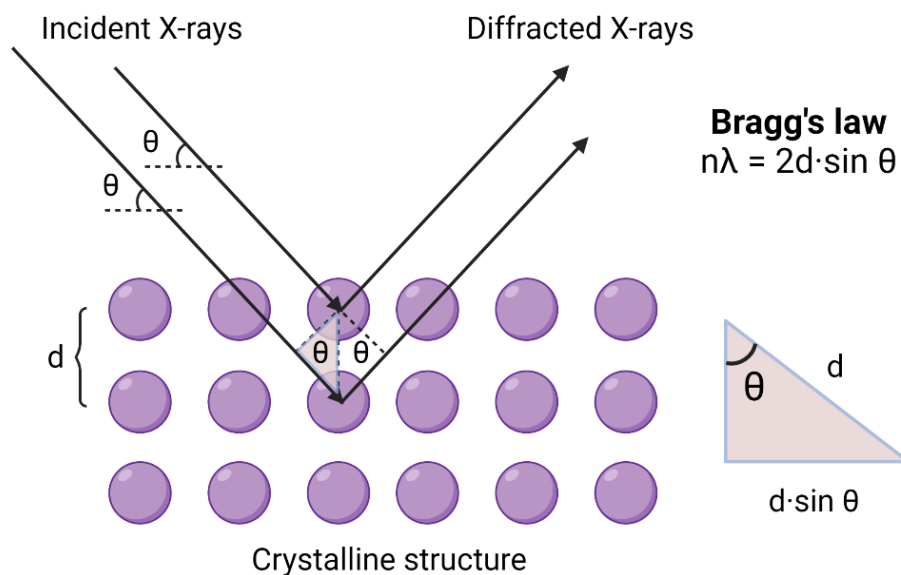


Figure 17. Schematic representation of Bragg's equation.

Scherrer equation is also used to determine the mean size of the MNPs by its relationship with the diffraction peaks:

$$D_{hkl} = \frac{K_S \lambda}{\beta \cos \theta} \quad (20)$$

Where D_{hkl} is the mean size of the crystal, hkl are the Miller's index of the planes, K is the crystallite shape factor (usually a value of 0.9 is a good approximation), and β is the full-width at half-maximum of the X-ray diffraction peak in radians. This equation can only be applied for average sizes up to 200 nm [104].

Dynamic light scattering

Dynamic light scattering (DLS) is a technique to monitor the size and agglomeration of MNPs in colloidal suspension. When a laser irradiates the sample, the scattered light is collected. Its intensity fluctuates induced from the Brownian movement of the particles present in the sample with sizes smaller than the incident wavelength at a fixed angle (see Figure 18). Through the Stokes-Einstein equation, the average hydrodynamic size can be calculated:

$$d_H = \frac{k_B T}{3\pi\eta D} \quad (21)$$

Where d_H is the hydrodynamic diameter, k_B is Boltzmann's constant, η is the medium viscosity, and D is the translational diffusion coefficient.

Since the raw data in DLS comes from the intensity measurements, the direct information about the sample comes from the intensity-weighted distribution. Only the refractive index and the solvent viscosity are needed. However, this intensity distribution is approximately proportional to size to the sixth power, making it very sensitive to agglomerates and cannot represent the real sizes of the particles. The intensity distribution can be converted into volume-weighted and number-weighted distributions assuming homogenous and spheric particles. In these cases, the distributions are proportional to size to the third power, showing more representative sample distributions. All three distributions provide the Z-average diameter that is the cumulant mean, and the polydispersity index (PDI). The latter indicates the polydispersity of the sample, being a monodisperse system when its value is $\sim 0,1$ and

nearly monodisperse with values of 0,1 to 0,7. When the values are over 0,7, there is a broad distribution of macromolecular sizes, indicating DLS is not the recommended technique [105].

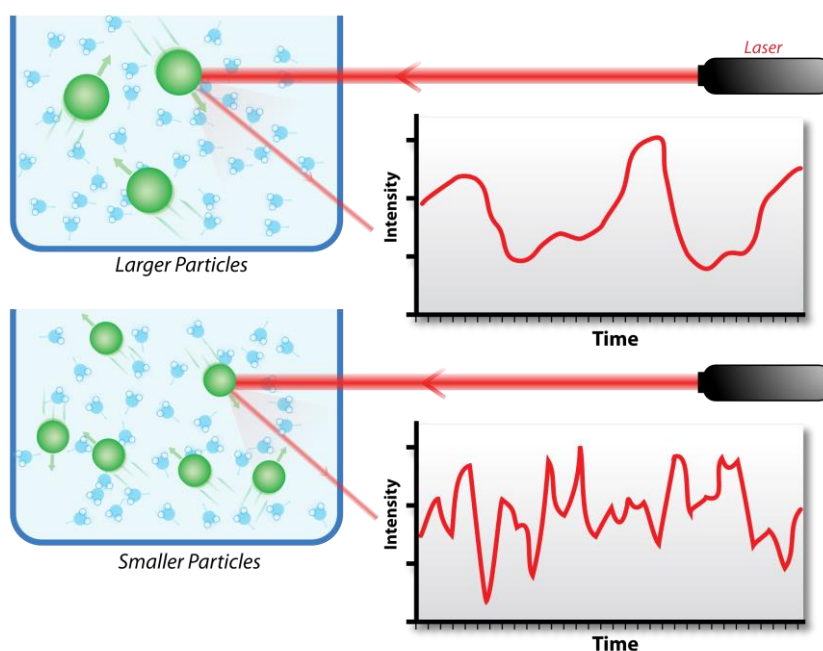


Figure 18. Schematic representation of the scattered light from MNPs with different sizes. Obtained from [106] without further modification.

It is important to remark that the d_H obtained by DLS includes the magnetic core, any polymer or biomolecule at its surface, and the solvation layer (if the suspension is aqueous). Therefore, this technique is interesting to check the success of any bioconjugation or biorecognition process by the MNPs. When monitoring any of these processes step by step, d_H should increase accordingly.

5.2. Composition and surface properties

Composition is intrinsically related to the magnetic properties of the MNPs. Additionally, biomedical applications *in vivo* have their requirements to avoid toxicity. Regarding the surface properties, they are crucial for further MNPs functionalization.

Electrophoretic light scattering

ζ -potential is used to characterize the colloidal stability of samples that comes from electrostatic repulsion, included in some DLS analyzers. When dispersed in a liquid, NPs are surrounded by ions strongly attached to their surface, called Stern layer, and a diffuse layer where they are not

so firmly fixed. The potential at this boundary is the ζ -potential. Direct measurement is not possible, so instead, its value is determined by electrophoresis. When an electric field is applied, charged particles will move with a velocity that allows determining their net surface charge. When this net charge is high enough, particles repel each other and do not agglomerate. Values of ζ -potential above 20 mV or larger are considered for stable solutions.

Energy-dispersive X-ray

Energy-dispersive X-ray (EDX) analysis is usually combined with transmission microscopy instruments to determine the elemental composition of a specific point of the sample. To do so, an electron beam excites a small region, and the X-ray emission is detected, which is element sensitive. The technique can be qualitative and quantitative, providing the spatial distribution of the elements present through mapping.

Thermogravimetry analysis

Thermogravimetric analysis (TGA) provides information about the nature and the proportion of the organic material in the MNPs surface. The technique uses a precision balance that monitors the changes in the sample's mass when heated in a regulated atmosphere. TGA is an important technique because it allows knowing the values of the magnetic mass in MNPs samples. When other properties such as magnetization are measured, the samples contain both the organic and the magnetic phase. It is necessary then to recalculate the values taking only into account the magnetic phase. TGA can also provide concentration values for MNPs liquid samples. Additionally, when coupled with the differential scanning calorimetry (DSC), it provides information about melting, crystallization, glass transition, and decomposition of nanomaterial-bioconjugates.

Mass spectrometry

Mass spectrometry (MS) can determine the elemental composition, its concentration, and the chemical structure of a sample at the trace level. MS generates ions from the sample and separates them by their mass-to-charge ratio (m/z). Different methods ionize the analyte. Inductively coupled plasma (ICP) is the form of ionization preferred for analyzing metal-containing nanomaterials [107]. Then, the ions formed that can be

single ionized atoms, clusters, molecules, or their fragments, are separated by static or dynamic electric or magnetic fields (see Figure 19). The samples are usually analyzed in liquid, so a preparation process for powder samples is required.

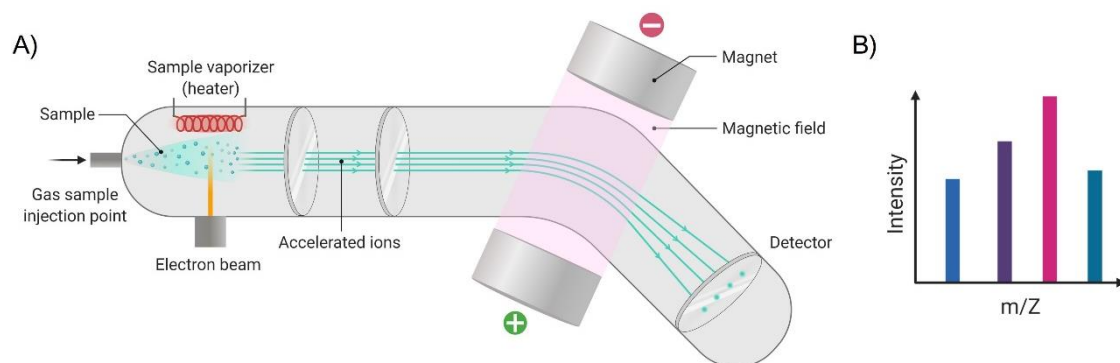


Figure 19. A) Schematic representation of a typical mass spectrometry instrument. B) Data output in an MS to detect qualitatively and quantitatively the elements in the sample by their respective m/z .

X-ray photoelectron spectroscopy

X-ray photoelectron spectroscopy (XPS) is a technique that allows the analysis of the surface chemistry in an ultra-high vacuum. It allows obtaining the electronic structure, the elemental composition, and the oxidation states of the MNPs. XPS is based on the photoelectric effect, in which photoelectrons are emitted from the sample surface when it is hit by a beam of X-rays (see Figure 20). An electron energy analyzer counts ejected photoelectrons over a range of energies. Then, these energies and their intensities permit the identification and quantification of the surface elements.

Infrared spectroscopy

Molecules can absorb electromagnetic radiation with wavelengths within the mid-infrared region ($4000\text{ cm}^{-1} - 400\text{ cm}^{-1}$). This changes its dipole moment and induces covalent bonds to stretch, bend or twist. Each type of bond vibrates differently, so a fingerprint of the molecule's structure is obtained when comparing the infrared absorption or the transmission versus the incident one. Fourier transform infrared (FTIR) spectroscopy is used to recognize the coating chemical groups present at the surface of the MNPs and their interactions and reveal NPs–biomolecules conjugation. There are different methods for the FTIR sample preparation. Some measurements can be done directly in the

liquid sample, but the most typical consist of the preparation of a KBr pellet containing the sample.

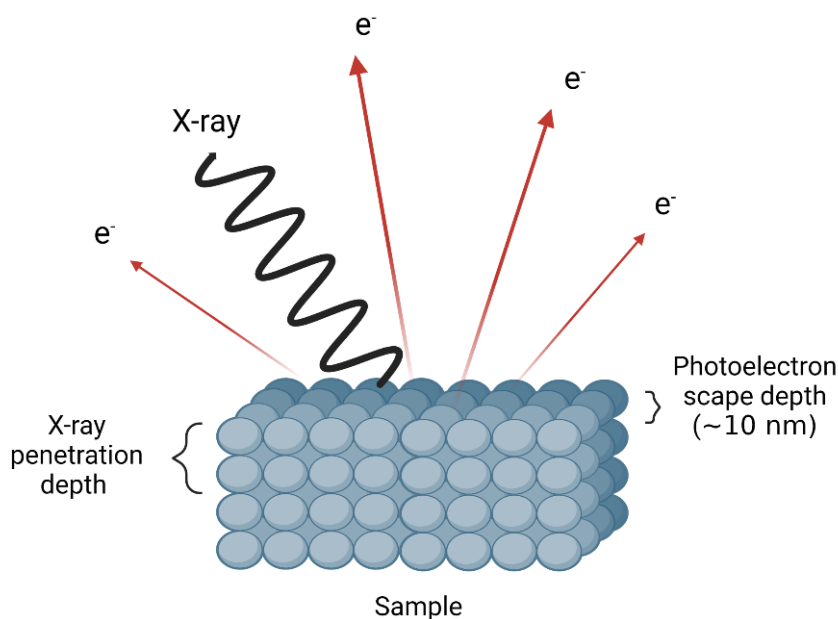


Figure 20. Schematic representation of the photoelectric effect.

5.3. Magnetic properties

Magnetometry allows the MNPs' magnetic moment as a function of field and temperature to be obtained. The most used techniques, which are vibrating sample magnetometry (VSM) and superconducting quantum interference device (SQUID) magnetometry, are induction based. When a magnetic sample is moved near a set of pickup coils, the associated change in the magnetic flux can be determined by Faraday's law.

Vibrating sample magnetometer

In a VSM, the sample is vibrating with fixed amplitude and frequency in a uniform magnetic field, and a voltage is induced in the pickup coils (see Figure 21A). This voltage is proportional to the magnetic moment of the sample, allowing its calculation.

Superconducting quantum interference device

Superconducting quantum interference devices (SQUIDs) are the most sensitive magnetometer (10^{-8} emu typical). They rely on superconductivity and the Josephson effect, requiring cryogenic temperatures to function [108]. An entirely superconducting ring only allows specific magnetic fluxes, meaning the magnetic field is quantized. However, the SQUID junctions allow a small electric current to pass

through (Josephson effect). This current is very sensitive to the magnetic field in the ring. When a magnetic sample is moved within the SQUID ring (see Figure 21B), in which a constant current is flowing, the voltage oscillates with a period of one flux quantum. Hence, when the oscillations are counted, the magnetic moment of the sample can be obtained by considering the variation of the flux.

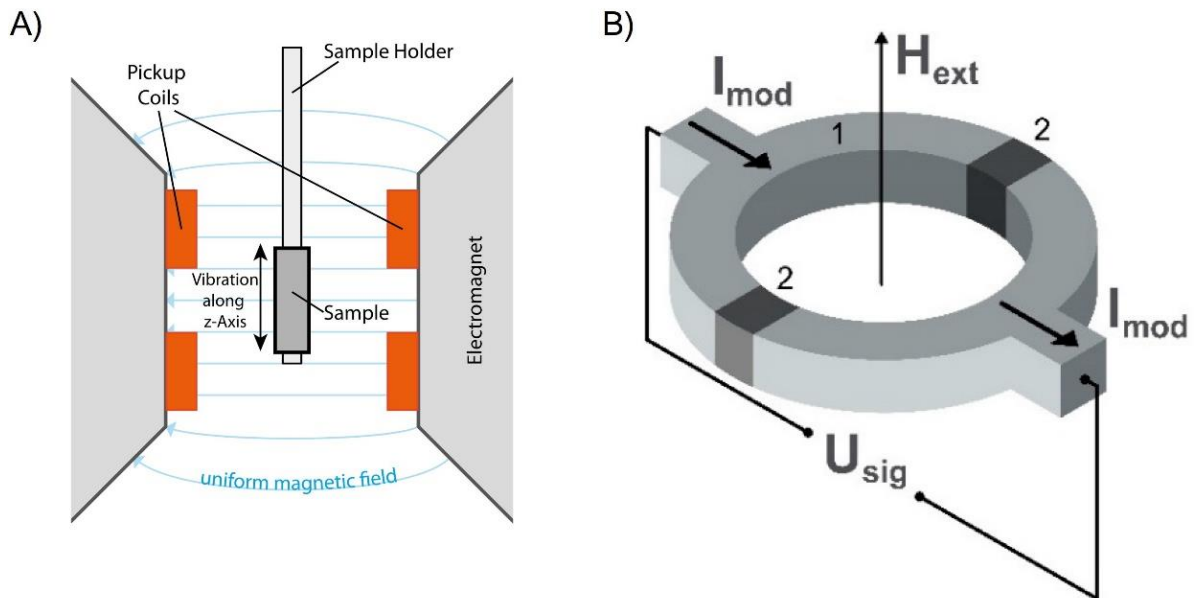


Figure 21. A) Schematic representation of a VSM. From [109]. B) Schematic illustration of the sensing element of the SQUID, where H_{ext} is the applied external magnetic field. The difference of voltage U_{sig} is detected by the magnetic field-induced imbalance of the current I_{mod} flowing through two semiconducting loops (1) and the two Josephson junctions (2) of the sensing ring. From [110].

Commercial SQUID magnetometers have different modes of operation (e.g., DC, SQUID-VSM, AC susceptibility). For reliable measurements, there must be precise control of sample shape and centering.

Table 2. Summary of the experimental techniques used during research for this thesis for the MNPs characterization.

Experimental technique	Information derived from the experimental technique
DLS	Hydrodynamic size, presence of agglomerates, bioconjugation monitoring.
EDX	Quick elemental composition data (when coupled to any of the EM techniques).
FTIR	Surface composition, ligands binding.
HRTEM	Size, shape, aggregation, crystal structure, defects.
ICP-MS	Elemental composition, concentration, and structure.
SEM	Size, shape, aggregation, superficial conformation.
TEM	Size, shape, aggregation.
TGA	Mass and composition of the coating layers, core information.
VSM & SQUID	Magnetic properties through M vs. H and M vs. T curves, remanence plots, and dynamic properties.
XPS	Elemental composition and oxidation state, electronic structure, ligand binding at the surface.
XRD	Crystal structure, composition, crystalline grain size.
ζ-potential	Colloidal stability, net surface charge.

6. Applications of magnetic nanoparticles

MNPs have a broad range of applications that include electronics (magnetic data storage and battery electrodes) [111], energy (solar cells and energy storage) [112], environment (bioremediation) [113], agriculture (plant genetic improvement and nanofertilizers) [114], and food (intelligent food packaging) [115]. However, biomedicine takes the honors with many applications both to diagnose and treat different illnesses. This potential has been gathered in the theranostic word, coming from the fusion-term of therapy and diagnosis. Therefore, MNPs can be engineered to be multiplatform in modern biomedicine.

6.1. Magnetic nanoparticles in biomedicine: A marriage of convenience

Magnetic nanoparticles have the ideal size to interact with biological entities at the cellular and molecular levels. They can be mixed with biological fluids, injected through blood vessels, and cross some physiological barriers. Their large surface-to-volume ratio provides enough space for binding biological entities to tag others, or act as cargo. An external magnetic field gradient can manipulate them. The force generated can direct them and immobilize them within the body. In a sample, the gradient can be used to separate the tagged biological entities magnetically. Moreover, when the field varies over time, MNPs respond by dissipating heat to their surroundings, which is helpful to damage diseased tissue in the body. Thanks to all of this, they are a powerful approach to solving major problems in biomedicine.

- **Magnetic separation**

Separation and concentration of specific biomolecules are primary steps in many biotechnological processes, such as purification of a final product and concentration or enrichment of a molecule in a sample [116,117]. The latter is very helpful for diagnostic purposes when the detection/quantification of the analytes is a challenge because they are in very low concentration or may have interference from the complex sample matrix [62]. The target analyte can be proteins, cells, toxins, pathogens, etc. Additionally, magnetic separation can be used for environmental purposes in water and soil remediation. Here, different contaminant species such as heavy metals or agrochemical residues are eliminated [118–120].

The principle behind magnetic separation is based on the specific recognition and capture of the target analyte via the elements attached to the MNPs' surface [121]. When mixed with the complex sample and after an incubation period, the target analyte binds to the MNPs, forming a complex easily trapped by a magnetic field gradient. After washing out the remaining sample, the isolated target is used for further work.

The force \vec{F} that is produced to separate MNPs of magnetic moment \vec{m} from the sample matrix is generated by the magnetic gradient as follows:

$$\vec{F} = \nabla(\vec{m} \cdot \vec{B}) \quad (22)$$

The simplest way to create a field gradient is with a permanent magnet. In this case, the magnetic field strength decreases when the distance to it increases. As a result, \vec{F} is greatest at the pole of the magnet and rapidly diminishes within a few millimeters from its surface.

Regarding the MNPs, they need a high magnetization value with high susceptibility. Chemical groups at their surfaces will allow the binding of the biorecognition elements. Superparamagnetic particles are ideal to avoid undesirable agglomeration.

Magnetic separation techniques have several advantages compared to traditional separation procedures, such as chromatography, centrifugation, or electrophoresis. Mainly, the process is straightforward and usually does not need expensive equipment. Additionally, it is gentle and non-destructive, which is essential when working with expensive products such as proteins or antibodies [122].

- **Magnetic biodetection**

Magnetic sensors profit from the magnetism of the MNPs to report the presence of an analyte. Thanks to the lack of magnetic signals within biological samples, magnetic biodetection ensures good specificity. The primary approach is to adapt a magnetic field sensor to both excite and detect MNPs magnetization. Common detection formats are based on spintronics, induction, and some bioanalytical techniques with extremely high accuracy, such as SQUID magnetometers or NMR. Additionally, MNPs offer a dual-modality for some formats of biosensing thanks to the color they provide.

The most important characteristics for a good sensing platform are related to the superficial and magnetic properties of the MNPs. The former is important because they will provide appropriate bioconjugation to bind to the target analyte specifically, the latter because the signal read-out mainly depends on them.

Spintronics sensors

Spintronics sensors are based on giant magnetoresistance (GMR), tunnel magnetoresistance (TMR), or planar Hall effect (PHE). All provide ultrasensitive detection. However, their implementation as biosensors involves challenges such as microfluidic integration for sample management, passivation of the surface and electronics, chemical surface modification, intermediate washing steps, and coupling of excitation magnetic fields [123–125].

Multilayer GMR sensors are based on a quantum mechanical effect generated in magnetic thin-films. They exhibit a large decrease in resistance due to reduced electron scattering when the magnetization of a soft free layer is rotated to be parallel to the magnetization of a hard fixed layer. When MNP-analyte complexes are present, they change the magnetization orientation of the free layer. In turn, this produces a variation in the magnetoresistance. TMR sensors are based on the tunnel magnetoresistance of a magnetic tunnel junction. TMR sensors differ from GMR sensors in the construction of the multilayers. In this case, two magnetic layers are separated by an insulating one. Nevertheless, TMR sensors have higher sensitivity at lower fields. PHE uses the generation of different voltages in a conductor subjected to a magnetic field. These sensors have a high signal-to-noise ratio and a linear response in the low and high field regions.

Relaxometry sensors

Magnetic relaxation switch (MRS) sensors are based on the differences in how water protons close to the MNPs in the sample relax before and after the interaction with the target analyte (see Figure 22) [126]. Interestingly, the samples used can be complex, such as blood or cell culture media, with scarce sample preparation. Usually, MRS signals are measured by NMR, but they require the complex acquisition of data from large amounts of sample [127]. To solve these problems, scientists have developed the miniaturized NMR (μ NMR) by introducing microfluidics. This way, μ NMR allows detecting various biomolecules such as proteins

or bacteria rapidly and sensitively [128,129].

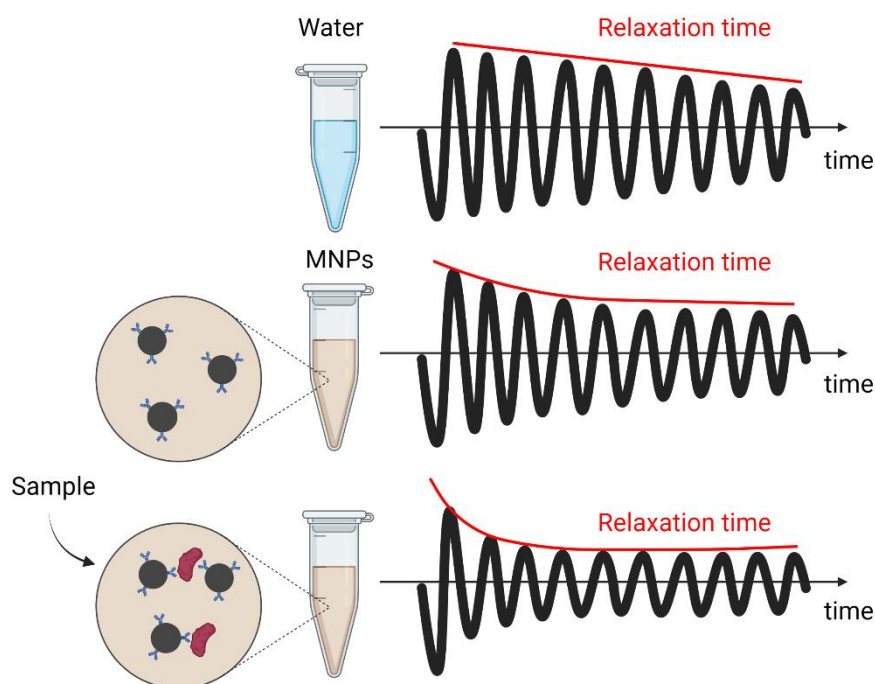


Figure 22. Schematic representation of the differences in the relaxation times for an NMR sensor.

SQUID magnetometers can also be used as biosensors thanks to their sensitivity [130,131]. Their principle is also based on the differences in the relaxation times. However, now it is the MNPs' magnetization that relaxes. The free MNPs relax fast by Brownian motion. But, when the bioconjugated MNPs catch the target analyte, there is an increase in their effective sizes that favors Néel relaxation. Therefore, the magnetization of the MNPs-analyte complex relaxes slower [132]. This difference can be detected by the SQUID magnetometer and used to detect different biomolecules [133,134].

Faraday induction sensors

Faraday coil magnetometers and susceptometers with different approaches can be used to detect MNPs [131,135]. They rely on a time-varying field generated in an excitation coil that excites the MNPs. The latter produces, in turn, a magnetic flux change that is detected in a second coil. Different signals can be registered, such as a change of its self-inductance, a variation of its resonance frequency, or monitoring the induced voltage. Interestingly, the system can be reduced to a single-coil with a dual role: excitation and detection when high frequencies are used to achieve a significant coil quality factor. In this case,

superparamagnetic NPs are recommended as their initial magnetic permeability drops only at very high frequencies, above those corresponding to their Néel relaxation times.

- **Magnetic hyperthermia**

Hyperthermia is based on heating tumor cells to about 40°C to 44°C. Differences in the pH in the cancerous microenvironment results in a lower thermotolerance of the cancerous cells [136,137]. Heating induces their apoptosis, necrosis, or just enhances their susceptibility to chemo and radio-therapy. Hyperthermia can be whole-body, regional, or local. Among them, local hyperthermia has more advantages, such as better control over the area exposed (thus avoiding damage to healthy cells) and better heat uniformity. However, local hyperthermia by laser or microwave light has only a few centimeters of penetration depth, so it can only be used to treat superficial tumors. Local hyperthermia using MNPs that are delivered and focused on the cancer cells solves these problems. Magnetic hyperthermia (MH) uses an external alternating magnetic field at frequencies between 100 kHz and 1 MHz to generate heat at a specific site in the body [138]. Consequently, it minimizes the method's invasiveness and the side effects while targeting deeper cancer cells (see Figure 23A).

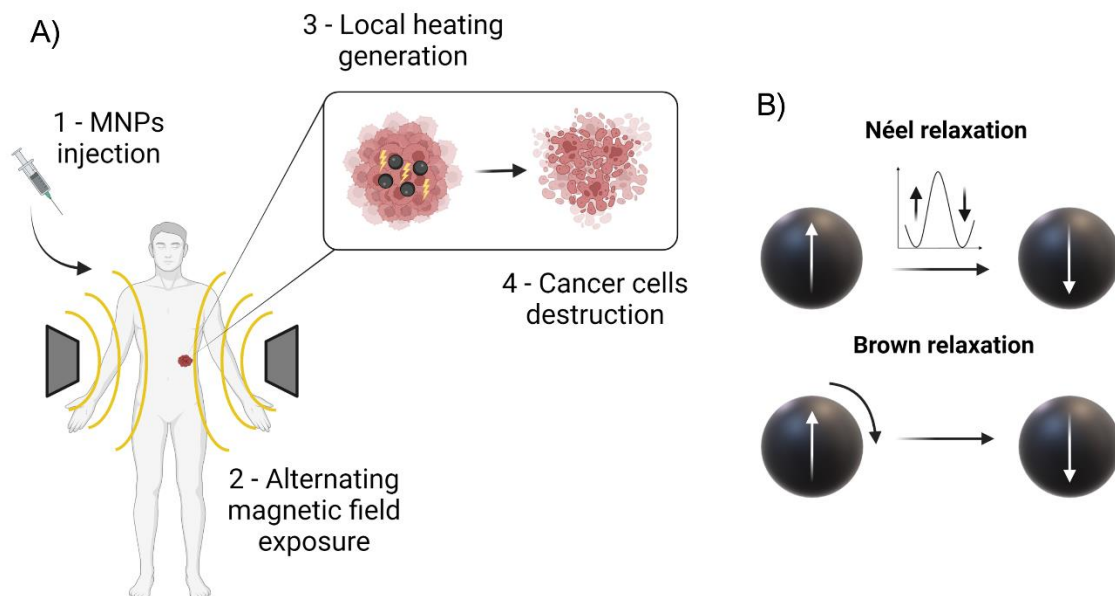


Figure 23. A) Schematic illustration of the magnetic hyperthermia process. B) Relaxation mechanisms for MNPs: Néel relaxation is the rotation of the magnetic moment inside the particle, while Brown relaxation process is the rotation of the particle itself.

Several heating mechanisms are possible in MH depending on the MNP sizes: hysteresis losses for multidomain particles and Néel and Brown relaxations for single-domain and superparamagnetic nanoparticles [139]. In the former, the heating is due to the shifting of the domain walls and magnetization rotation inside the domains. However, multidomain particles are not recommended because of their intrinsic dangers (e.g., their remanent magnetization after removing the applied field can lead to clot formation). In superparamagnetic NPs, heating is due to the magnetization rotation by two mechanisms: Néel and Brown. The first involves the rotation of the magnetization orientation, whereas, in the second, the particles physically rotate. Brown's relaxation strongly depends on the surrounding medium. When MNPs are inside tissues, they are practically immobilized, and Néel's relaxation is usually predominant (see Figure 23B). In any way, the effective relaxation time can be estimated following equation (16).

Experimentally, the MNPs' heating efficiency is represented by the specific absorption rate (SAR) or specific loss power (SLP) that can be calculated by different methodologies [101,140]. Commercial magnetometers can obtain the hysteresis loops when an alternating magnetic field is applied to a material. The area of the hysteresis loop enclosed within this cycle equals the heat generated per cycle, and it can be calculated as:

$$\text{SAR} = -\mu_0 \frac{f}{\rho} \oint M dH \quad (23)$$

where ρ is the density of the magnetic material and f the frequency.

AC susceptibility also allows for SAR calculation. When an alternating magnetic field is applied to an MNP, the value of its magnetization is proportional to H as long as the amplitude is small enough. In this linear response range, the susceptibility χ depends on the frequency but not on the amplitude. Considering the magnetic susceptibility in its complex form ($\chi_{AC} = \chi' + i\chi''$), where χ' and χ'' are the real (in-phase) and imaginary (out-of-phase) components, respectively, the SAR value can be calculated like [140]:

$$\text{SAR}(H, f) = \frac{\pi\mu_0\chi'' H^2 f}{\rho} \quad (24)$$

Experimentally, SAR values can also be obtained via the calorimetric method, in which the temperature increase of a sample subjected to an alternating magnetic field is measured, and then, SAR is calculated as follows:

$$\text{SAR/SLP} = \frac{C_s}{m_m} \frac{dT}{dt} \quad (25)$$

where C_d is the specific heat capacity of the sample, m_d is the dispersion mass, m_m is the magnetic core mass and dT/dt is the rate of temperature change. In equation (25), C_s is related to the individual parts of the solution, being the medium and the magnetic particles, through:

$$C_s = C_{dm}m_{dm} + C_m m_m \quad (26)$$

where C_{dm} and C_m are the specific heat capacity of the dispersion medium and the MNPs, respectively, and m_{dm} is the mass of the dispersion medium.

The experimental determination of dT/dt requires recording the temperature while applying the alternating magnetic field. How this is done depends on the system, i.e., if it is adiabatic or not. Thus, there is controversy on the accuracy of the results mainly due to the lack of standardized procedures. Nevertheless, the units for SAR are watts per gram, and it should be optimized to deliver the highest temperature increase with the minimum amount of MNPs.

SAR values depend on MNPs' extrinsic parameters such as the frequency and intensity of the alternating magnetic field and intrinsic ones, such as their physicochemical and magnetic properties [141,142]. In the former, a safety threshold must be applied to avoid serious side effects. Usually, MH safety limits are established below $H \cdot f = 4.85 \times 10^8 \text{ A}\cdot\text{m}^{-1}\cdot\text{s}^{-1}$ [143]. In the latter, MNPs sizes, shapes, anisotropy, magnetic interactions, and agglomeration play important roles in the SAR values [144]. Additionally, how the particles are injected, their long-term fate, and their bio-elimination must be addressed [145].

- **Magnetic resonance imaging**

Magnetic resonance imaging (MRI) is one of the most used and powerful tools in radiology. It gives detailed anatomical information of soft tissues with spatial resolution and high penetration depth without using harmful ionizing radiation [146].

In the absence of an external magnetic field, the magnetic moments of the hydrogen protons in the water in all tissues are randomly oriented, and therefore, there is a zero net magnetization. The small magnetic moment of the protons is counterbalanced with the large amount of them present in biological tissues, which makes possible its measurement in the presence of a large magnetic field. An applied field, usually provided by a superconducting solenoid, can align the magnetic moments of the protons in equilibrium in the z-axis (see Figure 24A). Then, a radio frequency (RF) pulse of sufficient duration derives a coherent response from the net magnetic moment of the protons and rotates them away from the z-axis. Upon removing the RF field, the magnetic moments relax back to their equilibrium stage, which is measured via induced currents in pick-up coils in the scanner [147]. The time magnetic moments take to reach equilibrium, called the relaxation time, depends on the tissue. There are two different relaxation times: T_1 , is the spin-lattice relaxation time, also known as the longitudinal relaxation time, and T_2 , which is the spin-spin relaxation time, also known as the transverse relaxation time. To differentiate among tissues in the body, different T_1 and T_2 signals need to be measured. The problem is that in most tissues, there are only small variations of these relaxation times. Hence, exogenous materials called contrast agents are used to enhance the signals between the tissue of interest and its surroundings (see Figure 24B). The efficiency of these agents is evaluated via their relaxivities r_1 and r_2 , which are defined as the rates at which protons relax to their initial equilibrium state [148]. They are defined as:

$$r_i = \frac{\left(\frac{1}{T_{i,\text{meas}}}\right) - \left(\frac{1}{T_{i,\text{dia}}}\right)}{c}; \quad i = 1,2 \quad (27)$$

where $\frac{1}{T_{i,\text{meas}}}$ is the value measured for the sample with a concentration c of the MNPs, and $\frac{1}{T_{i,\text{dia}}}$ is the value for the relaxation time of the host solution. The values of the relaxivities are expressed in s^{-1} per contrast

agent concentration. Generally, the higher the transverse relaxivity r_2 , the better the contrast efficiency. The r_2/r_1 ratio is also used to indicate the contrast efficiency: the greater the ratio the greater the T_2 efficiency, and vice versa for a T_1 agent (see Figure 24C).

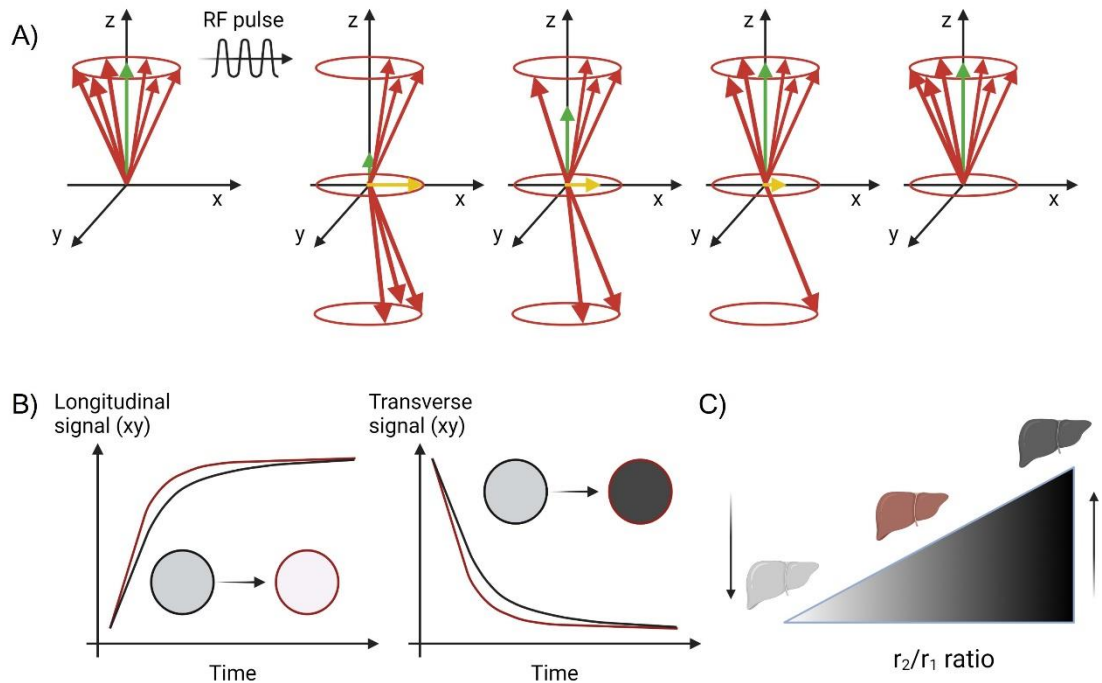


Figure 24. A) In an external magnetic field, spins align parallel or antiparallel and precess at the Larmor frequency. When the RF pulses, the magnetization of the spins changes, and when it is turned off, the excited spins undergo both T_1 and T_2 relaxation processes to return to their normal orientation. B) Shortening of T_1 (left) and T_2 (right) signals using contrast agents. The relaxation enhancement results in brighter contrast in T_1 and darker contrast in T_2 . B) Influence of the r_2/r_1 ratio on the image contrast. High values are characteristic of T_2 contrast agents, making organs appear darker in the image. Low values of r_2/r_1 define T_1 contrast agents, making organs clearer and brighter. Adapted from [148].

So far, the most common contrast agents are paramagnetic particles based on gadolinium, which usually behaves as T_1 contrast agents, meaning they provide a brighter image where they accumulate. However, some concerns have been raised about their toxicity [149]. Iron oxide MNPs are already available as commercial agents (e.g., Endorem (EU)/Feridex (USA), Sinerem) [146,150]. They behave as T_2 agents, meaning MNPs darken the regions of interest. Some efforts are being made to also make them act as T_1 contrast agents or even dual T_2 and T_1 agents [151,152]. Additionally, MNPs can be functionalized to attach specifically to a tissue or magnetically direct them. The physicochemical

properties of the MNPs determine the efficiency of these contrast agents, so they must be carefully controlled [153]. Moreover, they also influence the *in vivo* distribution, which should be optimized to avoid their sequestration by different body mechanisms, mostly by the liver [154], which unfortunately reduces their efficacy.

- **Magnetic particle imaging**

Magnetic particle imaging (MPI) was introduced in 2005 as a radiation-free, high signal-to-noise ratio and sensitive imaging modality [155]. The image formation is based on the non-linear magnetization of the MNPs tracers to generate maps of their distribution [156]. Since there is no magnetic signal within the human body other than the MNPs, this technique is quantitative. Additionally, MPI allows real-time visualization. Thus, it is of particular interest for applications such as angiographies or cell tracking. Other applications include passive and active tumor tracking [157].

MPI uses a time-varying magnetic field gradient, known as selection field, that has been designed to have a field-free point (FFP). Except around this FFP, the MNPs are saturated. The FFP is rapidly moved in the image volume, usually called field-of-view, by varying the excitation/drive field to produce an image. The signal is produced when the FFP passes through the MNPs' location and their magnetization changes nonlinearly, which are then picked up by the detecting coils. The voltages induced are proportional to the number of MNPs [158].

The principle of MPI is based on the MNPs used as tracers. Therefore, their characteristics and properties will determine the signal. The fundamental property governing both the spatial resolution and sensitivity is the MNPs diameter [159,160]. The sensitivity depends on the MNPs magnetic moment, which can be adjusted by increasing the sizes. Additionally, a large magnetic permeability allows larger variation in the magnetization, which gives better spatial resolution. All these parameters can be modified as long as the size of the MNPs remains below the superparamagnetic limit.

- **Drug delivery**

One of the goals of modern medicine is to increase the effectiveness of any drug while minimizing its side effects. Although many discovered

drugs are promising, some are limited by their low stability, high toxicity, elevated prices, and short circulating lifetimes [161,162]. Most of these problems could be eliminated by what Nobel laureate in medicine Paul Ehrlich called the “magic bullet” [163]. He referred to an ideal therapeutic agent that would act locally and specifically without relevant undesired side effects.

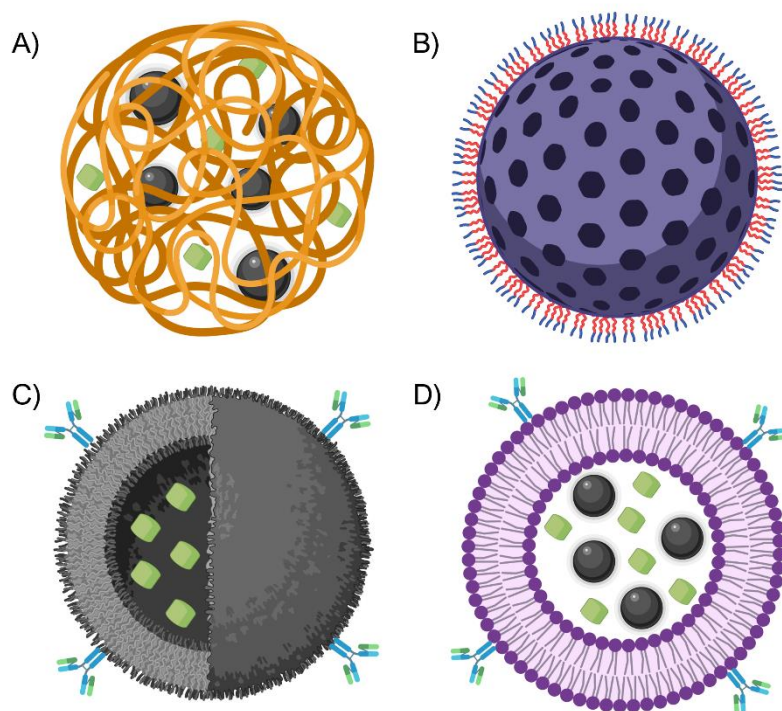


Figure 25. Schematic representation of different approaches for drug delivery. A) Polymeric NP with both the drug and the MNPs entrapped in the polymeric matrix. B) Porous MNPs with the drug within its internal structure. C) Hollow MNP with the drug entrapped in its nucleus. D) Magneto-liposome with both the drug and the MNPs entrapped in the inner aqueous compartment.

A drug delivery system is designed to enhance the local and controlled administration of a drug while protecting it and reducing the side effects. MNPs can act as these magic bullets, which involve three aspects: the cargo, the transport, and the release [164]. Regarding the cargo, their surface modification allows the binding of different biomolecules to entrap the drugs or to achieve target delivery. Thanks to their high surface-to-volume ratio, more drugs can be attached to their surface. Additionally, other approaches (see Figure 25), such as the formation of hollow or porous NPs and the encapsulation of the drug and the MNPs (for example, in liposomes) enable the increase and protection of the cargo [163,165,166]. External magnetic gradients guide the transport of the

MNP-drug complex. Finally, the release of the drug may be triggered by environmental changes within the target zone (such as pH changes), external stimuli (such as heating), or simply by degradation [167].

Section I – Chapter 1

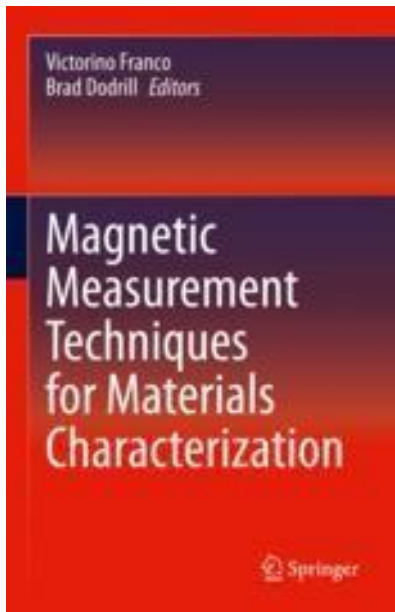
Biological and Medical Applications of Magnetic Nanoparticles

Introduction and motivation

It was not a lie: Size matters. Nanoparticles have sizes ranging from 1 nm to 100 nm. As a result, new properties emerge that differentiate them from their bulk counterparts. In addition, tailoring the composition can provide fascinating magnetic properties to face technological and life sciences challenges. Especially in biomedicine, MNPs offer great potential as diagnostic and therapeutic agents. This first chapter introduces this fascinating topic, in which the MNPs requirements, how they can be obtained, and the existing techniques to characterize them are revised. Finally, the essential MNPs applications are detailed, along with some examples.

Book Chapter

Biological and Medical Applications of Magnetic Nanoparticles



This work has been published in:

Magnetic Measurement Techniques
for Materials Characterization

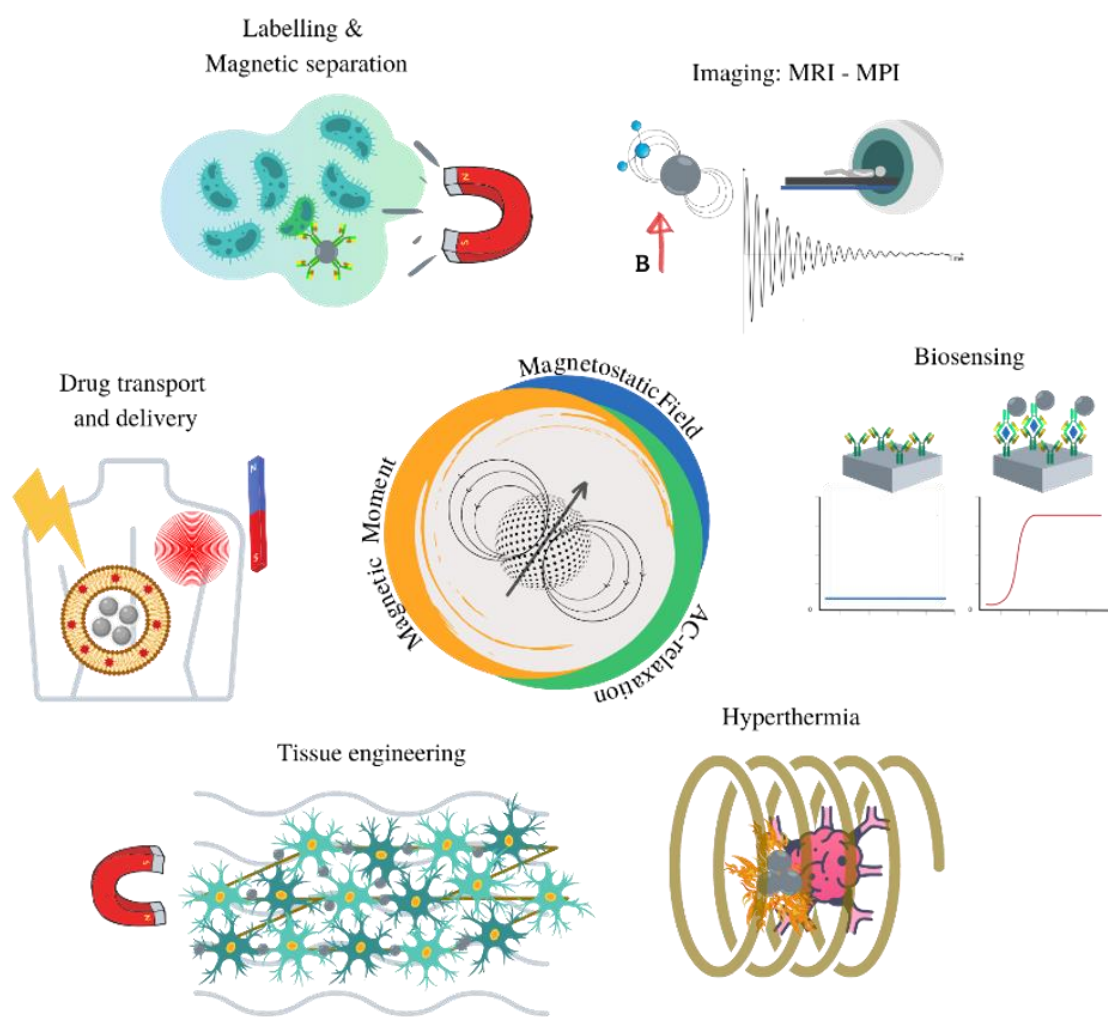
Springer Nature 2021

ISBN: 978-3-030-70443-8

Cite as:

Salvador M., Martínez-García J.C., Fernández-García M.P., Blanco-López M.C., Rivas M. (2021) Biological and Medical Applications of Magnetic Nanoparticles. In: Franco V., Dodrill B. (eds) Magnetic Measurement Techniques for Materials Characterization. Springer, Cham. https://doi.org/10.1007/978-3-030-70443-8_26

GRAPHICAL ABSTRACT



Biological and Medical Applications of Magnetic Nanoparticles

María Salvador^{1,2}, José C. Martínez-García¹, M. Paz Fernández-García¹, M. Carmen Blanco-López³ and Montserrat Rivas¹

¹*Department of Physics, University of Oviedo, Campus de Viesques, 33204 Gijón, Spain*

²*Istituto di Struttura della Materia - Consiglio Nazionale delle Ricerche (CNR), 00016 Monterotondo Scalo (RM), Rome, Italy*

³*Department of Analytical and Physical Chemistry, Institute of Biotechnology of Asturias, University of Oviedo, 33006 Oviedo, Spain*

Abstract

This chapter aims to give insight into the successes, challenges, and opportunities of magnetic nanoparticles for bio-applications. It reviews their general requirements and how they can be met by different synthesis methods and characterization techniques. It then focuses on examples of applications such as magnetic cell separation, magnetic detection (including imaging), and magnetic particle-based therapies, such as hyperthermia, magneto-mechanical destruction of tumors, localized drug delivery, and tissue engineering. We hope to guide the reader interested in applied research of magnetic nanoparticles through an exciting collection of investigations on their application in the life sciences.

Keywords: Magnetic nanoparticles, bio-application, biomedicine, biosensor, bio-detection, magnetic resonance imaging, magnetic particle imaging, magnetic immuno-separation, magnetic hyperthermia, drug delivery, tissue regeneration, magnetic detoxification.

1. Introduction

Today, more than ever, research is called upon to solve social problems, often those that affect public health and safety. The coronavirus that paralyzed the world in 2020 has an average size of 120 nm. The nanoscale

is the dimension at which biological events occur at the cellular and molecular level. Nanoparticles have the ideal size to interact with biological entities, such as proteins, genes, cells, viruses, and bacteria. They can be stabilized in colloidal suspensions to mix them with biological fluids or to inject them, and they can flow through blood vessels and cross some physiological barriers. Their large surface-to-volume ratio, and more importantly, the fundamental properties specific to their nanosize, have the potential to significantly contribute to solving major problems in biomedicine.

Additionally, magnetism adds capabilities such as remote manipulation, heat generation, and inductive detection. In the fields of life sciences (biomedicine, environment, and food safety), magnetic nanoparticles (MNPs) offer new tools to develop innovative methods for diagnosis and therapy in clinical practice, toxin detection in agrifood control, and environmental remediation.

Advances in the production of MNPs—control of their size, morphology, and crystalline quality—have stimulated their practical application. The design of new nanoarchitectures enables hybrid applications that take advantage of the combination of magnetism and optical or catalytic properties. For biological applications, the superficial coatings of the particles are crucial. They determine important properties of the chemical interaction of the MNPs with biological molecules or environments, such as biocompatibility, bioconjugation and circulation time.

2. Requirements of Magnetic Nanoparticles for Bio-applications

An essential feature of MNPs is their tunability. It allows them to be engineered for each application. Therefore, their crystal structure, size, shape, composition, agglomeration, superficial, and magnetic properties must be optimized. Biomedical applications can be classified into two main categories: *in vitro* and *in vivo*. The latter is the most challenging as it includes biocompatibility as a requirement.

Most of the advantages of MNPs come from their size, which confers them with properties entirely different from those of their bulk counterparts. Additionally, their size is particularly interesting for biomedical applications because it is comparable to that of most

biological entities of interest. The particles' size plays a vital role in their magnetic behavior, which may be superparamagnetic below a critical volume [1]. Superparamagnetism is preferable to other magnetic states because it reduces the magnetic attraction helping to stabilize colloidal suspensions required for biomedical applications [2]. For *in vivo* applications, the particles' size, shape, and superficial properties strongly influence their circulation time, targeting, and final bio-distribution or elimination [3–7].

For *in vivo* use, toxicity restricts the permissible composition. Iron oxide nanoparticles are approved by the U.S. Food and Drug Administration and the European Commission for clinical use because they can be metabolized [8]. On the contrary, Zn, Co, Ni, and Cu may be toxic [9–11]. Coating or encapsulation is an option to overcome this handicap [12, 13].

Biomedical applications require colloidal stability, but nanoparticles tend to aggregate and precipitate in aqueous suspensions. Proper surface preparation can avoid this by electrostatic forces and/or steric effects. Interestingly, aggregation can be either detrimental or advantageous, depending on the application. For *in vivo* processes, it increases the effective size, which may influence the circulation lifetime or heating efficiency [14, 15]. On the other hand, for *in vitro* purposes, as in reporter labeling of immunoassays, an increase in the number of MNPs per biomolecule enhances the detected signal [16, 17].

Surface properties are also crucial for functionalization. The adsorption of additional polymeric moieties onto the surface of the MNPs, known as electrosteric stabilization, is the most used approach to avoid agglomeration and prepare the particles for bioconjugation [18]. These coatings are usually polymers such as dextran, polyacrylic acid, polyethyleneimine, polyvinyl amine, and polyethylene glycol, or small molecules such as dimercaptosuccinic acid, silica, metals, or carbon [19–21].

Due to their small size, the MNPs' magnetic behavior is strongly dominated by their surface layer spins. The broken crystalline symmetry at a particle's surface may lead to undercoordination, relaxed magnetic exchange bonds, and spin canting; all of this translates into modifications of the magnetic behavior compared to that of the bulk material. The surface magnetic anisotropy increases, and the saturation

magnetization decreases, which is usually undesired for bio-applications. The action of the surfactant or polyelectrolyte can play a substantial role in improving this. Although capping organic molecules are not magnetic, they can restore the magnetic ordering of the core to the surface [22]. To explain this unexpected effect of nonmagnetic capping, Salafranca et al. [23] studied the magnetic order at the surface of Fe₃O₄ MNPs coated by oleic acid. They reported that some surface Fe ions bond to the organic acid's oxygen, so that the number of O nearest neighbors and their average distance closely resemble that of the bulk magnetite resulting in improved magnetic properties.

The specific magnetic requirements for various applications in the life sciences are treated in the following sections.

3. Synthesis methods

Many different synthesis routes have been proposed to obtain MNPs that accomplish the characteristics detailed above (Figure 1). The methods are commonly divided into 'bottom-up' or 'top-down' approaches. The latter, also known as physical methods (such as milling or grinding), consist of dividing a larger material into smaller units. These methods are not usually suitable for biomedical applications because they produce

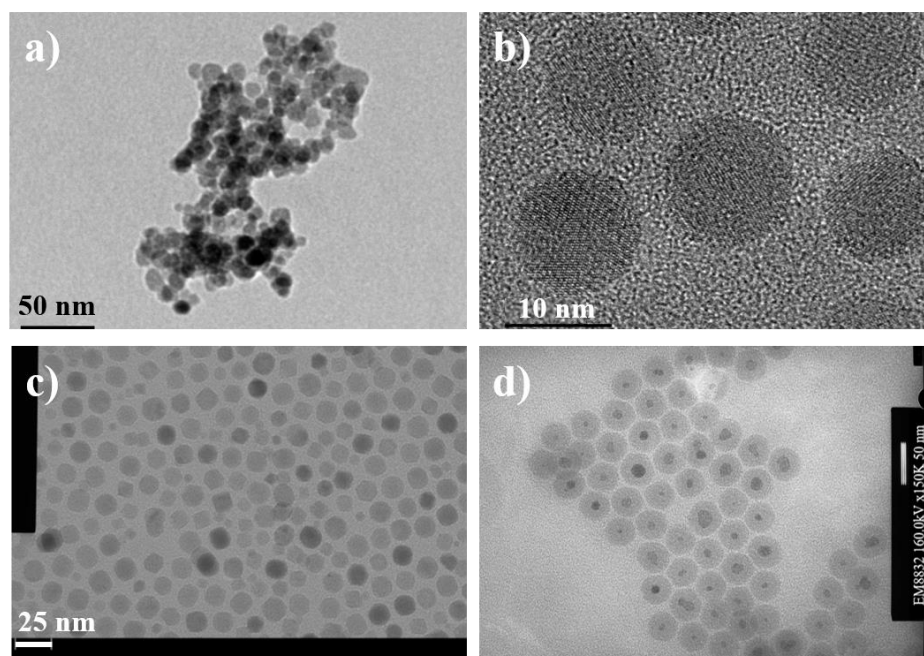


Figure 1. TEM images of Fe₃O₄ MNPs synthesized a) by co-precipitation and uncapped; b) by co-precipitation and coated with polyacrylic acid; c) by thermal decomposition with oleic acid coating (image courtesy of M. Puerto Morales, ICMM-CSIC); d) by co-precipitation and coated by a silica shell.

particles with high polydispersity. Bottom-up processes, or chemical methods, provide more precise control over the resulting characteristics. Starting from small units of the materials, further self-assembly processes lead to the formation of the nanostructures.

Co-precipitation, developed by Massart in 1981, is one of the most popular techniques due to its simplicity and high yield [24]. The oxides are precipitated from a solution with the metal precursors as the pH is tuned to a basic range. The addition of coating polymers allows obtaining a stable colloidal suspension and to introduce reactive chemical groups necessary for subsequent functionalization.

Thermal decomposition involves breaking down metal precursors, such as acetylacetonates, carbonyls, or oleates, in organic solvents, as octyl ether, benzyl ether, or octadecene, at their boiling temperatures and in the presence of dispersants and/or hydrophobic ligands. The high control over the particle size, shape, and polydispersity is obtained by separating the nucleation and growth stages, as stated by LaMer's theory [25]. However, the hydrophobic reaction media (which is usually toxic and cannot be used for functionalization of biomolecules), must be replaced or modified for biological applications. Different approaches such as ligand exchange or extra coating layers can be used for this purpose [26, 27].

Microwave synthesis is a variation of thermal decomposition methods in which heating is achieved by microwave induction. It is attracting attention because it improves the nanoparticle quality, reaction yield, and reproducibility, and reduces the synthesis duration [28]. The heating homogeneity in the reactor ensures a narrow size distribution and controlled physicochemical properties of the MNPs obtained directly in the hydrophilic medium. Although the reactors are small, their scaleup has already been proposed [29].

In **microemulsion** methods, micro- or nano-drops called micelles are formed thanks to the combination of the precursors, surfactants, and dispersing medium. The nucleation and growth of the particles occur inside them. This produces a narrow size distribution because the micelles, acting as nanoreactors, constrain the MNP growth [30].

Solvothermal synthesis is performed at high pressures above the

solvent's boiling temperature (it is called hydrothermal if the solvent is water). The sophisticated equipment and operation conditions renders high-quality monodisperse particles but may complicate the scaleup of this method.

The **sol-gel** method is a multi-step process based on the metal precursors' hydrolysis and polycondensation near room temperature. The first step forms the sol, transformed into the gel by successive condensation, vaporization, and solidification. Further heat treatments are needed to produce crystallization. However, it is still difficult to control particle morphology and reproducibility due to the complex mechanisms involved during the steps of the reaction.

Polyol methods use polyethylene glycols of different hydrocarbon chain length that act both as reducing and stabilizing agents during the particles' formation. Their amphiphilic character allows the direct obtention of hydrophilic suspensions for bio-applications. The high temperatures enable control over the size and crystallinity while reducing the starting materials' cost and toxicity.

Further information about traditional synthesis methods and new approaches like microfluidic systems and dendrimer templates may be found in Refs [31–33].

4. Characterization methods

Because the performance of colloidal MNPs essentially depends on their physicochemical properties, their thorough characterization is critical for finding the best routes to optimize their biomedical applications and to obtain a meaningful interpretation of the outcome. Additionally, standardization of the analysis protocols is crucial for inter-laboratory comparison and translation to the clinics and industry [34].

In this section, we review the physical characterization methods most frequently used for MNPs. Size, morphology, agglomeration, structure, and superficial and magnetic properties significantly influence the particles' bio-distribution, safety, and efficacy. They are evaluated by techniques commonly used for other materials, but which have peculiarities when applied to MNPs for bio-applications. In this section, we list some of the most popular characterization techniques, with a special focus on one of the most specific problems: sample preparation.

We provide starting points and references for interested readers to follow.

4.1. Sample preparation

Depending on the characterization technique and the specific application, particles are either dried, suspended in a liquid medium, or immobilized in a solid phase. Many characterization devices cannot handle liquids, so colloidal nanoparticles need to be dried. Although spontaneous evaporation of the solvent is an option, it often produces undesired oxidation of the particles' surface that would alter the characterization results. Oven drying at moderate temperatures in a protective atmosphere is a better choice. Freeze-drying (lyophilization) is an alternative that is especially recommended if the particles are conjugated to biological material. It consists of cooling the sample below the triple point of the solvent, reducing the pressure, heating it to produce sublimation (vacuum speeds it up), and heating again to produce desorption of the remaining water molecules [35, 36].

For some techniques or applications, the powder samples need to be suspended or re-suspended. The nature of the particle surface needs to be considered to find a suitable solvent (organic for hydrophobic particles; water, or other polar solvents for hydrophilic coatings.) The protocols involve mixing, sonicating, and syringe filtering.

Mainly for magnetometry, the colloidal particles may need to be immobilized because some instruments cannot handle liquids or to prevent Brownian motion or physical rotation of the particles. They can be immobilized in a compatible solid matrix. For hydrophobic particles (coated with hydrophobic polymers or suspended in organic phases), paraffin wax, docosane, or hydrocarbons of high molecular weight are adequate. Hydrophilic particles (coated with hydrophilic polymers, peptides, amino acids with amino or carboxylic residual groups) can be immobilized in silica, dimethacrylate trietilenglycol, or agar. The protocols involve mixing a known mass of nanoparticles with the initiator solution, sonication to disperse them, and placing them in an oil bath at 70 °C for some hours. The initiator polymerizes, forming a solid matrix.

4.2. Morphology, size, and structural characterization

The microstructure, size, and morphology of the MNPs are typically determined combining diffraction techniques, electron and atomic force

microscopies, and Mössbauer spectroscopy.

The most direct way to obtain the particles' metal (or metal oxide) core size and shape is transmission electron microscopy (TEM). It uses a beam of accelerated electrons, benefiting from their short wavelength to resolve distances in the nanoscale. TEM uses a static beam transmitted through a thin sample (the thickness must be below 100 nm) to get the structural information and provide magnified bidimensional images. The sample preparation starts with a diluted suspension. A droplet is deposited on a carbon membrane and placed on a copper grid (carbon-coated copper grids are commercialized). The sample must be then dried either by natural evaporation or in flowing nitrogen. Careful sample preparation is essential to avoid problems like aggregation while drying [37] or the formation of crystalline salts or films. Specimen preparation is more difficult when it contains biological material, such as cancer cells. In this case, the material must be embedded in a pure resin mixture, dried, and cured. Then, an ultramicrotome is used to cut thin sections [38]. TEM can achieve lateral spatial resolution and magnifications up to factors of 107. The MNPs' shape and size distribution can be inferred from the TEM images; its drawback is that a significant sampling requires the analysis of many micrographs. Transmitted beams also provide insights into the morphology and sample's structure and reveal atomic defects or dislocations. In TEM, the diffracted electrons can be used to obtain a selected area electron diffraction pattern (SAED), which provides information about the crystal structure, and the energy-dispersive x-ray spectroscopy, to get qualitative information about the chemical composition of individual particles. High-resolution TEM uses hardware to improve the resolution to 0.05 nm, enabling imaging of the atomic structure.

In scanning electron microscopy (SEM), the electron beam scans the specimen line by line. The electrons interacting with matter are scattered and can be collected in a variety of forms. The secondary electrons (from the sample's atoms) and the backscattered electrons (from elastic collisions) provide topological images and composition maps. Although monodisperse MNPs can be too small to be seen by SEM, this technique can help analyze beads containing embedded or encapsulated particles. For SEM experiments, the sample must be in powder, fixed on an adhesive tape on which a thin layer (15-20 nm) of a conductive metal is sputtered. This is an optimum thickness for obtaining good quality

images and, at the same time, a compositional analysis of the sample by energy-dispersive X-ray spectroscopy, which is frequently included in SEM. Field-emission SEM uses an electromagnetic electron generation, which notably improves the spatial resolution and avoids conducting coatings on insulating materials. Scanning TEM is a variation of TEM in which the focus electron beam is scanned across the specimen.

Atomic force microscopy (AFM) gives information in the three spatial dimensions. It scans the specimen with a probe that mechanically interacts with the specimen and measures the force as a function of their mutual separation. It creates three-dimensional images of nanoparticles with sizes between 0.5 and 50 nm. The MNPs can be deposited on a cleaned silicon substrate after sonication, left to dry for 5-10 minutes, and blown by a nitrogen stream to eliminate the residual solution [39]. AFM does not require conductive coating of the sample and can work in liquid medium. Magnetic force microscopy (MFM) is a variation of AFM that uses a magnetic tip to interact with the sample and visualize magnetic domains [40]. MFM has been used to distinguish between blocked and superparamagnetic magnetite particles in aggregates [41].

For many aspects of the bio-applications, the hydrodynamic size plays a vital role. This size includes not only the inorganic core of the particle but also the coating and solvation molecules. It can be obtained by dynamic light scattering (DLS). In this technique, a laser beam irradiates the sample, and the scattered light is collected. The intensity fluctuates depending on the particles' Brownian motion, which in turn is related to their size. One can also use DLS to assess the aggregation of the particles [42, 43] and to check the success of the biofunctionalization. When a bio-receptor is attached to the particles' surface, the hydrodynamic size increases. Specimen preparation for DLS usually requires dilution to avoid multiple scattering. The hydrodynamic size depends on the diluent salinity. Nanoparticle tracking analysis (NTA) is an increasingly popular technique that combines light scattering with a microscope to analyze the individual particles' Brownian motion. It then provides particle size distributions ranging from approximately 10–20 nm to 1000–2000 nm [44]. Because this technique individually tracks and sizes each particle, a low initial concentration to avoid crowded observation fields is required to achieve accurate results (usually 10^6 – 10^{10} particles/mL). This dilution process and its time-consuming handling make DLS measurements more widespread for a routine size characterization. On

the other hand, NTA offers a more accurate distinction between the smaller and larger particles, and information about nanoparticle concentration in the liquid sample.

A comparison of experimental methods to measure metal nanoparticle dimensions is found in Ref. [45] One can learn more about nanoparticle and biological sample preparation for electron microscopy in [46] and references therein.

X-ray diffraction (XRD) and neutron diffraction (ND) allow investigating the long-range crystal and magnetic structure, respectively, of the samples [47]. In both cases, the beam interacts with the material, and the raw data consist of the diffracted intensity as a function of the diffraction angle. The main difference is that X-rays interact with the atom's electron cloud, whereas neutrons interact with the nuclei (nuclear scattering) and with the unpaired electrons (magnetic scattering). In XRD, the diffracted intensity is related to the atomic number of the atom, revealing the symmetry and lattice parameters of the crystallographic unit cell based on the diffraction peaks' angular position. Additionally, the peaks' widths relate to the material's intrinsic properties, such as crystallinity, strain or grain size. XRD is more commonly used for structural studies because it is versatile and accessible to most researchers. ND, on the other hand, requires a large facility's neutron source but provides the magnetic structure. In materials combining light elements, XRD may not be adequate, but ND can be an alternative because it is not directly related to the atomic number. Additionally, the atoms that are neighbors in the table of elements are not easy to distinguish in an XRD pattern, but they can be with ND.

A full-profile fit based on Rietveld refinement can yield quantitative information from XRD and ND experiments. It is remarkable that even though Cu K α 1 radiation ($\lambda = 0.15418$ nm) is the most common wavelength for XRD experiments when the MNPs contain elements such as Cr, Mn, or Ni but especially Fe and Co, XRD with a source with a Mo anode ($\lambda = 0.07107$ nm) is more suitable because these elements fluoresce with X-rays from a Cu anode.

Both liquid and powder samples can be examined, although the latter is preferred in long experiments to prevent the change in the sample volume and particle position due to the solvent's evaporation [36]. The

powder for XRD experiments is placed in quartz sample holders of small depth. The preparation of the powdered specimen for characterization is critical because its surface must be extremely homogeneous. In the case of ND, double-walled vanadium cylinder sample holders are traditionally used to reduce neutron absorption.

X-ray absorption spectroscopy (XAS) is used to study the local environment around the metallic atoms. Even though XRD requires long-range order of atoms (>10 nm), XAS is not so limited. The principle of this technique is based on the absorption of X-rays by the atoms. Depending on the absorption spectrum's energy range, XAS is split into X-ray absorption near-edge spectroscopy (XANES) and extended X-ray absorption fine structure (EXAFS) [48, 49]. The first is sensitive to the oxidation state and coordination chemistry of the absorbing atoms, whereas the second is used to determine distances and coordination numbers of the neighboring shells around the central atom. Additionally, if the MNPs contain mixtures of phases with different valence states of a given element (e.g., Fe in α -Fe, γ -Fe, Fe_3O_4 , γ - Fe_2O_3) XANES analysis can also be used to estimate phase ratios [48]. The preparation of samples for XAS experiments is crucial because the thickness of the sample affects the absorption coefficient, and thus, the intensity of the oscillations. Two different procedures are commonly used. The first involves hydraulically compacted pellets that are a mixture of boron nitride and the powdered sample. In the second, a small amount of powder is spread over an adhesive Kapton tape. In both cases, one must optimize the samples' thickness and homogeneity to attain the best signal-to-noise ratio.

MNPs for bio-applications are often colloidal suspensions of mixed magnetite and maghemite. Both are spinel ferrites with almost identical lattice parameters, so their identification by XRD is not a trivial matter. However, Mössbauer spectroscopy (MS) has proved to be extremely helpful in distinguishing their composition and stoichiometry. The task is challenging in nanoparticle specimens because magnetic interparticle interactions cause broadening of the spectral lines, which hampers a profile-based distinction. A useful guide for Fe^{57} MS discrimination of maghemite and magnetite nanoparticles is in Ref. [50]. The basis of MS is recoilless γ -ray resonance absorption, and the recoil energy can be obtained only when both source and absorber are embodied in a solid lattice. The sample preparation varies with the configuration. For measurement at room temperature, several grams of powder sample

must be spread on adhesive Kapton tape, whereas for low-temperature spectra, small Teflon boxes may encompass the powder. The samples' thickness and homogeneity are crucial, and the thin-powdered layer must be optimized to contain around 5 mg of Fe per square centimeter.

4.3. Surface properties

Routine characterization of the surface condition of the nanoparticles for bio-applications involves ζ -potential and functional groups. The ζ -potential is the electrostatic potential difference between the dispersion medium and the stationary layer of fluid attached to the particle (Stern layer). It can be obtained by electrophoretic light scattering (included in some DLS analyzers). It determines the stability of the particles' suspension (absolute values of ζ -potential above 30 mV usually result in repulsive electrostatic forces strong enough to attain colloidal stability). Samples may require dilution, avoiding the addition of any electrolytes [51].

Fourier transform infrared spectroscopy (FTIR) enables investigation of the molecules attached to the particles' surface [52]. The spectrum gives information about the strength and nature of the bonds and the functional groups. The measurements are preferably on powder samples, usually grounded with potassium bromide (KBr). FTIR is one of the basic techniques to prove that a ligand exchange process has been successful [53].

Raman spectroscopy (RS) provides chemical and structural information. For quantification, some precautions regarding the laser-induced oxidation must be taken [54]. RS is suitable for all kinds of samples, even biological. It distinguishes the composition of the different phases in the core and shell [55, 56]. A thorough characterization of the surface can be done by X-ray photoelectron spectroscopy (XPS) [57]. This technique gives the elemental composition of the outer layers of the material and the chemical and electronic state of the elements at the surface. It is especially useful to get information about the oxidation state in iron oxide particles [58], core-shell structures [59], and ligands bound to the surface [60]. Samples for XPS must be dried powder because the measurements are made in ultra-high vacuum.

4.4. Concentration

The concentration of the inorganic magnetic cores of the particles in a solution is a parameter required for most studies and applications. One can give the total mass per unit volume, iron mass per unit volume, and number of particles per unit volume. It can be obtained by thermogravimetric analysis (TGA), taking great care to measure the deposited volume. Additionally, TGA provides information about the organic layers, the extent of coverage, and layer-mass to core-mass ratio [61]. Some instruments include differential scanning calorimetry, which shows the endothermic or exothermic nature of the processes. TGA requires a large sample volume and is a destructive test. Micro-TGA eliminates this drawback [62].

Inductively coupled plasma mass spectrometry (ICP-MS) and optical emission spectroscopy (ICP-OES) are used to determine the concentration of elements, providing high precision, accuracy, and sensitivity even with trace amounts of material. They are compatible with any kind of samples, although digestion processes are usually required [63, 64].

NTA devices, discussed above, can also estimate the concentration as the number of particles per volume [65].

4.5. Magnetic characterization

Classical and advanced magnetic characterization techniques are described in other chapters of this book. This section aims to focus on the most used techniques and sample preparation for MNPs that are typically used in the field of life sciences.

The most-used magnetometers for MNPs are vibrating sample magnetometers VSM [66], alternating gradient force magnetometers AGFM [67], and magnetometers based on superconducting quantum interference devices SQUIDs, often including AC susceptometry based on mutual induction [68]. Fluxgate magnetometers are often used to measure magnetorelaxometry.

The magnetic properties of MNPs that more substantially affect their biomedical applications are their DC and AC hysteresis, remanent magnetization M_R , saturation magnetization M_S , magnetic effective

anisotropy K_{eff} and magnetic interactions, blocking temperature T_B , DC and AC permeability, and relaxation. The methods to obtain them are with DC magnetization curves as a function of applied field or temperature (zero-field cooling and field cooling ZFC-FC; isothermal remanent magnetization IRM; demagnetization remanence curves DCD; and first-order reversal curves (FORC); and field, temperature, or frequency dependence of AC magnetic susceptibility.

ZFC curves are obtained by cooling the sample in zero applied field from room temperature to, usually, liquid-helium temperature (4.2K), then applying a DC field and measuring the magnetization (M_{ZFC}) while the sample is warmed. FC curves are obtained in the same way, but with the field applied during cooling (M_{FC}) [69]. The blocking temperature determines the transition between the blocked and the superparamagnetic state. Some authors identify the temperature at which the M_{ZFC} has a maximum (T_{max}) with the blocking temperature [70, 71], which is adequate for monodisperse populations. In other cases, the T_B is obtained from the T_B -distribution curve (calculated as the temperature derivative of the difference $M_{\text{FC}} - M_{\text{ZFC}}$). For monodisperse populations, the FC and ZFC curves would coincide for temperatures above T_B ; their separation, quantified by the difference of T_{max} and T_{irr} (temperature at which the two curves merge), is an indication of the degree of polydispersity [69]. We can calculate $K_{\text{eff}} = 25k_B T_B / V$ for average particle volume V and Boltzmann constant k_B . ZFC-FC curves are also effective to study the MNP interactions, which cause spin glass or superferromagnetic behavior [72, 73].

The remanent magnetization technique can provide a thorough insight into the MNP interaction. It consists of two curves: IRM and DCD. Both are obtained applying a field H and measuring M_R after its removal. For IRM, the sample starts demagnetized while for DCD it starts from negative saturation (The IRM is measured after the application and removal of a field with the sample initially demagnetized. The DCD is measured from the saturated state by application of increasing demagnetizing fields). In an ideal non-interacting system of monodomain particles, Wohlfarth's relation [74] holds:

$$\partial M = m_r^{\text{DCD}}(H) - (1 - 2m_r^{\text{IRM}}(H)) = 0 \quad (1)$$

Where $m_r^{\text{DCD}}(H)$ and $m_r^{\text{IRM}}(H)$ stands for the remanent magnetization in

DCD and IRM, respectively, normalized by the saturation magnetization value at $H \rightarrow \infty$. A non-zero value of ∂M is an indication of the magnetic interactions. This is traditionally represented in a Henkel plot or ∂M plot [70, 75]. Given that these techniques are related to the remanent state, the curves need to be obtained below the particles' blocking temperature.

First order reversal curve (FORC) analysis can provide distributions of the local interaction and switching fields [76]. To obtain a FORC, an initial saturating field (H_S) is applied and reduced to the return field (H_R); H is then increased up to H_S while measuring the magnetization $M(H_R, H)$; the procedure is repeated for equi-spaced values of H_R . For a non-interacting system of monodomain particles, the differential susceptibility

$$\chi_m(H, H_R) = \left. \frac{\partial M}{\partial H} \right|_{H_R} \quad (2)$$

is the same for all the values of H_R in the common range of H , but this equality is broken due to interactions. These interactions are then shown in the FORC diagram [77], that is the bidimensional plot of the FORC distribution,

$$\rho(H, H_R) = -\frac{1}{2} \frac{\partial^2 M}{\partial H \partial H_R} \quad (3)$$

on the H - H_R plane [78].

Dynamic magnetic susceptibility (DMS) (also called AC magnetic susceptibility) frequency spectra are essential to evaluate the MNPs' potential in many biomedical applications. For example, the DMS (103-108 Hz) of blocked nanoparticles can be used to determine their interaction with proteins in their protein corona [79]. DMS and AC magnetization curves and susceptibility are also crucial to assess the heating capacity of nanoparticles for magnetic hyperthermia, or their use as nanotags in inductive bio-sensing.

Magnetorelaxometry consists of magnetizing the MNPs by applying a static magnetic field, removing it, and measuring the sample's decaying magnetization as a function of time. For this purpose, one or several sensitive magnetometers monitor the magnetization evolution. For strictly monodisperse particles, one expects an exponential decay with a size-dependent time constant. A MNPs suspension has a non-trivial, non-

exponential decay that depends on the hydrodynamic size, size distribution, and aggregation.

Most magnetometers and susceptometers can measure either liquid or solid samples. Liquid samples are preferred, for example, when there is an interest in distinguishing effects associated with Brownian relaxation or changes in the magnetization dynamics produced by bio-conjugation, chaining, or agglomeration of particles. Nevertheless, solid samples are usually easier to handle, and the only possibility for measurements with a varying temperature that goes through the melting point of the solvent. One rough option is to dry the samples, encapsulate the powder in a gelatin capsule, and press it with cotton (to avoid movement during measurement). However, this may increase the interaction among the particles, which can affect the effective anisotropy constant, the distribution of blocking temperatures, or the characteristic relaxation times. In general, the particles' dispersion with a concentration smaller than 1 wt.% in a solid matrix can assure that the measured magnetic properties are intrinsic [80]. Ref. [81] has a detailed discussion of precautions needed for sample preparation for measurements of samples with low magnetic moments.

4.6. Preclinical characterization

For biomedical applications, especially *in vivo*, nanomedicines must be safe for the patient. A thorough study of the transport and fate of MNPs in the human body is vital before any diagnostic or therapeutic concept is transferred to the clinical field. Preclinical characterization involves assays for toxicity, sterility, and interactions with living biological matter, including MNP uptake by cells or macrophages, and thrombogenic or hemolytic effects. Ref. [82] and references therein contains a detailed description of these techniques for both *in vitro* and *in vivo* models.

When the nanoparticles enter a biological system, some effects can crucially affect their behavior: size growth due to protein corona, agglomeration due to interactions among proteins, the variation of their magnetic properties caused by biodegradation, or the change of Brownian relaxation due to viscosity. It is then essential to characterize the nanomaterials in biological matrices that mimic the application environment [83].

5. Magnetic bio-separation

Many areas of biosciences and biotechnology require the separation of specific biomolecules from a complex medium. The two main processes that involve bio-separation are (i) the isolation or purification of a target biomolecule for its study or further use (e.g., antibodies, viruses, or genes), and (ii) the enrichment or concentration of a molecule in the sample, for example, to ease its detection or quantification. Additionally, magnetic separation can be employed for environmental applications in water and soil remediation, either to remove iron-containing particles or to eliminate other contaminants adsorbed at the surface of a MNP [84, 85].

The basic principle of the magnetic bio-separation is simple: MNP bearing a specific surface functionalization to capture the target molecule are mixed with the complex sample and incubated for a few minutes to allow the molecule-particle binding, after which the particles are trapped by a magnetic field gradient, carrying the desired molecules. The supernatant can be removed, and the specific biomolecules resuspended in a fresh medium.

This kind of magnetic “fishing” relies on the affinity constant of the

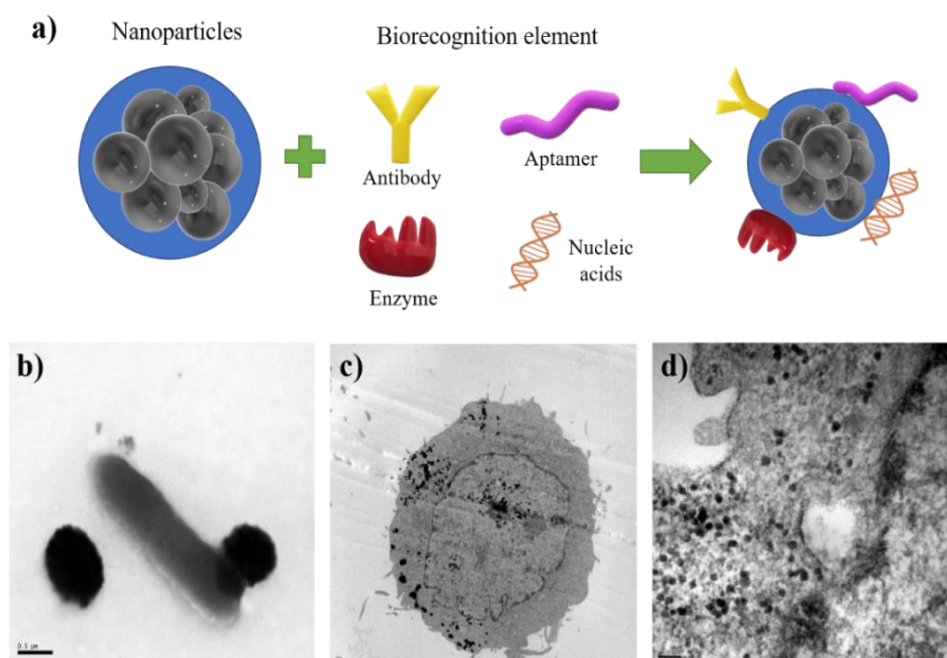


Figure 2. a) Schematic representation of the affinity ligands that can be attached to a MNP. b) TEM image of MNP-*Escherichia coli* recognition via anti-*E. coli* antibody attached to fluidMAG-Streptavidin (Chemicell GmbH, Germany). c) MNP internalized by a HeLa cell. d) Detail of the internalized MNP by a HeLa cell [86].

ligand (which determines the specificity and recovery), the magnetic moment of the particles, and the magnetic separator, as Figure 2 exemplifies.

The surface of magnetite or other ferrite nanoparticles can be modified for separation purposes. Although superparamagnetic particles can be stable in suspension and easily re-suspended, their magnetic moment is small and corresponds to their size. In this case, high magnetic gradients are needed to separate them. Small superparamagnetic particles can be encapsulated in biopolymers, porous glass, or magneto-liposomes, forming micrometer-sized beads to attain the large magnetic moments that favor efficient separation in low magnetic gradients.

Magnetism has some advantages versus alternative techniques such as column chromatography, precipitation, ultracentrifugation, or filtering. One of them is that all steps can be produced in only a tube, avoiding the sample losses associated with transfer. Magnetic separation does not involve costly reagents or equipment, and it can easily handle large-scale operations and automated processes. The magnetic technique can deal with samples containing particulate material, and, contrary to chromatography or filtering, it does not lead to very diluted molecule solutions. In fact, magnetic separation is useful for a preliminary concentration of bio-analytes for their detection, which can be done by the same particles used in the role of detection labels. Another excellent feature of magnetic separation compared to, for example, centrifugation, is that it involves only small shearing forces, which ensures the integrity of the molecules during the procedure.

To attract a particle of magnetic moment \vec{m} and separate it from the matrix, a magnetic gradient is required to produce a force $\vec{F} = \nabla(\vec{m} \cdot \vec{B})$. The simplest set-up to create a magnetic gradient is a permanent magnet, especially if it has a pole with a sharp or pointed shape.

In the literature and market, one can find various designs with different geometries and coatings depending on the specific needs, such as laboratory tubes, sample volume, biocompatibility, or disinfection. Flow-through magnetic separators obtain a high gradient useful to capture small volume or weak magnetization particles [87]. They consist of column filters made of densely packed ferromagnetic spheres or fibers magnetized by a permanent magnet or superconducting solenoid. The

sample containing MNPs flows through the magnetized column and is trapped by it. After removal of the applied field, the nanoparticles and their cargo are released from the filter by pushing water or another solvent through it. The column filters are disposable.

6. Magnetic nanoparticles for bio-sensing

Today, more than ever, biomedicine, food industry, and environmental safety demand procedures for bio-molecule detection that are as fast, specific, and sensitive as possible. Depending on the precise application, other specifications may be crucial, such as low cost, ease of use, or portability.

Various research groups are responding to these demands with solutions that rely on MNPs as signal reporters. Most biosensing platforms adapt magnetic field sensors to excite the nanoparticles and detect their magnetization. Small devices are based mainly on Hall-effect, magnetoresistive, or inductive sensors and microfluidics or surface biofunctionalization to bring particles into the sensing area [88–90]. Some bio-analytical systems with extremely high accuracy involve SQUID or atomic magnetometers, or nuclear magnetic resonance [91, 92].

Other chapters of this book treat in detail the basics of magnetic field sensing. We focus in this section on how to adapt them for biological specimens tagged with MNPs.

6.1. Spintronic sensors

Spintronic sensors based on either giant magnetoresistance GMR, tunnel magnetoresistance TMR, or planar Hall effect PHE can be used for ultrasensitive detection of MNPs and, consequently, for biosensing [89, 93]. Among them, GMR devices, specifically spin valves SPV, have been the most widely used for biosensing applications. As in the case of the bio-separation, for bio-detection the MNPs will tag the target analyte by affinity ligands attached to their surface. Once this step accomplished, the next steps consist of (i) removing the non-bound nanoparticles and (ii) detecting and quantifying the nanotags. The sensor arrays are coated with a corrosion-resistant passivation layer and then, a small area is biologically activated by immobilizing the bio-recognition molecules that selectively capture the target analyte. The latter is tagged with MNPs before or after this capture. In this way, the MNPs are very close to the

sensing layer, which is essential to detect the magnetic fringing fields. The geometry and size of the biologically activated area and the particles' spatial distribution are essential variables to consider for precise quantification.

The transformation of a spintronic sensor into a biosensor involves challenging tasks, such as integration with microfluidic channels to bring the fluid sample into the sensing area, passivation of the sensor surface and electronics, and chemical surface modification to bind the target molecule, and washing out of the unbound particles and molecules. Ref. [94] has further details on sensors' surface modification.

Uncontrolled agglomeration of MNPs should be avoided, as it could cause obstructions in microfluidic channels. Also, uneven agglomeration can produce calibration failures, as different sized agglomerates can attach to the biomolecule. Finally, magnetic dipolar interactions can modify the magnetic response of the particles and consequently, their quantification. For all these reasons, superparamagnetic particles are preferred for this application.

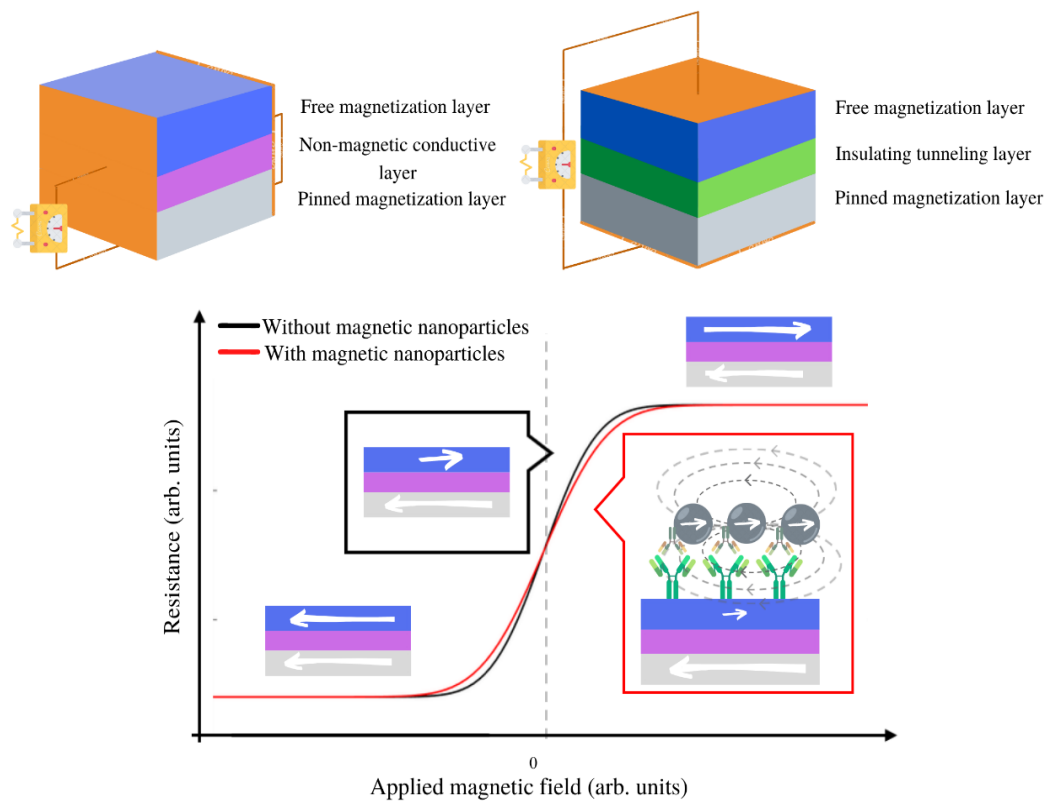


Figure 3. Scheme of a GMR sensor (top left), a TMR sensor (top right), and the resistance response in a biosensing application (bottom).

The magnetic nanotags must be excited by either a DC or an AC magnetic field to produce a detectable fringing field (Figure 3.) In addition, another biasing field may also be applied to define a proper working point for the sensing multilayer.

Using SPV sensors, some authors report the detection of only 20 Fe₃O₄ MNPs of 16 nm, equivalent to a total magnetic moment of 15×10^{-18} A·m². After the adequate surface biofunctionalization, they can detect proteins and DNA with limits of detection below 10 pM (0.4 ng/mL) and procedure durations below 2 h [93]. Cubic nanoparticles of Fe₇₀Co₃₀ with saturation magnetization as large as 226 A·m²/kg of FeCo have been used for GMR detection of proteins achieving sensitivities 13 times larger than that of standard ELISA techniques [95]. Nanometric trapezoidal multilayers consisting of two ferromagnetic nanolayers magnetostatically coupled through a ruthenium spacer, have been used for GMR quantification of proteins combined with magnetic tweezers. Their high saturation magnetization of 150 A·m²/kg of CoFe allowed limits of detection of 10 pM [96]. Configurations to detect influenza viruses, proteins, DNA strands, Escherichia coli, the liver cancer biomarker α -fetoprotein, and sentinel lymph nodes [97] are other examples of direct contact GMR and TMR biosensors. Biosensing platforms based on micro-Hall sensors have been reported for the detection of DNA [98] and circulating tumor cells in unprocessed biological samples [99].

6.2. SQUID and atomic magnetometers applied to biosensing

Magnetometers based on superconducting quantum interference devices (SQUIDs) are among the most sensitive magnetometers, capable of measuring magnetization relaxation, remanence, and susceptibility. For biosensing, the molecule to detect is tagged with MNPs in suspension. Magnetic relaxation immunoassays are based on modifying the magnetization relaxation time of the MNPs when they are bound to the molecule. The free MNPs relax fast by Brownian motion (involving physical rotation of the particles), but when they are bound, their relaxation takes place mainly by Néel relaxation (the magnetic moment of the particle rotates to align with the magnetic field), which is significantly slower. The measurements are usually done in liquid samples containing both the bound and free particles, thus avoiding the time-consuming washing steps or the microfluidic devices to separate them. For this reason, this method is usually called wash-free or liquid-phase

immunoassay. They can also be done by immobilization on a surface, or latex beads much larger than the MNP. In general, various measurements are necessary to interpret the relaxation rates and allow quantification, which is mainly done by comparing to reference curves for the relaxation of bound and unbound MNPs. For this application, iron oxides and spinel ferrites are the most used. The MNP solution must be very homogeneous in size and magnetic properties. Its colloidal stability and exhaustive control of their agglomeration must be assured to avoid false-positive detections.

SQUID magnetometers can also be used for detection based on AC susceptibility or remanence measurements and their change upon immuno-attachment of the MNP to the target analyte.

Atomic magnetometers are made of gases of rubidium or cesium. Their working principle is detection of the interaction between the atomic gas moments and the external magnetic field. They are highly sensitive, and unlike SQUIDs, they do not require cryogenics. For bio-detection, the magnetic response of the MNP before and after binding to the target molecule is studied.

Ref. [89] has an exhaustive description of these magnetometry bio-detection techniques and an extensive collection of applications on biomarkers, tumor cells, and DNA detection.

6.3. Faraday induction coil biosensors

Faraday coil magnetometers and susceptometers can also be adapted for bio-detection mediated by MNPs. A variety of approaches differ both in the transducer coil and the electronics. In most inductive biosensors, an excitation coil produces a time-varying field that affects the MNPs, which, in turn, produces a changing magnetic flux that is picked up by a second coil. The pickup coil's response can be measured as a change of its self-inductance by an impedance analyzer, a variation of its resonance frequency, or by monitoring the induced voltage. The system can be reduced to a single coil with a dual role: excitation and detection if high frequencies are used to achieve a significant coil quality factor. In this case, superparamagnetic particles are advantageous because their initial magnetic permeability drops only at very high frequencies, above those corresponding to their Néel relaxation times.

Depending on the coil geometry, inductive magnetometers can encompass a vial with the liquid sample or an immune-active substrate on which the magnetically tagged analyte is captured [89, 100].

6.4. Magnetic Lateral Flow Immunoassays

Bringing a liquid sample close to the transducer usually involves coating the sensing surface and electronics with a corrosion-resistive passivation layer, integrating microfluidics, and washing out the remaining liquid after immobilization of the target molecule. Additionally, the regeneration of binding sensor surfaces is necessary to make them reusable and keep the cost down. Removing the biological material without damaging the sensor is complex, and a research matter itself [101].

Paper-based microfluidics consists of a porous cellulose membrane that guides the liquid by capillary action and therefore without pumps. It may include filtering stages and has a high surface to volume ratio, which enables a large number of biorecognition events. Additionally, the membranes are disposable and biodegradable.

Among the paper-based microfluidic analytical devices, probably the best known is the lateral flow immunoassay (LFIA) [102]. A popular example of LFIA is the home pregnancy test. Its main element is a strip of nitrocellulose membrane along which the liquid sample can run (Fig. 5). In the first stage, the target molecule (e.g., the human chorionic gonadotropin hCG) is selectively labeled by a signal particle (which is attached to a specific anti-hCG antibody). Two lines of selective recognition molecules have been dispensed across the membrane strip: the test line, at which the target analyte is captured together with its signal tags, and the control line, that traps unbound particles and is used to assess the completion of the assay. This type of test is called a sandwich or direct assay. If it is not possible to attach two antibodies to the target molecule, an indirect or competitive assay is used.

A binary presence/absence response may be adequate for pregnancy tests, but many other biomedical, food safety, or environmental targets require quantification. In such cases, the LFIA must be combined with a sensor that does not compromise the advantages of low cost, portability, and easy use. MNPs used as tags can provide a quantifiable signal along with other benefits, such as magnetic immuno-separation or

concentration of the analyte, long-lasting signal, and lack of interference and background signal from the biological matrix or the paper.

Besides the conditions common to other magnetic immunoassays and biosensing applications, like the homogeneity of the magnetic properties and size, LFIA requires that the MNPs are dispersed in a water solution. The particles' hydrodynamic size must be kept below a threshold that depends on the membrane pore size (typically in the order of 0.1 to 1 μm), which determines the flow rate and the sensitivity. Other specifications are related to the sensing technology, mainly GMR or Faraday inductive sensors [103, 104]. Ref. [105] has more information on magnetic LFIA.

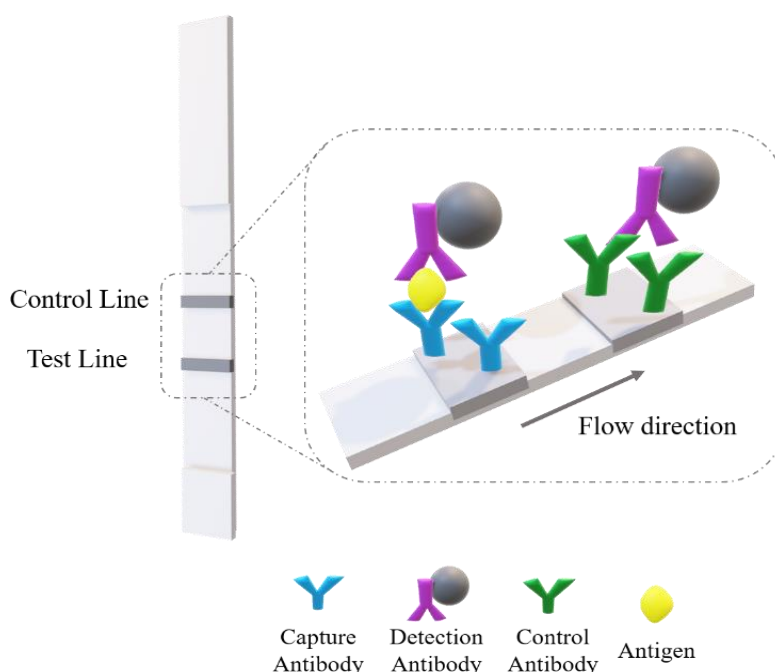


Figure 4. Schematic representation of a LFIA in sandwich format.

6.5. Magnetic nanoparticles in non-magnetic detection

Non-magnetic sensors can also use MNPs for pre-concentration, separation, and location of the target molecules.

In some non-magnetic affinity sensors (e.g., electrochemical, piezo-immunoassays, or impedance sensors), the MNPs are used as an interesting alternative to immobilize the antibody instead of a direct attachment. Disposal and renewal of the antibody layer is easy, allowing regeneration of the sensing surface. Additionally, in some enzymatic sensors (with conductimetric, amperometric, or potentiometric transducers), MNPs simplify the enzymes' storage and handling [106, 107]. In some Bio-Bar-Code sensors [108, 109] for high sensitivity

detection of protein and DNA, MNPs are used for immuno-separation.

7. Magnetic Nanoparticles for Bio-Imaging

Magnetic resonance imaging (MRI) is one of the most used techniques for non-invasive biomedical diagnosis due to its innocuousness, good spatial resolution, and penetration depth. It is based on the detection of water protons' magnetic relaxation; the contrast in soft tissues comes from the different proton density in different tissues, intra- or extracellular spaces, or lipidic environments, or different relaxation times.

MRI devices consist of a superconducting magnet, gradient magnetic fields, RF coils, and signal processing equipment. An intense magnetic field is applied to align the protons' magnetic moment in the field's direction. A magnetic gradient is superimposed on it to encode the signal spatially (because it causes the field strength to vary linearly in space). A radiofrequency field then reorients the protons' magnetic moment to align either at 90° or 180° with the applied magnetic field. When this pulse is turned off, the relaxation can be measured in longitudinal (T_1 , spin-lattice relaxation) and transverse (T_2 , spin-spin relaxation) modes. Protons that relax fast produce a large signal (the time-variation of the magnetic moment is picked up by inductive coils), whereas those that relax slowly produce a smaller one. The different signals lead to the contrast between tissues. MNPs enormously contribute to the enhancement of this contrast. In addition, MNPs can be functionalized to attach specifically to tumor cells, facilitating early cancer diagnosis.

Paramagnetic particles containing chelated gadolinium are widely used to shorten T_1 by coordinating with the water molecules, which increases the positive contrast. But their potential toxicity has led to the expansion of research on superparamagnetic iron oxide nanoparticles as contrast agents thanks to the dipolar coupling of their large magnetic moments to the water protons' moments. (MNPs have magnetizations that are 108 times larger and relaxations 104 times faster than those of water protons.) T_1 relaxation comes from the fluctuating electron spin moment of the contrast agents coupling with neighboring water protons' moments, which quickly relax back to their equilibrium magnetization, resulting in an increased $1/T_1$ rate MRI signal (positive contrast) and reduce the acquisition times [110, 111]. On the other hand, T_2 relaxation comes from long-range magnetic dipolar fields, which locally shift the proton

resonance frequency and dephase the proton spin precession. This leads to a faster T_2 relaxation and a reduced MRI signal (negative contrast) so that the affected regions appear darker [112]. The effect of particles' size and microstructure on the magnetic relaxivity are crucial [113]. The relaxation rate $1/T_2$ increases quadratically with the particle's size (the outer-sphere spins dominate it), until it reaches a limit value. On the other hand, ultrasmall superparamagnetic iron oxide particles have higher longitudinal relaxivity, leading to improved T_1 -weighted images.

While toxicity concerns hamper the *in vivo* application of many nanoparticle-based compounds, iron oxide MNPs of several formulations have been approved by the U.S. Food and Drug Administration and the European Medicines Agency as MRI contrast agents. The particle coating and thickness are crucial as they have a strong influence on MRI performance, pharmacokinetics, and biodistribution [114–116].

The emerging magnetic particle imaging (MPI) technique entirely relies on the MNPs used as tracers for image formation. The magnetic tracers are detected by Faraday induction with a pickup coil. The exciting field is its most peculiar feature. It consists of a time-varying magnetic field gradient (selection field) carefully designed to have a field-free point (FFP). The selection field is strong enough to align the MNPs except around the FFP. The FFP is rapidly moved in the image volume so that particles are misaligned around it, while the magnetization changes are picked up by the detecting coil. The signal is proportional to the number of particles and related to the location of the FFP, yielding a map of the tracer accumulation. This map is frequently superimposed on anatomical images such as those obtained by MRI, which provides accurate information about the tracer's distribution in the patient's body. In MPI there is no background noise coming from biological tissues, which enables high contrast. Its high spatial resolution (about 1 mm) combines with low acquisition times (on the order of or below 1 s) to allow real-time *in vivo* imaging [117, 118]. These characteristics make it an exciting tool for different clinical applications such as cardiovascular, pulmonary or gastrointestinal imaging, cancer diagnosis, brain injury detection, and *in vivo* tracking of stem cells [119, 120].

As in other *in vivo* applications, iron oxide nanoparticles stand out for MPI tracers. Sensitivity depends on the magnetic moment, which can be increased by increasing the particle size (staying below the

superparamagnetic limit) and by agglomerating or encapsulating small particles. A large initial magnetic permeability makes differences in magnetic field amplitude translate into large variations of the magnetic moment in the measurement direction, resulting in a better spatial resolution. Therefore, the optimal size depends on the operating frequency [121]. Gleich and Weizenecker did the first experiments on MPI in 2005 [117]. They recommended a magnetic core size of 30 nm to work at 25 kHz with field amplitudes of 10-20 mT. Since then, the commercial contrast agent Resovist® (Schering AG, Berlin) [122] is considered the gold standard for MPI tracers. Although most MNPs in Resovist® are very small, they form aggregates with average sizes of 24 nm that behave like monodomains. A variety of aggregation strategies are being investigated to increase the number of magnetic nuclei at a spot of interest while providing biocompatibility and functionality: micelles, liposomes, and bacterial magnetosomes (Ref. [121] and references therein.)

8. Magnetic hyperthermia, magneto-mechanical disruption, drug delivery, and tissue regeneration

MNPs can enable new tools for biomedical therapy, standing alone or in combination with plasmonic particles. Moreover, they are used for theranostics, a term derived from the contraction of “therapy” and “diagnostics.”

Localized therapy that avoids collateral damage is possible thanks to the small size of the MNPs and the possibility of remotely guiding them and targeting a specific location of interest. Whether thermal, mechanical, or chemical, the therapy can be focused, thereby reducing the required dosage. The most significant innovations are in magnetic hyperthermia, magneto-mechanical tumor destruction, and drug transport and delivery.

Heating cancer cells to 40-46 °C can destroy them or, at least, make them more susceptible to chemo- and radiotherapy. For localized tumors, local heating can be more efficient and safer than heating extensive body areas. This is the motivation for magnetic hyperthermia (MH) development, firstly proposed by Gilchrist et al. in 1957 [123]. This technique uses the MNPs as mediators that transform the energy provided by an alternating magnetic field into heat delivered to the tumor cell. This transformation mechanism is the magnetization rotation, which can take place by Brownian or Néel relaxation. Inside the biological tissue,

the MNP are practically immobilized, so Néel relaxation is the dominant mechanism. The delivered energy per cycle for a volume of particles V_{MNP} can be calculated as the hysteresis loop area: $E = \mu_0 V_{\text{MNP}} \oint M dH$, where μ_0 is the permeability of free space. Of course, E depends on the frequency and amplitude of the driving field H . Even for particles with minimal hysteresis in DC mode, the magnetization loop area increases significantly for frequencies in the order of several kilohertz because of the time lag between the induced magnetization and the applied field. This makes magnetic heating possible even for moderate frequencies. At higher frequencies, the particles behave as blocked and therefore do not respond to the magnetic field or have hysteresis. This is relevant because high frequencies and amplitudes are not safe for healthy organs (they can affect nerve synapses which produce undesired muscle stimulation and heart malfunctioning). Some studies suggest that the product of frequency and amplitude should not exceed $4.85 \times 10^8 \text{ A}\cdot\text{m}^{-1}\cdot\text{s}^{-1}$ [124].

The MNPs' heating capacity is characterized by the specific absorption rate (SAR, also known as specific loss power), defined as their heating power per unit mass:

$$\text{SAR} = \frac{P}{m} = \frac{C}{m} \frac{dT}{dt} \quad (4)$$

where C is the specific heat capacity of the colloidal suspension, m is the mass of the magnetic core, and dT/dt is the rate of temperature change. Obtaining the SAR from magnetometry, instead of calorimetry, makes it easier to maintain adiabatic conditions and obtain its dependence on temperature [125]. In this case, SAR can be calculated from the hysteresis loop area, the frequency f , and the particle concentration c as:

$$\text{SAR} = \frac{f}{c} \mu_0 \oint M dH \quad (5)$$

In general, the maximum SAR is achieved when the frequency of the applied field equals the inverse of the relaxation time of the MNPs, but it also depends on the field amplitude H_0 (in the linear response regime, the area of the magnetization curve is directly proportional to H_0^2). To facilitate comparison of the results of different laboratories, the heating capacity is identified by the intrinsic loss power ILP, defined as $\text{ILP} = \text{SAR}/(fH_0^2)$, with the advantage of it being independent of f and H_0 for moderate values.

For details on MH instrumentation, one can refer to Ref. [126].

The MNPs' heating power depends on extrinsic parameters, such as the exposure time, frequency, and amplitude of the applied field, and on intrinsic ones, such as their size, saturation magnetization, and anisotropy constant, which are interrelated [127]. If we compare, for example, magnetite and cobalt ferrite nanoparticles, we see that the latter have larger magnetic anisotropy and, consequently, wider hysteresis loops, but at the same time, will require larger field amplitudes. Additionally, the biological environment in which the MNPs are located, their agglomeration, and distribution, have an enormous influence on their mobility, and hence, on the type of magnetization relaxation permitted [128]. Magforce® developed a human-sized MH device working at 100 kHz and 0–18 kA/m, which obtained European Union regulatory permission to treat patients with brain tumors [129].

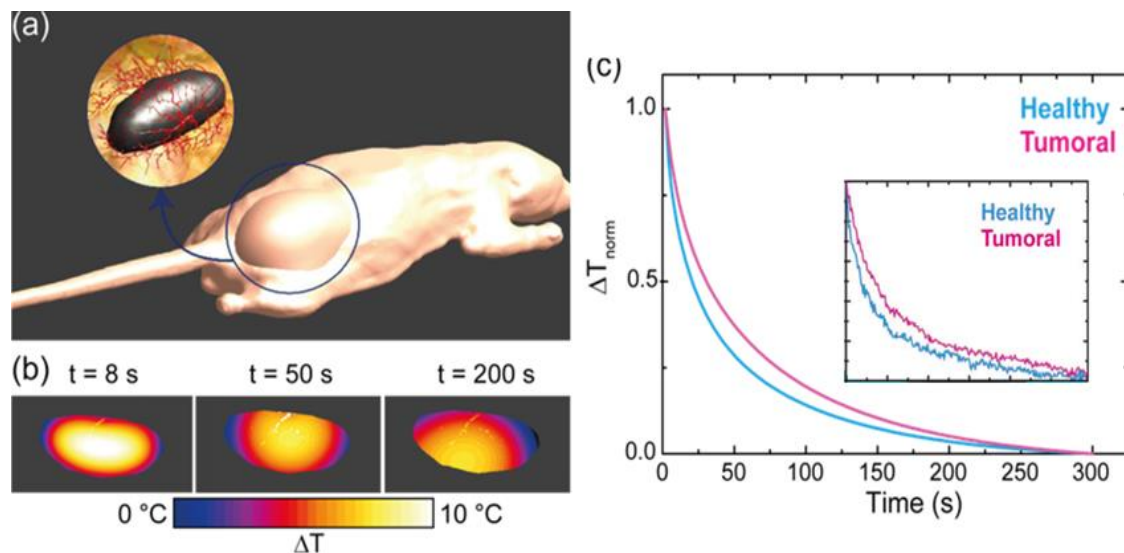


Figure 5. a) Computable mouse virtual phantom used for *in silico* testing. b) Temperature maps of a melanoma corresponding to different times after starting thermal relaxation. c) Time evolution of temperature extracted from the analysis of the thermal maps in (b) for an advanced-stage tumor and a healthy tissue. Copyright 2018 Wiley; used with permission from H. D. A. Santos et al. [130].

In silico testing is an emerging research line in the field of MH (Fig. 6) to predict heating efficiency. Modeling and simulating the temperature distribution, mass concentration, and heat transfer can significantly reduce the number of *in vivo* trials on animals and humans. Numerical computations must include the relevant parameters of the MNPs and the intracellular environment (i.e., the tumor cell). This technique's long-term goal is to guide clinicians in adjusting dosage and other variables to the

tumor's evolution.

Magneto-mechanical actuation has appeared recently as a new application of alternating magnetic fields in cancer cell destruction (some studies use rotating or precessing magnetic fields). In this case, the alternating magnetic field's desired action is the physical rotation or oscillation of the particles, which induces the cancer cells' death. The cell damage is provoked mainly by cell membrane disruption and the trigger of programmed cell death (apoptosis).

Magneto-mechanical action is mediated by anisometric particles that rotate or vibrate under rotating or alternating magnetic fields of moderate amplitudes and frequencies on the order of millitesla and tens of hertz. Magnetic microdisks that possess a spin-vortex configuration ground state are good candidates for this application, as they do not have remanent magnetization, which avoids their undesired agglomeration. When a field is applied, the magnetization vortex shifts, making the particle oscillate [131, 132]. The advantages of this technique over hyperthermia are that it avoids collateral thermal damage, and the power source requirements are much lower. On the other hand, their current microsize can be a problem for *in vivo* applications as they can be cleared by the immune system or do not cross biological barriers. Smaller anisometric particles [133, 134] such as nanodisks, nanorectangles, or nanorods can produce significant mechanical action if stimulated with stronger magnetic fields, easily achievable because the frequency required is low. However, one of the challenges is upscaling their fabrication.

Drug delivery is another biomedical challenge that can profit from MNPs. It is well recognized that large systemic drug doses may have adverse effects on healthy organs. Magnetic nanocarriers can significantly reduce them by local delivery of therapeutic doses of the drug, which can be sustained in time and have deeper penetration (for example, inside of tumors).

In 1908 Paul Ehrlich received the Nobel Prize in Medicine for his advances in immunology. He popularized the concept of "magic bullet" to refer to an ideal therapeutic agent that would act locally and specifically against a pathogen without relevant undesired side effects. This is the goal pursued by investigations on MNPs as drug or gene carriers. It

involves three aspects: the cargo, the transport, and the release. The drug's linkage can be obtained by covalent bonding, entrapment, adsorption, or microencapsulation in biocompatible polymers or vesicles [135]. The latter may facilitate the drug administration, favoring dosage control, and patients' compliance.

Once attached, the MNP-drug complex is injected in or close to the target and can be guided by magnetic field gradients. Targeting of the diseased site can be active or passive. Active targeting points to specific receptors that only tumors express or overexpress on their surface. The nanocarrier must then be accordingly functionalized against such a receptor. On the other hand, the passive targeting strategy relies on the selective accumulation of the MNPs at the tumor, which has limited lymphatic drainage and is particularly permeable compared to healthy cells. Once at the target, the MNPs can act at the tissue or be internalized by the cell, either by endocytosis or phagocytosis. The drug released may be triggered upon environmental changes or external stimuli, such as the temperature rise produced by magnetic hyperthermia (with a thermosensitive porous coating on the magnetic nanocarriers).



Figure 6. TEM image of a MTB with magnetosomes aligned along its body (Image courtesy of M. Luisa Fernández-Gubieda, University of Basque Country, Spain.)

One of the most challenging drug delivery goals is crossing the blood-brain barrier (BBB) to reach the central nervous system. Besides an adequate coating or encapsulation in liposomes, MNPs can be forced across the BBB by a magnetic force. Some studies propose the help of

magnetic drilling enabled by helical dynamic gradients and multilayered Au-Fe nanorods [136].

Some researches study magnetotactic bacteria MTB (see Fig. 7) as “smart” drug or gene carriers [137]. MTB are frequently found in freshwater reservoirs. They contain magnetosomes, which are highly crystalline magnetite nanoparticles (with sizes of 30-120 nm) surrounded by a phospholipid layer. MTB usually have around 15-20 magnetosomes aligned along their body, which act as a natural compass. They are natural swimmers that follow the magnetic field lines propelled by their flagella. Besides the targeting enabled by a magnetic gradient, MTB can use other natural properties. For example, aerotactic MTB have an affinity for oxygen-depleted hypoxic regions, which are the most active in tumors [138]. MTB can bear a high cargo loading, such as nanoliposomes attached to the bacteria or gold nanoparticles that favor endocytosis [139]. To release the therapeutic agent, MTB are subjected to an alternating magnetic field to produce hyperthermia [140], which eventually dissociates the bacteria.

Tissue regeneration refers to procedures that combine scaffolds, cells, and therapeutic agents to replace or regenerate tissues to undertake normal functions. Success at regeneration requires the precise delivery of transplanted cells and growth factors, and their retention and controlled release. Some keys for using MNPs in tissue regeneration have been already reviewed in this chapter: biocompatibility, magnetic targeting, surface modification with targeting moieties, magnetic heating, and ability to load therapeutic compounds.

MNPs can target cells, drugs, and nucleic acid and control their retention in diseased tissue until differentiation occurs. They are sometimes combined with magnetic scaffolds fabricated by dip-coating a conventional synthetic bone or vascular scaffold in a MNP solution. Such a scaffold can be magnetized by a magnetic field external to the body to attract the MNPs loaded with drugs. Alternatively, a porous magnetic scaffold can be loaded with MNPs. After transplantation, the particles' biological load is triggered and controlled by magnetic hyperthermia [141].

Magnetic stents can open vascular conduits and create magnetic gradients to capture MNPs. This procedure can avoid re-obstructions and reduce the drug dose [142]. Additionally, an external field can change the

stent's shape and volume to deliver therapeutic agents on demand.

Some types of regeneration involve introducing genes into cells, which is known as transfection. “Magnetofection” has been developed to enhance its efficiency. It consists of magnetically guided and forced delivery of nucleic acids by MNPs.

MNPs can promote cell proliferation thanks to their coatings' biochemical properties. (For example, calcium phosphate coating significantly improves bone tissue osteoblast density [143].

Vascularization is an essential requirement for the success of implants. Remote magneto-mechanical action based on MNPs can significantly enhance the formation of new vascularization, as this process is extremely sensitive to mechanical stimulation. More details and references on MNP applied to tissue regeneration can be found in Ref. [144].

9. Conclusion and Prospects

The growing evidence of the usefulness of MNPs for biomedical applications stimulates researchers to persist in their investigations. The worldwide 2020 coronavirus outbreak exemplifies the need for solutions to emerging biomedical and biosafety problems, like affordable rapid diagnostic tests. In this context, magnetism and, specifically, MNPs have unique properties that make them very interesting alone or combined with other materials and procedures (e.g., optical, chemical, or immunological) whose development and progress are also growing fast.

Thanks to the scientific community's intense activity in multidisciplinary research involving MNPs, one can envisage new effective and safe diagnostics and treatment procedures. Novel routes of fabrication give rise to particles with improved quality and varied morphologies, such as hollow MNPs, nanorods, or molecular imprinted MNPs. Hybrid nanostructures, combining different materials, hold promise for multiple functionalities such as simultaneous therapy and imaging. In this exciting scenario, much interest focuses on the standardization of terminology, synthesis routes (to ensure the batch-to-batch reproducibility), and characterization and metrology techniques (to enable reliable quality control) [145–147]. In 2019, ISO/TS 19807-1:2019 established the first standard on magnetic nanomaterials, specifying the

magnetic nanosuspensions' characteristics to be measured, and listing measurement methods for them [148].

After two decades of creative ideas on how MNP can improve health, food, and environment, there is still plenty of room for interdisciplinary laboratories to mimic the *in vivo* conditions for MNP applications. There are also opportunities for mathematical modeling and simulation to explain and even predict magnetic nanostructures' behavior in biological media and their effects on them.

A few technologies enabled by MNP already have been translated to the health care industry (MRI contrast agents), and some of them are currently undergoing human clinical trials (drug delivery and magnetic hyperthermia). Nevertheless, there is still some work to do for many promising inventions to be attractive enough to be adopted. One of the biggest challenges is the technology transfer to the medical industry and clinical medicine. Issues related to safety, protein corona (the layer of proteins that rapidly forms around MNPs and largely influence their performance), the non-effectiveness of magnetic gradients in deep body regions, and matters related to manufacturing and commercialization (large-scale fabrication, sustainability, packaging and storage, and standardization) are stimuli for future research and innovation on the bio-application of magnetic nanoparticles.

Acknowledgments

The authors sincerely thank R. B. Goldfarb, J. A. Blanco, and P. Gorria for fruitful discussions and valuable suggestions. The authors acknowledge the financial support of the Spanish Ministry of Economy and Competitiveness with grants MAT2017-84959-C2-1-R and RTI2018-094683-B-C52, the Principality of Asturias with project IDI/2018/000185 and the University of Oviedo with PAPI-18-EMERG-8-2018/006=008. M. Salvador thanks the University of Oviedo and the Principality of Asturias for their pre-doctoral grants (PA-20-PF-BP19-141), the Spanish Ministry of Education, Culture and Sport and Banco Santander for grant (CEI15-24).

References

- [1] M. Knobel, W.C. Nunes, L.M. Socolovsky, E. De Biasi, J.M. Vargas, J.C. Denardin, Superparamagnetism and other magnetic features in granular materials: A review on ideal and real systems, J.

- Nanosci. Nanotechnol. 8 (2008) 2836–2857.
<https://doi.org/10.1166/jnn.2008.15348>.
- [2] C. Vasilescu, M. Latikka, K.D. Knudsen, V.M. Garamus, V. Socoliuc, R. Turcu, E. Tombácz, D. Susan-Resiga, R.H.A. Ras, L. Vékás, High concentration aqueous magnetic fluids: structure, colloidal stability, magnetic and flow properties, *Soft Matter*. 14 (2018) 6648–6666. <https://doi.org/10.1039/C7SM02417G>.
- [3] N. Hoshyar, S. Gray, H. Han, G. Bao, The effect of nanoparticle size on in vivo pharmacokinetics and cellular interaction, *https://Doi.Org/10.2217/Nnm.16.5*. 11 (2016) 673–692. <https://doi.org/10.2217/NNM.16.5>.
- [4] A. Jurj, C. Braicu, L.-A. Pop, C. Tomuleasa, C.D. Gherman, I. Berindan-Neagoe, The new era of nanotechnology, an alternative to change cancer treatment, *Drug Des. Devel. Ther.* 11 (2017) 2871–2890. <https://doi.org/10.2147/DDDT.S142337>.
- [5] Y. Geng, P. Dalhaimer, S. Cai, R. Tsai, M. Tewari, T. Minko, D.E. Discher, Shape effects of filaments versus spherical particles in flow and drug delivery, *Nat. Nanotechnol.* 2007 24. 2 (2007) 249–255. <https://doi.org/10.1038/nnano.2007.70>.
- [6] A.B. Jindal, The effect of particle shape on cellular interaction and drug delivery applications of micro- and nanoparticles, *Int. J. Pharm.* 532 (2017) 450–465. <https://doi.org/10.1016/J.IJPHARM.2017.09.028>.
- [7] G. Sharma, D.T. Valenta, Y. Altman, S. Harvey, H. Xie, S. Mitragotri, J.W. Smith, Polymer particle shape independently influences binding and internalization by macrophages, *J. Control. Release.* 147 (2010) 408–412. <https://doi.org/10.1016/J.JCONREL.2010.07.116>.
- [8] A.L. Cortajarena, D. Ortega, S.M. Ocampo, A. Gonzalez-Garcia, P. Couleaud, R. Miranda, C. Belda-Iniesta, A. Ayuso-Sacido, Engineering Iron Oxide Nanoparticles for Clinical Settings:, *Http://Dx.Doi.Org/10.5772/58841*. 1 (2014). <https://doi.org/10.5772/58841>.
- [9] J. Ahmad, H.A. Alhadlaq, A. Alshamsan, M.A. Siddiqui, Q. Saquib, S.T. Khan, R. Wahab, A.A. Al-Khedhairi, J. Musarrat, M.J. Akhtar, M. Ahamed, Differential cytotoxicity of copper ferrite nanoparticles in different human cells, *J. Appl. Toxicol.* 36 (2016) 1284–1293. <https://doi.org/10.1002/JAT.3299>.
- [10] A. Hanini, M. El Massoudi, J. Gavard, K. Kacem, S. Ammar, O. Souilem, Nanotoxicological study of polyol-made cobalt-zinc ferrite nanoparticles in rabbit, *Environ. Toxicol. Pharmacol.* 45 (2016) 321–327. <https://doi.org/10.1016/J.ETAP.2016.06.010>.
- [11] S.Y. Srinivasan, K.M. Paknikar, D. Bodas, V. Gajbhiye, Applications of cobalt ferrite nanoparticles in biomedical nanotechnology,

- <https://doi.org/10.2217/Nnm-2017-0379>. 13 (2018) 1221–1238.
<https://doi.org/10.2217/NNM-2017-0379>.
- [12] Q. Feng, Y. Liu, J. Huang, K. Chen, J. Huang, K. Xiao, Uptake, distribution, clearance, and toxicity of iron oxide nanoparticles with different sizes and coatings, *Sci. Reports* 2018 81. 8 (2018) 1–13. <https://doi.org/10.1038/s41598-018-19628-z>.
- [13] D. Bobo, K.J. Robinson, J. Islam, K.J. Thurecht, S.R. Corrie, Nanoparticle-Based Medicines: A Review of FDA-Approved Materials and Clinical Trials to Date, 33 (2016) 2373–2387. <https://link.springer.com/article/10.1007/s11095-016-1958-5> (accessed September 20, 2021).
- [14] U. Engelmann, E.M. Buhl, M. Baumann, T. Schmitz-Rode, I. Slabu, Agglomeration of magnetic nanoparticles and its effects on magnetic hyperthermia, *Curr. Dir. Biomed. Eng.* 3 (2017) 457–460. <https://doi.org/10.1515/CDBME-2017-0096>.
- [15] B. Halamoda-Kenzaoui, M. Ceridono, P. Urbán, A. Bogni, J. Ponti, S. Gioria, A. Kinsner-Ovaskainen, The agglomeration state of nanoparticles can influence the mechanism of their cellular internalisation, *J. Nanobiotechnology* 2017 151. 15 (2017) 1–15. <https://doi.org/10.1186/S12951-017-0281-6>.
- [16] Y. Wang, H. Xu, M. Wei, H. Gu, Q. Xu, W. Zhu, Study of superparamagnetic nanoparticles as labels in the quantitative lateral flow immunoassay, *Mater. Sci. Eng. C.* 29 (2009) 714–718. <https://doi.org/10.1016/j.msec.2009.01.011>.
- [17] M. Salvador, Á. Gallo-Cordova, A. Moyano, J.C. Martínez-García, M.C. Blanco-López, M. Puerto Morales, M. Rivas, Improved magnetic lateral flow assays with optimized nanotags for point-of-use inductive biosensing, *Analyst.* 145 (2020) 5905–5914. <https://doi.org/10.1039/d0an00849d>.
- [18] E. Amstad, M. Textor, E. Reimhult, Stabilization and functionalization of iron oxide nanoparticles for biomedical applications, *Nanoscale.* 3 (2011) 2819–2843. <https://doi.org/10.1039/C1NR10173K>.
- [19] R.A. Bohara, N.D. Thorat, S.H. Pawar, Role of functionalization: strategies to explore potential nano-bio applications of magnetic nanoparticles, *RSC Adv.* 6 (2016) 43989–44012. <https://doi.org/10.1039/C6RA02129H>.
- [20] R. Mout, D.F. Moyano, S. Rana, V.M. Rotello, Surface functionalization of nanoparticles for nanomedicine, *Chem. Soc. Rev.* 41 (2012) 2539–2544. <https://doi.org/10.1039/C2CS15294K>.
- [21] A. Moyano, E. Serrano-Pertierra, M. Salvador, J.C. Martínez-García, Y. Piñeiro, S. Yañez-Vilar, M. González-Gómez, J. Rivas, M. Rivas, M.C. Blanco-López, Carbon-Coated Superparamagnetic Nanoflowers for Biosensors Based on Lateral Flow Immunoassays,

- Biosens. 2020, Vol. 10, Page 80. 10 (2020) 80.
<https://doi.org/10.3390/BIOS10080080>.
- [22] M. Vasilakaki, N. Ntallis, M. Bellusci, F. Varsano, R. Mathieu, D. Fiorani, D. Peddis, K.N. Trohidou, Effect of albumin mediated clustering on the magnetic behavior of MnFe₂O₄ nanoparticles: Experimental and theoretical modeling study, *Nanotechnology*. 31 (2020). <https://doi.org/10.1088/1361-6528/AB4764>.
- [23] J. Salafranca, J. Gazquez, N. Pérez, A. Labarta, S.T. Pantelides, S.J. Pennycook, X. Batlle, M. Varela, Surfactant organic molecules restore magnetism in metal-oxide nanoparticle surfaces, *Nano Lett.* 12 (2012) 2499–2503. https://doi.org/10.1021/NL300665Z/SUPPL_FILE/NL300665Z_SI_001.PDF.
- [24] R. Massart, Preparation of Aqueous Magnetic Liquids in Alkaline and Acidic Media, *IEEE Trans. Magn.* 17 (1981) 1247–1248. <https://doi.org/10.1109/TMAG.1981.1061188>.
- [25] V.K. LaMer, R.H. Dinegar, Theory, Production and Mechanism of Formation of Monodispersed Hydrosols, *J. Am. Chem. Soc.* 72 (2002) 4847–4854. <https://doi.org/10.1021/JA01167A001>.
- [26] G. Cotin, C. Kiefer, F. Pertion, D. Ihiawakrim, C. Blanco-Andujar, S. Moldovan, C. Lefevre, O. Ersen, B. Pichon, D. Mertz, S. Bégin-Colin, Unravelling the Thermal Decomposition Parameters for The Synthesis of Anisotropic Iron Oxide Nanoparticles, *Nanomater.* 2018, Vol. 8, Page 881. 8 (2018) 881. <https://doi.org/10.3390/NANO8110881>.
- [27] M. Unni, A.M. Uhl, S. Savliwala, B.H. Savitzky, R. Dhavalikar, N. Garraud, D.P. Arnold, L.F. Kourkoutis, J.S. Andrew, C. Rinaldi, Thermal Decomposition Synthesis of Iron Oxide Nanoparticles with Diminished Magnetic Dead Layer by Controlled Addition of Oxygen, *ACS Nano*. 11 (2017) 2284–2303. <https://pubs.acs.org/doi/abs/10.1021/acsnano.7b00609> (accessed March 4, 2021).
- [28] M.E.F. Brollo, S. Veintemillas-Verdaguer, C.M. Salván, M.D.P. Morales, Key parameters on the microwave assisted synthesis of magnetic nanoparticles for MRI contrast agents, *Contrast Media Mol. Imaging*. 2017 (2017). <https://doi.org/10.1155/2017/8902424>.
- [29] L. Gonzalez-Moragas, S.M. Yu, N. Murillo-Cremaes, A. Laromaine, A. Roig, Scale-up synthesis of iron oxide nanoparticles by microwave-assisted thermal decomposition, *Chem. Eng. J.* 281 (2015) 87–95. <https://doi.org/10.1016/J.CEJ.2015.06.066>.
- [30] A. Scano, V. Cabras, M. Pilloni, G. Ennas, Microemulsions: The Renaissance of Ferrite Nanoparticle Synthesis, *J. Nanosci. Nanotechnol.* 19 (2019) 4824–4838.

<https://doi.org/10.1166/JNN.2019.16876>.

- [31] S.S. Staniland, A. Rawlings, J. Bramble, J. Tolosa, O. Wilson, J.C. García-Martínez, C. Binns, Novel methods for the synthesis of magnetic nanoparticles, in: *Front. Nanosci.*, Elsevier Ltd, 2014: pp. 85–128. <https://doi.org/10.1016/B978-0-08-098353-0.00003-8>.
- [32] M. Salvador, A. Moyano, J.C. Martínez-García, M.C. Blanco-López, M. Rivas, Synthesis of Superparamagnetic Iron Oxide Nanoparticles: SWOT Analysis Towards Their Conjugation to Biomolecules for Molecular Recognition Applications, *J. Nanosci. Nanotechnol.* 19 (2019) 4839–4856. <https://doi.org/10.1166/JNN.2019.16931>.
- [33] A.G. Roca, R. Costo, A.F. Rebolledo, S. Veintemillas-Verdaguer, P. Tartaj, T. González-Carreño, M.P. Morales, C.J. Serna, Progress in the preparation of magnetic nanoparticles for applications in biomedicine, *J. Phys. D. Appl. Phys.* 42 (2009) 224002. <https://doi.org/10.1088/0022-3727/42/22/224002>.
- [34] S. Bogren, A. Fornara, F. Ludwig, M.D.P. Morales, U. Steinhoff, M.F. Hansen, O. Kazakova, C. Johansson, Classification of Magnetic Nanoparticle Systems—Synthesis, Standardization and Analysis Methods in the NanoMag Project, *Int. J. Mol. Sci.* 2015, Vol. 16, Pages 20308–20325. 16 (2015) 20308–20325. <https://doi.org/10.3390/IJMS160920308>.
- [35] L. Chang, S. Chang, W. Chen, W. Han, Z. Li, Z. Zhang, Y. Dai, D. Chen, Facile one-pot synthesis of magnetic Prussian blue core/shell nanoparticles for radioactive cesium removal, *RSC Adv.* 6 (2016) 96223–96228. <https://doi.org/10.1039/C6RA17525B>.
- [36] S. Upadhyay, K. Parekh, B. Pandey, Influence of crystallite size on the magnetic properties of Fe₃O₄ nanoparticles, *J. Alloys Compd.* 678 (2016) 478–485. <https://doi.org/10.1016/J.JALLCOM.2016.03.279>.
- [37] B. Michen, S. Balog, B. Rothe-Ruthishauser, A. Fink, D. Vanhecke, TEM Sample Preparation of Nanoparticles in Suspensions: Understanding the Formation of Drying Artefacts, *Imaging Microsc.* 6 (2014) 39.
- [38] S. Akhtar, F.A. Khan, A. Buhaimed, Functionalized magnetic nanoparticles attenuate cancer cells proliferation: Transmission electron microscopy analysis, *Microsc. Res. Tech.* 82 (2019) 983–992. <https://doi.org/10.1002/JEMT.23245>.
- [39] A. Rao, M. Schoenenberger, E. Gnecco, T. Glatzel, E. Meyer, D. Brändlin, L. Scandella, Characterization of nanoparticles using Atomic Force Microscopy, *J. Phys. Conf. Ser.* 61 (2007) 192. <https://doi.org/10.1088/1742-6596/61/1/192>.
- [40] A. Krivcov, T. Junkers, H. Möbius, Understanding electrostatic and magnetic forces in magnetic force microscopy: towards single

- superparamagnetic nanoparticle resolution, *J. Phys. Commun.* 2 (2018) 075019. <https://doi.org/10.1088/2399-6528/AAD3A4>.
- [41] C. Moya, Ó. Iglesias-Freire, X. Batlle, A. Labarta, A. Asenjo, Superparamagnetic versus blocked states in aggregates of Fe₃-xO₄ nanoparticles studied by MFM, *Nanoscale*. 7 (2015) 17764–17770. <https://doi.org/10.1039/C5NR04424C>.
- [42] C. Bantz, O. Koshkina, T. Lang, H.-J. Galla, C.J. Kirkpatrick, R.H. Stauber, M. Maskos, The surface properties of nanoparticles determine the agglomeration state and the size of the particles under physiological conditions, *Beilstein J. Nanotechnol.* 5188. 5 (2014) 1774–1786. <https://doi.org/10.3762/BJNANO.5.188>.
- [43] K. Rausch, A. Reuter, K. Fischer, M. Schmidt, Evaluation of Nanoparticle Aggregation in Human Blood Serum, *Biomacromolecules*. 11 (2010) 2836–2839. <https://doi.org/10.1021/BM100971Q>.
- [44] V. Filipe, A. Hawe, W. Jiskoot, Critical Evaluation of Nanoparticle Tracking Analysis (NTA) by NanoSight for the Measurement of Nanoparticles and Protein Aggregates, *Pharm. Res.* 2010 275. 27 (2010) 796–810. <https://doi.org/10.1007/S11095-010-0073-2>.
- [45] P. Eaton, P. Quaresma, C. Soares, C. Neves, M.P. de Almeida, E. Pereira, P. West, A direct comparison of experimental methods to measure dimensions of synthetic nanoparticles, *Ultramicroscopy*. 182 (2017) 179–190. <https://doi.org/10.1016/J.ULTRAMIC.2017.07.001>.
- [46] A. Méndez-Vilas, J. Díaz, *Microscopy: science, technology, applications and education*, Formatex Research Center, Badajoz, 2010.
- [47] T. Chatterji, *Neutron Scattering from Magnetic Materials*, 2006. <https://doi.org/https://doi.org/10.1016/B978-0-444-51050-1.X5000-9>.
- [48] M.P. Fernández-García, P. Gorria, J.A. Blanco, A.B. Fuertes, M. Sevilla, R. Boada, J. Chaboy, D. Schmool, J.M. Grenèche, Microstructure and magnetism of nanoparticles with γ -Fe core surrounded by α -Fe and iron oxide shells, *Phys. Rev. B - Condens. Matter Mater. Phys.* 81 (2010) 094418. <https://doi.org/10.1103/PhysRevB.81.094418>.
- [49] M.P. Fernández-García, P. Gorria, M. Sevilla, M.P. Proença, R. Boada, J. Chaboy, A.B. Fuertes, J.A. Blanco, Enhanced Protection of Carbon-Encapsulated Magnetic Nickel Nanoparticles through a Sucrose-Based Synthetic Strategy, *J. Phys. Chem. C*. 115 (2011) 5294–5300. <https://doi.org/10.1021/JP109669T>.
- [50] J. Fock, L.K. Bogart, D. González-Alonso, J.I. Espeso, M.F. Hansen, M. Varón, C. Frandsen, Q.A. Pankhurst, On the ‘centre of gravity’ method for measuring the composition of magnetite/maghemite

- mixtures, or the stoichiometry of magnetite-maghemite solid solutions, via ^{57}Fe Mössbauer spectroscopy, *J. Phys. D. Appl. Phys.* 50 (2017) 265005. <https://doi.org/10.1088/1361-6463/AA73FA>.
- [51] A. V. Delgado, F. González-Caballero, R.J. Hunter, L.K. Koopal, J. Lyklema, Measurement and interpretation of electrokinetic phenomena, *J. Colloid Interface Sci.* 309 (2007) 194–224. <https://doi.org/10.1016/j.jcis.2006.12.075>.
- [52] D.L. Pavia, G.M. Lampman, G.S. Kriz, J.A. Vyvyan, *Introduction to spectroscopy*, Cengage Learning, 2014.
- [53] O. Bixner, A. Lassenberger, D. Baurecht, E. Reimhult, Complete Exchange of the Hydrophobic Dispersant Shell on Monodisperse Superparamagnetic Iron Oxide Nanoparticles, *Langmuir*. 31 (2015) 9198–9204. <https://doi.org/10.1021/ACS.LANGMUIR.5B01833>.
- [54] R.L. McCreery, *Raman spectroscopy for chemical analysis*, John Wiley & Sons, 2005.
- [55] L. Slavov, M. V. Abrashev, T. Merodiiska, C. Gelev, R.E. Vandenberghe, I. Markova-Deneva, I. Nedkov, Raman spectroscopy investigation of magnetite nanoparticles in ferrofluids, *J. Magn. Mater.* 322 (2010) 1904–1911. <https://doi.org/10.1016/J.JMMM.2010.01.005>.
- [56] J.C. Rubim, M.H. Sousa, J.C.O. Silva, F.A. Tourinho, Raman spectroscopy as a powerful technique in the characterization of ferrofluids, *Brazilian J. Phys.* 31 (2001) 402–408. <https://doi.org/10.1590/S0103-97332001000300010>.
- [57] H. Konno, X-ray Photoelectron Spectroscopy, *Mater. Sci. Eng. Carbon.* (2016) 153–171. <https://doi.org/10.1016/B978-0-12-805256-3.00008-8>.
- [58] T. Radu, C. Iacovita, D. Benea, R. Turcu, X-Ray Photoelectron Spectroscopic Characterization of Iron Oxide Nanoparticles, *Appl. Surf. Sci.* 405 (2017) 337–343. <https://doi.org/10.1016/J.APSUSC.2017.02.002>.
- [59] A.G. Shard, A Straightforward Method For Interpreting XPS Data From Core–Shell Nanoparticles, *J. Phys. Chem. C*. 116 (2012) 16806–16813. <https://doi.org/10.1021/JP305267D>.
- [60] D. Farhanian, G. De Crescenzo, J.R. Tavares, Large-Scale Encapsulation of Magnetic Iron Oxide Nanoparticles via Syngas Photo-Initiated Chemical Vapor Deposition, *Sci. Reports* 2018 81. 8 (2018) 1–11. <https://doi.org/10.1038/s41598-018-30802-1>.
- [61] P. Gabbott, *Principles and Applications of Thermal Analysis*, *Princ. Appl. Therm. Anal.* (2008) 1–388. <https://doi.org/10.1002/9780470697702>.
- [62] E. Mansfield, K.M. Tyner, C.M. Poling, J.L. Blacklock,

- Determination of Nanoparticle Surface Coatings and Nanoparticle Purity Using Microscale Thermogravimetric Analysis, *Anal. Chem.* 86 (2014) 1478–1484. <https://doi.org/10.1021/AC402888V>.
- [63] D. Pröfrock, A. Prange, Inductively Coupled Plasma–Mass Spectrometry (ICP-MS) for Quantitative Analysis in Environmental and Life Sciences: A Review of Challenges, Solutions, and Trends, *Http://Dx.Doi.Org/10.1366/12-06681*. 66 (2012) 843–868. <https://doi.org/10.1366/12-06681>.
- [64] R. Costo, D. Heinke, C. Grüttner, F. Westphal, M.P. Morales, S. Veintemillas-Verdaguer, N. Gehrke, Improving the reliability of the iron concentration quantification for iron oxide nanoparticle suspensions: a two-institutions study, *Anal. Bioanal. Chem.* 2018 4119. 411 (2018) 1895–1903. <https://doi.org/10.1007/S00216-018-1463-2>.
- [65] F. C, S. C, Characterization of Polymeric Nanoparticle Dispersions for Biomedical Applications: Size, Surface Charge and Stability, *Pharm. Nanotechnol.* 6 (2018) 147–164. <https://doi.org/10.2174/2211738506666180706121515>.
- [66] S. Foner, Vibrating sample magnetometer, *Rev. Sci. Instrum.* 27 (1956) 548. <https://doi.org/10.1063/1.1715636>.
- [67] P.J. Flanders, A vertical force alternating-gradient magnetometer, *Rev. Sci. Instrum.* 61 (1990) 839–847. <https://doi.org/10.1063/1.1141451>.
- [68] R.B. Goldfarb, M. Leental, C.A. Thompson, Alternating-Field Susceptometry and Magnetic Susceptibility of Superconductors, (n.d.). <https://www.nist.gov/publications/alternating-field-susceptometry-and-magnetic-susceptibility-superconductors-0> (accessed September 20, 2021).
- [69] M.F. Hansen, S. Mørup, Estimation of blocking temperatures from ZFC/FC curves, *J. Magn. Magn. Mater.* 203 (1999) 214–216. [https://doi.org/10.1016/S0304-8853\(99\)00238-3](https://doi.org/10.1016/S0304-8853(99)00238-3).
- [70] D. Peddis, P.E. Jönsson, S. Laureti, G. Varvaro, Magnetic interactions: A tool to modify the magnetic properties of materials based on nanoparticles, in: *Front. Nanosci.*, Elsevier, 2014: pp. 129–188. <https://doi.org/10.1016/B978-0-08-098353-0.00004-X>.
- [71] K.L. Livesey, S. Ruta, N.R. Anderson, D. Baldomir, R.W. Chantrell, D. Serantes, Beyond the blocking model to fit nanoparticle ZFC/FC magnetisation curves, *Sci. Reports* 2018 81. 8 (2018) 1–9. <https://doi.org/10.1038/s41598-018-29501-8>.
- [72] O. Petravic, Superparamagnetic nanoparticle ensembles, Superlattices Microstruct. 47 (2010) 569–578. <https://doi.org/10.1016/J.SPMI.2010.01.009>.
- [73] J.A. De Toro, P.S. Normile, S.S. Lee, D. Salazar, J.L. Cheong, P.

- Muñiz, J.M. Riveiro, M. Hillenkamp, F. Tournus, A. Tamion, P. Nordblad, Controlled Close-Packing of Ferrimagnetic Nanoparticles: An Assessment of the Role of Interparticle Superexchange Versus Dipolar Interactions, *J. Phys. Chem. C*. 117 (2013) 10213–10219. <https://doi.org/10.1021/JP402444X>.
- [74] E.P. Wohlfarth, Relations between different modes of acquisition of the remanent magnetization of ferromagnetic particles, *American Institute of Physics AIP*, n.d. <https://doi.org/10.1063/1.1723232>.
- [75] J.L. Dormann, D. Fiorani, E. Tronc, Magnetic Relaxation in Fine-Particle Systems, (2007) 283–494. <https://doi.org/10.1002/9780470141571.CH4>.
- [76] E. De Biasi, J. Curiale, R.D. Zysler, Quantitative study of FORC diagrams in thermally corrected Stoner– Wohlfarth nanoparticles systems, *J. Magn. Magn. Mater.* 419 (2016) 580–587. <https://doi.org/10.1016/J.JMMM.2016.06.075>.
- [77] F. Groß, J.C. Martínez-García, S.E. Ilse, G. Schütz, E. Goering, M. Rivas, J. Gräfe, gFORC: A graphics processing unit accelerated first-order reversal-curve calculator, *J. Appl. Phys.* 126 (2019) 163901. <https://doi.org/10.1063/1.5120495>.
- [78] C.R. Pike, A.P. Roberts, K.L. Verosub, First order reversal curve diagrams and thermal relaxation effects in magnetic particles, *Geophys. J. Int.* 145 (2001) 721–730. <https://doi.org/10.1046/J.0956-540X.2001.01419.X>.
- [79] A.C. Bohorquez, C. Rinaldi, In situ evaluation of nanoparticle-protein interactions by dynamic magnetic susceptibility measurements, *Part. Part. Syst. Charact.* 31 (2014) 561–570. <https://doi.org/10.1002/ppsc.201300296>.
- [80] V.L. Calero-Diaz Del Castillo, C. Rinaldi, Effect of sample concentration on the determination of the anisotropy constant of magnetic nanoparticles, *IEEE Trans. Magn.* 46 (2010) 852–859. <https://doi.org/10.1109/TMAG.2009.2032240>.
- [81] M.A. Garcia, E.F. Pinel, J. de la Venta, A. Quesada, V. Bouzas, J.F. Fernández, J.J. Romero, M.S.M. González, J.L. Costa-Krämer, Sources of experimental errors in the observation of nanoscale magnetism, *J. Appl. Phys.* 105 (2009) 013925. <https://doi.org/10.1063/1.3060808>.
- [82] S.E. McNeil, Characterization of nanoparticles intended for drug delivery, 1st ed., Humana Press, 2011. <https://doi.org/https://doi.org/10.1007/978-1-60327-198-1>.
- [83] J.W. Wills, H.D. Summers, N. Hondow, A. Soresh, K.E. Meissner, P.A. White, P. Rees, A. Brown, S.H. Doak, Characterizing Nanoparticles in Biological Matrices: Tipping Points in Agglomeration State and Cellular Delivery In Vitro, *ACS Nano*. 11 (2017) 11986–12000.

<https://doi.org/10.1021/ACSNANO.7B03708>.

- [84] D. Baragaño, J. Alonso, J.R. Gallego, M.C. Lobo, M. Gil-Díaz, Magnetite nanoparticles for the remediation of soils co-contaminated with As and PAHs, *Chem. Eng. J.* 399 (2020) 125809. <https://doi.org/10.1016/J.CEJ.2020.125809>.
- [85] O. V. Kharissova, H.V.R. Dias, B.I. Kharisov, Magnetic adsorbents based on micro- and nano-structured materials, *RSC Adv.* 5 (2014) 6695–6719. <https://doi.org/10.1039/C4RA11423J>.
- [86] D. Lago-Cachón, M. Rivas, C. López-Larrea, A. López-Vázquez, G. Martínez-Paredes, J.A. García, HeLa cells separation using MICA antibody conjugated to magnetite nanoparticles, *Phys. Status Solidi Curr. Top. Solid State Phys.* 11 (2014) 1043–1047. <https://doi.org/10.1002/pssc.201300729>.
- [87] S.P. Schwaminger, P. Fraga-García, M. Eigenfeld, T.M. Becker, S. Berensmeier, Magnetic Separation in Bioprocessing Beyond the Analytical Scale: From Biotechnology to the Food Industry, *Front. Bioeng. Biotechnol.* 0 (2019) 233. <https://doi.org/10.3389/FBIOE.2019.00233>.
- [88] A. Sandhu, P. Southern, S.C. de Freitas, S. Knudde, F.A. Cardoso, P.P. Freitas, G. V. Kurlyandskaya, Sensing Magnetic Nanoparticles, in: *Magn. Nanoparticles Biosensing Med.*, Cambridge University Press, 2019: pp. 172–227. <https://doi.org/10.1017/9781139381222.007>.
- [89] Y.-T. Chen, A.G. Kolhatkar, O. Zenasni, S. Xu, T.R. Lee, Biosensing Using Magnetic Particle Detection Techniques, *Sensors* 2017, Vol. 17, Page 2300. 17 (2017) 2300. <https://doi.org/10.3390/S17102300>.
- [90] G. Lin, D. Makarov, O.G. Schmidt, Magnetic sensing platform technologies for biomedical applications, *Lab Chip.* 17 (2017) 1884–1912. <https://doi.org/10.1039/c7lc00026j>.
- [91] D. Budker, M. Romalis, Optical magnetometry, *Nat. Phys.* 3 (2007) 227–234. <https://doi.org/10.1038/nphys566>.
- [92] D. Alcantara, S. Lopez, M.L. García-Martin, D. Pozo, Iron oxide nanoparticles as magnetic relaxation switching (MRSw) sensors: Current applications in nanomedicine, *Nanomedicine Nanotechnology, Biol. Med.* 12 (2016) 1253–1262. <https://doi.org/10.1016/j.nano.2016.01.005>.
- [93] S.X. Wang, G. Li, Advances in giant magnetoresistance biosensors with magnetic nanoparticle tags: Review and outlook, in: *IEEE Trans. Magn.*, 2008: pp. 1687–1702. <https://doi.org/10.1109/TMAG.2008.920962>.
- [94] D. Su, K. Wu, R. Saha, C. Peng, J.-P. Wang, Advances in Magnetoresistive Biosensors, *Micromachines* 2020, Vol. 11, Page

34. 11 (2019) 34. <https://doi.org/10.3390/MI11010034>.
- [95] B. Srinivasan, Y. Li, Y. Jing, C. Xing, J. Slaton, J.-P. Wang, A Three-Layer Competition-Based Giant Magnetoresistive Assay for Direct Quantification of Endoglin from Human Urine, *Anal. Chem.* 83 (2011) 2996–3002. <https://doi.org/10.1021/AC2005229>.
- [96] A. Fu, W. Hu, L. Xu, R.J. Wilson, H. Yu, S.J. Osterfeld, S.S. Gambhir, S.X. Wang, Protein-Functionalized Synthetic Antiferromagnetic Nanoparticles for Biomolecule Detection and Magnetic Manipulation, *Angew. Chemie Int. Ed.* 48 (2009) 1620–1624. <https://doi.org/10.1002/ANIE.200803994>.
- [97] A. Cousins, G.L. Balalis, S.K. Thompson, D. Forero Morales, A. Mohtar, A.B. Wedding, B. Thierry, Novel Handheld Magnetometer Probe Based on Magnetic Tunneling Junction Sensors for Intraoperative Sentinel Lymph Node Identification, *Sci. Reports* 2015 51. 5 (2015) 1–10. <https://doi.org/10.1038/srep10842>.
- [98] K. Togawa, H. Sanbonsugi, A. Sandhu, M. Abe, H. Narimatsu, K. Nishio, H. Handa, Detection of magnetically labeled DNA using pseudomorphic AlGaAs/InGaAs/GaAs heterostructure micro-Hall biosensors, *J. Appl. Phys.* 99 (2006) 08P103. <https://doi.org/10.1063/1.2162041>.
- [99] D. Issadore, J. Chung, H. Shao, M. Liong, A.A. Ghazani, C.M. Castro, R. Weissleder, H. Lee, Ultrasensitive clinical enumeration of rare cells ex vivo using a micro-hall detector, *Sci. Transl. Med.* 4 (2012). <https://doi.org/10.1126/SCITRANSLMED.3003747>.
- [100] B. Cao, K. Wang, H. Xu, Q. Qin, J. Yang, W. Zheng, Q. Jin, D. Cui, Development of magnetic sensor technologies for point-of-care testing: Fundamentals, methodologies and applications, *Sensors Actuators A Phys.* 312 (2020) 112130. <https://doi.org/10.1016/J.SNA.2020.112130>.
- [101] J.A. Goode, J.V.H. Rushworth, P.A. Millner, Biosensor Regeneration: A Review of Common Techniques and Outcomes, *Langmuir*. 31 (2014) 6267–6276. <https://doi.org/10.1021/LA503533G>.
- [102] K.M.M. Koczula, A. Gallotta, P. Estrela, K.M.M. Koczula, A. Gallotta, Lateral flow assays, *Essays Biochem.* 60 (2016) 111–120. <https://doi.org/10.1042/EBC20150012>.
- [103] A. Moyano, M. Salvador, J.C. Martínez-García, V. Socoliuc, L. Vékás, D. Peddis, M.A. Alvarez, M. Fernández, M. Rivas, M.C. Blanco-López, Magnetic immunochromatographic test for histamine detection in wine, *Anal. Bioanal. Chem.* 2019 41125. 411 (2019) 6615–6624. <https://doi.org/10.1007/S00216-019-02031-6>.
- [104] C. Marquina, J.M. De Teresa, D. Serrate, J. Marzo, F.A. Cardoso, D. Saurel, S. Cardoso, P.P. Freitas, M.R. Ibarra, GMR sensors and

- magnetic nanoparticles for immuno-chromatographic assays, *J. Magn. Magn. Mater.* 324 (2012) 3495–3498.
<https://doi.org/10.1016/J.JMMM.2012.02.074>.
- [105] A. Moyano, E. Serrano-Pertierra, M. Salvador, J.C. Martínez-García, M. Rivas, M.C. Blanco-López, Magnetic lateral flow immunoassays, *Diagnostics*. 10 (2020) 288.
<https://doi.org/10.3390/diagnostics10050288>.
- [106] A. Elyacoubi, S.I.M. Zayed, B. Blankert, J.M. Kauffmann, Development of an Amperometric Enzymatic Biosensor Based on Gold Modified Magnetic Nanoporous Microparticles, *Electroanalysis*. 18 (2006) 345–350.
<https://doi.org/10.1002/ELAN.200503418>.
- [107] M.H. Liao, J.C. Guo, W.C. Chen, A disposable amperometric ethanol biosensor based on screen-printed carbon electrodes mediated with ferricyanide-magnetic nanoparticle mixture, *J. Magn. Magn. Mater.* 304 (2006) e421–e423.
<https://doi.org/10.1016/j.jmmm.2006.01.223>.
- [108] J.M. Nam, C.S. Thaxton, C.A. Mirkin, Nanoparticle-based bio-bar codes for the ultrasensitive detection of proteins, *Science (80-.)*. 301 (2003) 1884–1886.
https://doi.org/10.1126/SCIENCE.1088755/SUPPL_FILE/NAM.SOM.PDF.
- [109] S.I. Stoeva, J.S. Lee, C.S. Thaxton, C.A. Mirkin, Multiplexed DNA Detection with Biobarcode Nanoparticle Probes, *Angew. Chemie Int. Ed.* 45 (2006) 3303–3306.
<https://doi.org/10.1002/ANIE.200600124>.
- [110] B.H. Kim, N. Lee, H. Kim, K. An, Y. Il Park, Y. Choi, K. Shin, Y. Lee, S.G. Kwon, H. Bin Na, J.G. Park, T.Y. Ahn, Y.W. Kim, W.K. Moon, S.H. Choi, T. Hyeon, Large-scale synthesis of uniform and extremely small-sized iron oxide nanoparticles for high-resolution T₁ magnetic resonance imaging contrast agents, *J. Am. Chem. Soc.* 133 (2011) 12624–12631.
https://doi.org/10.1021/JA203340U/SUPPL_FILE/JA203340U_SI_002.AVI.
- [111] L. Wang, J. Huang, H. Chen, H. Wu, Y. Xu, Y. Li, H. Yi, Y.A. Wang, L. Yang, H. Mao, Exerting Enhanced Permeability and Retention Effect Driven Delivery by Ultrafine Iron Oxide Nanoparticles with T₁-T₂ Switchable Magnetic Resonance Imaging Contrast, *ACS Nano*. 11 (2017) 4582–4592.
https://doi.org/10.1021/ACSNANO.7B00038/SUPPL_FILE/NN7B00038_SI_001.PDF.
- [112] X. Yin, S.E. Russek, G. Zabow, F. Sun, J. Mohapatra, K.E. Keenan, M.A. Boss, H. Zeng, J.P. Liu, A. Viert, S.H. Liou, J. Moreland, Large T₁ contrast enhancement using superparamagnetic nanoparticles in ultra-low field MRI, *Sci. Reports* 2018 81. 8 (2018) 1–10.

<https://doi.org/10.1038/s41598-018-30264-5>.

- [113] M.P. Morales, O. Bomati-Miguel, R. Pérez de Alejo, J. Ruiz-Cabello, S. Veintemillas-Verdaguer, K. O'Grady, Contrast agents for MRI based on iron oxide nanoparticles prepared by laser pyrolysis, *J. Magn. Mater.* 266 (2003) 102–109. [https://doi.org/10.1016/S0304-8853\(03\)00461-X](https://doi.org/10.1016/S0304-8853(03)00461-X).
- [114] J. Estelrich, M.J. Sánchez-Martín, M.A. Busquets, Nanoparticles in magnetic resonance imaging: from simple to dual contrast agents, *Int. J. Nanomedicine.* 10 (2015) 1727–1741. <https://doi.org/10.2147/IJN.S76501>.
- [115] J.T. Jang, H. Nah, J.H. Lee, S.H. Moon, M.G. Kim, J. Cheon, Critical Enhancements of MRI Contrast and Hyperthermic Effects by Dopant-Controlled Magnetic Nanoparticles, *Angew. Chemie Int. Ed.* 48 (2009) 1234–1238. <https://doi.org/10.1002/ANIE.200805149>.
- [116] E. Peng, F. Wang, J.M. Xue, Nanostructured magnetic nanocomposites as MRI contrast agents, *J. Mater. Chem. B.* 3 (2015) 2241–2276. <https://doi.org/10.1039/C4TB02023E>.
- [117] B. Gleich, J. Weizenecker, Tomographic imaging using the nonlinear response of magnetic particles, *Nat.* 2005 4357046. 435 (2005) 1214–1217. <https://doi.org/10.1038/nature03808>.
- [118] L.M. Bauer, S.F. Situ, M.A. Griswold, A.C.S. Samia, Magnetic Particle Imaging Tracers: State-of-the-Art and Future Directions, *J. Phys. Chem. Lett.* 6 (2015) 2509–2517. <https://doi.org/10.1021/ACS.JPCLETT.5B00610>.
- [119] S. Zanganeh, M. Aieneravaie, M. Erfanzadeh, J.Q. Ho, R. Spitler, Chapter 5 - Magnetic Particle Imaging (MPI), in: M. Mahmoudi, S.B.T.-I.O.N. for B.A. Laurent (Eds.), *Met. Oxides*, Elsevier, 2018: pp. 115–133. <https://doi.org/https://doi.org/10.1016/B978-0-08-101925-2.00004-8>.
- [120] E.U. Saritas, P.W. Goodwill, L.R. Croft, J.J. Konkle, K. Lu, B. Zheng, S.M. Conolly, Magnetic particle imaging (MPI) for NMR and MRI researchers, *J. Magn. Reson.* 229 (2013) 116–126. <https://doi.org/10.1016/j.jmr.2012.11.029>.
- [121] N. Panagiotopoulos, R.L. Duschka, M. Ahlborg, G. Bringout, C. Debbeler, M. Graeser, C. Kaethner, K. Lüdtke-Buzug, H. Medimagh, J. Stelzner, T.M. Buzug, J. Barkhausen, F.M. Vogt, J. Haegele, Magnetic particle imaging: current developments and future directions, *Int. J. Nanomedicine.* 10 (2015) 3097–3114. <https://doi.org/10.2147/IJN.S70488>.
- [122] R. Lawaczeck, H. Bauer, T. Frenzel, M. Hasegawa, Y. Ito, K. Kito, N. Miwa, H. Tsutsui, H. Vogler, H.J. Weinmann, Magnetic iron oxide particles coated with carboxydextran for parenteral administration and liver contrasting: Pre-clinical profile of SH U555A, *Acta Radiol.* 38 (1997) 584–597.

<https://doi.org/10.1080/02841859709174391>.

- [123] R.K. Gilchrist, R. Medal, W.D. Shorey, R.C. Hanselman, J.C. Parrott, C.B. Taylor, Selective inductive heating of lymph nodes, *Ann. Surg.* 146 (1957) 596–606. <https://doi.org/10.1097/00000658-195710000-00007>.
- [124] W.J. Atkinson, I.A. Brezovich, D.P. Chakraborty, Usable Frequencies in Hyperthermia with Thermal Seeds, *IEEE Trans. Biomed. Eng.* BME-31 (1984) 70–75. <https://doi.org/10.1109/TBME.1984.325372>.
- [125] E. Garaio, O. Sandre, J.M. Collantes, J.A. Garcia, S. Mornet, F. Plazaola, Specific absorption rate dependence on temperature in magnetic field hyperthermia measured by dynamic hysteresis losses (ac magnetometry), *Nanotechnology*. 26 (2014) 015704. <https://doi.org/10.1088/0957-4484/26/1/015704>.
- [126] D. Cabrera, I. Rubia-Rodríguez, E. Garaio, F. Plazaola, L. Dupré, N. Farrow, F.J. Terán, D. Ortega, Instrumentation for Magnetic Hyperthermia, *Nanomater. Magn. Opt. Hyperth. Appl.* (2019) 111–138. <https://doi.org/10.1016/B978-0-12-813928-8.00005-3>.
- [127] L. Asín, M.R. Ibarra, A. Tres, G.F. Goya, Controlled cell death by magnetic hyperthermia: Effects of exposure time, field amplitude, and nanoparticle concentration, *Pharm. Res.* 29 (2012) 1319–1327. <https://doi.org/10.1007/S11095-012-0710-Z/FIGURES/9>.
- [128] N. Telling, High-Frequency Magnetic Response and Hyperthermia From Nanoparticles in Cellular Environments, *Nanomater. Magn. Opt. Hyperth. Appl.* (2019) 173–197. <https://doi.org/10.1016/B978-0-12-813928-8.00007-7>.
- [129] Magforce®, Magforce®: The nanomedicine company., (n.d.).
- [130] H.D.A. Santos, E.C. Ximendes, M. del C. Iglesias-de la Cruz, I. Chaves-Coira, B. del Rosal, C. Jacinto, L. Monge, I. Rubia-Rodríguez, D. Ortega, S. Mateos, J. GarcíaSolé, D. Jaque, N. Fernández, In Vivo Early Tumor Detection and Diagnosis by Infrared Luminescence Transient Nanothermometry, *Adv. Funct. Mater.* 28 (2018) 1803924. <https://doi.org/10.1002/ADFM.201803924>.
- [131] R. Mansell, T. Vemulkar, D.C.M.C. Petit, Y. Cheng, J. Murphy, M.S. Lesniak, R.P. Cowburn, Magnetic particles with perpendicular anisotropy for mechanical cancer cell destruction, *Sci. Rep.* 7 (2017) 1–7. <https://doi.org/10.1038/s41598-017-04154-1>.
- [132] E.A. Vitol, V. Novosad, E.A. Rozhkova, Microfabricated magnetic structures for future medicine: from sensors to cell actuators, *Nanomedicine*. 7 (2012) 1611–1624. <https://doi.org/10.2217/nnm.12.133>.
- [133] H. Chiriac, E. Radu, M. Țibu, G. Stoian, G. Ababei, L. Lăbușcă,

- D.D. Herea, N. Lupu, Fe-Cr-Nb-B ferromagnetic particles with shape anisotropy for cancer cell destruction by magneto-mechanical actuation, *Sci. Reports* 2018 81. 8 (2018) 1–9. <https://doi.org/10.1038/s41598-018-30034-3>.
- [134] M. Goirienea-Goikoetxea, A. Garcia-Arribas, M. Rouco, A. V. Svalov, J.M. Barandiaran, High-yield fabrication of 60 nm Permalloy nanodiscs in well-defined magnetic vortex state for biomedical applications, *Nanotechnology*. 27 (2016) 175302. <https://doi.org/10.1088/0957-4484/27/17/175302>.
- [135] R. Singh, J.W. Lillard, Nanoparticle-based targeted drug delivery, *Exp. Mol. Pathol.* 86 (2009) 215–223. <https://doi.org/10.1016/j.yexmp.2008.12.004>.
- [136] S. Jafari, L.O. Mair, I.N. Weinberg, J. Baker-McKee, O. Hale, J. Watson-Daniels, B. English, P.Y. Stepanov, C. Ropp, O.F. Atoyebi, D. Sun, Magnetic drilling enhances intra-nasal transport of particles into rodent brain, *J. Magn. Magn. Mater.* 469 (2019) 302–305. <https://doi.org/10.1016/J.JMMM.2018.08.048>.
- [137] D. Kuzajewska, A. Wszolek, W. Żwierzeło, L. Kirczuk, A. Maruszewska, Magnetotactic Bacteria and Magnetosomes as Smart Drug Delivery Systems: A New Weapon on the Battlefield with Cancer?, *Biol.* 2020, Vol. 9, Page 102. 9 (2020) 102. <https://doi.org/10.3390/BIOLOGY9050102>.
- [138] O. Felfoul, M. Mohammadi, S. Taherkhani, D. De Lanauze, Y. Zhong Xu, D. Loghin, S. Essa, S. Jancik, D. Houle, M. Lafleur, L. Gaboury, M. Tabrizian, N. Kaou, M. Atkin, T. Vuong, G. Batist, N. Beauchemin, D. Radzioch, S. Martel, Magneto-aerotactic bacteria deliver drug-containing nanoliposomes to tumour hypoxic regions, *Nat. Nanotechnol.* 2016 1111. 11 (2016) 941–947. <https://doi.org/10.1038/nnano.2016.137>.
- [139] S.K. Alsaiari, A.H. Ezzedine, A.M. Abdallah, R. Sougrat, N.M. Khashab, Magnetotactic bacterial cages as safe and smart gene delivery vehicles, *OpenNano*. 1 (2016) 36–45. <https://doi.org/10.1016/J.ONANO.2016.07.001>.
- [140] D. Gandia, L. Gandarias, I. Rodrigo, J. Robles-García, R. Das, E. Garaio, J. Ángel García, M.-H. Phan, H. Srikanth, I. Orue, J. Alonso, A. Muela, M. Luisa Fdez-Gubieda, D. Gandia, I. Rodrigo, J. Á García, A. Muela, M.L. Fdez-Gubieda, L. Gandarias, J. Robles-García, R. Das, M. Phan, H. Srikanth, Unlocking the Potential of Magnetotactic Bacteria as Magnetic Hyperthermia Agents, *Small*. 15 (2019) 1902626. <https://doi.org/10.1002/SMLL.201902626>.
- [141] M. Banobre-Lopez, Y. Pineiro-Redondo, M. Sandri, A. Tampieri, R. De Santis, V.A. Dediu, J. Rivas, Hyperthermia induced in magnetic scaffolds for bone tissue engineering, *IEEE Trans. Magn.* 50 (2014). <https://doi.org/10.1109/TMAG.2014.2327245>.

- [142] T. Kobayashi, M. Ochi, S. Yanada, M. Ishikawa, N. Adachi, M. Deie, K. Arihiro, Augmentation of Degenerated Human Cartilage In Vitro Using Magnetically Labeled Mesenchymal Stem Cells and an External Magnetic Device, *Arthroscopy*. 25 (2009) 1435–1441. <https://doi.org/10.1016/J.ARTHRO.2009.06.009>.
- [143] R.A. Pareta, E. Taylor, T.J. Webster, Increased osteoblast density in the presence of novel calcium phosphate coated magneticnanoparticles, *Nanotechnology*. 19 (2008) 265101. <https://doi.org/10.1088/0957-4484/19/26/265101>.
- [144] Y. Gao, J. Lim, S.H. Teoh, C. Xu, Emerging translational research on magnetic nanoparticles for regenerative medicine, *Chem. Soc. Rev.* 44 (2015) 6306–6329. <https://doi.org/10.1039/C4CS00322E>.
- [145] E. Mansfield, D.L. Kaiser, D. Fujita, M. Van de Voorde, *Metrology and Standardization of Nanotechnology*, John Wiley & Sons, Incorporated, 2017. <https://doi.org/10.1002/9783527800308>.
- [146] P. Schier, C. Barton, S. Spassov, C. Johansson, D. Baumgarten, O. Kazakova, P. Southern, Q. Pankhurst, M. Coisson, C. Grüttner, A. Price, R. Rüttinger, F. Wiekhorst, J. Wells, U. Steinhoff, *European Research on Magnetic Nanoparticles for Biomedical Applications: Standardisation Aspects*, in: *Adv. Intell. Syst. Comput.*, Springer Verlag, 2020: pp. 316–326. https://doi.org/10.1007/978-3-030-29885-2_29.
- [147] J. Wells, O. Kazakova, O. Posth, U. Steinhoff, S. Petronis, L.K. Bogart, P. Southern, Q. Pankhurst, C. Johansson, Standardisation of magnetic nanoparticles in liquid suspension, *J. Phys. D. Appl. Phys.* 50 (2017) 383003. <https://doi.org/10.1088/1361-6463/aa7fa5>.
- [148] ISO - ISO/TS 19807-1:2019 - Nanotechnologies — Magnetic nanomaterials — Part 1: Specification of characteristics and measurements for magnetic nanosuspensions, (n.d.). <https://www.iso.org/standard/66237.html> (accessed November 23, 2021).

SECTION II

MAGNETIC
NANOPARTICLES
AS LABELS

I. Magnetic nanoparticles as labels

Magnetic nanoparticles have been proposed as labels in different biosensors because their high surface-to-volume ratio allows different molecules to get attached to their surface. The biorecognition elements, whose different types are gathered in section 2.3 of section I of this thesis, give the specificity required. The bonding process between the nanoparticle and the biorecognition element is called bioconjugation, being a fundamental stage in the development of any biosensor in general and an LFA in particular.

Once the MNPs have been successfully conjugated to the appropriate biorecognition element, the nanolabel will be ready. Then, the quantification of the analyte is done thanks to the magnetism of the particles. The different detection principles have been detailed in part 6.1 of section I. This thesis uses an inductive sensor based on a planar coil, whose details will be described in this section.

1. Bioconjugation processes: "There is strength in numbers"

Biocompatibility and chemical stability are necessary for MNP bio applications. The high specific surface of the particles enables the immobilization of a vast number of biomolecules. However, this also promotes their agglomeration, and thus, different approaches have been proposed to prevent it. They are usually classified into organics (e.g., polymers or small organic molecules), inorganics (e.g., silica, carbon, or noble metals), and encapsulation in liposomes or nanovesicles [122,168]. All the approaches influence the MNPs' magnetic properties [169–171], but organic small molecules or polymers and the MNPs encapsulation are the most used for biosensing applications [172]. In others, like in hyperthermia, metals are preferred [173]. They excellently conduct the heat generated, and, for example, gold, allow an easy conjugation of many biomolecules [174].

Using a polymeric coating provides colloidal stability through electrostatic or steric repulsion, protects the rapid oxidation and leaching of the inorganic core, and offers biocompatibility for *in vivo* applications improving the stealth from the body defenses. It also has been stated that polymers restore the particles' magnetism thanks to reestablishing the surface ordering [169,175]. Additionally, polymers bring bioactive

multifunctional chemical groups, which are essential for further bioconjugation processes. The polymer addition can be done directly *in situ* during the synthesis or after it. For example, in co-precipitation, the former is preferred because its addition can control the MNPs size. The latter is done for bare MNPs or for synthesis methods in which hydrophobic nanoparticles are obtained to get a hydrophilic solution. There are different ways in which these polymers can interact with the MNP surface (see Figure 26). The most frequent ones are the attachment through a chemical group (anchor) at the end of the polymer directly to the MNPs surface, the covalent attachment or grafting of the polymer to a pre-existing coating, and electrostatic interactions between coatings with different superficial charges [176]. The typical chemical anchors for direct binding are catechol or its derivatives, carboxylate, phosphonates, and silanes [177].

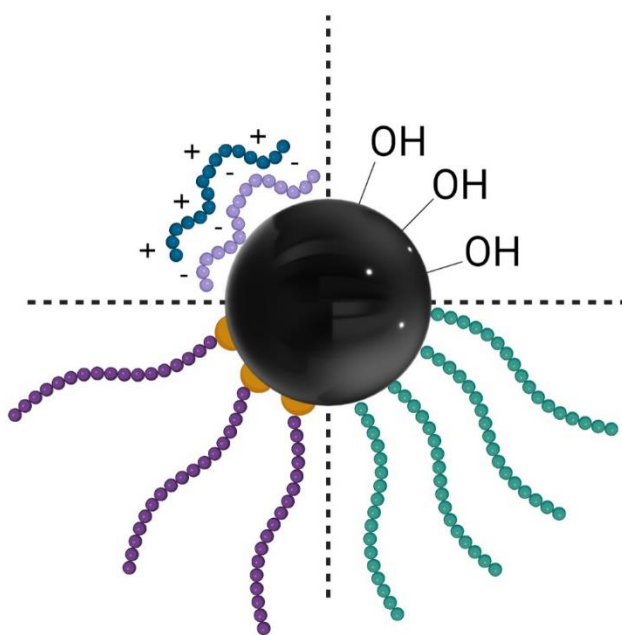


Figure 26. Schematic representation of the different superficial stabilizations for MNPs (clockwise direction): Bare precipitated MNPs with hydroxyl groups, polymer attached via a polymer end group, polymer grafted or covalently bound to a pre-existing coating, and electrostatic interactions among coatings.

Once the MNPs are stable in solution, they must be bioconjugated to the biorecognition element. This process usually involves a covalent bond between the residual chemical groups of the MNPs coatings and some other chemical groups of the biorecognition molecule. The most common groups in the MNPs are amines ($-NH_2$), thiols ($-SH$), and carboxylate ($-COOH$) groups, each requiring a different chemistry to form the

bound [178]. One drawback of the covalent bonding is the uncontrolled anchoring of the biomolecule. Orientation of the recognition elements, such as antibodies, plays a critical role in the performance of the biosensor. The optimum orientation is that in which the antigen binding sites are directed toward the solution phase [179], which is not always assured.

Another immobilization approach consists of taking advantage of supramolecular or coordinative interactions. The most famous example used in the field of biosensors is the biotin avidin (or streptavidin or neutravidin) interaction. The avidin protein is made up of four identical subunits, which can specifically recognize and bind to four biotins. The large dissociation constant makes this bond extremely stable, even in harsh chemical conditions and elevated temperatures [180]. All these characteristics allowed for a large variety of biotinylated reagents, such as peptides or antibodies, readily modified with biotin and commercially available. Therefore, MNPs with avidin (or streptavidin or neutravidin) can take advantage of this already well-established conjugation platform [181].

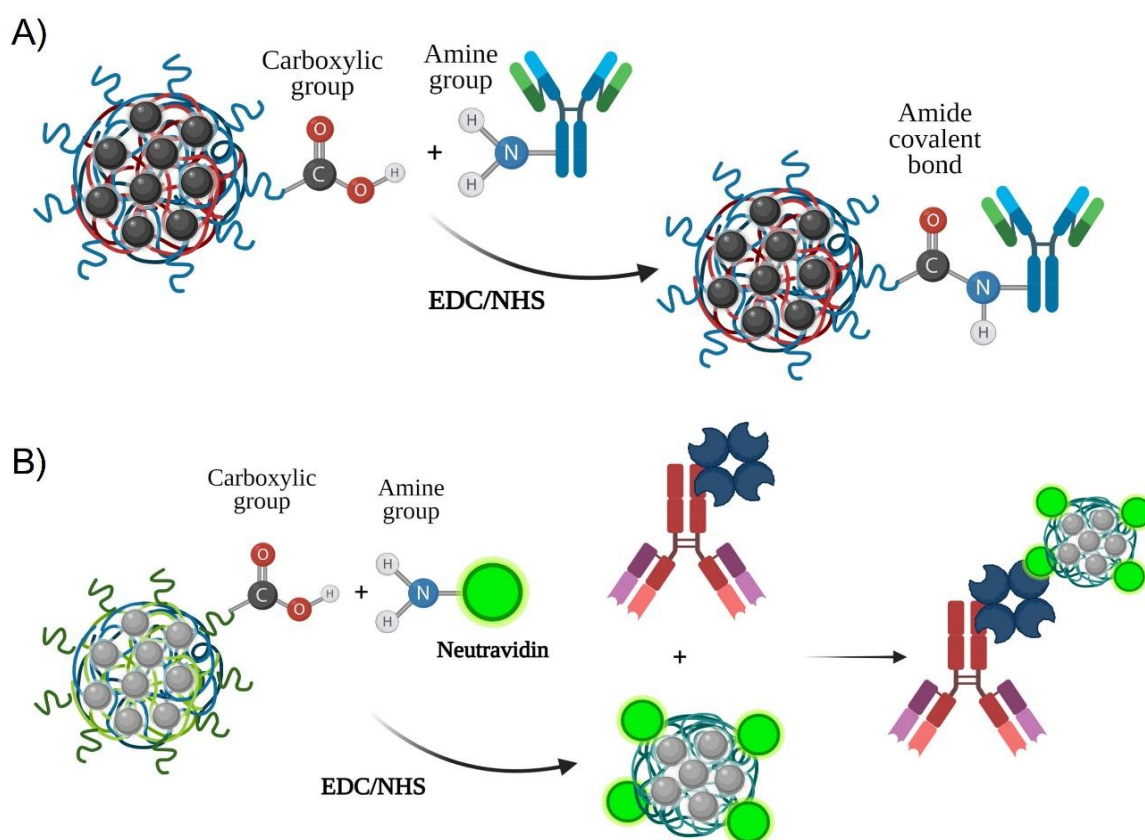


Figure 27. Schematic representation of the A) EDC/NHS and B) biotin/neutravidin bioconjugation processes.

During research for this thesis, two different approaches have been used (see Figure 27). The first one uses the carbodiimide crosslinker chemistry, which uses EDC (1-ethyl-3-(3-dimethylaminopropyl) carbodiimide hydrochloride) and NHS (N', N'-dicyclohexyl carbodiimide) reagents to form an amide bond from a carboxyl and a secondary amine. By this method, the recognition element, i.e., an antibody, is covalently attached to the MNPs. The other approach uses this methodology in the first step, but in this case, the covalent binding is between the neutravidin and the MNPs. This complex can be used as the antigen-antibody equivalent when the biotin is printed in the test line. For other uses, the MNP-neutravidin complex can be mixed with a biotinylated antibody specific against any target.

2. Magnetic detection by inductive biosensing

Inductive sensors are based on Faraday's law of induction, which relates the interaction between an electric current and a magnetic field to produce an electromotive force (voltage). In inductive sensors, an alternating current excites the magnetic material which, in turn, induces an AC magnetic field in the sensor that, usually is detected by a secondary coil. However, the sensor can be designed so that the primary

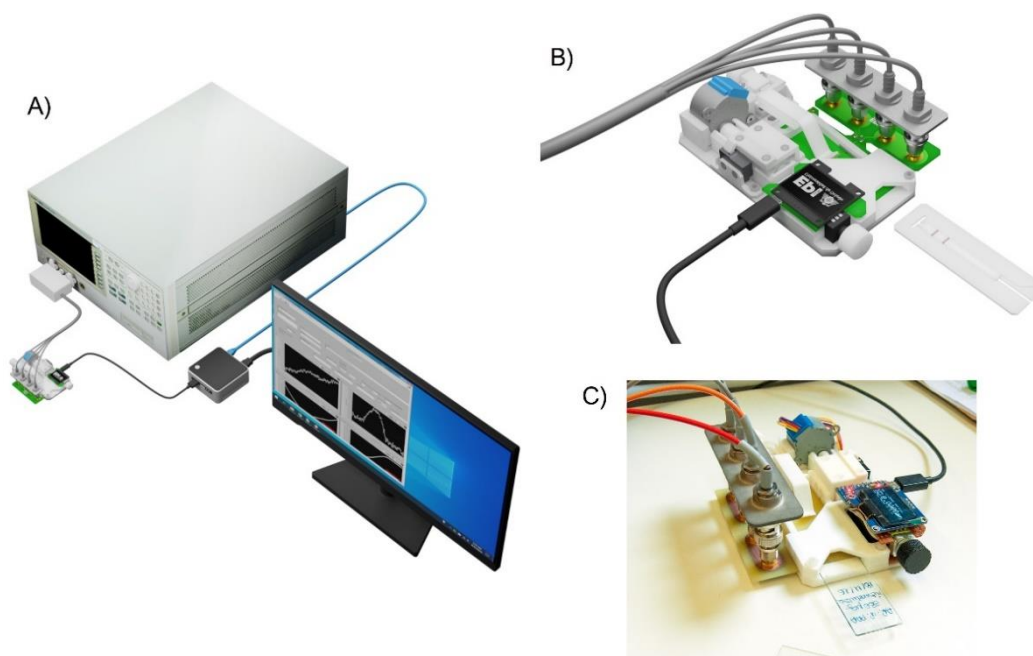


Figure 28. A) Schematic representation of the sensing system showing the impedance analyzer, the micro-positioner, and the personal computer used to control both. B) Image of the sensing device, which comprises the planar inductor, the LFAs holder, and the micro-positioner. C) Photography of the micro-positioner. Images provided by José Luis Marqués-Fernández.

coil itself induces and receives the induced signal. The latter design is even more straightforward in its construction. Several induced signals can be detected, being changes in the self-inductance, the impedance, or the coil's resonant frequency. One of the most significant advantages of inductive sensors is that they do not need external magnetic fields to excite the MNPs, allowing their miniaturization and portability. These are key characteristics to be used as POCTs because the sensor should not compromise the quickness, affordability, and simplicity of the LFAs.

An inductive sensor developed in the laboratory has been used during the research for this thesis. It consists of a planar coil, a micro-positioner to slide the samples over the sensing track, and an impedance analyzer (see Figure 28).

The planar coil is a conductive Cu-based track printed on an insulating substrate that acts as a transducer (see Figure 29A). Two types of samples have been characterized in this thesis. The first one consists of a known mass of the as-synthesized MNPs deposited on a blotting paper and left to dry. The second type consists of LFAs in which MNPs have been used as nanolabels. Since these two types of samples have different surfaces and to maximize the signal in the sensor, two types of planar coil designs were adapted to each one (see Figure 29B). Therefore, all the sample containing magnetic material is located inside the corresponding loop.

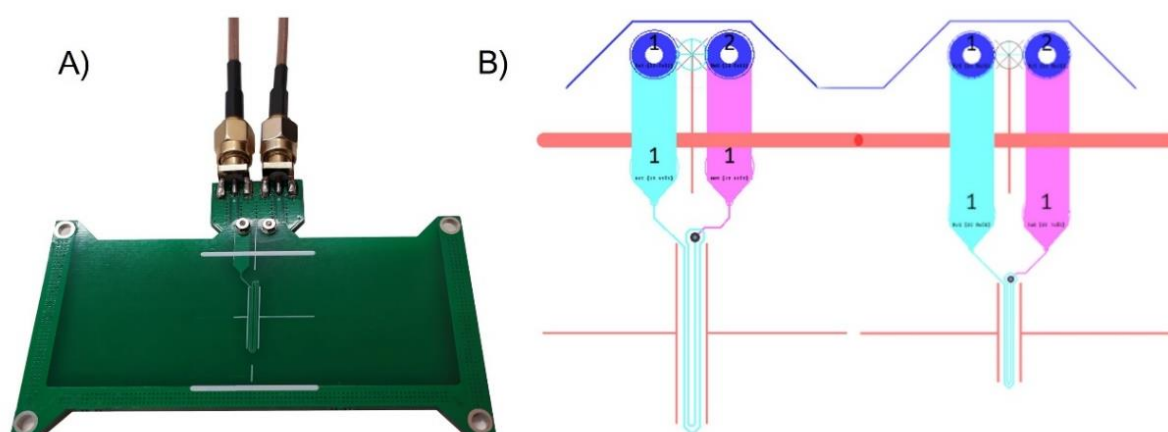


Figure 29. A) Detailed image of the planar inductor printed in the insulating substrate. B) Plan of the planar coils specifically designed to encompass the entire width of the MNPs and LFAs samples, respectively. Images provided by José Luis Marqués-Fernández.

The planar coil is fed with a low amplitude radio-frequency current flow while its impedance is continuously monitored by the precision four-point auto-balancing impedance analyzer (Agilent 4294A). The latter uses 16048G test leads, 500 mV excitation voltage, and a frequency range from 10 MHz to 110 MHz.

From an electric point of view, the sensing planar coil can be approximated by an RL circuit, equivalent to a resistance R and a self-inductance L . The electrical impedance Z of this circuit depends on the frequency ν and the magnetic relative permeability μ_r of the surrounding medium as:

$$Z_0(\nu, \mu) = R(\nu) + i2\pi\nu L\mu_r(\nu) \quad (28)$$

where the resistive part $R(\nu)$ depends on the frequency due to the eddy currents and skin effect, and L depends on the geometry of the conductor and any surrounding magnetic material.

In absence of any magnetic particles in the surroundings, the magnetic permeability can be approximated by the vacuum permeability, $\mu_r = 1$. When the sensing coil is completely covered by a magnetic material with an initial susceptibility $\chi(\nu)$, the relative permeability is $\mu_r(\nu) = \chi(\nu) + 1$. In this case, the magnetic particles do not surround the whole length of the conductor, and therefore, there is a need to introduce a correction factor ψ ($\psi < 1$) to account for the volume of particles. The impedance of the conductor when the MNPs are present is described by:

$$Z(\nu, \chi', \chi'', \psi) = R(\nu) + i2\pi\nu L[\psi\chi(\nu) + (1 - \psi)\mu_r] \quad (29)$$

Taking this into account, the difference in impedance measured with the particles (Z) and without them (Z_0) can be written as:

$$\Delta Z(\nu, \chi', \chi'', \psi) = \nu L\psi\chi''(\nu) + i\nu L\psi\chi'(\nu) \quad (30)$$

where χ' and χ'' correspond to the real and imaginary components of the magnetic initial susceptibility of the magnetic material. It is important to remark that due to the product of the two complex numbers, Z and χ , the real part of ΔZ depends on the imaginary component of the susceptibility and *vice versa*. According to this, for a fixed frequency, both the real and the imaginary parts of the impedance variation are directly proportional to the magnetic material mass present through the parameter ψ . This

linear dependence has been checked in previous works [182] and is shown in Figure 30.

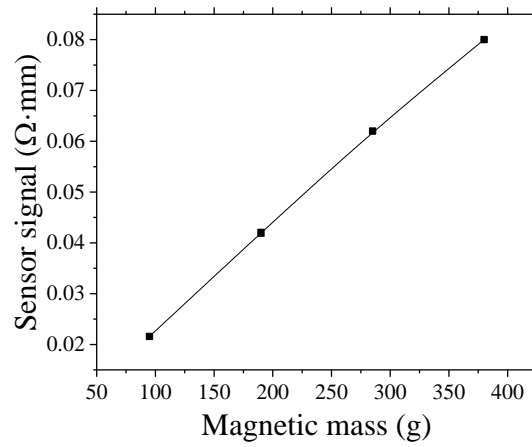


Figure 30. Calibration curve of the sensor signal with different MNPs masses.

Both the MNPs samples and the LFAs are measured by their smooth scanning over the planar coil thanks to the micro-positioner movement. All the micro-positioner components except the stepper motor were three-dimensionally printed using a PLA filament. This will reduce the induction of spurious signals by avoiding moving metallic parts. The

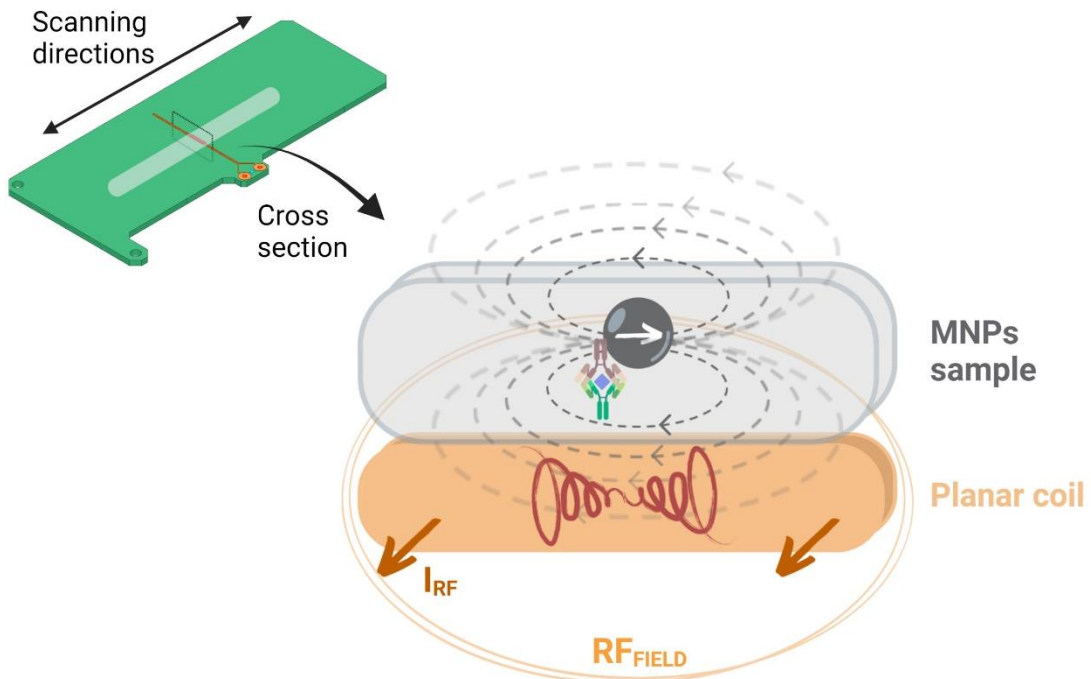


Figure 31. Schematic representation of a cross-section of the test line and the planar coil to show the auto-inductive sensing principle: A RF current flows through the Cu-based conductor. The RF field generated excites the MNPs, which in turn, increases the impedance of the planar coil. Only one MNPs has been represented for the shake of simplicity.

duration of one measurement is about 5 minutes.

During the scanning, the planar coil detects the varying magnetic flux produced by the presence of the MNPs. Their proximity produces a change in the electrical impedance which is directly proportional to the frequency of the driving current, the initial magnetic permeability of the particles and the total volume of their magnetic cores (see Figure 31).

The change in the impedance during the scanning is a peak, whose width is related to the width of the line that contains the MNPs. To account for all of them disregarding their distribution within the paper strip, the peak signal is integrated across the position (see Figure 32). Therefore, the signal S provided by the sensor is obtained in units of $\Omega \cdot \text{mm}$ coming from the cumulative integral of the impedance (Ω) across the width w of the line (mm) as follows:

$$S = \int_0^w \Delta Z dx \quad (31)$$

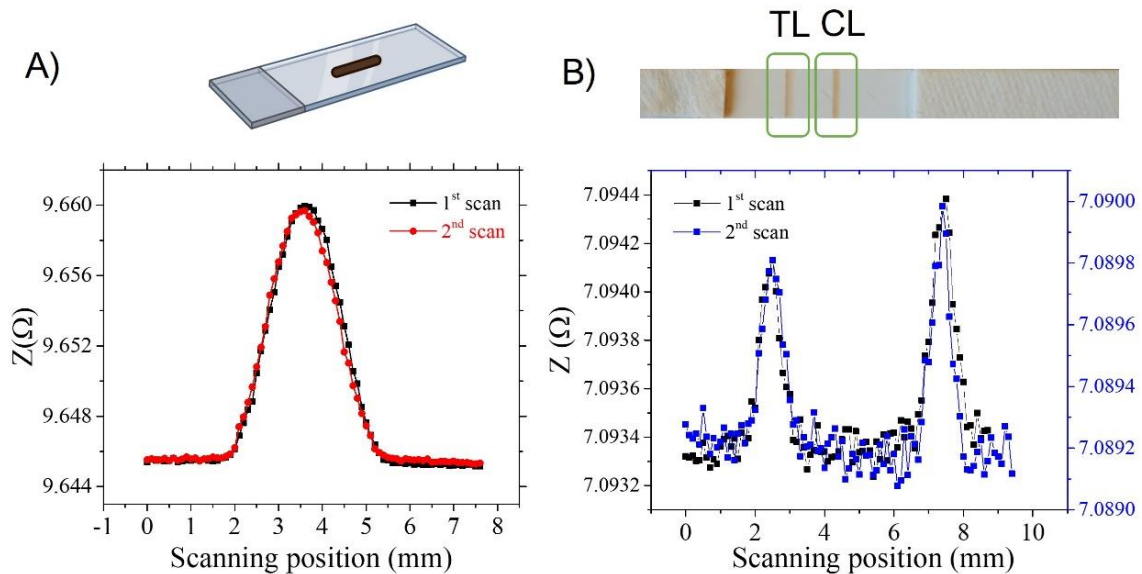


Figure 32. Sensor signal for two consecutive scans in opposite directions for a sample of A) MNPs and B) LFAs.

Additionally, the assessment of the MNPs as nanolabels in the inductive sensor was done measuring the paper samples previously prepared. Their performance was evaluated by the sensor sensitivity (Σ) stated as for magnetoimpedance and magnetoimpedance sensors. For a fixed frequency and type of particles, Σ is defined as the relative percentage increase of the impedance (Z) per unit mass of particles (m). For Z with

and Z_0 without particles in the inductive sensor:

$$\Sigma = \frac{1}{m} \frac{\Delta Z}{Z_0} \cdot 100 \quad (32)$$

The resolution R of the method is then defined as the smallest change in mass that the inductive sensor can resolve, as:

$$R = \frac{m \sigma_{\text{base}}}{\Delta Z} \quad (33)$$

where σ_{base} is the noise as the standard deviation of the signal over time when measuring a blank, and ΔZ is $Z - Z_0$.

The inductive sensor sensibility and resolution depend on its intrinsic characteristics, such as geometry, size, electronics, and on MNP properties. One of the objectives of this thesis is to establish the optimal MNP properties to be used as nanolabels in inductive biosensing.

Section II – Chapter 1

Synthesis of Superparamagnetic Iron Oxide Nanoparticles: SWOT Analysis Towards Their Conjugation to Biomolecules for Molecular Recognition Applications

Introduction and motivation

Section II of this thesis focuses on the use of magnetic labels in inductive biosensing. For that purpose, the MNPs characteristics, the biorecognition molecule used, and how these two are bounded are critical.

In the following pages, one can find a review focused on the strengths, weaknesses, opportunities, and threats of the different MNPs synthesis methods focusing on their biofunctionalization for molecular recognition. This review is intended as a journey through the main strategies for the preparation of nanocomposites, their stabilization, different strategies to get synergetic properties and controlled agglomeration methods for the sensitivity enhancement at molecular recognition events.

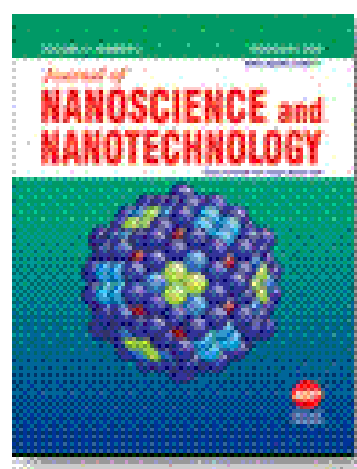
Review

Synthesis of Superparamagnetic Iron Oxide Nanoparticles: SWOT Analysis Towards Their Conjugation to Biomolecules for Molecular Recognition Applications

This work has been published in:

Journal for Nanoscience and Nanotechnology

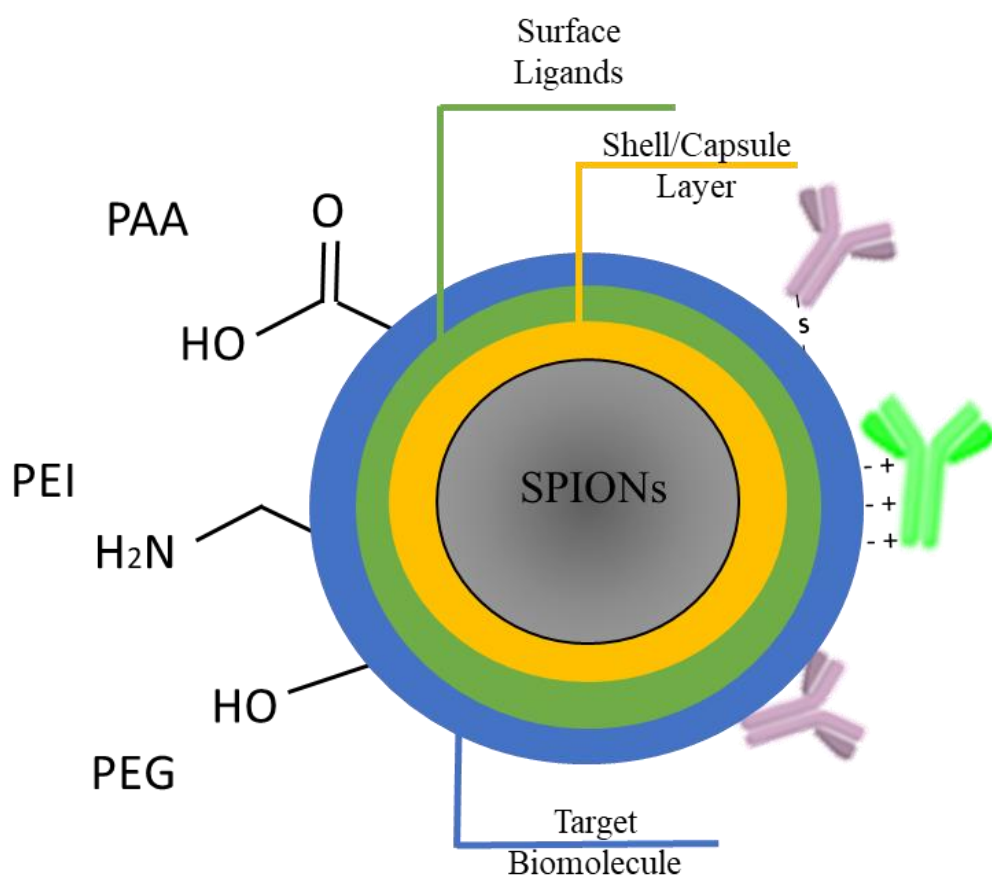
American Scientific Publishers



Cite as:

Salvador M, Moyano A, Martínez-García JC, Blanco-López MC, Rivas M. Synthesis of Superparamagnetic Iron Oxide Nanoparticles: SWOT Analysis Towards Their Conjugation to Biomolecules for Molecular Recognition Applications. *J Nanosci Nanotechnol*. 2019 Aug 1;19(8):4839-4856. doi: 10.1166/jnn.2019.16931. PMID: 30913798.

GRAPHICAL ABSTRACT



Synthesis of superparamagnetic iron oxide nanoparticles: SWOT analysis towards their conjugation to biomolecules for molecular recognition applications

María Salvador^{1,2}, Amanda Moyano^{1,3}, José Carlos Martínez-García¹, María Carmen Blanco-López³, Montserrat Rivas¹

¹*Department of Physics, University of Oviedo, Campus de Viesques, 33204 Gijón, Spain*

²*Istituto di Struttura della Materia - Consiglio Nazionale delle Ricerche (CNR), 00016 Monterotondo Scalo (RM), Rome, Italy*

³*Department of Analytical and Physical Chemistry, Institute of Biotechnology of Asturias, University of Oviedo, 33006 Oviedo, Spain*

Abstract

Superparamagnetic Iron Oxide Nanoparticles (SPIONs) have attracted a great deal of research attention due to their enormous possibilities of utilisation in different bioapplications such as magnetic particle imaging, drug delivery, hyperthermia, or magnetic bio-detection. The purpose of this review is to critically analyse the methods for synthesis of SPIONs reported at the literature taking into account their suitability in molecular recognition applications by means of their conjugation to biomolecules. In this work, we have summarized the main synthesis routes, and controlled agglomeration methods for enhancement of sensitivity at molecular recognition events. This includes conventional chemical precipitation methods, thermal decomposition, microemulsions, or microfluidic synthesis, and the main strategies for the preparation of nanocomposites or SPIONs nanoclusters, such as polymer or silica cross-linking reactions, entrapment in nanovesicles or flower-like structures through the appropriate use of different metals to get synergetic properties for the total nanoarchitecture. Since most of the actual applications in biomedicine require their conjugation to biomolecules, an analysis of the Strengths, Weaknesses, Opportunities and Threats of these methods was carried out for the first time, with a view to highlight the best routes for a given application at biomolecular recognition.

Keywords: Nanoparticles, SPIONs, bioconjugation, molecular recognition, SWOT analysis.

1. Introduction

Nanotechnology has emerged as a general-purpose field having significant impact on almost all industries and areas of society: from medicine to electronics, food, energy, agriculture or environment. In all of them, the application of nanoparticles is one of the most used approaches to establish fancy improvements. Among all the peculiar and appealing characteristics nanoparticles have, their small size is just the most interesting for biotechnological applications, due to its similarity to the size of several biomolecules.

Superparamagnetic Iron Oxide Nanoparticles (SPIONs) are the most widely investigated and used nanoparticles. Magnetite, Fe_3O_4 , and maghemite, Fe_2O_3 , are among all the iron oxides present in nature, and both phases are present the inverse spinel structure. They are physically and chemically stable, biocompatible and environmentally safe [1, 2]. Another attractive feature is their magnetic character, which switches from ferromagnetic to superparamagnetic at a critical temperature known as blocking temperature (T_B). For sizes below ca. 20 nm, SPIONs T_B is below room temperature. In the absence of applied magnetic field, the thermal energy is enough to overcome the magnetic anisotropy barrier between the two different equilibrium spin positions, allowing the magnetic moment of the nanoparticles to switch rapidly and arbitrarily. Hence, the net magnetization when no external field is applied appears to be null as far as the time window required to measure it is far larger than the relaxation time. However, in the presence of an external field, magnetic moments of the single-domain nanoparticles align parallel to it, producing a large magnetization in its low frequency hysteresis, as shown in the green magnetization curve of Figure 1 (for high frequencies, magnetization lags with respect to the applied field which results in a widening of the hysteresis loop). Because of this, a system composed by superparamagnetic nanoparticles has no apparent coercivity and remnant magnetisation in its low frequency hysteresis loop (Figure 1). This important characteristic makes easier to maintain the colloidal stability and avoid uncontrolled agglomeration. Those features, together with the others mentioned before, enable SPIONs to be used as a workhorse in biomedical applications where molecular recognition is a

key aspect, including biosensing [3, 4], magnetic [5, 6] or hybrid (magnetic-laser excited) hyperthermia [7, 8], drug delivery [9, 10], magnetic separation (isolation and concentration) [11, 12], magnetic resonance imaging (MRI) as contrast agents [13, 14] or magnetic particle imaging (MPI) [15, 16].

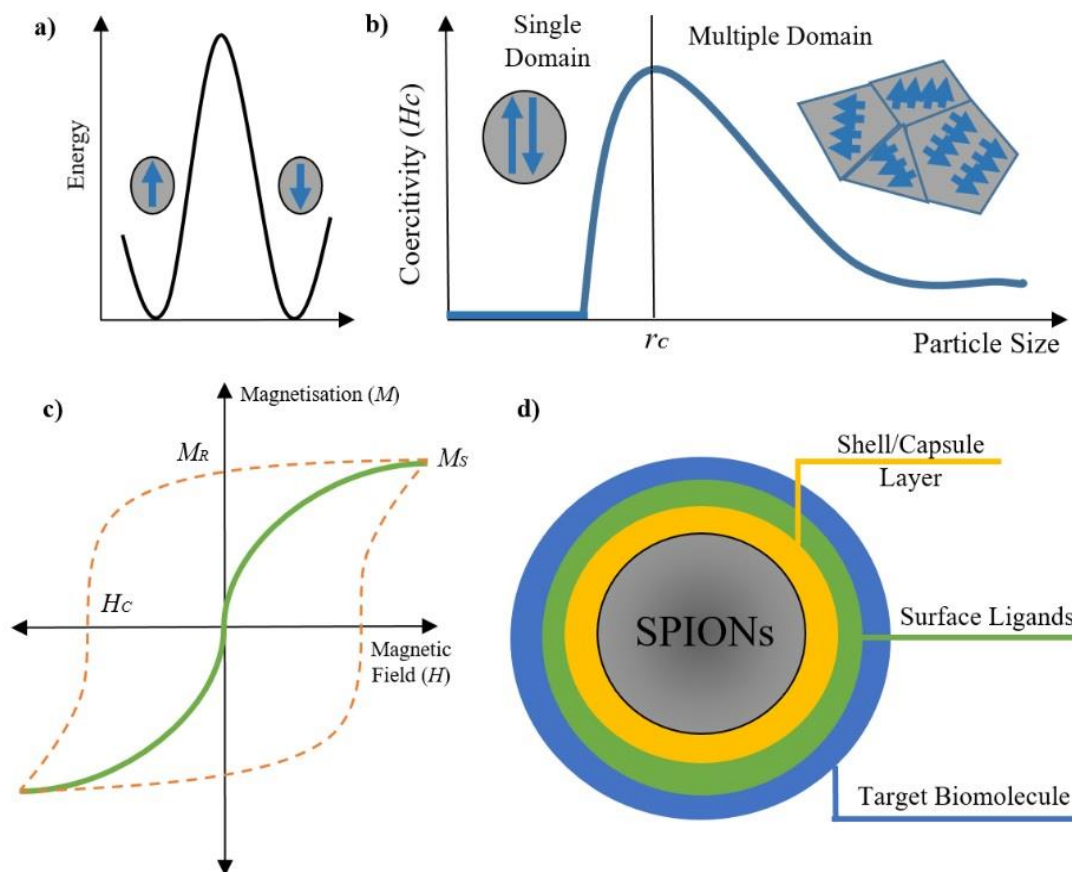


Figure 1. a) Schematic representation of the anisotropy energy barrier separating the two magnetization directions in a single domain particle with uniaxial anisotropy in the absence of external applied field. b) Schematic illustration of the relationship between coercivity and size for particles, showing the transition from multidomain to single-domain. c) Schematic representation of the hysteresis loops of a ferromagnetic (orange dashed line) and a superparamagnetic (green solid line) material. The first one shows non-zero remnant magnetisation (M_R) as well as coercivity (H_c) in contrast to the superparamagnetic loop which shows similar sigmoidal shape but no remanence and coercivity. d) Schematic representation of a multilayer SPIONs, with the different possible coatings, though not all of them should be necessarily present. The first yellow layer refers to capsule, which usually gathers several together. The green layer refers to the ligand, which supports the terminal chemical group for later functionalization and biorecognition of the last layer, which is the molecular receptor chosen.

Different synthesis routes described in the literature can be optimized to obtain SPIONs as platforms for the mentioned applications. For this purpose, a good control over the synthesis is crucial. This involves an appropriate selection of the governing parameters that influence the

synthesis in order to obtain narrow size distributions in a reproducible manner with the desired shape, crystal structure and magnetic properties.

The specific recognition of the molecule of interest it is not usually straightforward but through the mediation of another biomolecule attached to the surface of the particle. Proteins, enzymes, aptamers, DNA/RNA strands or antibodies are among the most common molecular receptors for this purpose (Figure 4). The process to attach the recognition element is regularly known as bioconjugation and can be done directly through physical interactions at the surface of the nanoparticle or more frequently by chemical reactions involving the terminal groups present in the polymer coatings of the SPIONs. The latter, not only confers the mentioned functionality, but also provides colloidal stability to the suspension. Besides, in order to get optimal detection sensitivity and efficiency, the highest possible saturation magnetisation should be achieved [17]. However, as the size of the nanoparticles decreases, the superficial structural defects gain importance due to the increase of the surface-volume ratio, which has a strong negative effect upon the saturation magnetization value [18]. One alternative way to overcome this situation and obtain even better properties is the encapsulation or controlled agglomeration of SPIONs. This approach takes advantage of the already-synthesised nanoparticles and joins them together through different procedures, i.e., using different polymers, silica, nanovesicles, etc. These alternatives should render nanocomposites that are, as the SPIONs first used, readily available to be bioconjugated at a later stage. This means that the surface of the agglomeration agent must be able to be used as a recognition element by itself through further and proper functionalisation. Moreover, it is possible to agglomerate the SPIONs together using structures where other properties of the nanoparticles are used.

This review focuses on the description of some of the most studied routes to obtain SPIONs, with emphasis on the characteristics and possibilities that all of them offer in order to be used lately for a biorecognition purpose. Different approaches described in the literature to obtain nanostructures that improve the characteristics of the nude SPIONs are included. These add sometimes more features than the primary particles themselves have, i.e., magnetic properties, allowing synergetic effects. However, the biorecognition of the molecule takes place

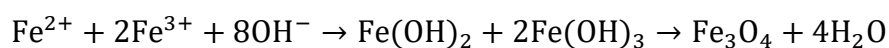
through a biomolecule able to specifically recognise it which is attached to the surface of the SPIONs for many applications. These kinds of molecules are usually antibodies, enzymes, DNA/RNA strands, aptamers, etc., and are bounded to the nanoparticles by different approaches in a process called biofunctionalisation. Here, we focused on the description of some of the most spread ones, such as the streptavidin-biotin bonds, the covalent chemistry and others. Finally, a SWOT analysis, (Strengths, Weaknesses, Opportunities and Threats), of the different methods to synthesise SPIONs is presented. The objective of this analysis is to critically summarize the possibilities of the methods used for obtaining nanoarchitectures for biorecognition platforms.

2. Synthesis of Superparamagnetic Iron Oxide Nanoparticles (SPIONs)

During the last years, much research effort has been devoted to preparation of superparamagnetic nanoparticles by different methodologies. This endeavour has not only been focused on achieving appropriate nanoparticles for their subsequent application but also on understanding the underlying correlation between the magnetic properties and the pathway of synthesis and its related parameters, i.e., temperature, time, ratio among reactants, surfactants nature and concentration, etc. However, there is still not the perfect method to synthesize SPIONs with altogether suitable size, shape, structure, magnetic and superficial properties, and colloidal stability. Some approaches offer better characteristics affecting negatively other desired ones. Normally, for biosensing applications it is essential to optimise both the superficial coating (necessary for the ulterior bioconjugation) and the magnetic properties (on which the sensing principle usually relies on), frequently saturation magnetization. The chemical methods used for the synthesis of SPIONs include co-precipitation, thermal decomposition, microemulsions, microfluidic and synthesis of “dual” nanoparticles.

2.1. Co-precipitation of iron salts

Co-precipitation is one of the most frequently used methods, due to its advantages such as simplicity, rapidity, gram-scale production, and high yield. The reaction can be simplified as:



The method was first demonstrated by Massart in 1981 [19]. An oxygen free environment is required to avoid the oxidation from magnetite to maghemite. Thermodynamically, the complete precipitation of Fe_3O_4 is expected at pH between 9 and 14. There are two main different co-precipitation methods to get SPIONs. In the first one, an aqueous suspension of ferrous hydroxide is partially oxidized using different oxidizing agents, for example nitrate ions. Spherical magnetite nanoparticles with a size distribution between 30 and 100 nm can be obtained using this method [20]. The second procedure is based on the stoichiometric mixtures of ferric and ferrous ions in basic medium at high temperature. In this case a narrower size distribution, from 2 to 15 nm [21], is achieved through a really elegant and simple way. Daoush has synthesised magnetic nanoparticles with 30 nm average particle size by using ethylenediaminetetraacetic acid (EDTA) [22]. The magnetite nanoparticles obtained have superparamagnetic behaviour with a saturation magnetization of 88.1 emu/g. Furthermore, it is possible to control the mean size of the nanoparticles by adjusting some parameters, such as the pH, the ionic strength of the medium, temperature, ratio of salts and stirring velocity on the synthesis. When the pH and the ionic strength are increased in the solution, the size decreases and because of this change, the chemical composition of the surface is affected [23]. Moreover, the average size of nanoparticles could be increased by means of increasing the reaction temperature [24, 25], stirring velocity [26] and the ratio of ferrous to ferric ions [27]. The influence of the initial pH of the solution has also been studied [25]. On the other hand, one important disadvantage of the co-precipitation is the tendency of the nanoparticles to agglomerate. To overcome this problem, it is possible to cover them with different polymers such as polyethylene glycol (PEG) [28, 29], polyacrylic acid (PAA) [30], polyethylenimine (PEI) [31] (Figure 3), increasing this way the repulsion between nanoparticles and achieving a stable solution by steric stabilisation.

2.2. Thermal decomposition of iron precursors

High temperature decomposition synthesis is generally used to obtain SPIONs with controlled size and morphology. Moreover, thanks to the elevated temperature used narrow size distributions and high crystallinity particles with high saturation magnetization are obtained. Iron precursors, typically metal acetylacetonates and metal oleates, such as iron (III) acetylacetonate, iron pentacarbonyl or iron oleate react in a

polar solvent environment with organic molecules, usually oleic acid or oleamine, used as stabilizing surfactants. The role of these compounds is really important because they regulate the nucleation and growth of the nanoparticles, favouring the formation of smaller ones as they bind to the nuclei and form a steric barrier [32, 33]. One of the most used procedure to carry out this synthesis with controllable size from 3 to 20 nm was reported by Sun [34]. The reaction of iron (III) acetylacetonate ($\text{Fe}(\text{acac})_3$) at 265°C in the presence of alcohol, oleic acid, and oleylamine was first described to be used to monodisperse SPIONs, and the starting point for new research and protocols.

The size and shape of the nanoparticles could be controlled by modifying parameters such as stirring [35], temperature [36], the nature and the ratio between the iron precursors and surfactants [35, 37-41]. Regarding the optimisation of the magnetic properties Unni et al. [42] have suggested in their work that the presence of some oxygen in the reaction media during the synthesis could lead to uniformly single-crystalline nanoparticles, reducing the so-called ‘magnetically dead layer’. Hence, similar magnetic properties to the bulk magnetite were obtained because of the similitude between the physical and magnetic diameter distributions obtained.

The use of expensive and sometime toxic reagents and the low amount of the nanoparticles obtained in one synthesis are some of the handicaps of this method, where large-scale batches of reproducible SPIONs are desired. Park and colleagues [43] reported a procedure to obtain up to 40 grams of monodisperse nanocrystals of Fe_3O_4 in one synthesis by using less expensive and more environmentally friendly compounds, such as metal chloride and sodium oleates. Also Berti et al [44] described an easier method which is able to save 86% of the total reagent cost but still produces monodispersed nanoparticles with very narrow distribution size and superparamagnetic behaviour. Moreover, research by Liang [45] suggests that thermal decomposition assisted by microwave radiation can lower the time necessary to obtain the highly crystalline nanoparticles. This is because the magnetite nanoparticles themselves are able to increase the reaction-rate by effectively converting the microwaves into heat.

However, the most important drawback of this method is that the hydrocarbon chains of the surfactants used make the nanoparticles

hydrophobic. For the use in biological applications, an additional step following the synthesis is usually necessary. This should be able to transfer the SPIONs into hydrophilic solutions. Different approaches can be used for this purpose. The first one is known as ligand exchange and consists on replacing the hydrophobic layer by a hydrophilic one. It is important to notice that the new ligand should have a higher affinity for the magnetic core, in order to effectively replace the first one and not to come apart during later processing. Zhang et al. [46] described a general procedure which involves the replacement of the original ligand by polyacrylic acid at high temperature in a glycol solvent. Another protocol for later biofunctionalization was developed by Wei et al [47]. Hydrophilic SPIONs were obtained by a two-step ligand exchange process. Oleate layer was first removed in methanol by 2-[2-(2-methoxyethoxy)ethoxy]acetic acid (MEAA) ligand to increase the solubility in the second solvent mixture used. Then, the MEAA ligand was replaced by zwitterionic dopamine sulfonate (ZDS), dopamine sulfonate (DS) or mixtures of ZDS with thiol-terminated catechol-derivative (TD). Avoiding this time consuming feature, a solvent-free protocol was developed by Korpany and colleagues [48], who were able to remove the oleic acid layer of the nanoparticles by a mechanochemical process of milling and retaining their size, shape, and superparamagnetic properties. However, these methodologies should be deeper investigated considering that they could not be able to replace all the oleic acid, as shown by isotope labelling by Kathleen et al [49]. Finally, Palma et al [50] studied not the ligand exchange protocol itself but how it affects important characteristics of the SPIONs, such as size, hydrodynamic diameter, colloidal stability and magnetic properties. From all of these, only the last one was altered.

The addition of another layer that makes the nanoparticles hydrophilic is another approach that can be used. Laurent [51] described a facile methodology to add a second layer of an amphiphilic copolymer consisting of polypropylene oxide (PPO) and polyethylene oxide (PEO). First, SPIONs were synthesized by the thermal decomposition of iron oleate and then, mixed in a hexane solution with the copolymer water solution for 30 minutes under vigorous stirring to allow the coupling of the two layers.

Another approach used is known as silane chemistry, where the hydrolization of alkoxy silane allows introducing a large variety of

functional groups in order to transfer the SPIONs to a hydrophilic solution but also to render them ready to be attached to the recognition biomolecule. Bloemen and colleagues [52] developed a methodology to convert oleic acid coated SPIONs in hydrophilic nanoparticles with carboxylic acid, polyethylene glycol, amine or thiol functional groups, although nanoparticles with this last one group were not sufficiently stable in water dispersion. An example of this methodology is given by Barrera and colleagues [53]. Firstly, magnetic nanoparticles were synthesised by a thermal decomposition of $\text{Fe}(\text{acac})_3$ and then, oleic acid onto their surface was exchanged for PEG-silane, previously obtained by the reaction of the carboxylic terminal groups of the polymer the amines present in 3-aminopropyl triethoxysilane (APS), in the presence of acetic acid to catalyse the hydrolysis and condensation of the process. The new nanoparticles were highly stable in water suspensions at pH from 3 to 9.

2.3. Microemulsions

Microemulsion is a thermodynamically stable single-phase system that consists of three components: two of them are immiscible (water phase and oil phase) and the third has an amphiphilic behavior, (e.g., surfactant, such as Triton X-100). In water-in-oil microemulsions, water droplets are used as nanoreactors in the oil phase. For the synthesis of SPIONs, soluble iron salt precursor is incorporated in the aqueous phase of the microemulsion precipitating iron oxide in this same phase, located in the centre of the micelles whereas unreactive iron precursors reside in the organic phase. The finely dispersed precipitate produced can be extracted from the surfactants. Furthermore, by controlling the size of the water droplets, generally in a range from 1 to 50 nm, it is possible to target size and shape nanoparticles with narrower distribution as compared with other methods. However, there are some disadvantages as agglomerated nanoparticles are often generated, most of them poorly crystalline due to relative low temperature used and also, a large amount of solvent is required to synthesise a very small amount of nanoparticles.

The synthesis of SPIONs using microemulsions has been reported by several groups. A novel approach to synthesise superparamagnetic nanoparticles with a polymeric shell of PEG have been developed using inverse microemulsion procedure, with a narrow size distribution around 40-50 nm [54]. Moreover, the saturation magnetization value of the magnetite nanoparticles was found to be between 45 and 50 emu/g and

the results of their characterization by Vibrating Sample Magnetometer (VSM) showed that the nanoparticles exhibited superparamagnetic behaviour. Lee et al. [55] were able to synthesise magnetite nanoparticles with a controlled size from 2 to 10 nm by reacting iron salts in microemulsion nanoreactors. The variation of some parameters such as concentrations of iron salts, surfactant and solvent enabled to achieve uniform and highly crystalline magnetic nanoparticles ranging among those different sizes. The saturation magnetization at 300K are 135, 152 and 173 emu/g for nanoparticles of 3, 5 and 7 nm, respectively.

2.4. Microfluidic synthesis

SPIONs are typically synthesised in bulk using traditional method such as those described above. Unfortunately, these types of methods provide only limited control over size, stoichiometry and magnetic characteristics. In order to controllably synthesise SPIONs with well-defined physical and chemical properties, microfluidic reactors have been recently employed as reaction vessels. The use of microscale devices has been shown to provide improvements in size, size distribution and crystallinity of the produced particles. Microfluidic reactors offer potential advantages such as the possibility of regulating some important variables for example temperature, reaction times and reagent concentrations. In this way, a microfluidic system would enable a better control over particle size and other physical and chemical properties overcoming some disadvantages of the traditional methods and specially leading to the production of high quality SPIONs.

To date, there have been some publications of SPIONs synthesis in microfluidic reactors. Hassan and colleagues [56] have synthesised iron oxide nanoparticles, with a size less than 7 nm, using a microfluidic system, described as a millimetric coaxial flow device. This is the route leading to the smallest particle size described. A study of the flow rate of different reagents was done in order to achieve a narrow size distribution with a saturation magnetization of 7.9 A/m for the suspension. Another study carried out by Kumar et al. [57] developed a stable passively-driven capillary-based droplet reactor in order to control the synthesis of dextran-coated SPIONs. Nanoparticles with a narrow size distribution of 3.6 nm as mean diameter were obtained, with high quality crystalline structure and a large saturation magnetisation of 58 emu/g. Also, Lee and others [58] were able to synthesise dispersed and uniform SPIONs of

around 6 nm in a short time (15 min) using also a microfluidic system, able to decrease the variation of the size distribution from 34% in normal large-scale system to 16% in the one they proposed. Lastly, Frenz et al. [59] were able to synthesised 4 nm monocrystalline SPIONs using a droplet-based microfluidic system, where the coalescence of two droplets containing each one of the reactants formed the product in a very fast and reproducible reaction.

2.5. Synthesis of “dual” nanoparticles

Dual nanoparticles refer to nanocomposites where two different features of two or more compounds are taken into advantage synergistically. Among all the characteristics to be combined with superparamagnetism, luminescence, catalytic or electroanalytical properties and surface functionalization are the most studied ones.

Luminescence is a feature that has been extensively used for detection and sensing. Dyes, especially organic dyes, have been widely used as signalling sources based on their emission properties. Ma et al. [60] used a silica double shell to solve the problem of luminescence quenching when dye molecules were directly attached to the magnetic surface. With this layer by layer approach, a silica shell coated first the magnetic nanoparticle and isolated the dye, which was doped in another second silica shell to concentrate the emission signal and enhance the photostability. A similar procedure was used by Runowski and colleagues [61]. Magnetite nanoparticles were obtained by a co-precipitation method and were encapsulated in a silica nanoscaffold composed of GdPO_4 , doped with Eu^{3+} ions as the emitter, in crystalline nanoneedles. Finally, with a silica layer again to provide the nanocomposite a hydrophilic character, Yi et al [62] described a two-step procedure involving microemulsions to synthesise Quantum Dots (QDs) and SPIONs, with a combination of magnetic and optical properties.

Catalytic properties are also desired at nanoparticles. The combination of a hydrotalcite (layered double hydroxides)-supported gold in a magnetite core, allowed a high activity in the oxidation of 1-phenylethanol but also could be lately separated by an external magnetic field after its use. The magnetite nanoparticles were obtained by a solvothermal method and coated carbonate-MgAl-LDH by means of the electrostatic attraction followed by the interface nucleation and the crystal growth by

addition of alkaline solutions and salts. Then, Au nanoparticles were attached to this nanostructure by a deposition–precipitation method. Another nanocomposite was developed by Ye et al [63]. In this case, a core–shell structure of $\text{Fe}_3\text{O}_4@\text{SiO}_2@\text{TiO}_2$ took advantage also of the photocatalytic activity of the Titania together with the fast magnetic separation provided by the magnetic core. The synthesis of these well-dispersed nanoparticles was carried out by firstly a high-temperature hydrolysis for SPIONs followed by a combination of a two-step process of a sol–gel method with calcination.

Another extra feature being studied is the addition of their use at nanostructured electrodes for applications. Advantages of this technique in biosensing, include the possibility of achieving low limits of detection with low cost and simple devices [64]. There are a lot of different nanostructures proposed in the literature and their synthesis depends on the combination of the characteristics needed. For example, Jahanbani [65] described a magnetic bar carbon paste electrode with Fe_3O_4 magnetic nanoparticles and oleic acid for the detection of the antibiotic tetracycline in real samples, such as milk and honey. Nanoparticles were synthesized by a simple co-precipitation method and later surface modified with oleic acid. Gerent et al [66] proposed a magnetite-platinum electrode stabilized with a polymer to electrochemically detect nitrophenols in rain water and human urine. Here, the synergetic effect was due to the high specific area provided by the magnetite nanoparticles plus the catalytic effect produced by those made of platinum. In other work, Liu and colleagues [67] proposed also a modified glassy carbon electrode to detect dopamine, which may cause several neurological diseases. The main advantage of this sensor relied on its ability to determine dopamine even in the presence of uric acid, a biomolecule also electroactive and with an oxidation potential close to dopamine. The synthesis of the nanocomposite was carried out first by a solvothermal method to obtain magnetite functionalized with amine groups onto the surface. Then, palladium atoms were attached through this amine groups by the reduction of Pd^{2+} by ethanol. Lastly, another example is published by Feng et al. [68] who developed a sandwich-type electrochemical immunosensor using oxide core and silica shell with terminal amino groups. Those were covalently bonded to the secondary antibody for detection and to ferrocene, in order to electrochemically quantify carcinoembryonic antigen, a specific bio marker for diagnosis of different cancers, such as liver, colon or breast. In this case, magnetic

nanoparticles were synthesised by a solvothermal reaction.



Figure 2. Schematic illustration of the different dual nanoparticle architectures where the grey ball represents the SPIONs and the yellow one represents the noble metal nanoparticle. From left to right: core-shell and a dumbbell-like nanoparticle while the other two represent the structure of a nanoflower with two and four domains.

Finally, one of the most used and desired characteristics of the nanoparticles is their possibility of easy biofunctionalization, especially in biosensing. For this reason, the synergetic effect possible between noble metals, such as gold (Au) and silver (Ag) and SPIONs has been recently exploited. One of the reasons for this is that thiol groups are considered to have the highest affinity to these metals surfaces [69], allowing biomolecules to attach easily and strongly [70] in which is usually called ‘chemisorption’. However, this is not the single advantageous feature: the optical properties of these metal nanoparticles NPs, especially the large optical field enhancements and intense colours resulting from the strong scattering and absorption of light are also interesting for imaging and sensing. These properties are due to the oscillation of the conduction electrons induced by the incident light field, which is the responsible of what is called Localized Surface Plasmon Resonance (LSPR) [71]. The different structures that make possible to use these characteristics together with the ones present in SPIONs are core/shell structures, nanoflower structures and dumbbell-like structures. However, among them, the core/shell structure (Figure 2) is the most used one and it is normally synthesised by obtaining first the magnetite core and later, using them as seeds for growing of the noble metal shell [72-74]. Kalska-Szostko et al. [75] described a simple methodology to cover the magnetite nanoparticles synthesised before by thermal decomposition acting as seeds in the following procedures to obtain Au@Fe₃O₄ and Ag@Fe₃O₄. In both cases, the nanoparticles obtained had sizes around 10 nm. Also, Xu [76] described a thermal decomposition process of iron oleate to get 10 nm magnetite nanoparticle followed by a reduction of hydrogen tetrachloroaurate hydrate (HAuCl₄·3H₂O) in a chloroform solution of oleylamine. However, they also

used these nanoparticles as seeds for continued growth of Au or Ag layers. Regarding the magnetic moment of the core/shell structure synthesized, they found that as the shell thickness increase there is a decrease in magnetic moment due to the weight contribution from the nonmagnetic Au and Ag. To understand how these features vary it is important to control the junction between the two components. Some interesting studies have been reported on this field [77-79].

Dumbbell like structures are composed by the union of two different nanoparticles: in our case of interest, magnetite and noble metals (Figure 2). This structure offers two distinct surfaces in contrast to the one available at the core shell structure. Yu et al [80] reported a method to obtain Fe_3O_4 from 4 to 20 nm together with Au nanoparticles from 2 to 8 nm by decomposition of iron pentacarbonyl on the surface of the Au nanoparticles followed by oxidation in 1-octadecene solvent. The size, structure, and chemical nature of each part of the dumbbell structure was controlled by regulating the synthetic conditions. Moreover, the polarity of the solvent showed influence on the structure as the use of diphenyl ether resulted in flower-like Au/ Fe_3O_4 nanoparticles. Also, Wang and colleagues [81] described a general approach to obtain these dumbbell like structures but also with other metals such as Pt to exploit another features as its catalytic power. Again, the procedure was seed-mediated and the magnetite nanoparticles epitaxially grown over the noble metal ones.

Lastly, nanoflowers structure is really similar to the previous one, but in this case more than one nanoparticle is attached to the surface of the other one, forming a flower-like shape (Figure 2). Huang et al [82] described the synthesis of Au/ Fe_2O_3 nanoflowers firstly by co-precipitation of the maghemite nanoparticle with an average size of 5 nm. Then, iterative *in situ* gold growth was performed through the reduction of HAuCl_4 by hydroxylamine hydrochloride. Also, Wei et al [83] reported a thermal decomposition process in order to get Au/ Fe_3O_4 nanoflower particles. They studied how size and number of iron oxide domains could be changed by modifying the proportion of the starting materials and the reaction time. The results showed that, as the proportion of the reactants Fe/Au was increased, the Fe_3O_4 domains on the nanoparticles obtained were also higher, and unattached magnetic nanoparticle were not found. When the reaction time was increased from 2 to 5 hours, more dumbbell like structures were synthesised.

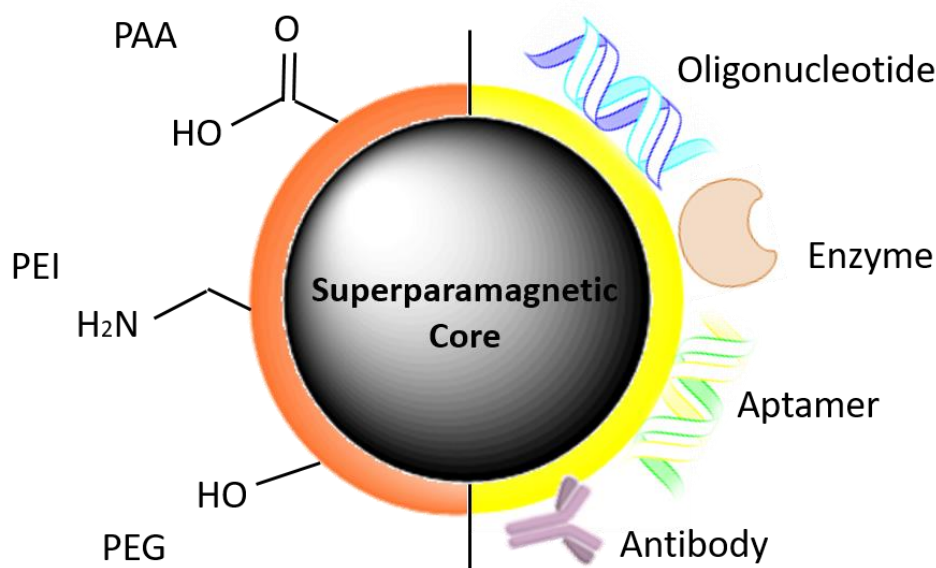


Figure 3. Schematic illustration of the different terminal chemical groups present in some polymers on the left and different biomolecules attached to the surface of SPIONs on the right.

3. Methods for the preparation of (controlled) agglomerates for sensitivity enhancement

One of the most important characteristics of the nanoparticles used for biomedical applications, is the stability of the suspension in water, preventing their agglomeration. Different approaches such as electrostatic or steric stabilisation by polymers have been proposed to achieve this. This also offers the possibility to attach other molecules later if the polymer has the right chemical groups available. Nevertheless, it should be taken into account that a somehow controlled agglomeration of the nanoparticles, especially in nanosensors, could be beneficial whether the signal depends on the quantity of SPIONs, as demonstrated by Wang et al. [84] at a quantitative magnetic labelled lateral flow immunoassays. This means that the higher the amount of magnetic phase present, the higher the signal, and therefore, sensitivity could be greatly enhanced. However, control of this agglomeration is advised since the nanoparticles should keep other properties such as superparamagnetism, stability or functionality for later bioconjugation. In the following sections, we report some ways in which SPIONs could be agglomerated in a controlled manner.

3.1. Polymers

The use of different polymers as functional coverage in SPIONs has been

reported in a lot of studies, as it has been mentioned before. Not only they provide the required steric stabilisation of the nanoparticles but also the terminal chemical groups for subsequent conjugation to biomolecules. Although the ideal coverage of the polymer should render monodispersed nanoparticles, a controlled entrapment of the SPIONs in the polymer chains is also possible.

An agglomeration pathway of SPIONs has been described by Liu et al [85] using poly-L-lysine (PLL). Firstly, they synthesised the nanoparticles by a thermal decomposition method with a dicarboxyl-terminated PEG (HOOC-PEG-COOH) as the particle surface capping agent. This provided carboxylic acid groups available at the surface. Those groups played an important role for the agglomeration by means of cross-linking the individual nanoparticles with the amine groups present at PLL single monomers. The aggregates obtained showed a larger size i.e., the hydrodynamic diameter increased from 47.5 nm to 113.6 nm as the amount of PLL was also increased from none to 1.56×10^{-2} mg. Moreover, coagulation was not observed.

Other approach was reported by Kim and colleagues [86], who described the synthesis of a multifunctional platform for drug delivery. Although in this case they used more than one type of nanoparticle to be agglomerated at a multifunctional composite (with quantum dots), the procedure could be applied to join together just SPIONs. The latter were synthesised by the thermal decomposition method described by Park et al. [43]. The polymer used in this case was poly(D,L-lactic-co-glycolic acid) (PLGA) and the procedure to agglomerate the nanoparticles was an oil-in-water emulsification assisted by sonication, putting together the SPIONs, CdSe/ZnS and the drug. After the evaporation of the organic solvent, the negatively charged surface of the PLGA was adsorbed by electrostatic interactions with the positively charged poly(L-lysine) domain of poly(L-lysine)-poly(ethylene glycol)-folate (PLL-PEG-FOL). This is the polymer that remained at the outer layer of the multinanocomposite and could be used for later functionalization of the agglomerates. Dozens of SPIONs were inside the agglomerates, with a typical size from 7 to 15 nm. This could be varied by the number of the initial Fe_3O_4 present in the reaction mixture with PLGA. Another agglomeration pathway also using PEG derivatives has been described by Bakandritsos et al. [87]. In this case, poly(lactide)-block-poly(ethylene glycol) (PLA-PEG) was used to form a micelle-like structure. The SPIONs inside them were firstly

synthesised also by a thermal decomposition process. The nanoclusters were then obtained by a nanoprecipitation process in tetrahydrofuran (THF) and water under sonication. The mean size of the nanoparticles was 5 nm while the whole nanocomposite showed a diameter of 100 nm.

Finally, Ming et al. [88] have recently described a process to get SPIONs clusters with polydopamine (PDA) by growing shells of this compound around the superparamagnetic Fe_3O_4 through the seeded-emulsion polymerization of dopamine. This process formed a firmly adhering hydrophilic layer on the agglomerates with the advantage of a providing multiple functional groups, ($-\text{NH}_2$, $-\text{COOH}$, $-\text{OH}$) for subsequent biofunctionalisation. Despite the superparamagnetic character kept by the nanoclusters, the saturation magnetisation was compromised because of the broad size distribution and irregular shape of synthesised SPIONs. This drawback could be skipped by a better control of the quality of the magnetic nanoparticles during their synthesis.

3.2. Silica

Another way to get an agglomeration of SPIONs is by means of a uniform silica layer. This outer coating can be easily bioconjugated to molecules, as has already been reported in several studies [89-91]. This process is usually carried out by two different methods. The first one involves an initial ligand exchange with silane molecules such as tetraethoxysilane (TEOS) followed by shell growth and condensation. The second one is done in a reverse microemulsion, where the hydrolysis happens inside the micelle. With this approach, Tadic et al. [92] have reported what they have called an iNANOvativeTMSilica nanoparticle clusters of about 80 nm in size which contain inside several maghemite nanoparticles in the core, and an amorphous silica shell. The SPIONs were approximately 10 nm in size and showed superparamagnetic character even after the agglomeration, whereas the silica shell had a thickness of 15 nm. The maghemite nanoparticles were first synthesised by a co-precipitation method using PAA as capping agent/surfactant and polyvinylpyrrolidone (PVP) as promoter for later silica shell. This approach of agglomeration with a silica shell was also used by Lee et al. [93] but with FePt nanoparticles as the multicore phase. The encapsulation was made by water-in-oil microemulsions and the SiO_2 thickness of the layer could be controlled by the ratio of the reactants. This methodology seems easy to adopt and the nanoclusters obtained presented good dispersibility and

reproducibility, hence it could be transferred to the synthesis of the same structure but with SPIONs as the multicore.

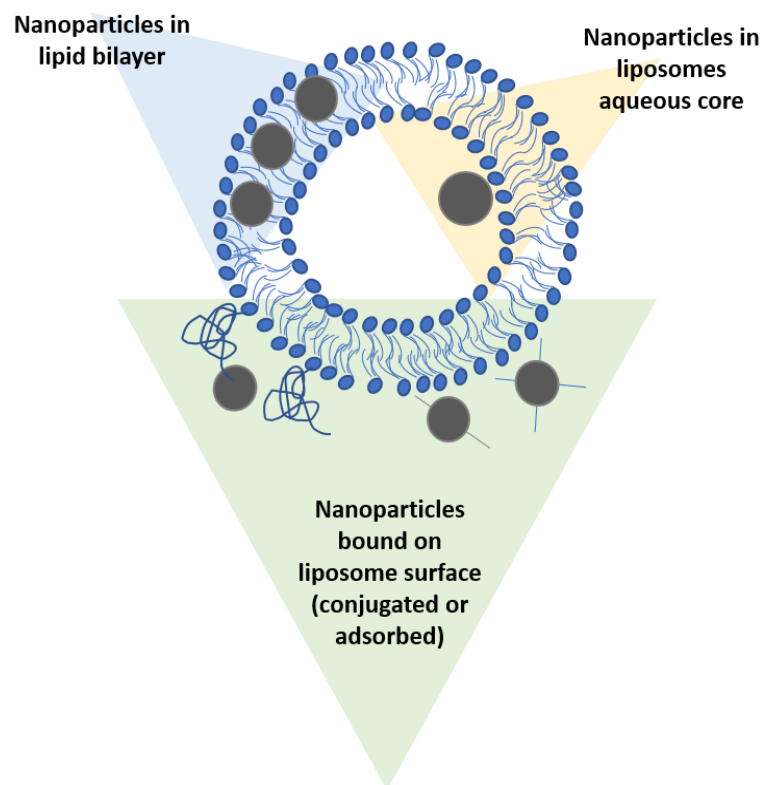


Figure 4. Schematic illustration of the different routes to conjugate SPIONs and liposomes.

3.3. Nanovesicles

Liposomes are vesicles with a membrane which consist of polar head-groups and hydrophobic chains. The polar part is oriented towards the extravascular solution and inner cavity, and the other part forms a lipids bilayer. This kind of structures shows some important advantages such as high surface area, large internal volume, and ability to conjugate bilayer lipids with a variety of biorecognition elements. Due to these properties, liposomes and related vesicles are used to encapsulate different molecules and nanomaterials with interest in multiple fields, such as drug delivery or analysis. Liposomes are versatile structures to encapsulate or bind to SPIONs to form liposomes-nanoparticles hybrids. With this approach, a greater number of magnetic nanoparticles per unit could be reached. This should result on an increase of the magnetic signal at the desired biomedical application. Because of the versatility of the liposomal structure, it is possible to get these hybrids following different routes (Figure 4). For example, hydrophobic SPIONs could be incorporated within lipid bilayer, or hydrophilic SPIONs could be

encapsulated in the liposome inner aqueous core. The establishment of a chemical or physical link between liposomal surface and nanoparticles is another option. Moreover, the surface of liposomes could be modified through the choice of lipids to allow their conjugation to a variety of biorecognition elements [94] for molecular recognition purposes.

Different techniques to encapsulate SPIONs within liposomes can be found in the literature: reverse evaporation [95, 96], extrusion [97], freeze-thawing [98] and sonication [99, 100]. Depending on the operating conditions and concentrations, micelles could be formed and used as nanocarriers. Marina Talelli has encapsulated hydrophobic SPIONs in mPEG-b-p(HPMAm-Lac2)-based polymeric micelles with a size of 150-300 nm. A loading capacity up to 40% was achieved [101]. Du Cheng has prepared two kinds of biodegradable polymeric micelles loaded with non-clustered SPIONs, PEG4.3k-PCL1k-SPIONs and PEG4.3k-PCL7.2k-SPIONs. At room temperature both samples and SPIONs showed superparamagnetic behaviour. For SPIONs the value of saturation magnetization was 64.7 Fe emu/g, and in the others two cases 65.6 and 64.4 Fe emu/g for PEG4.3k-PCL1k-SPIONs and PEG4.3k-PCL7.2k-SPIONs, respectively. The results show that there is not a great loose in magnetization per Fe unit [13]. Alonso and colleagues [102] described also a method based on size exclusion chromatography (SEC) to prepare a monolayer vesicle with SPIONs inside. The maghemite nanoparticles were synthesised by a thermal decomposition method with a mean size of 13 nm and later uniformly distributed at the interior and exterior of the lipid vesicles by freeze-thaw process. The SEC was then used to separate the liposomes with the SPIONs inside, from the free ones in solution. These magnetoliposomes showed a higher hyperthermia efficiency and were detected in low concentrations, showing great opportunities in different bioapplications. Finally, a multifunctional liposome with nitroDOPA-palmityl stabilized SPIONs of 5 nm embedded in its PEGylated membranes was described by Amstad et al [103]. The nanoparticles were obtained by a non-aqueous sol-gel route. Then, liposomes and SPIONs were obtained by extrusion and those not encapsulated were separated from the rest by Sephadex columns. These multifunctional nanostructures represent a promising drug delivery system but also should allow to locate the vesicles using MRI, and possibly, magnetic targeting prior to the release.

3.4. Others

A nanoflower like structure, which has been described before but using different components to form the nanocomposite, could be another way of agglomeration. In this case, the general idea is to grow a flower-like structure solely composed by SPIONs, allowing a more concentrated (or agglomerated) state of the nanoparticles. This methodology has been deeply revised lately by Gavilán and colleagues [104], focusing on some key-parameters for the self-assembly process of the nanoflowers structure and the methodologies used to obtain them. As examples, in a recent study, Thomas et al. [105] described a one-step method to synthesise magnetite nanoparticles with flower-shaped aggregates that can be bond to other molecules in a second stage, due to the presence of amine and carboxylic groups onto their surface. The nanoparticles obtained had sizes between 11 nm and showed superparamagnetic character, with a saturation magnetization of 65 emu/g. In other work presented by Hu and colleagues [106] they reported highly dispersible nanoflower structures of Fe₃O₄ obtained in different media, such as water, phosphate buffer solution (PBS) and cell culture media. These structures were made by thermal decomposition of Fe(acac)₃ in phenyl ether at 260°C using PEG-derivative and oleylamine as surfactants. In this case, nanoflowers of 42, 30 and 19 nm were obtained with superparamagnetic behaviour but with lower saturation magnetisation than the previous method.

4. Conjugation of SPIONs to biomolecules

Once the most suitable SPIONs have been designed for a given application, the next step is to effectively bind them to the biomolecular receptor (bioconjugation). This family of compounds usually comprises proteins, enzymes, DNA or RNA sequences, aptamers, etc (Figure 3). As it has been mentioned before, the polymer that usually stabilises the nanoparticles also carries different chemical groups. Different principles, such as electrostatic, hydrophobic/hydrophilic interactions, Van der Waals forces or covalent bonds, can be used at this step. It is important to take into account that the physical or chemical link should yield nanoparticles still stable in the solution and with the highest possible efficiency, in a way that the functional conformation and the recognition sites are not altered. Here we focus on different forms of attaching these molecules to the synthesised SPIONs, with some examples recently

reported in the literature.

4.1. Streptavidin-Biotin bonds

One of the strongest non-covalent bond known is the (strept)avidin-biotin interaction with an association constant (K_a) of 10^{15} M. Avidin, is a glycoprotein with four identical subunits and a molecular weight of approximately 67 kDa. It was discovered in egg whites. Each of these subunits could be bonded to one molecule of biotin hence each molecule contains a maximum of four possible biotin binding sites (Figure 5). One clearly advantage that make it possible to have a wide spread use is that its structure is stable to a broad range of conditions of temperature, denaturants and pH, showing an isoelectric point (pI) of ~ 10 [107]. Although both avidin and streptavidin bind biotin with very high affinity, avidin shows some disadvantages such as high nonspecific binding which is attributed to the presence of the sugars and high pI. An alternative to overcome this problem is the use of streptavidin or deglycosylated avidins(neutravidin), which still preserve the same biotin-binding properties. Streptavidin is more expensive to produce but has lower nonspecific binding and a near to neutral pH.

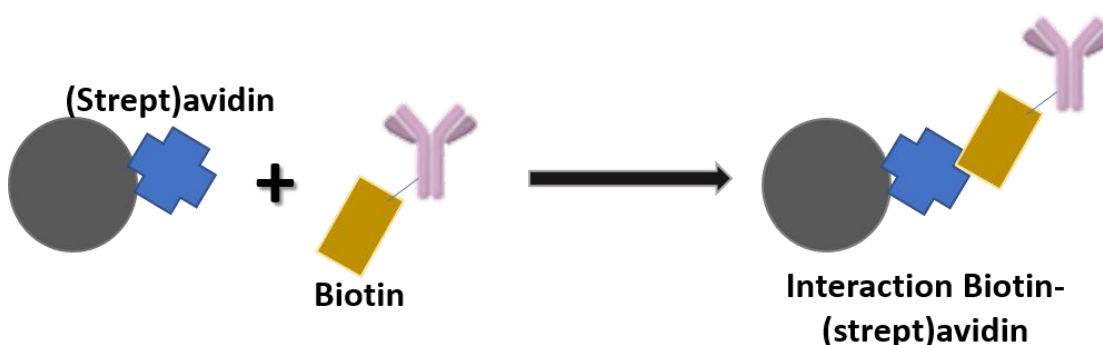


Figure 5. Schematic illustration of the interaction biotin-(strept)avidin.

The extremely high affinity is the result of the combination of several types of intermolecular interactions, such as hydrogen bonds, hydrophobic and Van der Waals forces. However, this union is not free of disadvantages and the presence of nonspecific binding in many applications due to the high content of carbohydrates in the (strep)avidin structure was reported [108, 109] until researchers did overcome this issue using recombinant or deglycosylating structures without affecting the high affinity between the two molecules. Biotin, however, is a relatively simple water-soluble organic compound, also known as vitamin B7 or vitamin H, and is a coenzyme for several carboxylase enzymes

present in many species including humans. An extensive range of commercial modification reagents, such as maleimide or NHS ester, are available to add a functional biotin group to proteins, antibodies, nucleic acids and other molecules of interest in a process called biotinylation. The strength and the high affinity of (strept)avidin-biotin interaction have made it a useful tool in bioconjugation and it is a common approach to attach biotinylated biomolecules onto the surface of SPIONs.

The specificity of biotin-(strept)avidin interactions provides the basis for developing assay systems to detect and quantify several biochemical targets through immunoassays. There are several publications which use this affinity to establish bonds between biotinylated molecules (DNA, antibodies...) and (strept)avidin-functionalized SPIONs. For example, Kouassi et al. [110] studied how to conjugate different kind of magnetic nanoparticles ($\text{Fe}_3\text{O}_4\text{-APTMS}$, $\text{Fe}_3\text{O}_4\text{-LAA}$ and $\text{Fe}_3\text{O}_4\text{@Au}$) to single stranded biotinylated oligonucleotides in order to develop a DNA sensor. In order to get SPIONs with a streptavidin coverage, they had to follow a first chemical carbodiimide activation. Therefore, the bond is established between streptavidin-coated nanoparticles and single-stranded biotinylated oligonucleotides. More recently, we have reported a magnetic sensor based on lateral flow immunoassay [111] to detect Prostate Specific Antigen (PSA) by using this strategy. In this case, SPIONs were coated with neutravidin using the 1-ethyl-3-[3-dimethylpropyl]carbodiimide (EDC)/N-hydroxy-sulfosuccinimide (sulfo-NHS) chemistry, for their subsequent conjugation to biotinylated antibodies against PSA.

4.2. Covalent Chemistry

A covalent bond could be considered as a direct link between the nanoparticle surfaces and other biomolecules, where an electron pair is shared between two atoms (Figure 6). For this purpose, some chemical groups, such as amines ($-\text{NH}_2$), carboxylate ($-\text{COOH}$) and hydroxyl ($-\text{OH}$) residues at the biomolecules or nanoparticle surface, could be activated by means of commercial products through relatively simple protocols.

Carbodiimides are one of the reagents most frequently used. They are known as zero-length crosslinkers since the resulting bond contains no additional atoms, with no additional spacers. These kind of crosslinkers are used to mediate the formation of amide linkages between carboxylates

and amines or phosphoramidate linkages between phosphates and amines. There are two different types of carbodiimides: water-soluble and water-insoluble. Those water-soluble are the most used because most of the biomolecules are soluble in aqueous buffer solutions. EDC (or EDAC; 1-ethyl-3-(3-dimethylaminopropyl) carbodiimide hydrochloride) is the most popular water-soluble carbodiimide used for conjugating biological molecules containing carboxylates and amines groups. This compound could react with carboxylic acids to form a highly reactive intermediate which can react with a nucleophile, such as amine, to form an amide bond. The main disadvantage of this method is the competing reactions, being the hydrolysis in aqueous solutions the most frequent. To overcome the problem, EDC is used with sulfo-NHS, increasing the solubility and stability of the active intermediate. Therefore, EDC/sulfo-NHS coupled reactions are highly efficient and usually increase the yield of conjugation significantly over that obtainable solely with EDC (Figure 7).

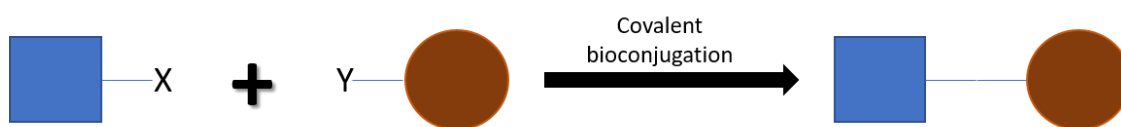


Figure 6. Schematic illustration of the process of covalent bioconjugation.

One of the most popular families of biomolecules conjugated to SPIONs for biosensing applications are the immunoglobulins or antibodies. These special proteins have a complex structure, usually a Y-like shape (Figure 8), with two identical domains for antigen recognition (Fab-fragments for antigen binding) and other two identical domains with effector functions (Fc-crystallisable fragment). The complexity of these proteins requires knowledge of which functional groups are located in their structure and where they are placed. This is relevant to avoid steric hindrance between antigen, antibodies, and nanoparticles.

The EDC/NHS chemistry is widely used to attach antibodies to the surface of polymer/silica/noble metals coated SPIONs. The major advantage of this method could be the combination of simplicity with the stability that it confers to the bond. However, this is usually inefficient, requiring an excess of the antibody. Besides, orientation is usually not controlled [112]. Amine and carboxyl groups are abundant in the antibody structure, usually at its surface, and therefore the site-directed covalent attachment is frequently difficult. Zhang et al. [113] described a

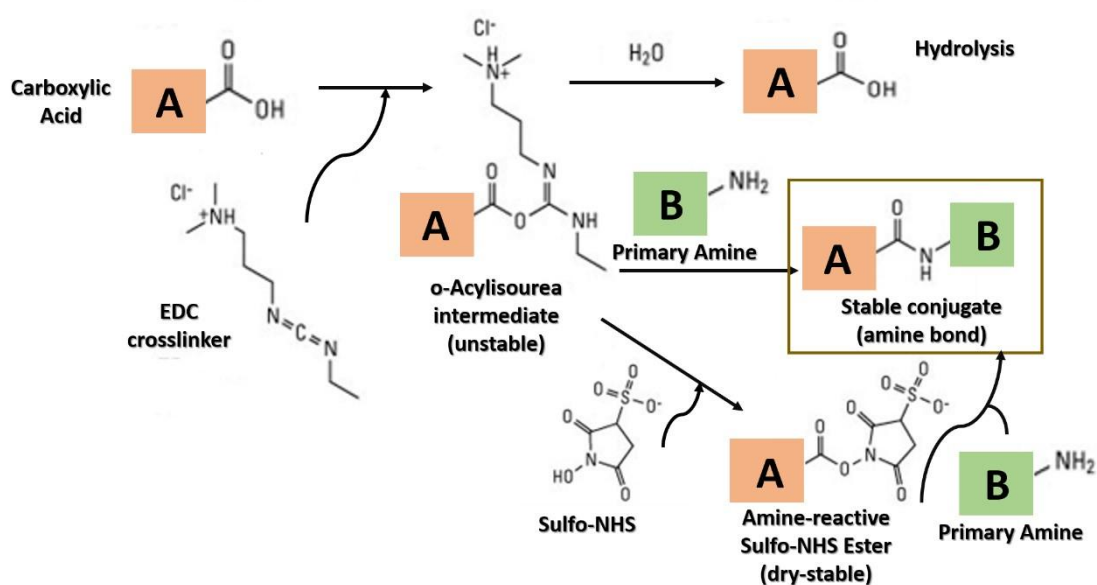


Figure 7. Reaction scheme of sulfo-NHS plus EDC crosslinking chemistry.

cardiac troponin (cTnI) immunomagnetic sensor using meso-2,3-dimercaptosuccinic acid (DMSA) coated SPIONs. The outer layer of the nanoparticles has unbound carboxyl groups (–COOH) and thiol groups (–SH) that were used to graft the anti-human cTnI antibodies using the linker of EDC. Another work published by Yan et al. [114] also used this approach to covalently bind anti *Vibrio parahaemolyticus* antibodies to SPIONs synthesised by a solvothermal reaction. In this case, the carboxylic groups present on the surface of the silica coating were activated by EDC/NHS chemistry to be covalently attached to the antibodies used to the detection of the pathogenic bacteria in a LFIA.

Another target for immobilisation is the Fc region, which is glycosylated and hence, the carbohydrates present could be used to anchor the antibody to the SPIONs without damaging the antigen binding domains in Fab chains. Puertas et al. [115] compared the immobilisation on magnetic nanoparticles by a EDC/NHS strategy (random immobilisation) with the linkage via the polysaccharidic region (oriented immobilisation) for the development of a LFIA to detect the human chorionic gonadotropin (hCG) hormone. Their results showed that the latter improved the recognition of the test, increasing its sensitivity by one order of magnitude. Using also this approach, Lin et al [116] reported a simple method to effective site-specific and self-oriented immobilisation of antiserum antibody on magnetic nanoparticles through a boronate bond formation within the carbohydrates present on the long chains. This new strategy

yielded enhanced activity because of the optimal exposure of the antigen binding sites at the immunoassay. These methods could be applied to the bioconjugation of other proteins for different tests and immunoassay formats.

Although antibodies are very popular biomolecules used for molecular recognition applications, enzymes and DNA/RNA strands or aptamers are also used. Enzymes are molecules that act as biological catalysts and are involved in many different metabolic processes. As an example, tissue plasminogen activator (tPA) is a natural enzyme used as drug for ischemic stroke due to its ability to dissolve clots. Friedrich et al. [117] have recently reported the covalent conjugation of this enzyme using an amino-reactive activated ester reaction with polyacrylic acid-co-maleic acid (PAM)-coated SPIONs via EDC/NHS chemistry. Also, they compared this way of bonding the molecules with electrostatically adsorbed tPA, showing a significantly improved attachment with the covalent approach rather than the adsorptive one.

Aptamers are artificial receptors based on short and synthetic single DNA/RNA oligonucleotides chains or peptide molecules which bind to a specific target molecule, such as proteins. This kind of molecules could be easily obtained and could even replace antibodies due to its superior characteristics, i.e., aptamers are smaller size, can be easily modified and cheaper to produce [118-120]. Wang and colleagues [121] reported the process to attach an aptamer against prostatic cancer cells using a thermally cross-linked SPION (TCL-SPION) for both therapy and imaging applications. The conjugation was performed via the conventional EDC/NHS chemistry described before between the carboxylated nanoparticles and amine terminated aptamer.

4.3. Others

Thiol bonds could be established with Au or Ag coated SPIONS. As it was mentioned before, this is one of the strongest unions and it has been used in the conjugation of gold nanoparticles in imaging and biosensing because of its simplicity and effectiveness. In an Au@Fe₃O₄ core-shell structure, Xia et al. [4] developed a lateral flow immunoassay (LFIA) to detect *Salmonella choleraesuis* in milk. The procedure to attach the antibody to the Au surface was as simple as mixing them, without the use of other reactants or more complex chemical reactions. Another LFIA

has been reported by Oliveira and colleagues [70] to detect extracellular vesicles using a thiolated spacer as crosslinker, to anchor the detection antibody to colloidal gold.

Finally, another approach that has been reported in the literature is the use of protein A, protein G or a combination of both. These proteins are able to specifically bind to the Fc chain of the antibodies and therefore, they can leave the Fab binding region towards the outer space of the nanoparticle, free to recognise the target analyte. In a work cited before,

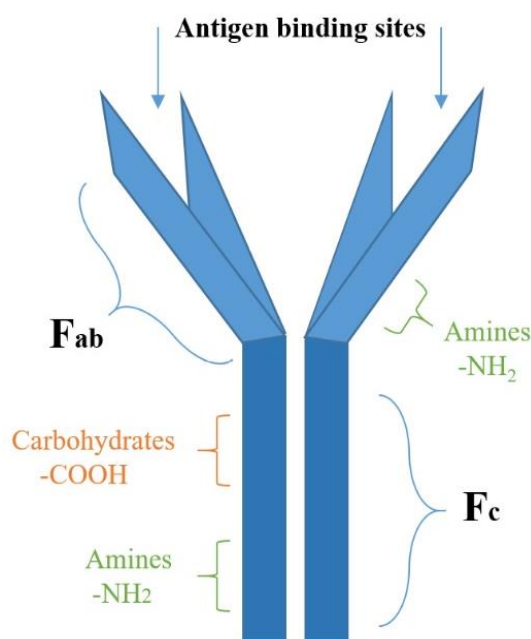


Figure 8. Schematic illustration of an antibody with its usual Y-shape, where two identical chains form the Fab and two identical chains the Fc region. The antigen binding sites, and the residual chemical groups are also specified.

Lin et al. [116] also compared the efficiency of their new proposed boronate bond with a protein G orientation approach at magnetite nanoparticles. Although the protein G binding showed great results, some dissociation because of the non-covalent nature of the bond could lead to a decrease in the efficiency in comparison with the boronate bond. This approach is also reported in other sensor with nonmagnetic nanoparticles. For example, Chung et al [122] reported the orientation of the antibody a combination of the union biotin-avidine, described previously, and protein A for a Surface Plasmon Resonance (SPR) gold sensor to detect carcinoembryonic antigen (CA). By using NeutrAvidin–protein A complex together with the biotinylated surface and a sandwich assay for signal amplification, the sensitivity was increased 1.5 times for

CEA detection. This approach was also used for SPR sensing of human growth hormone [123]. This study focused on the comparison of the attachment of antibodies onto the surface by three different ways: random covalent immobilization as a reference technique in contrast to site-directed protein G and protein G mediated stabilized by a chemical cross-linking to avoid dissociation. These last two approaches showed an enhancement of the analytical signal by a factor of 2.6 and 3.5 times respectively.

5. SWOT analysis

A SWOT analysis is normally useful as a tool where the strengths, weaknesses, opportunities and threats of a product or process are gathered together. Here, we have applied this method for the first time to the SPIONs synthesis routes, with the purpose of highlighting their advantages and limitations towards the subsequent biofunctionalisation for molecular recognition applications. The summary can be found in Table 1.

The synthesis of SPIONs is a complex process due to all the properties that must be simultaneously optimized, such as particle size and shape, size distribution, surface chemistry of the particles and magnetic properties. For this reason, it is difficult to develop standards protocol to get reproducibility using the same or different methods [124]. Moreover, stable and reproducible analysis methods [125] are also needed to characterise the SPIONs which will allow the rapid, agile and ease obtaining of their properties.

The SWOT analysis has been carried out for the different routes of synthesis of SPIONs and their agglomeration pathways previously cited in this paper, towards their latter functionalisation with different molecules for biomolecular recognition applications.

Table 1. Results of the SWOT analysis applied to the different synthesis routes of SPIONs and their possible agglomeration discussed before towards their biofunctionalisation for molecular recognition applications.

SYNTHESIS ROUTE	STRENGTHS	WEAKNESSES	OPPORTUNITIES	THREATS
CO-PRECIPITATION	<ul style="list-style-type: none"> - Easy - Economic equipment and reagents - Polymer coating in a single-step synthesis 	<ul style="list-style-type: none"> - Wide size distribution - Limited microstructural characteristics 	<ul style="list-style-type: none"> - Obtaining large quantities (scaling-up) - <i>In-situ</i> size selection process 	<ul style="list-style-type: none"> - Scarce control of all the parameters that influence the process
THERMAL DECOMPOSITION	<ul style="list-style-type: none"> - High microstructural properties - Narrow size distribution - Good control of mean diameter 	<ul style="list-style-type: none"> - Expensive and toxic reagents - Long reaction times - Hydrophobic environment: necessity to a ligand exchange step. - Small amount of product obtained 	<ul style="list-style-type: none"> - Substitution of organic solvents by PEG (polyol method) avoiding ligand exchange process 	<ul style="list-style-type: none"> - Little possibility to scale-up and standardization
MICROEMULSION	<ul style="list-style-type: none"> - Easy and not expensive - Narrow size distribution 	<ul style="list-style-type: none"> - Agglomeration - Poor crystallization - Large amounts of solvents needed. - Low production yield 	<ul style="list-style-type: none"> - Simple equipment 	<ul style="list-style-type: none"> - Little possibility to scaling-up and standardization - Difficult to develop green protocols
MICROFLUIDIC SYNTHESIS	<ul style="list-style-type: none"> - Extreme control of parameters of the reactions, such as temperature, time, reagents concentration. - Good control over size - High quality SPIONs obtained - Automatic process 	<ul style="list-style-type: none"> - Scarce reports yet - Necessity to optimize the development of microfluidic devices to get the required parameters 	<ul style="list-style-type: none"> - Possibility to design multistep channel reactor for additional steps, such as the polymer coating 	<ul style="list-style-type: none"> - Limitation in equipment development and scale-up and standardization
DUAL NANOPARTICLES	<ul style="list-style-type: none"> - Combination of several properties 	<ul style="list-style-type: none"> - Properties could be affected by the combination with others 	<ul style="list-style-type: none"> - Multifunctional nanocomposites 	<ul style="list-style-type: none"> - Multistep process - Optimization of the properties at the same time for both nanomaterials used

AGGLOMERATION ROUTES	STRENGTHS	WEAKNESSES	OPPORTUNITIES	THREATS
POLYMERS	<ul style="list-style-type: none"> - Readily available for biorecognition protocols due to the specific terminal groups 	<ul style="list-style-type: none"> - Long protocols - Efficiency of the reactions involved 	<ul style="list-style-type: none"> - Large choice of polymers 	<ul style="list-style-type: none"> - Control of the agglomeration degree
SILICA	<ul style="list-style-type: none"> - Very well -known silanol chemistry - Easy bioconjugation - Biocompatibility 	<ul style="list-style-type: none"> - Control of the thickness of the silica layer - Possibility of magnetic properties shielding 	<ul style="list-style-type: none"> - Multifunctional nanocomposites 	<ul style="list-style-type: none"> - Control of the number of nanoparticles inside the silica shell
NANOVESICLES	<ul style="list-style-type: none"> - Easy procedure - Large choice of membrane components 	<ul style="list-style-type: none"> - Possibility of shielding of magnetic properties - Low efficiency of encapsulation - Stability 	<ul style="list-style-type: none"> - Multifunctional nanocomposites - Possibility to encapsulate hydrophobic nanoparticles avoiding ligand exchange processes 	<ul style="list-style-type: none"> - Control of polydispersity of the agglomerates

Thermal decomposition and microfluidic synthesis were found the most appropriate methods to synthesise SPIONs to get the highest control over fundamental properties, such as size distribution and microstructural properties. However, weaknesses for thermal decomposition include the usually toxic and expensive reactants, the low amount of nanoparticles obtained and especially the necessity to add an extra step to transform hydrophobic materials to hydrophilic ones. On the other hand, most of this drawbacks could be avoided by a light modification of the process in what is known as polyol method, where less problematic chemical are used and PEG substitution make the resultant nanocomposites amphiphilic, eliminating the ligand exchange process while conserving the good microstructural properties [126]. Regarding the microfluidic systems, there are still scarce reports using this technology, and hence a huge effort has to be done with the aim of developing the microfluidic channels and optimising the parameters involved. Microemulsion offers also good opportunities due to their easy and non-expensive procedure. Nevertheless, the low yield and high amount of solvents needed as well as the poor microstructural properties of the nanoparticles obtained limit their application to the obtaining of optimized SPIONs for subsequent functionalisation. With all of this, co-precipitation routes seem to be the most adequate methodology to develop ready-as-synthesised SPIONs for molecular recognition application. This approach is easy and economical and offers the possibility to cover the nanoparticles directly in a single step process with a multitude of different polymers, with different terminal chemical groups readily available. However, the parameters that influence these reactions should be carefully controlled, especially as the procedure is scaled up. The combination of different and interesting properties through the synthesis of dual nanoparticles makes the latter especially fascinating. Despite all, their use is still limited due to the necessity to optimize all variables at the same time. This includes the interactions between them that could have a beneficial or detrimental effect [127-129].

Different agglomeration routes have been discussed previously as sensitivity enhancement strategies. All of them show the control of the agglomeration and the polydispersity of the agglomerates obtained as limitations. The entrapment of the SPIONs onto polymers seems to be the most versatile, offering the possibility to obtain a lot of different terminal chemical groups for bioconjugation protocols. Silica is also a good option due to its biocompatibility for in vivo applications and the very well-known silanol chemistry that makes the nanocomposites synthesised also readily available for subsequent uses. Yet, the possible shielding of the magnetic properties by

the silica layer must be taken into account even considering the difficulty of keeping its thickness under control. Finally, despite the low efficiency still reported in the encapsulation of the SPIONs by means of nanovesicles, long protocols due to ligand exchange process could be avoided with this method, making it also a promising strategy for biorecognition applications.

6. Conclusions

In this review the information related to the main synthesis and biofunctionalisation methods for SPIONs reported in the literature has been analysed. Focus has been put on the relevant properties for biorecognition applications, such as biosensors, hyperthermia or drug delivery. The discussion includes some of the most studied routes such as co-precipitation, thermal decomposition, microemulsion and microfluidic synthesis together with the novel trends towards the production of dual composite nanoparticles that combine interesting features of their components. The controlled agglomeration of these nanostructures by means of different agents, such as polymers, silica or nanovesicles, is extremely relevant as a way to enhance sensitivity. The SWOT analysis indicates that the best control of the particle size distribution and microstructural characteristics is achieved by thermal decomposition or microfluidic methods, but co-precipitation is more suitable for large-scale synthesis. As sensitivity enhancement, polymeric agglomerates are very versatile, whereas silanol chemistry appears as a suitable option for multifunctional nanoparticles. Encapsulation of SPIONs in nanovesicles, in turn, seems less efficient, but with possibilities to simplify the protocols by avoiding ligand exchange steps. The interest of these methods was discussed with a view to attach the bioreceptors to the SPIONs surface by means of affinity bonds, (such as streptavidin-biotin), or carbodiimide chemistry.

Acknowledgments

This study was financed by the Consejería de Economía y Empleo del Principado de Asturias (Plan de Ciencia, Tecnología e Innovación 2013-2017), under the Grant GRUPIN14-022 and GRUPIN14-037. Financial support from the Instituto Universitario de Tecnología Industrial de Asturias (IUTA (Gijón Council)) under the grants SV-14-GIJON-1-10 and SV-15-GIJON-1-14, and from the European Regional Development Fund (ERDF) is gratefully acknowledged

References

1. Cornell, R.M. and U. Schwertmann, Introduction to the Iron Oxides, in The Iron Oxides. 2004, Wiley-VCH Verlag GmbH & Co. KGaA. p. 1-7.
2. Sharifi, I., H. Shokrollahi, and S. Amiri, Ferrite-based magnetic nanofluids used in hyperthermia applications. *Journal of Magnetism and Magnetic Materials*, 2012. 324(6): p. 903-915.
3. Kaushik, A., R. Khan, P.R. Solanki, P. Pandey, J. Alam, S. Ahmad, and B.D. Malhotra, Iron oxide nanoparticles–chitosan composite based glucose biosensor. *Biosensors and Bioelectronics*, 2008. 24(4): p. 676-683.
4. Xia, S., Z. Yu, D. Liu, C. Xu, and W. Lai, Developing a novel immunochromatographic test strip with gold magnetic bifunctional nanobeads (GMBN) for efficient detection of *Salmonella choleraesuis* in milk. *Food Control*, 2016. 59: p. 507-512.
5. Nemati, Z., R. Das, J. Alonso, E. Clements, M.H. Phan, and H. Srikanth, Iron Oxide Nanospheres and Nanocubes for Magnetic Hyperthermia Therapy: A Comparative Study. *Journal of Electronic Materials*, 2017. 46(6): p. 3764-3769.
6. Latorre, M. and C. Rinaldi, Applications of magnetic nanoparticles in medicine: magnetic fluid hyperthermia. *P R Health Sci J*, 2009. 28(3): p. 227-38.
7. Espinosa, A., R. Di Corato, J. Kolosnjaj-Tabi, P. Flaud, T. Pellegrino, and C. Wilhelm, Duality of Iron Oxide Nanoparticles in Cancer Therapy: Amplification of Heating Efficiency by Magnetic Hyperthermia and Photothermal Bimodal Treatment. *ACS Nano*, 2016. 10(2): p. 2436-2446.
8. Vegerhof, A., M. Motei, A. Rudinzky, D. Malka, R. Popovtzer, and Z. Zalevsky, Thermal therapy with magnetic nanoparticles for cell destruction. *Biomedical Optics Express*, 2016. 7(11): p. 4581-4594.
9. Guo, S., D. Li, L. Zhang, J. Li, and E. Wang, Monodisperse mesoporous superparamagnetic single-crystal magnetite nanoparticles for drug delivery. *Biomaterials*, 2009. 30(10): p. 1881-1889.
10. Salem, M., Y. Xia, A. Allan, S. Rohani, and E.R. Gillies, Curcumin-loaded, folic acid-functionalized magnetite particles for targeted drug delivery. *RSC Advances*, 2015. 5(47): p. 37521-37532.

11. Bloemen, M., C. Denis, M. Peeters, L. De Meester, A. Gils, N. Geukens, and T. Verbiest, Antibody-modified iron oxide nanoparticles for efficient magnetic isolation and flow cytometric determination of *L. pneumophila*. *Microchimica Acta*, 2015. 182(7): p. 1439-1446.
12. Xu, H., Z.P. Aguilar, L. Yang, M. Kuang, H. Duan, Y. Xiong, H. Wei, and A. Wang, Antibody conjugated magnetic iron oxide nanoparticles for cancer cell separation in fresh whole blood. *Biomaterials*, 2011. 32(36): p. 9758-9765.
13. Cheng, D., G. Hong, W. Wang, R. Yuan, H. Ai, J. Shen, B. Liang, J. Gao, and X. Shuai, Nonclustered magnetite nanoparticle encapsulated biodegradable polymeric micelles with enhanced properties for in vivo tumor imaging. *Journal of Materials Chemistry*, 2011. 21(13): p. 4796-4804.
14. Chung, H.J., H. Lee, K.H. Bae, Y. Lee, J. Park, S.-W. Cho, J.Y. Hwang, H. Park, R. Langer, D. Anderson, and T.G. Park, Facile Synthetic Route for Surface-Functionalized Magnetic Nanoparticles: Cell Labeling and Magnetic Resonance Imaging Studies. *ACS Nano*, 2011. 5(6): p. 4329-4336.
15. Du, Y., P.T. Lai, C.H. Leung, and P.W.T. Pong, Design of Superparamagnetic Nanoparticles for Magnetic Particle Imaging (MPI). *International Journal of Molecular Sciences*, 2013. 14(9): p. 18682-18710.
16. Ferguson, R.M., A.P. Khandhar, and K.M. Krishnan, Tracer design for magnetic particle imaging (invited). *Journal of Applied Physics*, 2012. 111(7): p. 07B318-07B318-5.
17. Colombo, M., S. Carregal-Romero, M.F. Casula, L. Gutierrez, M.P. Morales, I.B. Bohm, J.T. Heverhagen, D. Prosperi, and W.J. Parak, Biological applications of magnetic nanoparticles. *Chemical Society Reviews*, 2012. 41(11): p. 4306-4334.
18. Battle, X. and A. Labarta, Finite-size effects in fine particles: magnetic and transport properties. *Journal of Physics D: Applied Physics*, 2002. 35(6): p. R15-R42.
19. Massart, R., Preparation of aqueous magnetic liquids in alkaline and acidic media. *IEEE Transactions on Magnetism*, 1981. 17(2): p. 1247-1248.

20. Sugimoto, T. and E. Matijević, Formation of uniform spherical magnetite particles by crystallization from ferrous hydroxide gels. *Journal of Colloid and Interface Science*, 1980. 74(1): p. 227-243.
21. Vayssières, L., C. Chanéac, E. Tronc, and J.P. Jolivet, Size Tailoring of Magnetite Particles Formed by Aqueous Precipitation: An Example of Thermodynamic Stability of Nanometric Oxide Particles. *Journal of Colloid and Interface Science*, 1998. 205(2): p. 205-212.
22. Daoush, W.M., Co-Precipitation and Magnetic Properties of Magnetite Nanoparticles for Potential Biomedical Applications. *Journal of Nanomedicine Research*, 2017. 5(3).
23. Jolivet, J.P., L. Vayssieres, C. Chaneac, and E. Tronc, Precipitation of Spinel Iron Oxide : Nanoparticle Size Control. *MRS Proceedings*, 2011. 432.
24. Petcharoen, K. and A. Sirivat, Synthesis and characterization of magnetite nanoparticles via the chemical co-precipitation method. *Materials Science and Engineering: B*, 2012. 177(5): p. 421-427.
25. Gnanaprakash, G., S. Mahadevan, T. Jayakumar, P. Kalyanasundaram, J. Philip, and B. Raj, Effect of initial pH and temperature of iron salt solutions on formation of magnetite nanoparticles. *Materials Chemistry and Physics*, 2007. 103(1): p. 168-175.
26. Valenzuela, R., M.C. Fuentes, C. Parra, J. Baeza, N. Duran, S.K. Sharma, M. Knobel, and J. Freer, Influence of stirring velocity on the synthesis of magnetite nanoparticles (Fe_3O_4) by the co-precipitation method. *Journal of Alloys and Compounds*, 2009. 488(1): p. 227-231.
27. Iida, H., K. Takayanagi, T. Nakanishi, and T. Osaka, Synthesis of Fe_3O_4 nanoparticles with various sizes and magnetic properties by controlled hydrolysis. *Journal of Colloid and Interface Science*, 2007. 314(1): p. 274-280.
28. Ja Young, P., D. Patel, L. Gang Ho, W. Seungtae, and C. Yongmin, Highly water-dispersible PEG surface modified ultra small superparamagnetic iron oxide nanoparticles useful for target-specific biomedical applications. *Nanotechnology*, 2008. 19(36): p. 365603.
29. Kim, M.J., Y.H. Choa, D.H. Kim, and K.H. Kim, Magnetic Behaviors of Surface Modified Superparamagnetic Magnetite Nanoparticles. *IEEE Transactions on Magnetics*, 2009. 45(6): p. 2446-2449.

30. Hajdú, A., M. Szekeres, I.Y. Tóth, R.A. Bauer, J. Mihály, I. Zupkó, and E. Tombácz, Enhanced stability of polyacrylate-coated magnetite nanoparticles in biorelevant media. *Colloids and Surfaces B: Biointerfaces*, 2012. 94: p. 242-249.
31. McBain, S.C., H.H.P. Yiu, A. El Haj, and J. Dobson, Polyethyleneimine functionalized iron oxide nanoparticles as agents for DNA delivery and transfection. *Journal of Materials Chemistry*, 2007. 17(24): p. 2561-2565.
32. Yin, M., A. Willis, F. Redl, N.J. Turro, and S.P. O'Brien, Influence of Capping Groups on the Synthesis of γ -Fe₂O₃ Nanocrystals. *Journal of Materials Research*, 2011. 19(4): p. 1208-1215.
33. Patsula, V., L. Kosinová, M. Lovrić, L. Ferhatovic Hamzić, M. Rabyk, R. Konefal, A. Paruzel, M. Šlouf, V. Herynek, S. Gajović, and D. Horák, Superparamagnetic Fe₃O₄ Nanoparticles: Synthesis by Thermal Decomposition of Iron(III) Glucuronate and Application in Magnetic Resonance Imaging. *ACS Applied Materials & Interfaces*, 2016. 8(11): p. 7238-7247.
34. Sun, S. and H. Zeng, Size-Controlled Synthesis of Magnetite Nanoparticles. *Journal of the American Chemical Society*, 2002. 124(28): p. 8204-8205.
35. Salas, G., C. Casado, F.J. Teran, R. Miranda, C.J. Serna, and M.P. Morales, Controlled synthesis of uniform magnetite nanocrystals with high-quality properties for biomedical applications. *Journal of Materials Chemistry*, 2012. 22(39): p. 21065-21075.
36. Sun, S., H. Zeng, D.B. Robinson, S. Raoux, P.M. Rice, S.X. Wang, and G. Li, Monodisperse MFe₂O₄ (M = Fe, Co, Mn) Nanoparticles. *Journal of the American Chemical Society*, 2004. 126(1): p. 273-279.
37. Park, J., E. Lee, N.-M. Hwang, M. Kang, S.C. Kim, Y. Hwang, J.-G. Park, H.-J. Noh, J.-Y. Kim, J.-H. Park, and T. Hyeon, One-Nanometer-Scale Size-Controlled Synthesis of Monodisperse Magnetic Iron Oxide Nanoparticles. *Angewandte Chemie International Edition*, 2005. 44(19): p. 2872-2877.
38. Guardia, P., B. Batlle-Brugal, A.G. Roca, O. Iglesias, M.P. Morales, C.J. Serna, A. Labarta, and X. Batlle, Surfactant effects in magnetite nanoparticles of controlled size. *Journal of Magnetism and Magnetic Materials*, 2007. 316(2): p. e756-e759.

39. Haracz, S., M. Hilgendorff, J.D. Rybka, and M. Giersig, Effect of surfactant for magnetic properties of iron oxide nanoparticles. *Nuclear Instruments and Methods in Physics Research Section B: Beam Interactions with Materials and Atoms*, 2015. 364: p. 120-126.
40. MAITY, D., J. DING, and J.-M. XUE, Synthesis of magnetite nanoparticles by thermal decomposition: time, temperature, surfactant and solvent effects. *Functional Materials Letters*, 2008. 01(03): p. 189-193.
41. Chin, S.F., S.C. Pang, and C.H. Tan, Green synthesis of magnetite nanoparticles (via thermal decomposition method) with controllable size and shape. *Journal of Materials and Environmental Science*, 2011. 2(3): p. 299 - 302.
42. Unni, M., A.M. Uhl, S. Savliwala, B.H. Savitzky, R. Dhavalikar, N. Garraud, D.P. Arnold, L.F. Kourkoutis, J.S. Andrew, and C. Rinaldi, Thermal Decomposition Synthesis of Iron Oxide Nanoparticles with Diminished Magnetic Dead Layer by Controlled Addition of Oxygen. *ACS Nano*, 2017. 11(2): p. 2284-2303.
43. Park, J., K. An, Y. Hwang, J.-G. Park, H.-J. Noh, J.-Y. Kim, J.-H. Park, N.-M. Hwang, and T. Hyeon, Ultra-large-scale syntheses of monodisperse nanocrystals. *Nat Mater*, 2004. 3(12): p. 891-895.
44. Berti, I.O.P.D., M.V. Cagnoli, G. Pecchi, J.L. Alessandrini, S.J. Stewart, J.F. Bengoa, and S.G. Marchetti, Alternative low-cost approach to the synthesis of magnetic iron oxide nanoparticles by thermal decomposition of organic precursors. *Nanotechnology*, 2013. 24(17): p. 175601.
45. Liang, Y.J., Y. Zhang, Z. Guo, J. Xie, T. Bai, J. Zou, and N. Gu, Ultrafast Preparation of Monodisperse Fe₃O₄ Nanoparticles by Microwave-Assisted Thermal Decomposition. *Chemistry*, 2016. 22(33): p. 11807-15.
46. Zhang, T., J. Ge, Y. Hu, and Y. Yin, A General Approach for Transferring Hydrophobic Nanocrystals into Water. *Nano Letters*, 2007. 7(10): p. 3203-3207.
47. Wei, H., N. Insin, J. Lee, H.-S. Han, J.M. Cordero, W. Liu, and M.G. Bawendi, Compact Zwitterion-Coated Iron Oxide Nanoparticles for Biological Applications. *Nano Letters*, 2012. 12(1): p. 22-25.

48. Korpany, K.V., C. Mottillo, J. Bachelder, S.N. Cross, P. Dong, S. Trudel, T. Friscic, and A.S. Blum, One-step ligand exchange and switching from hydrophobic to water-stable hydrophilic superparamagnetic iron oxide nanoparticles by mechanochemical milling. *Chemical Communications*, 2016. 52(14): p. 3054-3057.
49. Davis, K., B. Qi, M. Witmer, C.L. Kitchens, B.A. Powell, and O.T. Mefford, Quantitative Measurement of Ligand Exchange on Iron Oxides via Radiolabeled Oleic Acid. *Langmuir*, 2014. 30(36): p. 10918-10925.
50. Palma, S.I.C.J., M. Marciello, A. Carvalho, S. Veintemillas-Verdaguer, M.d.P. Morales, and A.C.A. Roque, Effects of phase transfer ligands on monodisperse iron oxide magnetic nanoparticles. *Journal of Colloid and Interface Science*, 2015. 437: p. 147-155.
51. Qin, J., S. Laurent, Y.S. Jo, A. Roch, M. Mikhaylova, Z.M. Bhujwala, R.N. Muller, and M. Muhammed, A High-Performance Magnetic Resonance Imaging T2 Contrast Agent. *Advanced Materials*, 2007. 19(14): p. 1874-1878.
52. Bloemen, M., W. Brulot, T.T. Luong, N. Geukens, A. Gils, and T. Verbiest, Improved functionalization of oleic acid-coated iron oxide nanoparticles for biomedical applications. *Journal of Nanoparticle Research*, 2012. 14(9): p. 1100.
53. Barrera, C., A.P. Herrera, and C. Rinaldi, Colloidal dispersions of monodisperse magnetite nanoparticles modified with poly(ethylene glycol). *Journal of Colloid and Interface Science*, 2009. 329(1): p. 107-113.
54. Gupta, A.K. and S. Wells, Surface-modified superparamagnetic nanoparticles for drug delivery: preparation, characterization, and cytotoxicity studies. *IEEE Trans Nanobioscience*, 2004. 3(1): p. 66-73.
55. Lee, Y., J. Lee, C.J. Bae, J.G. Park, H.J. Noh, J.H. Park, and T. Hyeon, Large-Scale Synthesis of Uniform and Crystalline Magnetite Nanoparticles Using Reverse Micelles as Nanoreactors under Reflux Conditions. *Advanced Functional Materials*, 2005. 15(3): p. 503-509.
56. Abou Hassan, A., O. Sandre, V. Cabuil, and P. Tabeling, Synthesis of iron oxide nanoparticles in a microfluidic device: preliminary results in a coaxial flow millichannel. *Chemical Communications*, 2008(15): p. 1783-1785.

57. Kumar, K., A.M. Nightingale, S.H. Krishnadasan, N. Kamaly, M. Wylenzinska-Arridge, K. Zeissler, W.R. Branford, E. Ware, A.J. deMello, and J.C. deMello, Direct synthesis of dextran-coated superparamagnetic iron oxide nanoparticles in a capillary-based droplet reactor. *Journal of Materials Chemistry*, 2012. 22(11): p. 4704-4708.
58. Lee, W.-B., C.-H. Weng, F.-Y. Cheng, C.-S. Yeh, H.-Y. Lei, and G.-B. Lee, Biomedical microdevices synthesis of iron oxide nanoparticles using a microfluidic system. *Biomedical Microdevices*, 2009. 11(1): p. 161-171.
59. Frenz, L., A. El Harrak, M. Pauly, S. Bégin-Colin, A.D. Griffiths, and J.-C. Baret, Droplet-Based Microreactors for the Synthesis of Magnetic Iron Oxide Nanoparticles. *Angewandte Chemie International Edition*, 2008. 47(36): p. 6817-6820.
60. Ma, D., J. Guan, S. Dénommée, G. Enright, T. Veres, and B. Simard, Multifunctional Nano-Architecture for Biomedical Applications. *Chemistry of Materials*, 2006. 18(7): p. 1920-1927.
61. Runowski, M., T. Grzyb, and S. Lis, Magnetic and luminescent hybrid nanomaterial based on Fe(3)O(4) nanocrystals and GdPO(4):Eu(3+) nanoneedles. *Journal of Nanoparticle Research*, 2012. 14(10): p. 1188.
62. Yi, D.K., S.T. Selvan, S.S. Lee, G.C. Papaefthymiou, D. Kundaliya, and J.Y. Ying, Silica-Coated Nanocomposites of Magnetic Nanoparticles and Quantum Dots. *Journal of the American Chemical Society*, 2005. 127(14): p. 4990-4991.
63. Ye, M., Q. Zhang, Y. Hu, J. Ge, Z. Lu, L. He, Z. Chen, and Y. Yin, Magnetically Recoverable Core–Shell Nanocomposites with Enhanced Photocatalytic Activity. *Chemistry – A European Journal*, 2010. 16(21): p. 6243-6250.
64. Hammond, Jules L., N. Formisano, P. Estrela, S. Carrara, and J. Tkac, Electrochemical biosensors and nanobiosensors. *Essays in Biochemistry*, 2016. 60(1): p. 69-80.
65. Jahanbani, S. and A. Benvidi, Comparison of two fabricated aptasensors based on modified carbon paste/oleic acid and magnetic bar carbon paste/Fe₃O₄@oleic acid nanoparticle electrodes for tetracycline detection. *Biosensors and Bioelectronics*, 2016. 85: p. 553-562.
66. Gerent, G.G. and A. Spinelli, Magnetite-platinum nanoparticles-modified glassy carbon electrode as electrochemical detector for

- nitrophenol isomers. *Journal of Hazardous Materials*, 2017. 330: p. 105-115.
67. Liu, Y., W. Zhu, D. Wu, and Q. Wei, Electrochemical determination of dopamine in the presence of uric acid using palladium-loaded mesoporous Fe₃O₄ nanoparticles. *Measurement*, 2015. 60: p. 1-5.
68. Feng, T., X. Qiao, H. Wang, Z. Sun, and C. Hong, A sandwich-type electrochemical immunosensor for carcinoembryonic antigen based on signal amplification strategy of optimized ferrocene functionalized Fe₃O₄@SiO₂ as labels. *Biosensors and Bioelectronics*, 2016. 79: p. 48-54.
69. Sperling, R.A. and W.J. Parak, Surface modification, functionalization and bioconjugation of colloidal inorganic nanoparticles. *Philosophical Transactions of the Royal Society A: Mathematical, Physical and Engineering Sciences*, 2010. 368(1915): p. 1333-1383.
70. Oliveira-Rodriguez, M., S. Lopez-Cobo, H.T. Reyburn, A. Costa-Garcia, S. Lopez-Martin, M. Yanez-Mo, E. Cernuda-Morollon, A. Paschen, M. Vales-Gomez, and M.C. Blanco-Lopez, Development of a rapid lateral flow immunoassay test for detection of exosomes previously enriched from cell culture medium and body fluids. *J Extracell Vesicles*, 2016. 5: p. 31803.
71. Lismont, M. and L. Dreesen, Comparative study of Ag and Au nanoparticles biosensors based on surface plasmon resonance phenomenon. *Materials Science and Engineering: C*, 2012. 32(6): p. 1437-1442.
72. Bao, F., J.L. Yao, and R.A. Gu, Synthesis of magnetic Fe₂O₃/Au core/shell nanoparticles for bioseparation and immunoassay based on surface-enhanced Raman spectroscopy. *Langmuir*, 2009. 25(18): p. 10782-7.
73. Bao, J., W. Chen, T. Liu, Y. Zhu, P. Jin, L. Wang, J. Liu, Y. Wei, and Y. Li, Bifunctional Au-Fe₃O₄ nanoparticles for protein separation. *ACS Nano*, 2007. 1(4): p. 293-8.
74. Iglesias-Silva, E., J. Rivas, L.M. León Isidro, and M.A. López-Quintela, Synthesis of silver-coated magnetite nanoparticles. *Journal of Non-Crystalline Solids*, 2007. 353(8-10): p. 829-831.

75. Kalska-Szostko, B., U. Wykowska, and D. Satuła, Core-shell and multilayered magnetite nanoparticles—Structural and Mössbauer studies. *Applied Surface Science*, 2014. 306: p. 7-15.
76. Xu, Z., Y. Hou, and S. Sun, Magnetic Core/Shell Fe₃O₄/Au and Fe₃O₄/Au/Ag Nanoparticles with Tunable Plasmonic Properties. *Journal of the American Chemical Society*, 2007. 129(28): p. 8698-8699.
77. Moon, S.H., S.-h. Noh, J.-H. Lee, T.-H. Shin, Y. Lim, and J. Cheon, Ultrathin Interface Regime of Core-Shell Magnetic Nanoparticles for Effective Magnetism Tailoring. *Nano Letters*, 2017. 17(2): p. 800-804.
78. León Félix, L., J.A.H. Coaquira, M.A.R. Martínez, G.F. Goya, J. Mantilla, M.H. Sousa, L.d.l.S. Valladares, C.H.W. Barnes, and P.C. Morais, Structural and magnetic properties of core-shell Au/Fe₃O₄ nanoparticles. *Scientific Reports*, 2017. 7: p. 41732.
79. Duan, S. and R. Wang, Bimetallic nanostructures with magnetic and noble metals and their physicochemical applications. *Progress in Natural Science: Materials International*, 2013. 23(2): p. 113-126.
80. Yu, H., M. Chen, P.M. Rice, S.X. Wang, R.L. White, and S. Sun, Dumbbell-like Bifunctional Au-Fe₃O₄ Nanoparticles. *Nano Letters*, 2005. 5(2): p. 379-382.
81. Wang, C., H. Yin, S. Dai, and S. Sun, A General Approach to Noble Metal-Metal Oxide Dumbbell Nanoparticles and Their Catalytic Application for CO Oxidation. *Chemistry of Materials*, 2010. 22(10): p. 3277-3282.
82. Huang, J., M. Guo, H. Ke, C. Zong, B. Ren, G. Liu, H. Shen, Y. Ma, X. Wang, H. Zhang, Z. Deng, H. Chen, and Z. Zhang, Rational Design and Synthesis of gamma-Fe₂O₃@Au Magnetic Gold Nanoflowers for Efficient Cancer Theranostics. *Adv Mater*, 2015. 27(34): p. 5049-56.
83. Wei, Y., R. Klajn, A.O. Pinchuk, and B.A. Grzybowski, Synthesis, Shape Control, and Optical Properties of Hybrid Au/Fe₃O₄ “Nanoflowers”. *Small*, 2008. 4(10): p. 1635-1639.
84. Wang, Y., H. Xu, M. Wei, H. Gu, Q. Xu, and W. Zhu, Study of superparamagnetic nanoparticles as labels in the quantitative lateral flow immunoassay. *Materials Science and Engineering: C*, 2009. 29(3): p. 714-718.

85. Liu, C., Q. Jia, C. Yang, R. Qiao, L. Jing, L. Wang, C. Xu, and M. Gao, Lateral Flow Immunochromatographic Assay for Sensitive Pesticide Detection by Using Fe₃O₄ Nanoparticle Aggregates as Color Reagents. *Analytical Chemistry*, 2011. 83(17): p. 6778-6784.
86. Kim, J., J.E. Lee, S.H. Lee, J.H. Yu, J.H. Lee, T.G. Park, and T. Hyeon, Designed Fabrication of a Multifunctional Polymer Nanomedical Platform for Simultaneous Cancer- Targeted Imaging and Magnetically Guided Drug Delivery. *Advanced Materials*, 2008. 20(3): p. 478-483.
87. Bakandritsos, A., G. Mattheolabakis, R. Zboril, N. Bouropoulos, J. Tucek, D.G. Fatouros, and K. Avgoustakis, Preparation, stability and cytocompatibility of magnetic/PLA-PEG hybrids. *Nanoscale*, 2010. 2(4): p. 564-572.
88. Ming, W., Z. Da, Z. Yongyi, W. Lingjie, L. Xiaolong, and L. Jingfeng, Nanocluster of superparamagnetic iron oxide nanoparticles coated with poly (dopamine) for magnetic field-targeting, highly sensitive MRI and photothermal cancer therapy. *Nanotechnology*, 2015. 26(11): p. 115102.
89. Gofman, V.V., T. Aubert, D.V. Ginste, R. Van Deun, N.V. Beloglazova, Z. Hens, S. De Saeger, and I.Y. Goryacheva, Synthesis, modification, bioconjugation of silica coated fluorescent quantum dots and their application for mycotoxin detection. *Biosensors and Bioelectronics*, 2016. 79: p. 476-481.
90. Liu, S.H. and M.Y. Han, Synthesis, Functionalization, and Bioconjugation of Monodisperse, Silica-Coated Gold Nanoparticles: Robust Bioprobes. *Advanced Functional Materials*, 2005. 15(6): p. 961-967.
91. Qhobosheane, M., S. Santra, P. Zhang, and W. Tan, Biochemically functionalized silica nanoparticles. *Analyst*, 2001. 126(8): p. 1274-8.
92. Tadic, M., S. Kralj, M. Jagodic, D. Hanzel, and D. Makovec, Magnetic properties of novel superparamagnetic iron oxide nanoclusters and their peculiarity under annealing treatment. *Applied Surface Science*, 2014. 322: p. 255-264.
93. Lee, D.C., F.V. Mikulec, J.M. Pelaez, B. Koo, and B.A. Korgel, Synthesis and Magnetic Properties of Silica-Coated FePt Nanocrystals. *The Journal of Physical Chemistry B*, 2006. 110(23): p. 11160-11166.

94. Rongen, H.A.H., A. Bult, and W.P. van Bennekom, Liposomes and immunoassays. *Journal of Immunological Methods*, 1997. 204(2): p. 105-133.
95. Elmi, M.M. and M.N. Sarbolouki, A simple method for preparation of immuno-magnetic liposomes. *International Journal of Pharmaceutics*, 2001. 215(1): p. 45-50.
96. Viroonchatapan, E., M. Ueno, H. Sato, I. Adachi, H. Nagae, K. Tazawa, and I. Horikoshi, Preparation and characterization of dextran magnetite-incorporated thermosensitive liposomes: an on-line flow system for quantifying magnetic responsiveness. *Pharm Res*, 1995. 12(8): p. 1176-83.
97. Martina, M.-S., J.-P. Fortin, C. Ménager, O. Clément, G. Barratt, C. Grabielle-Madelmont, F. Gazeau, V. Cabuil, and S. Lesieur, Generation of Superparamagnetic Liposomes Revealed as Highly Efficient MRI Contrast Agents for in Vivo Imaging. *Journal of the American Chemical Society*, 2005. 127(30): p. 10676-10685.
98. Chen, H. and R. Langer, Magnetically-responsive polymerized liposomes as potential oral delivery vehicles. *Pharm Res*, 1997. 14(4): p. 537-40.
99. Shinkai, M., M. Yanase, M. Suzuki, H. Hiroyuki, T. Wakabayashi, J. Yoshida, and T. Kobayashi, Intracellular hyperthermia for cancer using magnetite cationic liposomes. *Journal of Magnetism and Magnetic Materials*, 1999. 194(1): p. 176-184.
100. Yanase, M., M. Shinkai, H. Honda, T. Wakabayashi, J. Yoshida, and T. Kobayashi, Antitumor Immunity Induction by Intracellular Hyperthermia Using Magnetite Cationic Liposomes. *Japanese Journal of Cancer Research*, 1998. 89(7): p. 775-782.
101. Talelli, M., C.J.F. Rijcken, T. Lammers, P.R. Seevinck, G. Storm, C.F. van Nostrum, and W.E. Hennink, Superparamagnetic Iron Oxide Nanoparticles Encapsulated in Biodegradable Thermosensitive Polymeric Micelles: Toward a Targeted Nanomedicine Suitable for Image-Guided Drug Delivery. *Langmuir*, 2009. 25(4): p. 2060-2067.
102. Alonso, J., H. Khurshid, J. Devkota, Z. Nemati, N.K. Khadka, H. Srikanth, J. Pan, and M.-H. Phan, Superparamagnetic nanoparticles encapsulated in lipid vesicles for advanced magnetic hyperthermia and biodetection. *Journal of Applied Physics*, 2016. 119(8): p. 083904.

103. Amstad, E., J. Kohlbrecher, E. Müller, T. Schweizer, M. Textor, and E. Reimhult, Triggered Release from Liposomes through Magnetic Actuation of Iron Oxide Nanoparticle Containing Membranes. *Nano Letters*, 2011. 11(4): p. 1664-1670.
104. Gavilán, H., A. Kowalski, D. Heinke, A. Sugunan, J. Sommertune, M. Varón, L.K. Bogart, O. Posth, L. Zeng, D. González-Alonso, C. Balceris, J. Fock, E. Wetterskog, C. Frandsen, N. Gehrke, C. Grüttner, A. Fornara, F. Ludwig, S. Veintemillas-Verdaguer, C. Johansson, and M.P. Morales, Colloidal Flower-Shaped Iron Oxide Nanoparticles: Synthesis Strategies and Coatings. *Particle & Particle Systems Characterization*, 2017. 34(7): p. 1700094-n/a.
105. Thomas, G., F. Demoisson, R. Chassagnon, E. Popova, and N. Millot, One-step continuous synthesis of functionalized magnetite nanoflowers. *Nanotechnology*, 2016. 27(13): p. 135604.
106. Hu, F., K.W. MacRenaris, E.A. Waters, E.A. Schultz-Sikma, A.L. Eckermann, and T.J. Meade, Highly dispersible, superparamagnetic magnetite nanoflowers for magnetic resonance imaging(). *Chemical communications (Cambridge, England)*, 2010. 46(1): p. 73-75.
107. Hermanson, G.T., Chapter 11 - (Strept)avidin-Biotin Systems, in *Bioconjugate Techniques (Third edition)*. 2013, Academic Press: Boston. p. 465-505.
108. Clark, R.K., Y. Tani, and I. Damjanov, Suppression of nonspecific binding of avidin-biotin complex (ABC) to proteins electroblotted to nitrocellulose paper. *J Histochem Cytochem*, 1986. 34(11): p. 1509-12.
109. Norton, R., M. Heuzenroeder, and P.A. Manning, Non-specific serum binding to streptavidin in a biotinylated peptide based enzyme immunoassay. *J Immunoassay*, 1996. 17(3): p. 195-204.
110. Kouassi, G.K. and J. Irudayaraj, Magnetic and Gold-Coated Magnetic Nanoparticles as a DNA Sensor. *Analytical Chemistry*, 2006. 78(10): p. 3234-3241.
111. Lago-Cachón, D., M. Oliveira-Rodríguez, M. Rivas, M.C. Blanco-López, J.C. Martínez-García, A. Moyano, M. Salvador, and J.A. García, Scanning Magneto-Inductive Sensor for Quantitative Assay of Prostate-Specific Antigen. *IEEE Magnetism Letters*, 2017. 8: p. 1-5.

112. Welch, N.G., J.A. Scoble, B.W. Muir, and P.J. Pigram, Orientation and characterization of immobilized antibodies for improved immunoassays (Review). *Biointerphases*, 2017. 12(2): p. 02D301.
113. Zhang, S., Z. Bian, C. Gu, Y. Zhang, S. He, N. Gu, and J. Zhang, Preparation of anti-human cardiac troponin I immunomagnetic nanoparticles and biological activity assays. *Colloids and Surfaces B: Biointerfaces*, 2007. 55(2): p. 143-148.
114. Yan, J., Y. Liu, Y. Wang, X. Xu, Y. Lu, Y. Pan, F. Guo, and D. Shi, Effect of physiochemical property of Fe₃O₄ particle on magnetic lateral flow immunochromatographic assay. *Sensors and Actuators B: Chemical*, 2014. 197: p. 129-136.
115. Puertas, S., M. Moros, R. Fernández-Pacheco, M.R. Ibarra, V. Grazú, and J.M.d.l. Fuente, Designing novel nano-immunoassays: antibody orientation versus sensitivity. *Journal of Physics D: Applied Physics*, 2010. 43(47): p. 474012.
116. Lin, P.-C., S.-H. Chen, K.-Y. Wang, M.-L. Chen, A.K. Adak, J.-R.R. Hwu, Y.-J. Chen, and C.-C. Lin, Fabrication of Oriented Antibody-Conjugated Magnetic Nanoprobes and Their Immunoaffinity Application. *Analytical Chemistry*, 2009. 81(21): p. 8774-8782.
117. Friedrich, R.P., J. Zaloga, E. Schreiber, I.Y. Tóth, E. Tombácz, S. Lyer, and C. Alexiou, Tissue Plasminogen Activator Binding to Superparamagnetic Iron Oxide Nanoparticle—Covalent Versus Adsorptive Approach. *Nanoscale Research Letters*, 2016. 11: p. 297.
118. Chen, A. and S. Yang, Replacing antibodies with aptamers in lateral flow immunoassay. *Biosensors and Bioelectronics*, 2015. 71: p. 230-242.
119. Nezlín, R., Use of aptamers in immunoassays. *Molecular Immunology*, 2016. 70: p. 149-154.
120. Toh, S.Y., M. Citartan, S.C.B. Gopinath, and T.-H. Tang, Aptamers as a replacement for antibodies in enzyme-linked immunosorbent assay. *Biosensors and Bioelectronics*, 2015. 64: p. 392-403.
121. Wang, A.Z., V. Bagalkot, C.C. Vasilliou, F. Gu, F. Alexis, L. Zhang, M. Shaikh, K. Yuet, M.J. Cima, R. Langer, P.W. Kantoff, N.H. Bander, S. Jon, and O.C. Farokhzad, Superparamagnetic Iron Oxide Nanoparticle—Aptamer Bioconjugates for Combined Prostate Cancer Imaging and Therapy. *ChemMedChem*, 2008. 3(9): p. 1311-1315.

122. Chung, J.W., J.M. Park, R. Bernhardt, and J.C. Pyun, Immunosensor with a controlled orientation of antibodies by using NeutrAvidin–protein A complex at immunoaffinity layer. *Journal of Biotechnology*, 2006. 126(3): p. 325-333.
123. Makaraviciute, A., A. Ramanavicius, and A. Ramanaviciene, Development of a reusable protein G based SPR immunosensor for direct human growth hormone detection in real samples. *Analytical Methods*, 2015. 7(23): p. 9875-9884.
124. Gutierrez, L., R. Costo, C. Gruttner, F. Westphal, N. Gehrke, D. Heinke, A. Fornara, Q.A. Pankhurst, C. Johansson, S. Veintemillas-Verdaguer, and M.P. Morales, Synthesis methods to prepare single- and multi-core iron oxide nanoparticles for biomedical applications. *Dalton Transactions*, 2015. 44(7): p. 2943-2952.
125. Bogren, S., A. Fornara, F. Ludwig, M. del Puerto Morales, U. Steinhoff, F.M. Hansen, O. Kazakova, and C. Johansson, Classification of Magnetic Nanoparticle Systems—Synthesis, Standardization and Analysis Methods in the NanoMag Project. *International Journal of Molecular Sciences*, 2015. 16(9).
126. Hachani, R., M. Lowdell, M. Birchall, A. Hervault, D. Mertz, S. Begin-Colin, and N.T.K. Thanh, Polyol synthesis, functionalisation, and biocompatibility studies of superparamagnetic iron oxide nanoparticles as potential MRI contrast agents. *Nanoscale*, 2016. 8(6): p. 3278-3287.
127. Baskakov, A.O., A.Y. Solov'eva, Y.V. Ioni, S.S. Starchikov, I.S. Lyubutin, I.I. Khodos, A.S. Avilov, and S.P. Gubin, Magnetic and interface properties of the core-shell Fe₃O₄/Au nanocomposites. *Applied Surface Science*, 2017. 422: p. 638-644.
128. Umut, E., F. Pineider, P. Arosio, C. Sangregorio, M. Corti, F. Tabak, A. Lascialfari, and P. Ghigna, Magnetic, optical and relaxometric properties of organically coated gold–magnetite (Au–Fe₃O₄) hybrid nanoparticles for potential use in biomedical applications. *Journal of Magnetism and Magnetic Materials*, 2012. 324(15): p. 2373-2379.
129. WangWang, J. Luo, Q. Fan, M. Suzuki, I.S. Suzuki, M.H. Engelhard, Y. Lin, N. Kim, J.Q. Wang, and C.-J. Zhong, Monodispersed Core–Shell Fe₃O₄@Au Nanoparticles. *The Journal of Physical Chemistry B*, 2005. 109(46): p. 21593-21601.

SECTION III

RESULTS

Section III - Chapter 1

Double-layer Fatty Acid Nanoparticles as Multiplatform for Diagnostics and Therapy

Introduction and motivation

Nowadays, public health is one of the most critical challenges in society. Unfortunately, the global increase in population and a higher quality of life promotes a higher incidence of diseases. Among them, cancer leads the way, according to the World Health Organization.

Sections I and II of this thesis revise the potential bioapplications of magnetic nanoparticles (MNPs). This first chapter of the results section tests three different samples as magnetic resonance imaging contrast agents, detection tags for *in vitro* biosensing, and mediators of tumor heating in magnetic hyperthermia. The samples are magnetite-based particles, each with a different double layer of fatty acids that render them hydrophilic and suitable for their use in body fluids. The particles were characterized structurally, superficially, and magnetically, which correlated their response in the three bioapplications mentioned above.

All the samples showed significant transverse relaxation times for magnetic relaxation, clearly exceeding the commercial agents. Regarding magnetic hyperthermia, the three samples were able to deliver significant amounts of heat. Finally, the results of the three samples in magnetic biodetection showed the importance of the initial magnetic susceptibility and the agglomeration process of the particles to be effective labels in inductive biosensing.

This work is the result of the bilateral project between the Institute for the Structure of Matter (CNR) in Italy and the Center for Fundamental and Advanced Technical Research - Laboratory for Magnetic Fluids, in Romania, under the supervision of Davide Peddis in the first and Ladislau Vekas and Vlad Socoliuc in the second.

The complete research details are presented below.

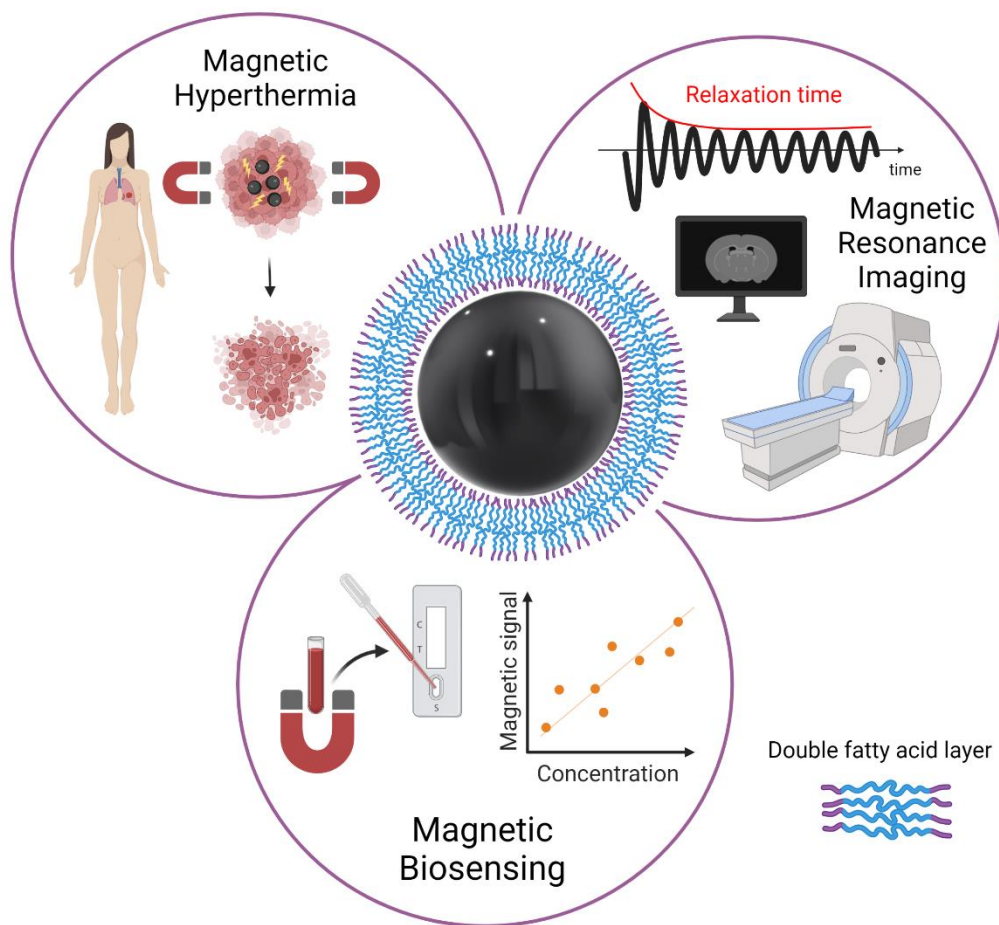
Scientific article (in preparation)

Double-layer Fatty Acid Nanoparticles as Multiplatform for Diagnostics and Therapy

This work has been published in:

Cite as:

GRAPHICAL ABSTRACT



Double-layer fatty acid nanoparticles as multiplatform for diagnostics and therapy

María Salvador^{1,2}, José Luis Marqués-Fernández¹, José Carlos Martínez-García¹, Dino Fiorani², Paolo Arosio³, Matteo Avolio⁴, Francesca Brero⁴, Florica Balanean⁵, Andrea Guerrini⁶, Claudio Sangregorio^{6,7}, Vlad Socoliuc⁵, Ladislau Vekas⁵, Davide Peddis^{2,8}, Montserrat Rivas¹

¹*Department of Physics & IUTA, University of Oviedo, Campus de Viesques, 33203 Gijón, Spain*

²*Institute of Structure of Matter – National Research Council (CNR), 00016 Monterotondo Scalo (RM), Rome, Italy*

³*Department of Physics, Università degli studi di Milano and INFN, 20133 Milano, Italy*

⁴*Department of Physics, Università degli studi di Pavia and INFN, 27100 Pavia, Italy*

⁵*Romanian Academy - Timisoara Branch, Center for Fundamental and Advanced Technical Research, Laboratory for Magnetic Fluids, 300222 Timisoara, Romania*

⁶*INSTM & Dipartimento di Chimica “Ugo Schiff”, Università di Firenze, 50019 Sesto Fiorentino, Italy*

⁷*ICCOM-CNR and INSTM, 50019 Sesto Fiorentino, Italy*

⁸*Department of Chemistry and Industrial Chemistry, Università degli Studi di Genova, 16146 Genova, Italy*

Abstract

Today public health is one of the most important challenges in society. Cancer is the leading cause of death, so early diagnosis and localized treatments that minimize side effects are a priority. Magnetic nanoparticles have shown great potential as magnetic resonance imaging contrast agents, detection tags for in vitro biosensing, and mediators of tumor heating in magnetic hyperthermia. One of the critical characteristics of nanoparticles to adjust to the biomedical needs of each application is their polymeric coating. Fatty acid coatings are known to contribute to colloidal stability and good surface crystalline quality. While monolayer coatings make the particles hydrophobic, a fatty acid double-layer renders them hydrophilic, and therefore suitable for use in body

fluids. In addition, they provide the particles with functional chemical groups that allow their bioconjugation. This work analyzes three types of self-assembled bilayer fatty acid coatings of superparamagnetic iron oxide nanoparticles: oleic, lauric, and myristic acids. We characterize the particles magnetically and structurally and study their potential for resonance imaging, magnetic hyperthermia, and labeling for biosensing in lateral flow immunoassays. We found that the myristic acid sample reported a large r_2 relaxivity, superior to existing iron-based commercial agents. For magnetic hyperthermia, a significative SAR value was obtained for the oleic sample. Finally, the lauric acid sample showed promising results for nanolabeling.

Keywords: Magnetic nanoparticles; magnetic hyperthermia, magnetic relaxation, magnetic resonance imaging, biosensor, lateral flow immunoassays, inductive sensing.

1. Introduction

Today more than ever, there is the need to develop tools that help us solve emerging biomedical problems. According to the World Health Organization, cancer ranks as the leading cause of death in every country of the world [1]. Nearly 10 million cancer deaths happened in 2020. The recent coronavirus disease 2019 (COVID-19) pandemic pushed the health systems to their limits. While they were focusing their resources on COVID-19 patients, others suffered from severe delays. In particular, undiagnosed cancers might emerge in the next few years with incremented risk due to these screening gaps [2,3]. Unquestionably, any disease, especially cancer, should be diagnosed and treated without delay: Treatments are simpler and more effective at an initial stage.

The public scene is now used to the term “rapid diagnostic tests” thanks to the ongoing COVID-19 pandemic. Most of them are based on lateral flow assays (LFAs), which have carved out a solid reputation thanks to their quickness, portability, easy use, and affordability [4]. These characteristics make them ideal for a point-of-care solution for diagnostic. LFAs rely on paper microfluidics and bio-recognition. The tests consist of a strip of nitrocellulose along which the biological sample flows by capillarity. A recognition molecule previously immobilized across a line in the strip captures the molecule of interest. A yes/no answer (presence/absence) is observed by the naked eye when the biomolecule

is labeled with a colored particle or enzyme, as in the home pregnancy test. When it is necessary to quantify the signal, commercial optical readers can be used. However, this method is sensitive to interferences coming from the ambient light or staining from the membrane. Optical methods can detect only the labeling particles on the membrane surface but not those below it [5]. Overcoming these limitations will boost the spread of the technique to more biomedical applications that require quantifying capacity.

Non-invasive diagnosis *in vivo* by magnetic resonance imaging (MRI) provides good spatial resolution, real-time imaging with good penetration depth. Despite the excellent quality of the images, there are cases in which contrast is too poor [6]. Exogenous contrast agents selectively shorten the proton relaxation time in the region of interest, and thus, the contrast is enhanced. So far, contrast agents based on gadolinium have been used, but they lack specificity and are toxic [7].

Once the disease is present, less aggressive, more effective, and affordable treatments are needed. Hyperthermia consists of increasing the temperature to induce irreversible damage to the malignant cells. Locally applied hyperthermia is well controlled in terms of heat uniformity and collateral damages to healthy cells and is preferred to extensive treatments [8]. However, only regions close to the surface can be treated this way. In principle, hyperthermia by laser or microwave light only penetrates a small depth into the tissues and can be used to treat superficial tumors. Nanoparticles that serve as hyperthermia mediators by absorbing radiation and heating their surroundings are used to penetrate deeper regions of the body.

Nanoparticles have the same size as biological entities of interest, allowing their interaction at the molecular level. Moreover, when these particles are magnetic, new capabilities arise, offering new possibilities in the life science fields [9]. Magnetic nanoparticles (MNPs) can be used as magnetic reporters in biosensing. In LFAs, for example, they provide a quantitative signal from the whole volume and are independent of optical conditions [10,11]. They offer the possibility to magnetically isolate and pre-concentrate the analyte, improving the detection [12,13]. MNPs can be designed to be biocompatible and safe. When reduced below a critical size, their behavior is superparamagnetic and avoids self-aggregation, favoring colloidal stability [14]. This allows their use *in vivo* for imaging

and therapy. In the former, MNPs act as contrast agents thanks to their short magnetic relaxation time [15]. In the latter, MNPs are used for the controlled generation of heat. They can be injected into the body and passively (e.g., by the surface biofunctionalization) or actively (e.g., by an external magnetic gradient) target the zone. When exposed to an alternating magnetic field, their magnetic relaxation increases the temperature up to 40-46°C, damaging or inducing the apoptosis of the cancer cells [16].

In this work, three magnetite core particles have been synthesized by co-precipitation and coated by three different fatty acids: oleic acid (OA), lauric acid (LA), and myristic acid (MA). In principle, fatty acid coatings promote a high superficial crystalline quality of hydrophobic nanoparticles. Then, coating them with a double layer renders the solution hydrophilic (an aqueous suspension is necessary for bioapplications.) Additionally, it provides accessible chemical moieties for bioconjugation.

We have tested these magnetic colloids as nanoheaters, MRI contrast agents, and labels in LFA. The results show these MNPs are a good multi-purpose platform for their application in diagnostics and therapy.

2. Materials and Methods

2.1. Chemicals and reagents

FeSO₄·7H₂O (>99%), FeCl₃ (97%), NH₄OH, oleic acid (90%), myristic acid (>98%), and lauric acid (>98%) were purchased from Sigma-Aldrich and used without any further modification.

Neutravidin protein was obtained from Thermo Fischer Scientific (USA). 1-ethyl-3-[3-dimethylpropyl] carbodiimide (EDC), bovine serum albumin (BSA), biotin-conjugated bovine serum albumin (BBSA), N-hydroxysuccinimide (NHS), 2-(N-morpholino) ethanesulfonic acid (MES), and Tween20 were purchased from Sigma-Aldrich (Spain). Glass fiber membrane (GFCP001000), used as sample pad and backing cards (HF000MC100), were purchased from Millipore (Germany). Other materials used were nitrocellulose membranes (UniSart CN95, Sartorius, Spain) and absorbent pads (Whatman, USA).

2.2. Synthesis of the magnetic nanoparticles

Three different sets of magnetic nanoparticles were synthesized through a chemical co-precipitation method. This procedure was followed by combining steric and electrostatic stabilization in water by adding one of the three fatty acids: OA, LA, and MA. The resulting samples are named OA@NP, LA@NP, and MA@NP. The whole procedure is described elsewhere [17]. Briefly, two solutions of FeSO_4 and FeCl_3 with a ratio of iron ions $\text{Fe}^{3+}/\text{Fe}^{2+} = 1.7$ are mixed under continuous stirring in atmospheric conditions and heated up to 80 °C. To precipitate the particles, a solution of 25% NH_4OH is added, and just after the co-precipitation reaction, the surfactant is incorporated in a significant excess to start its chemisorption on the magnetite nanoparticles surface. Finally, the phases are separated, followed by decantation, washing steps with distilled water, and elimination of residual salts to disperse the double layer coated magnetic nanoparticles in a weak solution of NH_4OH , then purified by magnetic separation or filtration.

2.3. Physicochemical and magnetic characterization of the magnetic nanoparticles

Measurements of the particle size were obtained from TEM images (MET JEOL-2000 EX-II), analyzing around 200 particles, and fitting the distribution to a log-normal curve. X-ray diffraction (XRD) analysis was carried out in a Seifert XRD 3000 T/T equipment using a Mo emitter ($K\alpha$: $\lambda_1=0.709316 \text{ \AA}$ and $\lambda_2= 0.713607 \text{ \AA}$). As a standard, we used Iron (II; III) oxide Puratronic® CAS 1317-61-9 from Alfa Aesar. Thermogravimetric Analysis (TGA) was done in a 20 μL sample using a Mettler-Toledo TGA/SDTA851 in the temperature range from 25 °C to 990 °C, with the heating rate of 10 °C/minute, under standard atmosphere.

Fourier-Transform Infrared Spectroscopy (FTIR) was performed in liquid, using an FTIR spectrometer coupled with the Varian 620-IR image recorder. Hydrodynamic diameter and ζ -Potential were obtained using Dynamic Light Scattering (DLS) in freshly prepared samples with a Zetasizer Nano ZS ZEN3600 equipped with a solid-state He-Ne laser.

DC-magnetization measurements were performed using a Quantum Design SQUID magnetometer equipped with a superconducting magnet producing fields up to $\pm 5 \text{ T}$. Initial magnetic susceptibility at room

temperature from 1 Hz to 10 000 Hz were measured by a Quantum Design PPMS magnetometer equipped with a superconducting coil. The magnetization values are referred to the mass of Fe_3O_4 derived from the concentration obtained by the TGA analysis.

2.4. Magnetic hyperthermia measurements

The evaluation of specific absorption rate (SAR) was performed through calorimetric measurements by recording temperature kinetics of water suspension of MNPs under exposition to an alternating magnetic field (AMF). Measurements were performed using an in-house assembled system comprising a commercial 6 kW Fives Celes power supply, a water-cooled induction coil and a series of variable capacitors for setting the required frequency (183 kHz and 17 kA/m in this case). The amplitude of the magnetic field was assessed using an AMF Life Systems high frequency probe. Measurements of the sample temperature were performed by an optical fiber thermometer connected to a digital temperature recorder (Fotemp). The SAR was evaluated using the following expression:

$$\text{SAR} = \frac{m_{\text{np}}C_{\text{np}} + m_{\text{s}}C_{\text{s}}}{m_{\text{np}}} \left| \frac{\Delta T}{\Delta t} \right|_{t \approx 0} \quad (1)$$

where m_{np} , m_{s} and C_{np} , C_{s} correspond to the mass and specific heat capacities of the magnetic particles and the solvent. the slope of the temperature; ΔT is the temperature increase in the interval of time Δt of field application. Since the measurements were carried in non-adiabatic conditions, the $\Delta T/\Delta t$ values were extrapolated for $t \approx 0$ from the temperature kinetic curves (initial slope value).

2.5. Relaxometric characterization

^1H nuclear magnetic resonance (NMR) relaxometric measurements were performed at room temperature by measuring the longitudinal T_1 and transverse T_2 nuclear relaxation times at the frequencies $\nu = 56.7$ MHz, 21.3 MHz, and 8.5 MHz. The NMR signal detection and generation were obtained by Stellar Spinmaster Fourier transform-nuclear magnetic resonance (FT-NMR) spectrometer. Saturation Recovery (SR) and Carr Purcell Meiboom Gill (CPMG) pulse sequences were used for T_1 and T_2 measurements, respectively.

2.6. Biofunctionalization of the magnetic nanoparticles

The MNPs were conjugated to neutravidin. We used the carboxylic groups present in the fatty acids' outer layer to link the neutravidin via the carbodiimide chemistry (see Figure 1a). For that purpose, 10 μL of the particles were mixed with 100 μL of EDC (5 mg/mL, MES 50 mM, pH 6.00) and 100 μL of NHS (5 mg/mL, MES pH 6.00), both freshly prepared, and stirred for 10 min. Then, 100 μL of a neutravidin solution with different concentrations (0.75, 1, and 2 mg/mL) was added and shaken for 4 h. To block the residual carboxyl groups on the particle surface, we added 100 μL of the blocking solution (1% BSA, PBS 10 mM, pH 7.4) for 30 min while agitating. The samples were then centrifuged at 14600 rpm for 20 min, and 300 μL of the supernatant was removed. The pellets were resuspended in fresh PBS 10 mM, pH 7.4. We used DLS measurements to monitor the neutravidin-MNP conjugation.

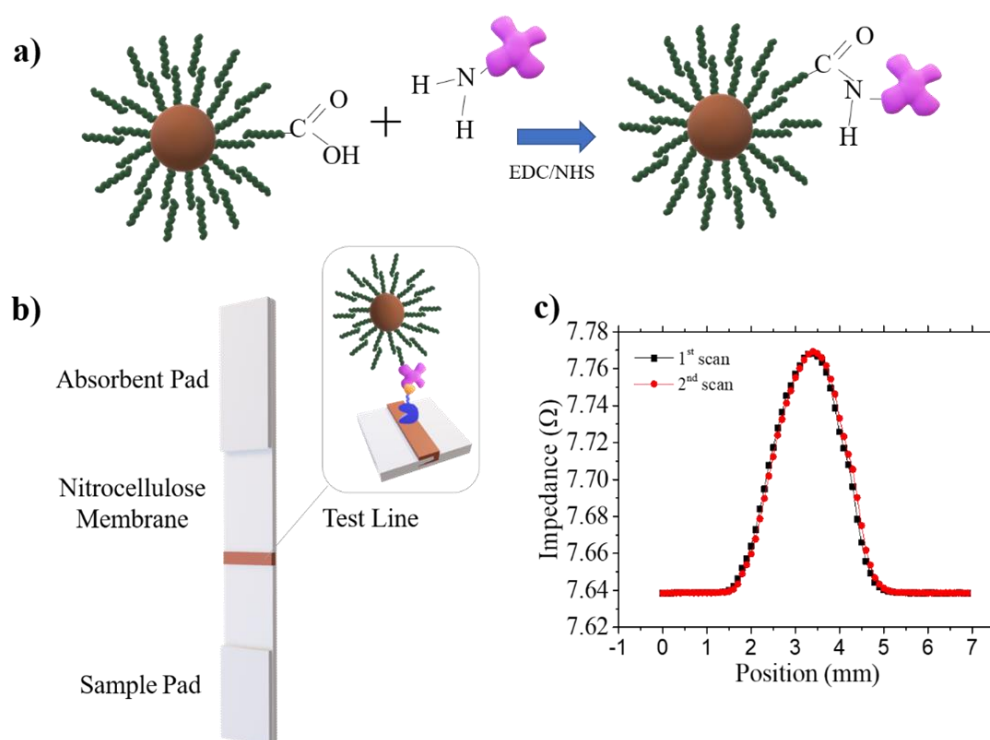


Figure 1. a) Scheme of the particles' biofunctionalization process with neutravidin by the EDC/NHS chemistry. For simplification, only one functional group has been represented on the surface of the MNPs and the neutravidin. b) Schematic view of a lateral flow strip and its test line: a neutravidin-MNP complex captured by a molecule of biotin. c) Impedance variation for two scannings of the OA@NP sample.

2.7. Lateral Flow Assays

To capture the neutravidin-MNP conjugate in the LFA strip, a test line

of biotin has been immobilized across the lateral flow membrane. For this purpose, a 1 mg/mL BBSA solution has been automatically dispensed at a rate of 0.1 $\mu\text{L}/\text{mm}$ and then left to dry at room temperature. The sample and absorbent pads were placed onto the plastic adhesive backing card with an overlap of 2 mm. Then, single 5 mm width LFA strips were cut off with a guillotine.

The biotin-neutravidin is widely known in biochemistry for its strength, high thermal and chemical stability, and low non-specific binding. Many biotinylated antibodies are used in lateral flow or other types of immunoassays. For this reason, we chose the neutravidin-biotin paradigm in our experiment to mimic the LFA process and assess the performance of the MNPs as detection nanolabels.

To run the test, 20 μL of the neutravidin-biofunctionalized MNPs were mixed with 80 μL of freshly prepared running buffer (RB) containing 10 mg/mL BSA, 0.5% (w/v) Tween20 in PBS (10 mM, pH 7.4). The tests were then carried out in dipstick format by introducing the LFA strip's sample pad in the microtube, allowing it to flow and dry (see Figure 1b).

2.8. Scanning magneto-inductive sensor measurements

An inductive sensor specifically developed to read out the signal from LFAs was used to evaluate the samples [18]. Its sensing area consists of a planar micro-coil printed on an insulating substrate. The coil is fed with a low amplitude radiofrequency current while its impedance is continuously monitored by a precision four-point auto-balancing impedance analyzer (Agilent 4294A) using 16048G test leads, 500 mV, and 20–110 MHz excitation voltage. For quantification purposes, we slide the sample in smooth contact over the planar coil using a micro-positioner. The coil picks up the varying magnetic flux produced by the magnetic particles on top of it. The electromagnetic induction produces a change in the electric impedance directly proportional to the frequency of the driving current, the particle initial magnetic permeability, and the total volume of their magnetic cores.

The impedance variation during the scanning in 100 micrometers steps (see Figure 1c) is integrated by a trapezoidal method to account for all the MNPs in the sample. The measurement result is given in units of $\Omega\cdot\text{mm}$.

The fatty acid-MNPs have been evaluated at two different stages:

previously to their bioconjugation and used in the immunoassays.

Firstly, for evaluating the bare fatty acid-MNPs, 10 μL of the three ferrofluids were deposited onto 10 mm \times 2 mm blotting papers and left to dry for at least 12 h. The linear correlation between the change of impedance and particle mass was checked for a fixed frequency and type of particles. To facilitate the comparison of the results, we have calculated the sensor sensitivity (Σ) following the use of magnetoimpedance sensors; Σ is defined as the percentage relative impedance variation per unit particle mass m with (Z) and without (Z_0) MNPs:

$$\Sigma = \frac{1}{m} \frac{Z - Z_0}{Z_0} \cdot 100 \quad (2)$$

Secondly, the complexes neutravidin-MNPs were tested as detection labels in LFAs. The biotin test line retains the complexes, and the sensor detects the MNPs in them. In this case, the quantifying result relies not exclusively on the particles' properties but very significantly on the bioconjugation process efficiency.

3. Results and discussion

3.1. Physicochemical characterization

The images obtained by TEM showed a quasi-spherical shape for all the fatty acid-MNPs, as observed in Figure 2. The particle size distribution was obtained by measuring about 200 nanoparticles in various TEM images using ImageJ software. Then, the data was fitted by a log-normal function [19] to obtain the mean particle diameter d_{TEM} and the standard deviation σ (see Table 1). Our results agree with previous works on particles obtained with the same protocol, which bespeaks for the reproducibility of the synthesis method [20]. XRD patterns (See supplementary information Figure S1) of the three particle types are in good concordance with the magnetite standard. The broad shape of the diffraction peaks is a clear sign of their nanostructured character. We have used Rietveld refinement and Scherrer equation to calculate the crystallite size presented in Table 1 as d_{XRD} . It is known that d_{XRD} is an effective size which is smaller than the physical one due to the particle's non-sphericity. Our results agree with the commonly accepted relation $d_{\text{XRD}} = 3/4 d_{\text{TEM}}$ [21].

We have used the Langevin-Chantrell function [22] to fit our magnetization curves and calculate the magnetic diameter d_{MAG} . All the values obtained for the three samples are slightly smaller than the d_{TEM} , indicating that there is a superficial layer where spin canting and other phenomena may lead to the disorder of the magnetic moments [23]. This dead layer does not seem to be greatly influenced by the coating since it has a very similar value in all of them.

The hydrodynamic diameter d_{DLS} and the ζ -potential were obtained by DLS and collected in Table 1. The ζ -potential values are negative, and their absolute value is larger than 40 mV, indicating that excellent stability is possible thanks to electrostatic repulsion, which inhibits the particles agglomeration and settling [24]. However, it is worth noticing that all the samples exhibited a certain degree of agglomeration reflected in the high d_{DLS} values when compared to d_{TEM} . The OA and MA-stabilized ferrofluids present the largest agglomerates. This agglomeration can be seen in Figure 2. Additionally, MA@NP has two mean sizes: 9.5 nm and 25 nm in equal proportions. Agglomeration is a concern in most of the MNPs studies and the results are not fully conclusive. However, depending on the bioapplication, it can be beneficial or detrimental. Regarding biodetection, it can be advantageous. Stable agglomerated nanoparticles of controlled size provide an amplification of the signal per biomolecule, increasing the detection sensitivity [25]. Also for magnetic hyperthermia, a slight controlled agglomeration of the nanoheaters can increase the SAR [26].

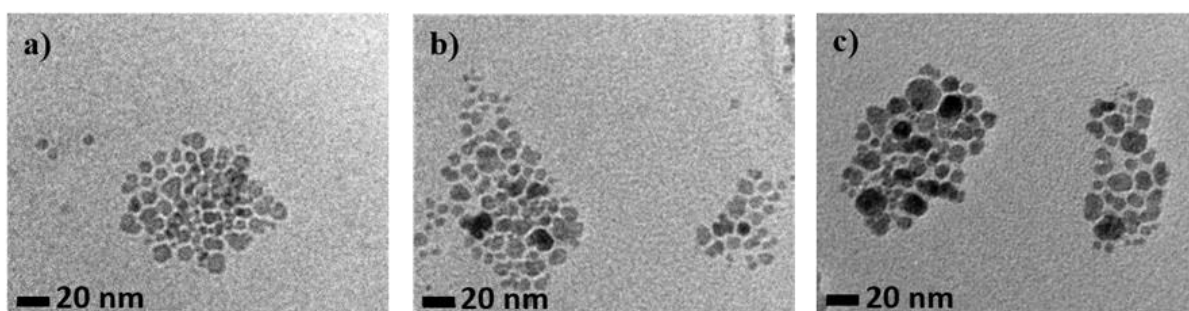


Figure 2. TEM images for samples a) OA@NP, b) LA@NP, and c) MA@NP.

Table 1. Mean particle diameter d_{TEM} by TEM and its standard deviation σ ; average crystallite size d_{XRD} and its uncertainty, magnetic diameter d_{MAG} from the Langevin equation and its standard deviation σ , hydrodynamic diameter d_{DLS} and its polydispersity index (PDI) and ζ -potential.

Sample	d_{TEM}		d_{XRD}		d_{MAG}		d_{DLS}		ζ -Potential (mV)
	(nm)	σ	(nm)	\pm	(nm)	σ	(nm)	PDI	
OA@NP	10.3	0.3	6.7	0.9	9.1	0.4	120	0.120	-50
LA@NP	7.9	0.2	5.8	0.6	7.6	0.3	23	0.169	-47
MA@NP	9.5	0.3	5.8	0.9	8.9	0.4	99	0.176	-50

We performed TGA measurements to elucidate the superficial compounds, their amount, and the magnetic core concentration (See Supplementary Information Figure S2). Most of the weight loss (83% for OA@NP, 81% for LA@NP and 68% for MA@NP) occurred from 50 °C to 135 °C, attributed to the evaporation of the water and the solvation layer. Another two significant weight losses can be distinguished at 420 °C. These peaks agree with the desorption, decomposition, and evaporation of the surfactant molecules. Specifically, the first weight loss, from 190 °C to 290 °C, suggests the release and decomposition of slightly bound or physically adsorbed surfactant molecules. On the contrary, the second weight loss at higher temperatures (from 290 °C to 420 °C) can be caused by the break of stronger bonds, i.e., chemically bound surfactant molecules decomposition. This double peak pattern in the weight loss curve of fatty acid stabilized nanoparticles confirms the double surfactant layer [27–29].

The double layer of fatty acids aims to provide water dispersion and get superficial carboxylic acid groups that enable the bioconjugation of proteins. Supplementary Information Figure S3 contains the FTIR spectra. They all show the beginning of a steep peak at about 598 cm^{-1} due to the Fe-O bonds' vibration of the particles' iron oxide core [30]. The carboxylic acid groups' vibration is evident in the peak at around 1710 cm^{-1} [31]. Regarding an OA double-layer, Yang et al. studied the differences in the FTIR spectra of a single and a double layer OA-stabilized nanoparticles [32]. They found that only the peak at 1709 cm^{-1} was present, corresponding to the C-O stretching vibration for free COOH (COO⁻), which endorses the bi-layer formation. This peak exists in the three samples; however, it is better defined in OA@NP and

LA@NP but almost imperceptible in MA@NP. Previous studies on similar samples [20,33] pointed out the MA coating's lower effectiveness when compared to OA and LA. If the coating is incomplete, these residual groups at the MNP surface could be too scarce, and hence, the peak almost negligible. The normal vibration of methyl groups (-CH₂) due to their symmetric bending is at 1465 cm⁻¹. However, it has been reported that when these alkyl chains are closely packed, this peak splits into two, and the second one shifts to lower wavenumbers. This happens in all our samples and more significantly in OA@NP; in the latter, the bigger organic chains and their double bond bending produce a denser package compared to LA@NP and MA@NP [34].

At the right side of the spectra, all samples showed two characteristic bands at 2920 cm⁻¹ and 2850 cm⁻¹ due to the symmetric and asymmetric stretching, and the scissoring of C-H bonds of aliphatic compounds, which, mainly in LA@NP and MA@NP, are superimposed to the peak signal of the O-H stretch (usually present at 3300 – 2500 cm⁻¹.) Finally, the C-O stretch appeared in the region from 1320 cm⁻¹ to 1210 cm⁻¹. In summary, the FTIR spectra of OA@NP, LA@NP, and MA@NP confirmed the double layer of fatty acids on the nanoparticle surface and the carboxylic groups.

3.2. Magnetic properties

Magnetization curves at 5 K show no hysteresis at 298 K, while at 5 K there is magnetic hysteresis in all three samples (See Figure 3a and b.) The saturation magnetization M_s values, calculated by fitting the experimental data to the law of approach to saturation [35], are gathered in Table 2. All the samples show very similar values, close to the value of bulk magnetite (90 Am²/kg) [36].

To assess the particles' superparamagnetic behavior, we recorded the ZFC-FC curves (see Figure 4). For monodisperse populations with homogeneous magnetic anisotropy, ZFC and FC curves should coincide above the blocking temperature T_B at which the particles transit from blocked to superparamagnetic regime [37]. For a polydisperse particle sample, in the absence of interparticle interactions, the difference between the temperature of the maximum T_{MAX} and the temperature at which both curves merge T_{IRR} , is related to the width of the blocking temperature distribution, and hence, to the particle size distribution. On

the other hand, interparticle interactions are present in our samples, as clearly shown by the tendency to flatten the FC curves below T_{MAX} . In such a case, T_{MAX} is also dependent on the strength of the interparticle interactions.

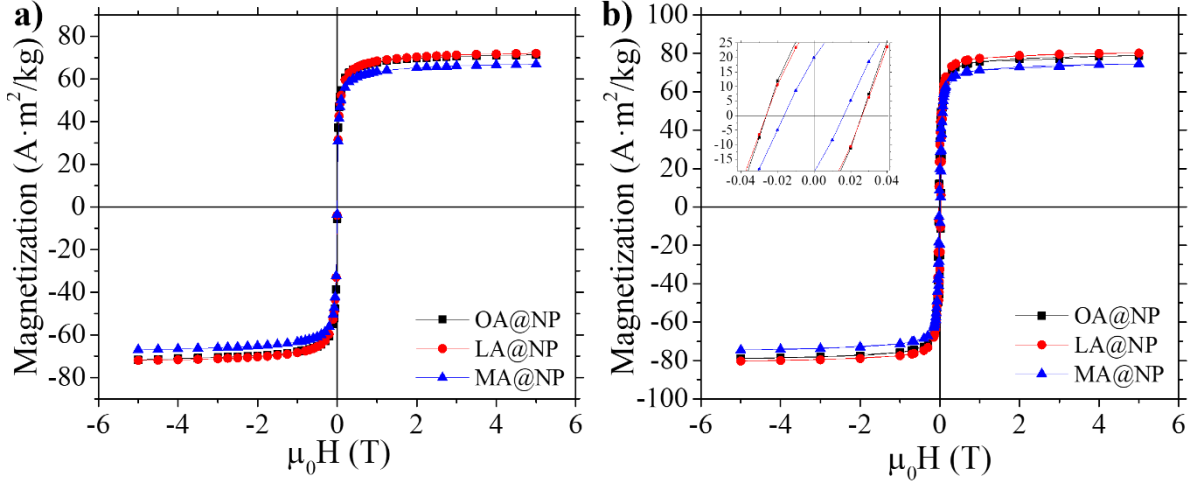


Figure 3. Magnetization curves at a) 250 K and b) 5 K for the three samples OA @NP, LA @NP, and MA@NP.

Table 2. Saturation magnetization at 250 K (M_S^{250K}), saturation magnetization at 5 K (M_S^{5K}), coercive field at 5 K ($\mu_0 H_C^{5K}$), reduced remanence (M_S/M_R^{5K}), effective anisotropy constant (K), and real and imaginary components of the initial magnetic susceptibility, χ' and χ'' , respectively. Uncertainties in the last digits are given in parenthesis.

Sample	M_S^{250K} (Am ² /kg)	M_S^{5K} (Am ² /kg)	$\mu_0 H_C^{5K}$ (T)	M_S / M_R^{5K}	K (J/m ³)	χ'	χ''
OA@NP	71(1)	79(1)	0.024	0.37	2.2(2)·10 ⁴	21.03	0.01
LA@NP	73(1)	80(1)	0.026	0.41	2.1(2)·10 ⁴	15.88	0.03
MA@NP	67(1)	74(1)	0.016	0.25	1.9(2)·10 ⁴	10.14	0.02

The reduced remanence (M_S/M_R) at 5K (see Table 2) is far from the theoretical value of 0.5 for non-interacting uniaxial single-domain particles, confirming the presence of non-negligible interparticle interactions, especially for MA@NP.

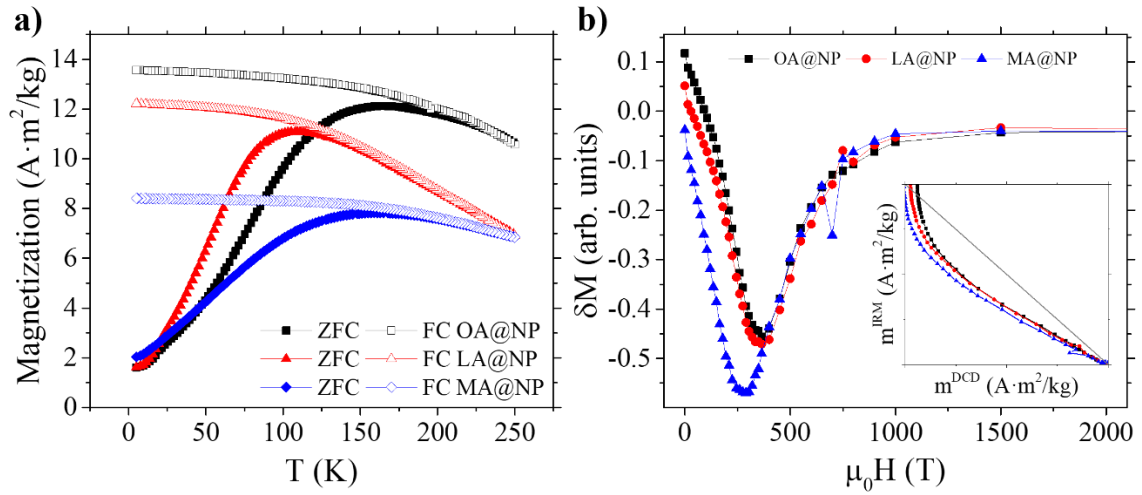


Figure 4. a) ZFC-FC curves of the three samples. b) δM curves calculated from m^{IRM} and m^{DCD} curves measured at 5 K. The inset graph shows the Henkel Plots for the three samples OA@NP, LA@NP, and MA@NP.

To further investigate the interaction among particles, we measured the remanent magnetization curves (m^{IRM} and m^{DCD}) at 5 K with a maximum field of 5 T (see a detailed definition in Supplementary Information S4). For an assembly of non-interacting single-domain particles with uniaxial anisotropy and coherent rotation magnetization process, the two remanence curves accomplish Wohlfarth's equation [38]:

$$m^{\text{DCD}}(H) = 1 - 2m^{\text{IRM}}(H) \quad (3)$$

where $m^{\text{DCD}}(H)$ and $m^{\text{IRM}}(H)$ represent the reduced terms $M^{\text{DCD}}(H)/M_S^{\text{DCD}}$ and $M^{\text{IRM}}(H)/M_S^{\text{IRM}}$, and M_S^{DCD} and M_S^{IRM} are the remanence saturation values for the DCD and IRM curves, respectively. The interparticle interactions are confirmed by the $m^{\text{DCD}}(H)$ versus the $m^{\text{IRM}}(H)$ curve shape in the Henkel plot (See inset Figure 4b). All the samples lie below the Wohlfarth diagonal line, indicating the predominance of demagnetizing interactions (negative dipolar interactions), i.e., interactions that have the effect of stabilizing the demagnetized state. In contrast, a curve in the region above the Wohlfarth line represents interactions promoting the magnetized state (exchange interactions). δM (See Figure 4b) is defined as:

$$\delta M = m^{\text{DCD}}(H) - [1 - 2m^{\text{IRM}}(H)] \quad (4)$$

Its dependence on the applied field H allows us to give a quantitative description of the deviations from Wohlfarth equation (3). MA@NP has the most intense demagnetizing interactions, probably due to its largest

particles, with larger magnetic moments, and agglomerates.

3.3. Magnetic hyperthermia measurements

The hyperthermic efficiency of the coated nanoparticles was estimated by recording the temperature increase under the application of an alternating magnetic field of 183 kHz frequency and 17 kA/m amplitude, which is below the safety threshold for clinical application [39]. The three samples display a high SAR of 29.3 W/g, 12.5 W/g, and 23.8 W/g for OA@NP, LA@NP, and MA@NP, respectively. The observed SAR values well scale with the physical and magnetic diameters of the inorganic core, and their magnetic properties. Despite the small average size of the nanoparticles, their intrinsic loss power $ILP = SAR \cdot H_0^{-2} \cdot f^{-1}$ values, 0.55 nHm²kg⁻¹, 0.24 nHm²kg⁻¹, and 0.45 nHm²kg⁻¹ for OA@NP, LA@NP, and MA@NP, respectively, are remarkably high [40,41]. When considering the concentration, the ILP value of OA@NP outperforms the other samples. Interparticle interactions have been found to be either positive or negative [26,42–44]. For OA@NP, the latter and that it shows some agglomeration [45], might be favoring the values obtained.

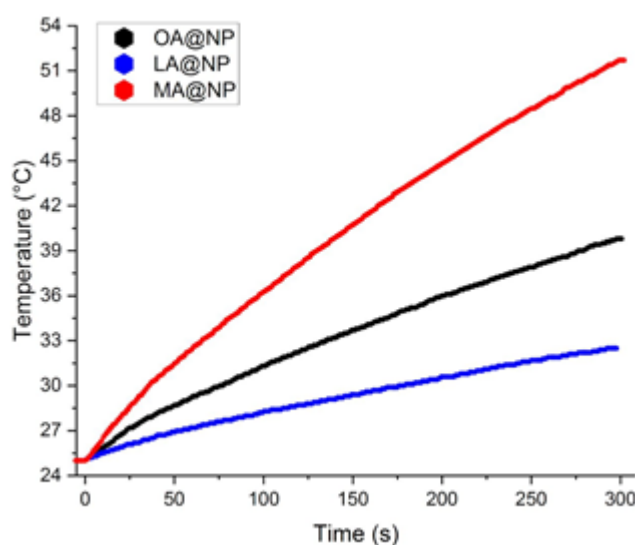


Figure 5. Temperature kinetics of water suspension of OA@NP, (conc. 12,0 mg/mL) LA@NP (13,6 mg/mL) and MA@NP (27,5 mg/mL) exposed to an alternating field (17 kA/m amplitude and 183 kHz frequency).

3.4. Relaxometric characterization

In the framework of biomedical applications, since compounds based on magnetite nanoparticles have been reported as good MRI contrast agents [15], we performed NMR relaxometry studies to evaluate the ability

of the fatty-acid-coated MNPs to act, as well as MRI agents.

The measurements of the nuclear relaxivities are suitable to predict the efficiency of magnetic nanoparticles in contrasting MR images [46], given that the nuclear relaxivities, both longitudinal, r_1 , and transverse, r_2 , are defined as:

$$r_i = \frac{1/T_{i,\text{meas}} - 1/T_{i,\text{dia}}}{c} \quad i = 1,2 \quad (5)$$

where $1/T_{i,\text{meas}}$ is the value measured for the sample with the iron concentration c (mmol/L) and $1/T_{i,\text{dia}}$ represents the nuclear relaxation rate of the diamagnetic host solution (water in our case).

In detail, we performed ^1H -NMR measurements at frequencies of 56.7 MHz, 21.3 MHz, and 9.0 MHz, respectively, that cover most of the typical fields, $H = 1.33$ T (near $H = 1.5$ T), 0.5 T, and 0.2 T, respectively, of MRI tomographs, used both in clinics and in research laboratories.

At these fields, the r_1 ^1H -NMR longitudinal nuclear relaxivity values of fatty acid MNPs (reported in Table 3) were a little bit lower or comparable, depending on the MNPs and on the field, to those of Endorem® [47], the withdrawn commercial T_2 contrast agent still generally used for comparison in literature.

Table 3. Longitudinal (r_1) and transverse (r_2) relaxivities of fatty acid MNPs at given fields, $H = 0.2$ T, 0.5 T and 1.33 T and for comparison of Endorem®, withdrawn commercial product.

Sample	$r_1@0.2\text{T}$ ($\text{s}^{-1} \cdot$ mmol^{-1} $\cdot \text{L}$)	$r_1@0.5\text{T}$ (s^{-1} mmol^{-1} L)	$r_1@1.33\text{T}$ (s^{-1} mmol^{-1} L)	$r_2@0.2\text{T}$ (s^{-1} mmol^{-1} L)	$r_2@0.5\text{T}$ (s^{-1} mmol^{-1} L)	$r_2@1.33\text{T}$ (s^{-1} mmol^{-1} L)

However, in the same clinical fields, the r_2 ^1H -NMR transverse nuclear relaxivity values of all fatty acid MNPs (see Table 3) showed on average a 100% increase compared to Endorem®, envisaging a potential use of these systems as T_2 contrast agents in MRI, in particular for MA@NP that show the highest values. Size and M_S are the fundamental parameters for

a good r_2 relaxivity. The broad size distribution of the MA@NP sample will favor the larger r_2 with respect to Endorem® [6].

Moreover, the higher r_2 values obtained in our system concerning Endorem® allow us to conclude that, with the same amount of contrast agent, in principle, the contrast-to-noise-ratio in magnetic resonance images might reduce the injected doses.

3.5. Biosensing Application

The particles' applicability as detection labels in inductive sensing with low amplitude magnetic field depends mainly on their initial magnetic susceptibility (for detection and quantification) and their clustering (for signal amplification).

Our inductive sensor has been described elsewhere [48]. It consists of a planar coil whose radio frequency impedance is monitored while the LFA strip is displaced on it in smooth contact in 100 μm steps. In the presence of a magnetic material, the coil acts both as exciting and detecting probe, producing an increase of the impedance proportional to the initial magnetic susceptibility and the number of particles. For monodomain magnetic nanoparticles the susceptibility is maximum at the critical superparamagnetic size (following Néel relaxation model, the initial susceptibility is proportional to the volume as far as the particles are small enough to be superparamagnetic) [49].

Initial magnetic susceptibility (χ^{DC}) spectra were obtained for the three particles in the range of 10–10000 Hz, showing no significant variation. Table 2 gathers the χ^{DC} values at 10 Hz, which agree with Néel's model for a MNPs ensemble with randomly oriented easy axes:

$$\chi^{\text{DC}} = \frac{2}{3} \left(\frac{\mu_0 \rho^2 M_S^2 V}{k_B T} + \frac{\mu_0 \rho^2 M_S^2 V}{K_{\text{eff}}} \right) \quad (6)$$

In equation (6), μ_0 is the vacuum permeability, ρ the magnetite density (5170 kg m⁻³), V the particle mean volume, T the temperature, k_B the Boltzmann constant, and K_{eff} the effective anisotropy constant. Using the parameters of Table 2, and the sizes obtained by TEM, equation (6) yields χ^{DC} values of 21, 13, and 8 for OA@NP, LA@NP, and MA@NP, respectively.

To evaluate the MNPs effect on the sensor signal, we prepared samples

depositing original solution droplets on a blotting paper (2 mm × 10 mm size) as described in Section 2.8. The sensitivity for each ferrofluid is shown in the inset of Figure 6a, being 2.60%, 2.22%, and 1.54% per mg for OA@NP, LA@NP, and MA@NP, respectively. Their relative values match the corresponding initial susceptibility results given in Table 2. As expected in an inductive sensor that uses a very low amplitude exciting field, the particles' signal should increase with their initial magnetic susceptibility.

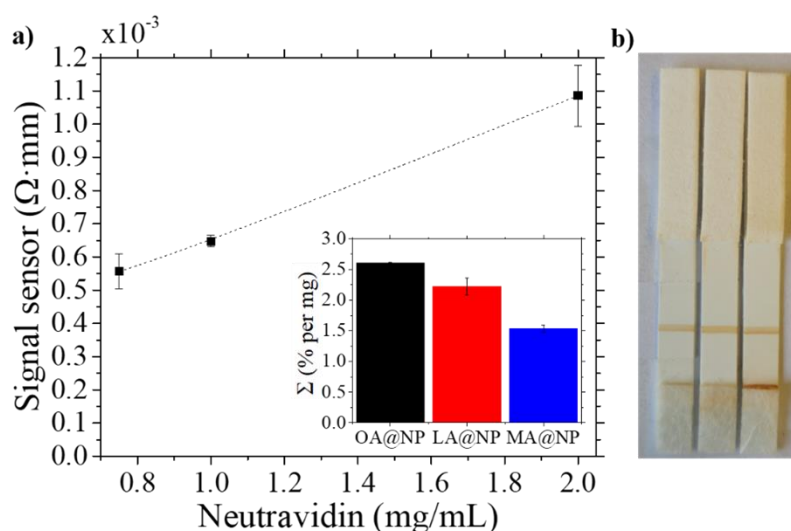


Figure 6. a) Magnetic signal obtained in the sensor for the LFA with neutravidin-conjugated LA@NP particles. The error bars show the standard deviation. The dashed lines serve as a guide to the eye. Inset: Percentage increase per mg of the magnetic signal in the sensor for the three samples. b) Image of the 1 mg/mL of neutravidin LFA run with, from left to right, OA@NP, LA@NP, and MA@NP.

Once we assessed the particle performance in the sensor, the next step involved studying the bioconjugation reaction's influence. The procedure implies the attachment of a biomolecule to the particle. It is done via the superficial modification of the MNPs, involving the activation of the carboxylic groups at the fatty acid's outer shell (see Figure 1a and b). During these chemical reactions, some agglomeration of the particles may occur, affecting the number of particles that attach to each protein and, consequently, the signal of the magnetic LFA. This process has been monitored by the d_{DLS} measurements before and after the biofunctionalization.

In this work, we used neutravidin-biotin affinity to study the three particle types as labels in the LFAs. For this purpose, we have bioconjugated them using three different concentrations of neutravidin.

Table 4 displays the parameters of the volume-fraction distributions of sizes obtained from DLS measurements. Although, the DLS technique directly provides intensity-weighted distributions of size, this type of representation is not the best choice for our application because the larger particles become overrepresented (the scattered light is proportional to the 6th power of the particle size) [50]. Transforming into another type of distribution relies on acceptable assumptions like the sphericity of the particles. Number-weighted distributions are suitable to compare with TEM, but in this study, the most influential parameter is the volume of magnetic material, which is directly proportional to the magnetic moment and, correspondingly, to the sensor detected signal. For this reason, we present in Table 4 the volume fractions of the two-peaked size distributions. Supplementary Information Figure S5 contains additional information on DLS measurements.

Table 4. Neutravidin concentrations for the particle bioconjugation and the corresponding main parameters of the two-peaked volume distribution of sizes.

	Neutravidin concentration (mg/ mL)	Peak 1 d_{DLS} (nm)	Peak 2 d_{DLS} (nm)	Peak 1 Volume fraction (%)	Peak 2 Volume fraction (%)
OA@NP	0	45	158	34	66
	0.75	59	208	25	75
	1	58	446	11	89
	2	107	553	9	91
LA@NP	0	23	0	100	0
	0.75	36	141	58	42
	1	38	149	45	55
	2	41	175	50	50
MA@NP	0	46	141	44	56
	0.75	105	442	26	74
	1	118	540	14	86
	2	53	212	15	85

Table 4 shows the hydrodynamic sizes before the biofunctionalization in the row labeled as zero-neutravidin content. Typically, hydrodynamic

sizes are 10–15% larger than TEM sizes due to the diffuse layer and surfactant at the particle surface. The values for OA@NP and MA@NP indicate that in them, there is already some particle agglomeration before the neutravidin addition.

The agglomerate sizes significantly increase with increasing amount of protein added, proving the successful neutravidin's conjugation to the particle surface. Some agglomeration can be beneficial for a detection label because it increases the ratio particle:molecule. However, agglomerates larger than 200 nm can be detrimental to the fluid sample flow through the membrane pores and can hamper the antigen-antibody reaction due to steric impediments. These characteristics, the agglomerate size, and abundance, are decisive in applying the particles for LFA.

The DLS-size before bioconjugation in sample LA@NP is 23 nm. Considering the size observed by TEM plus an increase of 10-15%, typical of the diffuse layer and surfactant at the particle surface, the individual DLS-particle size should be around 10 nm. The measured value indicates the existence of clusters formed by few individual nanoparticles. After bioconjugation, the cluster size increases to approximately 40 nm due to the protein. Only a few larger agglomerates (less than 1% of the total number) with sizes around 150 nm, appear at this stage. They can only be detected in the volume-weighted distributions, as can be seen in Figure S5. The dominating agglomerate size flows through the membrane pores, and the detected signal presents an only peak as expected when the particles distribute themselves homogeneously at the test line. Figure 7 shows the scanning of the LFA with LA@NP sample and 2 mg/mL of neutravidin.

The biofunctionalization of MA@NP produces oversized agglomerates (larger than 200 nm) that correspond to more than 75% of the sample volume, even with the lowest neutravidin concentration. This can be caused by an insufficient MA coating, leading to a higher proportion among the EDC/NHS reagents and the available carboxylic groups during the biofunctionalization. Hence, more of the latter are activated in the process, favoring the agglomeration through the neutravidin. These enormous agglomerates have two different and undesirable effects on the LFAs. The first one is the difficulty of the sample to flow through the membrane pores. It can be seen in the LFAs as a brownish line just after

the conjugate pad, as the biggest particles cannot flow and hinder the smaller ones (see Figure 6b). The second effect happens at the test line. Here, the MNPs functionalized with the neutravidin get trapped by the biotin. However, some large neutravidin-MNPs agglomerates form a shield when facing the test line, hindering the rest of the particles' regular flow, whether functionalized or not. Figure 7 shows the LFA scanning with MA@NP and 2 mg/mL of neutravidin. A darker and thin line can be appreciated and associated with an additional peak in the detected signal. In this case, the larger signal observed for the MA@NP LFA is not due to better detection but to the unspecific accumulation of MNPs.

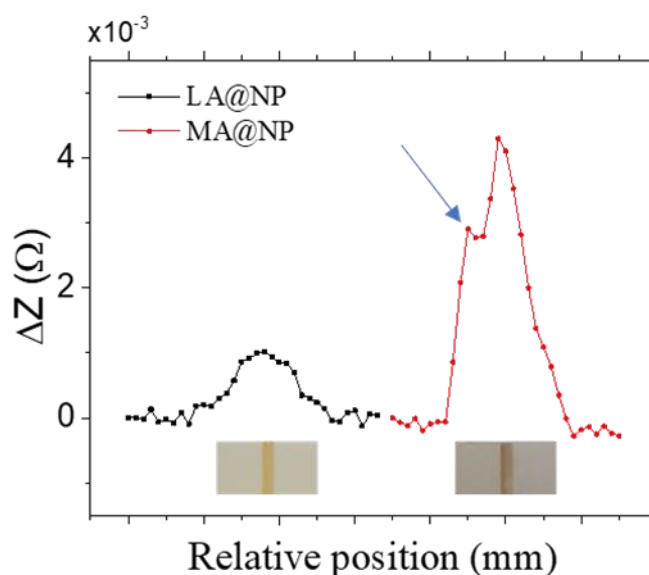


Figure 7. Test line sensor evaluation for the LFAs using LA@NP (black) and MA@NP (red) with 2 mg/mL neutravidin. The horizontal ticks represent 1 mm displacement steps. Bottom: Photographs of both LFAs. The blue arrow points at the peak corresponding to the particle accumulation in the LA@NP.

For sample OA@NP, this behavior is also patent for neutravidin concentration of 1 mg/mL, and hence, the only valid LFA is the one with the lowest concentration, 0.75 mg/mL (for this concentration, the number of large particles is small and not evident in the number-weighted size distribution.) In this case, the excessive agglomeration is likely to be caused by cross-linking among the preexisting agglomerates.

This work has determined that the LA-coating yields the best particles in the study for detection nanolabeling in LFAs. They have superparamagnetic behavior at room temperature, which provides a high initial magnetic susceptibility and contributes to excellent colloidal stability, surface carboxylic groups before bioconjugation, and an initial beneficial monodisperse agglomeration, which increases the magnetic

material per unit molecule without hindering the regular flowing.

4. Conclusions

Magnetic nanoparticles are a driving force in current solutions for medical problems. Their properties can make them an ideal multiplatform for fast, safe, and reliable diagnosis and therapy. In this work, three different magnetite-based ferrofluids have been synthesized by co-precipitation. A double-fatty acid layer of OA, LA, and MA renders the aqueous solutions stable and biocompatible. The characterization of the samples shows similar inorganic cores around 10 nm, with large size distributions, which is noticeable for MA@NP. The surface characterization confirmed the fatty acids' presence, whose extents are different for the MA@NP sample. The magnetic characterization showed superparamagnetic particles with saturation values close to 80 Am²/kg. The assessment of δM and Henkel plots showed the dominant presence of demagnetizing interactions for the three samples, but especially for MA@NP, probably again because of larger particles within the sample.

We tested these samples in three different bioapplications. They all showed promising results for magnetic hyperthermia and relaxation measurements. The r_2 values of our samples largely exceed those of commercial Endorem®, and their ILP values were also satisfactory.

The clustered LA@NP are excellent for detection labeling, as concluded from the application of the studied particles for lateral flow immunoassays and their magnetic quantification. These nanolabels are superparamagnetic at room temperature, which provides a high initial magnetic susceptibility and contributes to excellent colloidal stability. The fatty acid's carboxylic groups can be activated permitting the amide bond for conjugation to the protein. The LA@NP form monodisperse-sized clusters gathering a few particles, which increases the magnetic material per unit molecule without hindering the regular flowing or the antigen-antibody reactions. The fatty acid coating also enabled a smooth flow along the LFA membrane that presented no detectable residuals out of the test and control lines and the fiber pads.

5. Acknowledgments

This work was partially funded by the Spanish Ministry of Economy and

Competitiveness under projects MAT2017-84959-C2-1-R and the Principality of Asturias (Spain) under project IDI/2018/000185. The work of Fl.B., V.S., and L.V. was mainly supported by the RA-TB/CFATR/LMF multiannual research program 2021–2025 and JNIR-RO grant 04-4-1142-2021/2025 - item 34 - JINR Order no. 365/11.05.2021. M.S., D.P., Fl.B., V.S. and L.V. are indebted for the partial support from the bilateral agreement between Romanian Academy and Italian National research Council project Ferro-Tera. M.S. was supported by a “Severo Ochoa” fellowship (Consejería de Educación y Cultura del Gobierno del Principado de Asturias, grant BP19-141). She also thanks the University of Oviedo, the Ministry of Education, Culture and Sport, and Banco Santander for grant CEI15-24. J.L.M. was supported by the University Technological Institute of Asturias (IUTA) under grant SV-20-GIJÓN-1-22.

The authors would like to acknowledge the technical support provided by Scientific and Technical Service of the University of Oviedo. Some of the figures of this articles have been created with Biorender.com

References

- [1] H. Sung, J. Ferlay, R.L. Siegel, M. Laversanne, I. Soerjomataram, A. Jemal, F. Bray, Global Cancer Statistics 2020: GLOBOCAN Estimates of Incidence and Mortality Worldwide for 36 Cancers in 185 Countries, *CA. Cancer J. Clin.* 71 (2021) 209–249. <https://doi.org/10.3322/CAAC.21660>.
- [2] W. Hamilton, Cancer diagnostic delay in the COVID-19 era: what happens next?, *Lancet Oncol.* 21 (2020) 1000–1002. [https://doi.org/10.1016/S1470-2045\(20\)30391-0](https://doi.org/10.1016/S1470-2045(20)30391-0).
- [3] J.Y. Blay, S. Boucher, B. Le Vu, C. Cropet, S. Chabaud, D. Perol, E. Barranger, M. Campone, T. Conroy, C. Coutant, R. De Crevoisier, A. Debreuve-Theresette, J.P. Delord, P. Fumoleau, J. Gentil, F. Gomez, O. Guerin, A. Jaffré, E. Lartigau, C. Lemoine, M.A. Mahe, F.X. Mahon, H. Mathieu-Daude, Y. Merrouche, F. Penault-Llorca, X. Pivot, J.C. Soria, G. Thomas, P. Vera, T. Vermeulin, P. Viens, M. Ychou, S. Beaupere, Delayed care for patients with newly diagnosed cancer due to COVID-19 and estimated impact on cancer mortality in France, *ESMO Open.* 6 (2021) 100134. <https://doi.org/10.1016/J.ESMOOP.2021.100134>.
- [4] D. Quesada-González, A. Merkoçi, Nanomaterial-based devices for point-of-care diagnostic applications, *Chem. Soc. Rev.* 47 (2018) 4697–4709. <https://doi.org/10.1039/C7CS00837F>.

- [5] P. Chun, Colloidal Gold and Other Labels for Lateral Flow Immunoassays, *Lateral Flow Immunoass.* (2009) 1–19. https://doi.org/10.1007/978-1-59745-240-3_5.
- [6] J. Estelrich, M.J. Sánchez-Martín, M.A. Busquets, Nanoparticles in magnetic resonance imaging: from simple to dual contrast agents, *Int. J. Nanomedicine.* 10 (2015) 1727–1741. <https://doi.org/10.2147/IJN.S76501>.
- [7] M. Rogosnitzky, S. Branch, Gadolinium-based contrast agent toxicity: a review of known and proposed mechanisms, *BioMetals.* 29 (2016) 365–376. <https://doi.org/10.1007/S10534-016-9931-7/TABLES/2>.
- [8] D. Chang, M. Lim, J.A.C.M. Goos, R. Qiao, Y.Y. Ng, F.M. Mansfeld, M. Jackson, T.P. Davis, M. Kavallaris, Biologically Targeted Magnetic Hyperthermia: Potential and Limitations, *Front. Pharmacol.* 0 (2018) 831. <https://doi.org/10.3389/FPHAR.2018.00831>.
- [9] M. Salvador, J.C. Martínez-García, M.P. Fernández-García, M.C. Blanco-López, M. Rivas, Biological and Medical Applications of Magnetic Nanoparticles, in: *Magn. Meas. Tech. Mater. Charact.*, Springer, Cham, 2021: pp. 771–804. https://doi.org/10.1007/978-3-030-70443-8_26.
- [10] A. Moyano, E. Serrano-Pertierra, M. Salvador, J.C. Martínez-García, M. Rivas, M.C. Blanco-López, Magnetic lateral flow immunoassays, *Diagnostics.* 10 (2020) 288. <https://doi.org/10.3390/diagnostics10050288>.
- [11] D. Quesada-González, A. Merkoçi, Nanoparticle-based lateral flow biosensors, *Biosens. Bioelectron.* 73 47–63. <http://dx.doi.org/10.1016/j.bios.2015.05.050> (accessed September 6, 2021).
- [12] V.G. Panferov, I. V. Safenkova, A. V. Zherdev, B.B. Dzantiev, Setting up the cut-off level of a sensitive barcode lateral flow assay with magnetic nanoparticles, *Talanta.* 164 (2017) 69–76. <https://doi.org/10.1016/j.talanta.2016.11.025>.
- [13] Z. Huang, S. Hu, Y. Xiong, H. Wei, H. Xu, H. Duan, W. Lai, Application and development of superparamagnetic nanoparticles in sample pretreatment and immunochromatographic assay, 2019. <https://doi.org/10.1016/j.trac.2019.03.004> (accessed March 24, 2021).
- [14] T. Lam, P. Pouliot, P.K. Avti, F. Lesage, A.K. Kakkar, Superparamagnetic iron oxide based nanoprobe for imaging and theranostics, *Adv. Colloid Interface Sci.* 199–200 (2013) 95–113. <https://doi.org/10.1016/J.CIS.2013.06.007>.
- [15] Z.R. Stephen, F.M. Kievit, M. Zhang, Magnetite nanoparticles for medical MR imaging, *Mater. Today.* 14 (2011) 330–338.

[https://doi.org/10.1016/S1369-7021\(11\)70163-8](https://doi.org/10.1016/S1369-7021(11)70163-8).

- [16] D. Ortega, Q.A. Pankhurst, Magnetic hyperthermia, in: 2012: pp. 60–88. <https://doi.org/10.1039/9781849734844-00060>.
- [17] D. Bica, L. Vékás, M. V. Avdeev, O. Marinică, V. Socoliuc, M. Bălăsoiu, V.M. Garamus, Sterically stabilized water based magnetic fluids: Synthesis, structure and properties, *J. Magn. Mater.* 311 (2007) 17–21. <https://doi.org/10.1016/j.jmmm.2006.11.158>.
- [18] D. Lago-Cachón, M. Oliveira-Rodríguez, M. Rivas, M.C. Blanco-López, J.C. Martínez-García, A. Moyano, M. Salvador, J.A. García, Scanning Magneto-Inductive Sensor for Quantitative Assay of Prostate-Specific Antigen, *IEEE Magn. Lett.* 8 (2017). <https://doi.org/10.1109/LMAG.2017.2702108>.
- [19] G. Muscas, G. Singh, W.R. Glomm, R. Mathieu, P.A. Kumar, G. Concas, E. Agostinelli, D. Peddis, Tuning the size and shape of oxide nanoparticles by controlling oxygen content in the reaction environment: Morphological analysis by aspect maps, *Chem. Mater.* 27 (2015) 1982–1990. <https://doi.org/10.1021/cm5038815>.
- [20] M. V. Avdeev, B. Mucha, K. Lamszus, L. Vékás, V.M. Garamus, A. V. Feoktystov, O. Marinica, R. Turcu, R. Willumeit, Structure and in vitro biological testing of water-based ferrofluids stabilized by monocarboxylic acids, *Langmuir.* 26 (2010) 8503–8509. <https://doi.org/10.1021/la904471f>.
- [21] H. Borchert, E. V. Shevchenko, A. Robert, I. Mekis, A. Kornowski, G. Grübel, H. Weller, Determination of nanocrystal sizes: A comparison of TEM, SAXS, and XRD studies of highly monodisperse CoPt₃ particles, *Langmuir.* 21 (2005) 1931–1936. <https://doi.org/10.1021/la0477183>.
- [22] R.W. Chantrell, J. Popplewell, S.W. Charles, Measurements of particle size distribution parameters in ferrofluids, *IEEE Trans. Magn.* 14 (1978) 975–977. <https://doi.org/10.1109/TMAG.1978.1059918>.
- [23] M. Unni, A.M. Uhl, S. Savliwala, B.H. Savitzky, R. Dhavalikar, N. Garraud, D.P. Arnold, L.F. Kourkoutis, J.S. Andrew, C. Rinaldi, Thermal Decomposition Synthesis of Iron Oxide Nanoparticles with Diminished Magnetic Dead Layer by Controlled Addition of Oxygen, *ACS Nano.* 11 (2017) 2284–2303. <https://pubs.acs.org/doi/abs/10.1021/acsnano.7b00609> (accessed March 4, 2021).
- [24] J.D. Clogston, A.K. Patri, Zeta potential measurement., *Methods Mol. Biol.* 697 (2011) 63–70. https://doi.org/10.1007/978-1-60327-198-1_6.
- [25] Y. Wang, H. Xu, M. Wei, H. Gu, Q. Xu, W. Zhu, Study of superparamagnetic nanoparticles as labels in the quantitative lateral flow immunoassay, *Mater. Sci. Eng. C.* 29 (2009) 714–718.

<https://doi.org/10.1016/j.msec.2009.01.011>.

- [26] D. Niculaes, A. Lak, G.C. Anyfantis, S. Marras, O. Laslett, S.K. Avugadda, M. Cassani, D. Serantes, O. Hovorka, R. Chantrell, T. Pellegrino, Asymmetric Assembling of Iron Oxide Nanocubes for Improving Magnetic Hyperthermia Performance, *ACS Nano*. 11 (2017) 12121–12133. https://doi.org/10.1021/ACSNANO.7B05182/SUPPL_FILE/NN7B05182_SI_001.PDF.
- [27] Q. Lan, C. Liu, F. Yang, S. Liu, J. Xu, D. Sun, Synthesis of bilayer oleic acid-coated Fe₃O₄ nanoparticles and their application in pH-responsive Pickering emulsions, *J. Colloid Interface Sci.* 310 (2007) 260–269. <https://doi.org/10.1016/j.jcis.2007.01.081>.
- [28] R. Lenin, P.A. Joy, Role of Primary and Secondary Surfactant Layers on the Thermal Conductivity of Lauric Acid Coated Magnetite Nanofluids, *J. Phys. Chem. C*. 120 (2016) 11640–11651. <https://doi.org/10.1021/acs.jpcc.5b12476>.
- [29] M.J. Chen, H. Shen, X. Li, J. Ruan, W.Q. Yuan, Magnetic fluids' stability improved by oleic acid bilayer-coated structure via one-pot synthesis, *Chem. Pap.* 70 (2016) 1642–1648. <https://doi.org/10.1515/chempap-2016-0096>.
- [30] L. Zhang, R. He, H.C. Gu, Oleic acid coating on the monodisperse magnetite nanoparticles, *Appl. Surf. Sci.* 253 (2006) 2611–2617. <https://doi.org/10.1016/j.apsusc.2006.05.023>.
- [31] W. Li, Jan Zaloga, Y. Ding, Y. Liu, C. Janko, M. Pischetsrieder, C. Alexiou, A.R. Boccaccini, Facile preparation of multifunctional superparamagnetic PHBV microspheres containing SPIONs for biomedical applications, *Sci. Rep.* 6 (2016) 1–12. <https://doi.org/10.1038/srep23140>.
- [32] K. Yang, H. Peng, Y. Wen, N. Li, Re-examination of characteristic FTIR spectrum of secondary layer in bilayer oleic acid-coated Fe₃O₄ nanoparticles, *Appl. Surf. Sci.* 256 (2010) 3093–3097. <https://doi.org/10.1016/j.apsusc.2009.11.079>.
- [33] M. V. Avdeev, D. Bica, L. Vekas, V.L. Aksenov, A. V. Feoktystov, L. Rosta, V.M. Garamus, R. Willumeit, Structural aspects of stabilization of magnetic fluids by mono-carboxylic acids, in: *Solid State Phenom.*, Trans Tech Publications Ltd, 2009: pp. 182–185. <https://doi.org/10.4028/www.scientific.net/SSP.152-153.182>.
- [34] M. Bloemen, W. Brullot, T.T. Luong, N. Geukens, A. Gils, T. Verbiest, Improved functionalization of oleic acid-coated iron oxide nanoparticles for biomedical applications, *J. Nanoparticle Res.* 14 (2012) 1–10. <https://doi.org/10.1007/s11051-012-1100-5>.
- [35] H. Zhang, D. Zeng, Z. Liu, The law of approach to saturation in ferromagnets originating from the magnetocrystalline anisotropy, *J. Magn. Mater.* 322 (2010) 2375–2380.

<https://doi.org/10.1016/j.jmmm.2010.02.040>.

- [36] R.M. Cornell, U. Schwertmann, *The Iron Oxides*, Wiley, 2003. <https://doi.org/10.1002/3527602097>.
- [37] K.L. Livesey, S. Ruta, N.R. Anderson, D. Baldomir, R.W. Chantrell, D. Serantes, Beyond the blocking model to fit nanoparticle ZFC/FC magnetisation curves, *Sci. Reports* 2018 81. 8 (2018) 1–9. <https://doi.org/10.1038/s41598-018-29501-8>.
- [38] E.P. Wohlfarth, Relations between different modes of acquisition of the remanent magnetization of ferromagnetic particles, *American Institute of Physics AIP*, n.d. <https://doi.org/10.1063/1.1723232>.
- [39] W.J. Atkinson, I.A. Brezovich, D.P. Chakraborty, Usable Frequencies in Hyperthermia with Thermal Seeds, *IEEE Trans. Biomed. Eng. BME-31* (1984) 70–75. <https://doi.org/10.1109/TBME.1984.325372>.
- [40] L. Lartigue, C. Innocenti, T. Kalaivani, A. Awwad, M.D.M. Sanchez Duque, Y. Guari, J. Larionova, C. Gueírin, J.L.G. Montero, V. Barragan-Montero, P. Arosio, A. Lascialfari, D. Gatteschi, C. Sangregorio, Water-dispersible sugar-coated iron oxide nanoparticles. An evaluation of their relaxometric and magnetic hyperthermia properties, *J. Am. Chem. Soc.* 133 (2011) 10459–10472. https://doi.org/10.1021/JA111448T/SUPPL_FILE/JA111448T_SI_001.PDF.
- [41] A. Lasoialfari, M. Filibian, C. Sangregorio, P. Carretta, In vivo biomedical applications of magnetic resonance and magnetic materials, *Riv. Del Nuovo Cim.* 36 (2013) 211–271. <https://doi.org/10.1393/NCR/I2013-10089-8>.
- [42] C. Haase, U. Nowak, Role of dipole-dipole interactions for hyperthermia heating of magnetic nanoparticle ensembles, *Phys. Rev. B - Condens. Matter Mater. Phys.* 85 (2012) 045435. <https://doi.org/10.1103/PHYSREVB.85.045435/FIGURES/6/ME DIUM>.
- [43] I. Andreu, E. Natividad, L. Solozábal, O. Roubeau, Nano-objects for addressing the control of nanoparticle arrangement and performance in magnetic hyperthermia, *ACS Nano.* 9 (2015) 1408–1419. https://doi.org/10.1021/NN505781F/SUPPL_FILE/NN505781F_SI_001.PDF.
- [44] U. Engelmann, E.M. Buhl, M. Baumann, T. Schmitz-Rode, I. Slabu, Agglomeration of magnetic nanoparticles and its effects on magnetic hyperthermia, *Curr. Dir. Biomed. Eng.* 3 (2017) 457–460. <https://doi.org/10.1515/CDBME-2017-0096>.
- [45] M. Jeong, S. Lee, D.Y. Song, S. Kang, T.-H. Shin, J. Choi, Hyperthermia Effect of Nanoclusters Governed by Interparticle

- Crystalline Structures, ACS Omega. (2021) acsomega.1c04632. <https://doi.org/10.1021/ACSOMEGA.1C04632>.
- [46] D. Kruk, A. Korpała, S.M. Taheri, A. Kozłowski, S. Förster, E.A. Rössler, ^1H relaxation enhancement induced by nanoparticles in solutions: Influence of magnetic properties and diffusion, *J. Chem. Phys.* 140 (2014) 174504. <https://doi.org/10.1063/1.4871461>.
- [47] M. Basini, A. Guerrini, M. Cobiañchi, F. Orsini, D. Bettega, M. Avolio, C. Innocenti, C. Sangregorio, A. Lascialfari, P. Arosio, Tailoring the magnetic core of organic-coated iron oxides nanoparticles to influence their contrast efficiency for Magnetic Resonance Imaging, *J. Alloys Compd.* 770 (2019) 58–66. <https://doi.org/10.1016/j.jallcom.2018.08.120>.
- [48] D. Lago-Cachón, M. Rivas, J.C. Martínez-García, M. Oliveira-Rodríguez, M.C. Blanco-López, J.A. García, High frequency lateral flow affinity assay using superparamagnetic nanoparticles, *J. Magn. Magn. Mater.* 423 (2017) 436–440. <https://doi.org/10.1016/j.jmmm.2016.09.106>.
- [49] M. Salvador, Á. Gallo-Cordova, A. Moyano, J.C. Martínez-García, M.C. Blanco-López, M. Puerto Morales, M. Rivas, Improved magnetic lateral flow assays with optimized nanotags for point-of-use inductive biosensing, *Analyst.* 145 (2020) 5905–5914. <https://doi.org/10.1039/d0an00849d>.
- [50] J. Stetefeld, S.A. McKenna, T.R. Patel, Dynamic light scattering: a practical guide and applications in biomedical sciences, *Biophys. Rev.* 8 (2016) 409–427. <https://doi.org/10.1007/S12551-016-0218-6/TABLES/3>.

SUPPLEMENTARY INFORMATION

S1. X-ray diffraction

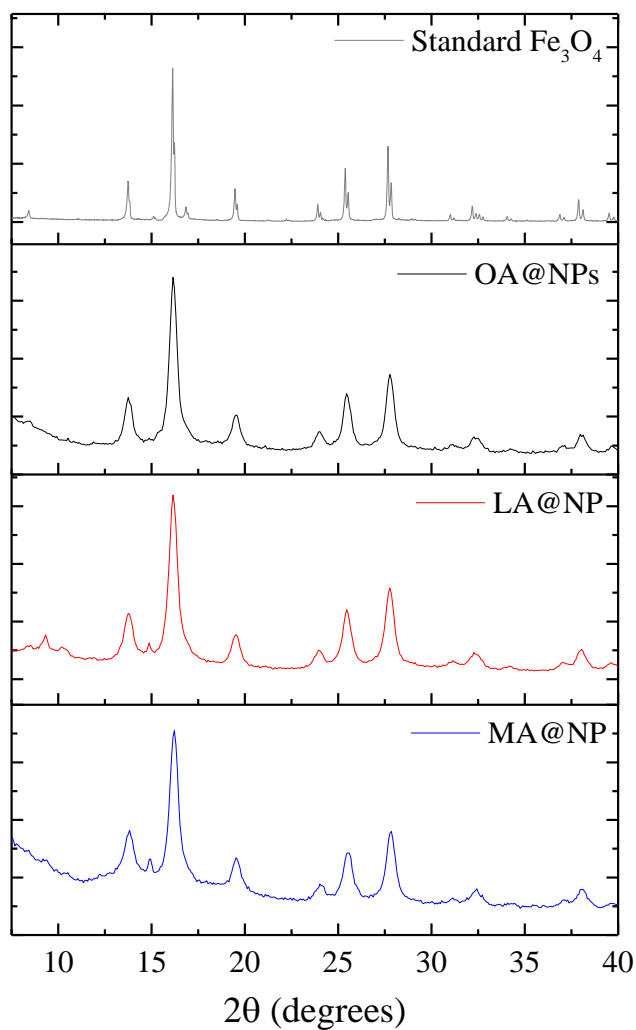


Figure S1. XRD patterns for the three samples OA@NP, LA@NP, and MA@NP compared with the standard Fe_3O_4 . The value for the mean crystallite size d_{XRD} has been estimated from the Rietveld refinement of the XRD patterns.

S2. TGA curves

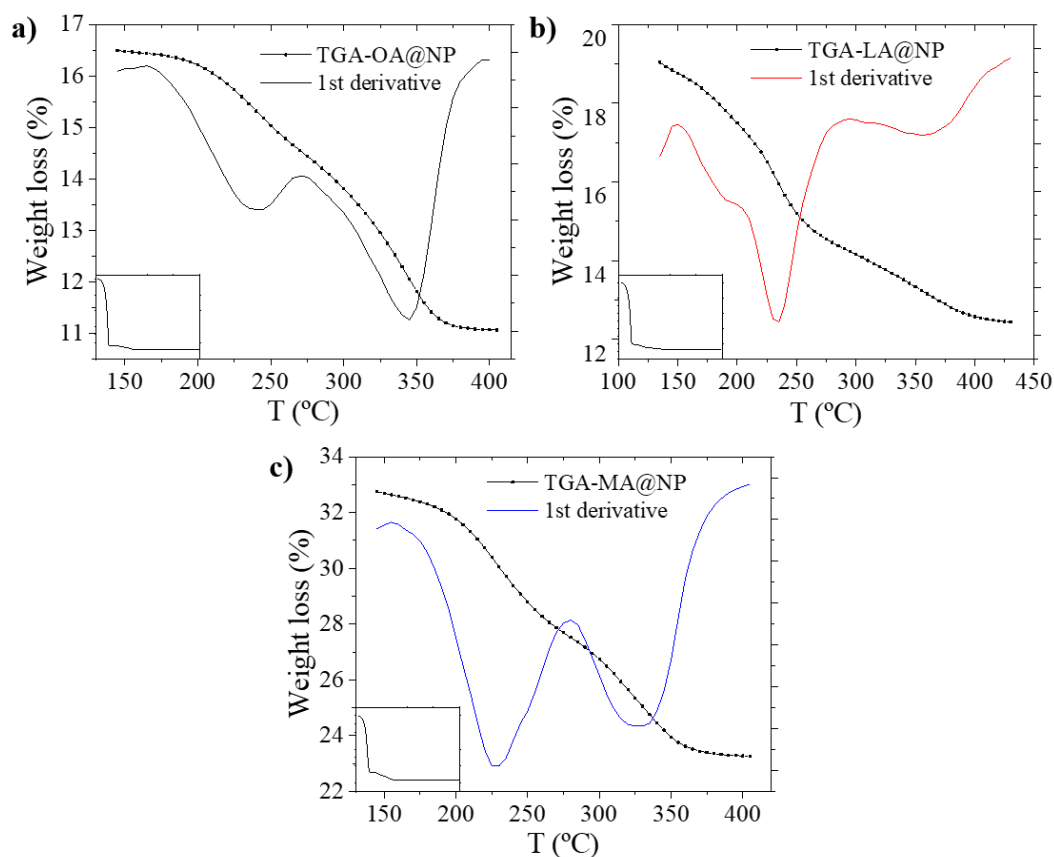


Figure S2. TGA curves and their first derivative of the three samples a) OA@NP, b) LA@NP and c) MA@NP. The presence of a double peak in the derivative of the curves suggests the presence of a double layer of surfactant on the surface of the particles. The first peak suggests the release and decomposition of slightly bound or physically adsorbed surfactant molecules. On the other hand, the second weight loss that took place at higher temperatures could be due to the breaking of stronger bonds, i.e., chemically bound surfactants molecules to the surface of the particles, and their decomposition. Inset of the graphs show the whole TGA thermogram from 25 to 950 °C.

S3. FTIR spectra

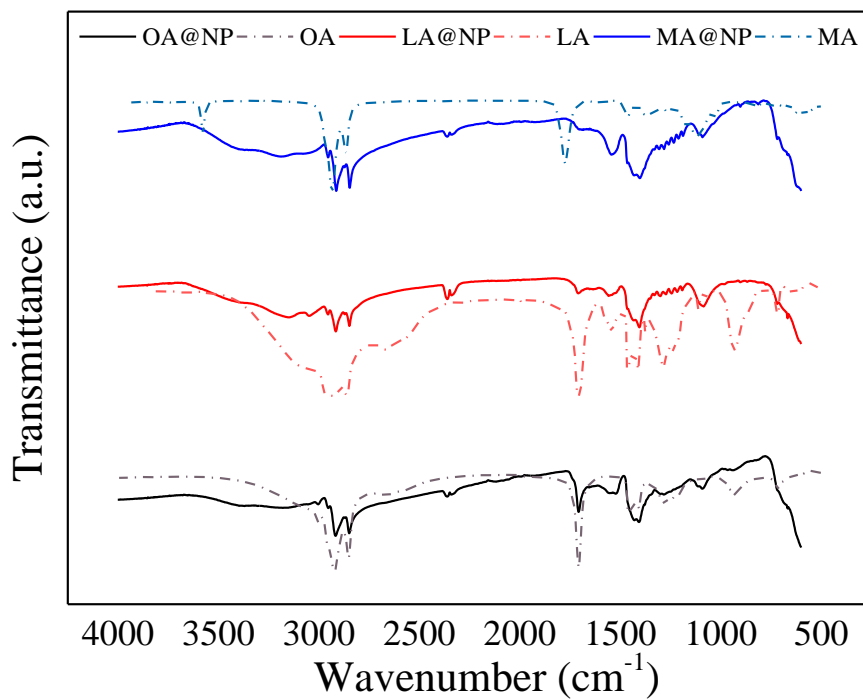


Figure S3. From bottom to top, FTIR spectrum comparison of the OA@NP and OA, LA@NP and LA and MA@NP and MA.

S4. IRM and DCD remanence curves

The field dependence of remanent magnetization was measured using the IRM (Iso-thermal Remanent Magnetization) and DCD (Direct Current Demagnetization) protocols. According to the IRM protocol, the samples, in the demagnetized state, were cooled in a zero magnetic field down to 5 K. At this temperature, a small external field was applied for 10 s, then switched off, and finally, the remanence (m^{IRM}) was measured. The process was repeated, increasing the field in steps up to 5 T. In a DCD measurement, the initial state was the magnetically saturated one. After cooling the sample at 5 K, an external field of -5 T was applied for 10 s, then it is turned off and the remanence (m^{DCD}) was measured. As in IRM, a small external field in the opposite direction to magnetization was applied for 10 s and then switched off. Finally, the remanent magnetization was measured. This was repeated increasing the field up to +5 T.

S5. Biofunctionalization process

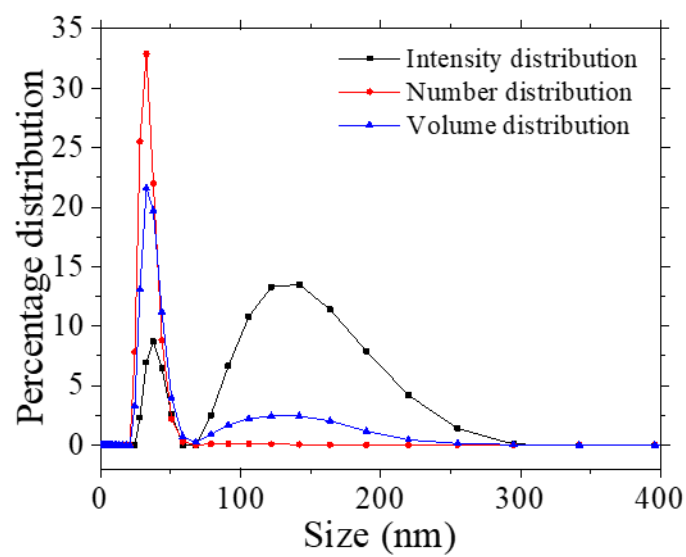


Figure S4. Intensity (black), number (red) and volume (blue) distributions for the sample LA@NP functionalized with 0.75 mg/mL of neutravidin.

Section III - Chapter 2

Improved Magnetic Lateral Flow Assays with Optimized Nanotags for Point-of-use Inductive Biosensing

Introduction and motivation

Fast, inexpensive bioanalytical techniques have become crucial in our days for biomedicine and food control. Lateral flow immunoassays are already an established technique whose further extension is only hindered by its moderate sensitivity compared with other more complex techniques. The use of magnetic labels combined with inductive detection is a realistic promise to improve the sensitivity of detection and quantification, yielding a new generation of friendly portable biosensors to be deployed in the field.

One way to improve the sensitivity of lateral flow tests is to optimize the nanolabels used in inductive sensors. Several samples with sizes from 5 nm to 23 nm were synthesized and characterized in collaboration with Dr. M^a del Puerto Morales and her research group Materials for Medicine and Biotechnology (MaMBIO) of the Institute of Materials Science of Madrid - CSIC. This chapter presents the study with those magnetite nanoparticles and the correlation of their properties with the response of the radiofrequency inductive sensor. We proved that the most critical variables influencing the method's sensitivity are the particles' initial magnetic susceptibility and the total magnetic volume attached to each biomolecule. The former is an intrinsic characteristic of the particles, while the latter depends on their bioconjugation process.

Therefore, the initial magnetic susceptibility optimization depends on the MNPs size that should be in the superparamagnetic threshold. Thanks to the thermal excitation, the magnetic susceptibility of superparamagnetic particles at high frequencies remains larger than that of their ferri or ferromagnetic counterparts. For magnetite-based particles, this size is around 12 nm.

Regarding the magnetic mass attached, we tested the MNPs in lateral flow assays using the neutravidin–biotin model system. We proved that

agglomeration of the particles increases enormously the magnetic moment captured at the test, thus, increases the signal obtained. The only way to achieve this without losing the superparamagnetic character of the MNPs is by a controlled agglomeration of MNPs with the adequate critical superparamagnetic size. The conclusion, therefore, is that superparamagnetic nanoparticles around 12 nm and agglomerated in bigger particles give the best results in all types of inductive sensing, but especially in inductively read magnetic LFAs.

This collaboration work was published in the journal *Analyst*. All the research and its details are presented hereafter.

Scientific article

Improved Magnetic Lateral Flow Assays with Optimized Nanotags for Point-of-use Inductive Biosensing

This work has been published in:

Analyst

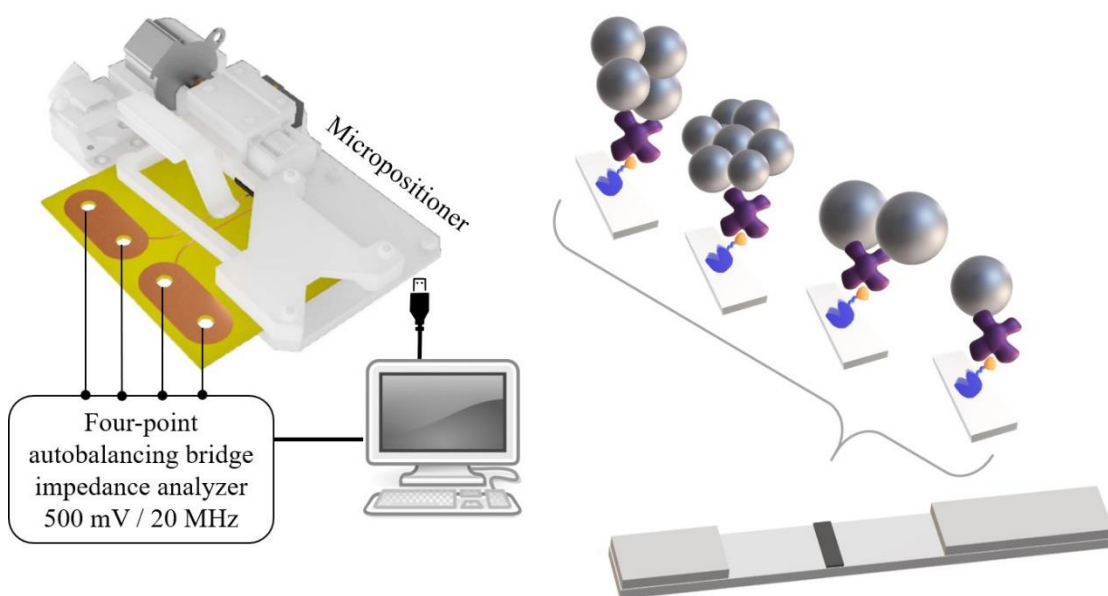
Royal Society of Chemistry



Cite as:

Salvador, M., Gallo-Cordova, Á., Moyano, A., Martínez-García, J. C., Blanco-López, M. C., Morales, M. P., & Rivas, M. (2020). Improved magnetic lateral flow assays with optimized nanotags for point-of-use inductive biosensing. *Analyst*, 145(17), 5905-5914

GRAPHICAL ABSTRACT



Improved Magnetic Lateral Flow Assays with Optimized Nanotags for Point-Of-Use Inductive Biosensing

María Salvador^{1,2}, Álvaro Gallo-Cordova³, Amanda Moyano^{1,4}, J. Carlos Martínez-García¹, M. Carmen Blanco-López⁴, M. Puerto Morales³, Montserrat Rivas¹

¹Department of Physics & IUTA, University of Oviedo, Campus de Viesques, 33204 Gijón, Spain

²Istituto di Struttura della Materia - Consiglio Nazionale delle Ricerche (CNR), 00016 Monterotondo Scalo (RM), Rome, Italy

³Instituto de Ciencia de Materiales de Madrid (ICMM-CSIC), 28049 Madrid, Spain

⁴Department of Analytical and Physical Chemistry, University of Oviedo, 33006 Oviedo, Spain

Abstract

Lateral flow assays may be used by minimally trained personnel for fast and inexpensive bioanalyses in decentralized non-exigent environments. Their extension to a broader catalog of applications depends on improvements in their quantification and their sensitivity. We report a strategy that combines nanomagnetic tagging of the analyte of interest with radiofrequency inductive sensing, easy to achieve in friendly and portable format. To optimize nanotag performance, we investigated the influences of their magnetic core size and agglomeration. Iron oxide nanoparticles, with sizes from 5 to 23 nm, were synthesized by thermal decomposition and then coated with dimercaptosuccinic acid and functionalized with neutravidin protein. We tested the system by immobilizing biotin in lateral flow membrane strips. When a sample containing the particles flows along the membrane, the biotin captures the neutravidin together with the magnetic nanotags, which are detected by the inductive sensor. The optimal nanotag core size is the critical threshold for superparamagnetic behavior, which maximizes both the initial magnetic permeability and the saturation magnetization. Controlled agglomeration of the nanotags increases the magnetic mass captured in the test line and further amplifies the signal.

Keywords: magnetic nanoparticles, inductive sensor, lateral flow immunoassays, magnetic labels, magnetic permeability

1. Introduction

Lateral flow immunoassay is a bio-testing method that is spreading thanks to its many advantages for point-of-care applications, such as quickness, portability, easy use, and low cost. Since its well-known use for home pregnancy tests launched in the early 1980s, its increasing application for diagnosis and prognosis in health [1–4] and food and environmental safety [5–9] have conferred it a solid reputation as a routine screening tool. In applications that need rapid decision-making [10–12] the advantages of the lateral flow method stand up, even when sometimes its sensitivity is lower than that of other immunoanalytical techniques (e.g., the enzyme-linked immunosorbent assay). To improve sensitivity and reduce the limits of detection, some ideas, such as chemical signal enhancement [13–15], test design [16], or more sensitive transducers or read-out instrumentation [17] have been explored.

The keys of lateral flow assays (LFA) are paper microfluidics and bio-recognition. The test consists of a strip of a nitrocellulose nanoporous membrane along which the liquid sample (urine, saliva, blood, serum, or plasma, or food or environmental samples) flows by capillary action. The analyte of interest is selectively captured by a bio-recognition molecule that is previously immobilized across the strip, forming the test line. In order to develop the test, the bioreceptor used for detection is labeled by colored nanoparticles that are detectable by the naked eye and provide a yes/no response. The presence/absence test or a semiquantitative one is satisfactory for some applications such as pregnancy, but for many others, such as diagnosis by biomarkers in cancer or myocardial infarction and toxin thresholds, one needs reliable, quantitative results.

Optical readers based on image analysis, reflectance or fluorescence measurements can be used to quantify the signal [18]. However, these readings are very sensitive to ambient light, humidity, and staining or aging of the paper strip, which frequently cause difficulties in calibration and reproducibility, especially in samples with a complex or strongly colored matrix [19].

Some authors have proposed magnetic nanoparticles (MNPs) as an efficient label in LFA [20]. MNPs have a tunable size and surface chemistry, which make them physically and chemically stable,

biocompatible and easily biofunctionalizable. Additionally, their production is not expensive [21]. MNPs produce a magnetic perturbation around them that can be detected by an adequate magnetic sensor without interference from the biological sample or the paper. Moreover, one can use their magnetism for pre-concentration or separation of the target analyte from the sample matrix, which can enormously help enhance the sensitivity without complex manipulation [22–24]. Additionally, magnetic signals do not degrade significantly with time, and sense not only particles on the surface but in the whole volume of the test line [25].

We recently developed a detection method using superparamagnetic nanoparticles combined with inductive detection with a single planar coil [26]. We proved the feasibility of the methodology in the quantification of prostatic cancer biomarkers [27] and toxic biogenic amines [19].

To optimize magnetic LFA, we need to analyze the properties of the separate components as well as their cooperative behavior. In inductive detection, the most critical parameters of the nanoparticles should be their magnetic moment and their initial magnetic permeability at the working frequency. To determine the possibility to control these variables, we have studied in this work the influence of the magnetic core size of the nanoparticles on their efficiency as LFA labels. For this purpose, iron oxide nanoparticles with sizes ranging from 5 to 23 nm were synthesized, characterized, and calibrated in the magnetic sensor. We have then tested them in lateral flow assays by using the model system neutravidin-biotin. We want to remark that neutravidin-biotin affinity has long been used in lateral flow immunoassays for the detection of clinical analytes as many commercial antibodies are biotinylated. Therefore, here it is used as a dummy in which the target of the detection is the neutravidin.

2. Materials and methods

2.1. Chemicals and Reagents

Iron chloride hexahydrate, oleic acid, sodium oleate, ethanol, toluene, hexane, octadecene, dimethyl sulfoxide (DMSO), meso-2,3-dimercaptosuccinic acid (DMSA), 1-ethyl-3-[3-dimethylpropyl]carbodiimide (EDC), bovine serum albumin (BSA), biotin-conjugated bovine serum albumin (BBSA) and Tween20 were purchased from Sigma-Aldrich (Spain). Neutravidin protein was obtained from Thermo Fischer Scientific (USA).

2.2. Magnetic Nanoparticles Synthesis and Characterization

The synthesis of MNPs with different core sizes was carried out by thermal decomposition using iron oleate as an iron precursor, which was prepared by a modification of the procedure published by Bronstein et al [28]. In a typical experiment, 10.8 g of $\text{FeCl}_3 \cdot 6\text{H}_2\text{O}$ were mixed with 45 g of sodium oleate in 60 mL of distilled water, 80 mL of ethanol, and 140 mL of hexane. The mixture was heated to 343 K and the reaction was left for 4 hours in a well-sealed system. Once the mixture was cooled, the aqueous phase was separated and discarded with a separation funnel and the final product was washed 3 times with distilled water. The remnant hexane and ethanol were evaporated by using a rotary evaporator. The final product was left in an inox-oven at 323 K for 12 h.

For MNPs preparation, 4.5 g of liquid iron oleate were weighted with 1.4 g of oleic acid and mixed in 50 mL of octadecene. The mixture was then placed in a three-neck round-bottom flask in nitrogen environment. First, the mixture was agitated at 340 rpm and heated to 333 K so the reactants could dissolve. Then, the mixture was heated at a rate of 3.4 K/min until the octadecene boiling point was reached (593 K), where the reaction was left for one hour. The sample was collected by centrifugation at 8000 rpm for 15 min and then washed several times with ethanol until organic precursors and reactants were removed. The obtained MNPs were dispersed in toluene for further functionalization. The final particle size was increased by reducing the amount of oleic acid in the reaction media [29]. Specifically, 1.4, 0.7, and 0 g of oleic acid were used to achieve particle sizes around 8, 12, and 23 nm respectively.

The MNPs were coated by DMSA by a ligand exchange process to remove the oleic acid [30]. A previously prepared mixture of 90 mg of DMSA with 5 mL of DMSO was added into 20 mL of a MNP dispersion of 2.5 mg/mL. After 24 hours of mechanical stirring, the solvent was discarded and the precipitated MNPs were collected and washed three times with ethanol. Afterwards, the pH of the MNPs dispersion was increased to 10 with a 0.25 M NaOH solution and dialyzed and filtered through a 0.22 μm pore-size filter before adjusting the pH to 7. The iron concentration was measured by inductively coupled plasma optical emission spectroscopy (ICP-OES) with an apparatus from Perkin Elmer, model OPTIME 2100DV, after digestion with aqua regia. The surface chemistry and nature of the iron oxide nanoparticles were studied using a Nicolet FT-IR 20SXC spectrometer recorded in the range of 400–4000 cm^{-1} . Powdered samples

were mixed with KBr and pressed in pellets.

Colloidal properties of the MNPs were studied in a Malvern Instruments Zetasizer Nano SZ by dynamic light scattering (DLS) measurement equipped with a solid-state He-Ne laser (wavelength $\lambda = 633$ nm) that provided the hydrodynamic size distribution and average ζ -potential. The magnetic core size was obtained by transmission electron microscopy (TEM) using a JEOL JEM 1010 microscope at 100 keV. For sample preparation, a drop of a dilute particle suspension was placed on a copper grid coated with amorphous carbon and then the solvent was left for evaporation at room temperature. The TEM particle size distributions were evaluated by measuring the largest core dimension of at least 200 particles. The data were fitted to a lognormal distribution from which the mean size and the standard deviation were obtained.

The magnetic properties of the MNPs were studied using a vibrating sample magnetometer MagLabVSM, Oxford Instruments, with a maximum field of 5 T. A known amount of a sample was dried at 323 K for 12 h, and then placed in the sample holder. The hysteresis loop of the samples was measured at 290 K up to ± 5 T. Following the same sample protocol preparation at room temperature, zero-field-cooled (ZFC) and field-cooled (FC) curves were obtained using a Quantum Design PPMS magnetometer equipped with a superconducting coil that produces magnetic fields in the range from -14 T to +14 T. Initial magnetic susceptibility was measured with the same device from 1-10,000 Hz. The magnetization values given in this work are referred to the mass of Fe_3O_4 derived from the iron concentration obtained by ICP-OES analysis.

To evaluate the MNPs in the LFA's scanning inductive sensor, some droplets of known mass from each sample were deposited onto a 10 mm \times 2 mm blotting paper and left to dry for at least 12 h.

2.3. Nanoparticle Biofunctionalization

MNPs of three representative core sizes (8, 12, and 23 nm) and different degrees of agglomeration were functionalized with neutravidin and tested on an LFA across which we had printed a biotin test line.

The neutravidin-biotin system is here used as a model to assess the performance of the particles as tags. The biotin-neutravidin combination is widely known in biochemistry for its high affinity constant, high thermal and chemical stability, and low non-specific binding. Neutravidin-conjugated magnetic labels are attractive because many

biotinylated antibodies are commercialized for immunoassays [31, 32]. They are also used as a signal amplification method [15, 33].

Here, we use this binding as the antibody-antigen paradigm of the immunoassay. The carboxylic group present in the DMSA that covers the MNPs was used to link the neutravidin via an EDC-mediated coupling reaction. We adapted the protocol from [34]. Briefly, 1 mg of EDC was dissolved in 1 mL of phosphate-buffered saline (PBS, 1 mM pH 7.4) freshly prepared and kept refrigerated during the process. A solution of neutravidin (1 mg/mL) was prepared and mixed with a certain amount of the MNPs. After being placed in a refrigerated ultrasonic bath, subsequent 10 μ L additions of the EDC solution were done at 0, 2, 4, 6, 8, 24, and 30 hours. We carried out DLS measurements to monitor the biofunctionalization of the particles with neutravidin.

2.4. Preparation of Lateral Flow Strips

For the LFA assembly, we purchased nitrocellulose membranes (UniSartCN95, Sartorius, Spain), glass fiber sample pads (GFCP001000, Millipore, Germany), absorbent pads (Whatman, USA) and backing cards (KN-V1080, Kenoshatapex, Netherlands).

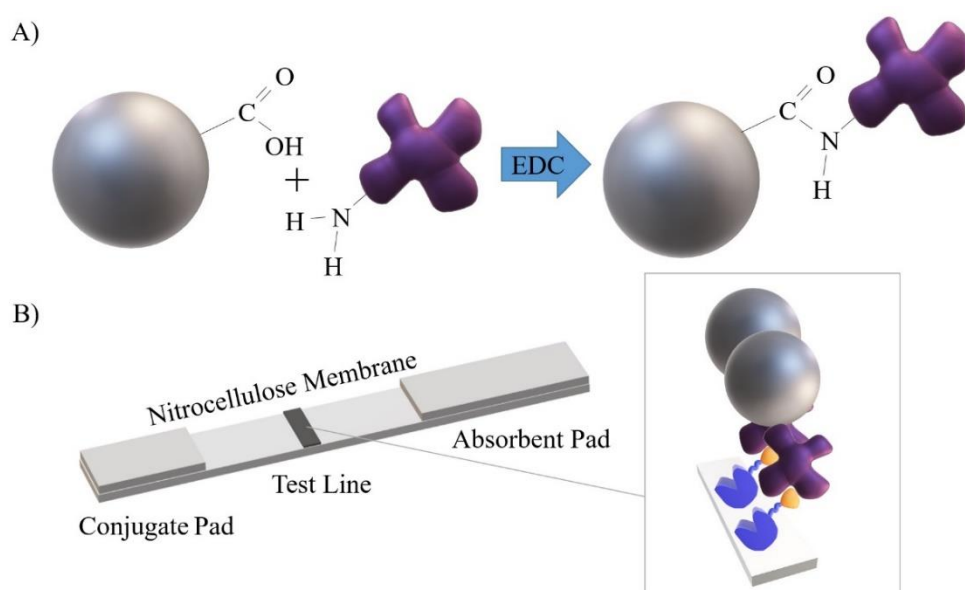


Figure 1. A) Schematic illustration of the MNPs biofunctionalization with neutravidin by EDC chemistry. B) Scheme of a lateral flow strip for neutravidin capture via biotin affinity. For simplification, only one-COOH group has been drawn at the MNPs, and only one -NH₂ group at the neutravidin.

The nitrocellulose membrane (25 mm-wide) was attached to an adhesive backing plastic card to make it sturdy. To form the test line at which the neutravidin will be immobilized (together with the magnetic

labels), we have dispensed across the nitrocellulose membrane a solution of 1 mg/mL of BBSA at a rate of 0.100 $\mu\text{L}/\text{mm}$ (with an IsoFlow reagent dispensing instrument, Imagen Technology, USA.) After drying, the sample pad (which enables a controlled transfer of the sample to the membrane) and the absorbent pad (which acts as a wick and prevents the backflow) were placed onto the backing card with an overlap of 2 mm. Single 5 mm wide strips were cut with a guillotine (Fellowes Gamma, Spain).

To obtain the sample solution, 80 μL of freshly prepared running buffer (RB) containing 10 mg/mL BSA and 0.5% Tween20 in PBS (10 mM, pH 7.4) were mixed with 20 μL of the neutravidin-MNP conjugate. The tests were then carried out in dipstick format by vertically introducing the sample pad end in the sample solution. The solution flows up by capillary action, and the neutravidin gets trapped by the biotin in the test line (see Figure 1). After 10 min of immersion, the strip was taken out and let dry.

2.5. Quantification of the Immunoassays

We evaluated the magnetic LFA signal by means of an inductive sensor that was developed specifically for lateral flow strips (see Figure 2) [27]. Its sensing head consists of a double copper line printed on a rigid insulating substrate across which an alternating current flows. The magnitude and phase of the sensing head impedance are continuously monitored by a precision impedance analyzer (Agilent 4294A) using 16048G test leads and 500 mV, 20–110 MHz excitation voltage.

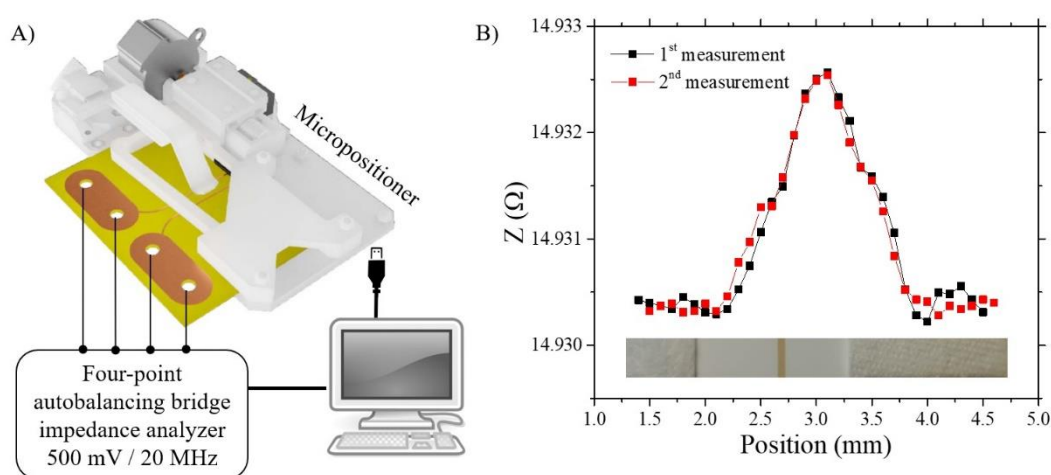


Figure 2. A) Schematic representation of the inductive sensor. B) Sensor signal for two scannings of the test line of an LFA. Bottom: image of the LFA where the brownish test line can be seen.

The sensing planar coil can be approximated by an RL circuit whose electrical impedance depends on the frequency ν and magnetic relative permeability μ_r of the surrounding medium, as:

$$Z(\nu, \mu) = R(\nu) + i2\pi\nu L\mu_r(\nu) \quad (1)$$

where the resistive part $R(\nu)$ depends on the frequency due to the skin effect, and L is the self-inductance, dependent on the geometry of the conductor and any surrounding magnetic material. In absence of any magnetic particles, the magnetic permeability can be approximated by the vacuum permeability, $\mu_r = 1$. When the sensing coil is completely covered by a magnetic material with an initial susceptibility $\chi(\nu)$, the relative permeability becomes $\mu_r(\nu) = \chi(\nu) + 1$. In the present application, the magnetic particles do not surround the whole length of the conductor, hence, a correction factor ψ ($\psi < 1$) must be included to account for the volume of particles. Taking this into account, the difference in impedance measured with and without the particles can be written as:

$$\Delta Z(\nu, \chi', \chi'', \psi) = \nu L \psi \chi''(\nu) + i\nu L \psi \chi'(\nu) \quad (2)$$

where χ' and χ'' stand for the real and imaginary components of the magnetic initial susceptibility of the magnetic material (we want to highlight that due to the product of the two complex numbers, Z and χ , the real part of ΔZ depends on the imaginary component of the susceptibility and vice versa.) According to this, for a fixed frequency, both the real and the imaginary parts of the impedance variation are directly proportional to the mass of the magnetic material through ψ . This linear dependence has been checked in previous works [26].

The test lines of the LFAs were scanned laterally over the sensing coil with a micro-positioner, producing a peak in impedance whose width is related to the width of the line. We integrate the peak signal across the position to account for all the particles, disregarding their distribution in the test line (with this we avoid inaccuracies coming from dispensing flaws.) The signal S provided by the sensor is then obtained in units of $\Omega \cdot \text{mm}$ coming from the cumulative integral of the impedance (Ω) across the width w of the test line (mm) [26, 27] (see Figure 2B):

$$S = \int_0^w \Delta Z dx \quad (3)$$

We define the resolution R of the method as the smallest change in mass that our sensor can resolve:

$$R = \frac{m \sigma_{noise}}{\Delta Z} \quad (4)$$

where $\Delta Z = Z - Z_0$ is the variation of the impedance with and without MNP on the sensor. The sensitivity Σ can be calculated following the use of giant magnetoimpedance and magnetoimpedance sensors like:

$$\Sigma = \frac{1}{m Z_0} \Delta Z 100 \quad (5)$$

3. Results and discussion

Crossing, equations (4) and (5) with (2), we can see that both Σ and R depend on the characteristics of the MNP that are used to label the biomolecule in the test strip (in this paper, the neutravidin.) The two variables that affect the sensitivity of the method are (i) the initial magnetic susceptibility χ and (ii) the total volume of the MNPs that we can attach to each molecule (directly proportional to ψ .) While the latter depends on the bioconjugation and immobilization of at the LFA, the former is an intrinsic property of the particles. For this reason, we have done a thorough investigation of the optimal characteristics for inductive detection of the unmodified MNP.

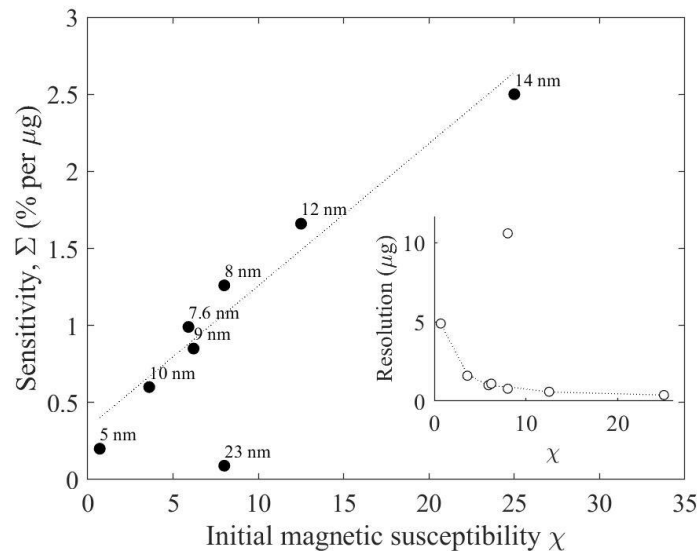


Figure 3. Sensitivity Σ of the sensor at 20 MHz as a function of the initial magnetic susceptibility χ (10 Hz) of the nanoparticles. Inset: Resolution versus χ . In both graphs, the point that goes out of the general trend corresponds to the 23 nm particles, which are not superparamagnetic.

We evaluated nine sample solutions with different average particle sizes ranging from 5 to 23 nm with the inductive sensor. The dependence of Σ and R with the initial susceptibility χ ($\nu = 10$ Hz) is plotted in Figure 3.

These results have been obtained at 20 MHz (although the sensitivity increases with frequency, also does the level of noise, which considerably worsens the resolution.) The linear correlation between Σ and χ applies to all the particles except one: The values for 23 nm do not follow the general trend, and both Σ and R are worse for this sample.

A likely explanation for the worse performance of the 23 nm particles is an excessive particle size. Particles with sizes below 50 nm are magnetic monodomains, whose magnetic moment lies along the easy magnetization direction determined by the crystallographic structure and the shape. Switching the magnetic moment from one direction to the opposite requires an energy that depends on the nature of the particle through its magnetic anisotropy constant K and volume V : $E = KV$. When V is very small, it is probable that the thermal energy $k_B T$ (where k_B stands for Boltzmann constant and T for the temperature) enables the switching at such a high rate that, for many measurements and practical applications, the observed magnetization vanishes. This behavior is known as superparamagnetism [35] and occurs above a critical volume (for a given temperature), or a transition temperature known as blocking temperature T_B (for a given volume). Particles whose combination of volume and temperature leaves them out of the superparamagnetic regime are said to be blocked. Superparamagnetism significantly affects the susceptibility of the particles [36]. A substantial magnetic susceptibility is essential for inductive detection. On the other hand, the operation frequency must be high (10-200 MHz) to get a measurable signal. At such frequencies it is more difficult for the magnetization to follow the exciting field than at 10 Hz. This lag provokes the reduction of the susceptibility and the appearance of an out-of-phase component (mathematically described by χ'' .) Thanks to the thermal excitation, the magnetic susceptibility of superparamagnetic particles at high frequencies remains larger than that of their ferri- or ferromagnetic counterparts. Then, we presume that the sample with average size of 23 nm contains a large proportion of particles that are blocked and worsen the inductive sensor signal. On the contrary, particles of 12-14 nm optimize the signal. To confirm this, we have studied the magnetic behavior and the initial susceptibility of the particles at high frequency.

3.1. Magnetometry

From here on, the discussion will focus on a selection of three particle samples, with average sizes of 8, 12, and 23 nm, named NP8, NP12, and

NP23, respectively. The nature of these nanoparticles is mainly magnetite with different degrees of oxidation as a function of the particle size. The oxidation is a consequence of the transference of the particles to water by ligand exchange with DMSA, followed by infrared spectroscopy. Thus, IR spectrum confirms the presence of DMSA on the surface and shows a certain degree of oxidation, more critical for particles smaller than 10 nm (NP8) (see Supplementary Information S2.)

Figure 4 shows their magnetization curves at room temperature. For NP8 and NP12, they are anhysteretic, consistent with superparamagnetic behavior, while NP23 has magnetic hysteresis (the inset in Figure 4 shows clearly the opening of the magnetization curve of NP23.) The saturation magnetization M_S was calculated by fitting the experimental data of Figure 4 to the law of approach to saturation [37]. The results for the three types of particles, given in Table 1, are close to that of bulk magnetite ($M_S = 98 \text{ A}\cdot\text{m}^2/\text{kg}$) [38].

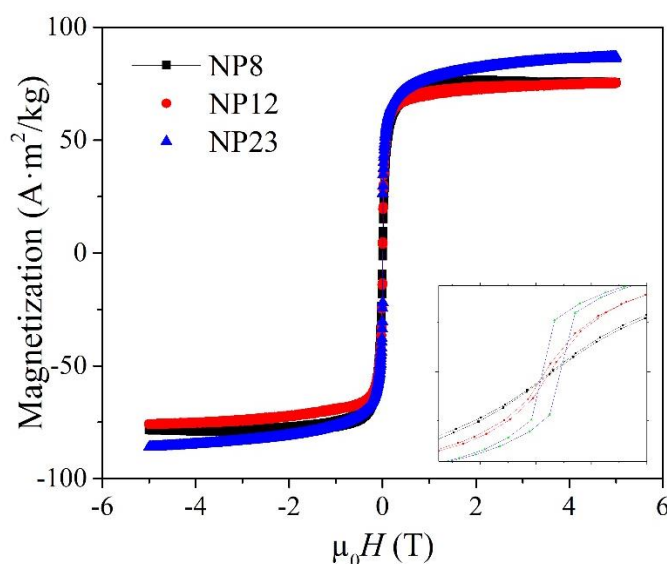


Figure 4. Hysteresis loops of the three samples NP8 (black), NP12 (red) and NP23 (blue) at room temperature from 5 to -5 T. Inset: Central area detail of the magnetization curves.

To assess the superparamagnetic behavior of the particles, we recorded the ZFC-FC curves, shown in Figure 5A, in an applied magnetic field of 5 mT. For NP8 and NP12, the ZFC curve shows a maximum below 200 K, confirming that, at room temperature, in these solutions, most particles are in the superparamagnetic regime. On the contrary, for NP23, the slope of the ZFC curve is positive even at 350 K. We obtained the blocking temperature T_B at which the particles transit from blocked to the superparamagnetic regime from the distribution of T_B obtained as the

temperature derivative of the difference $M_{ZFC} - M_{FC}$ of both curves [39] (see Figure 5B.) T_B was calculated as the peak of the normal-curve fit. For monodisperse populations with homogeneous magnetic anisotropy, the two curves should coincide above T_B ; their separation, quantified by the difference between the temperature of the maximum T_{max} and the temperature at which both curves merge T_{irr} , is related to the width of the blocking temperature distribution, and hence, a measure of the particle size distribution [40]. The effective anisotropy constant (K_{eff}) can be then estimated as $K_{eff} = 25k_B T_B/V$ [41]. The values obtained, shown in Table 1, are on the order of magnitude of published data for magnetite nanoparticles [42]. The largest anisotropy corresponds to the smallest particles with an extra anisotropy source coming from the surface and the smallest value for the largest particles and very close to the magnetocrystalline anisotropy for bulk magnetite ($1.1 \times 10^4 \text{ J/m}^3$).

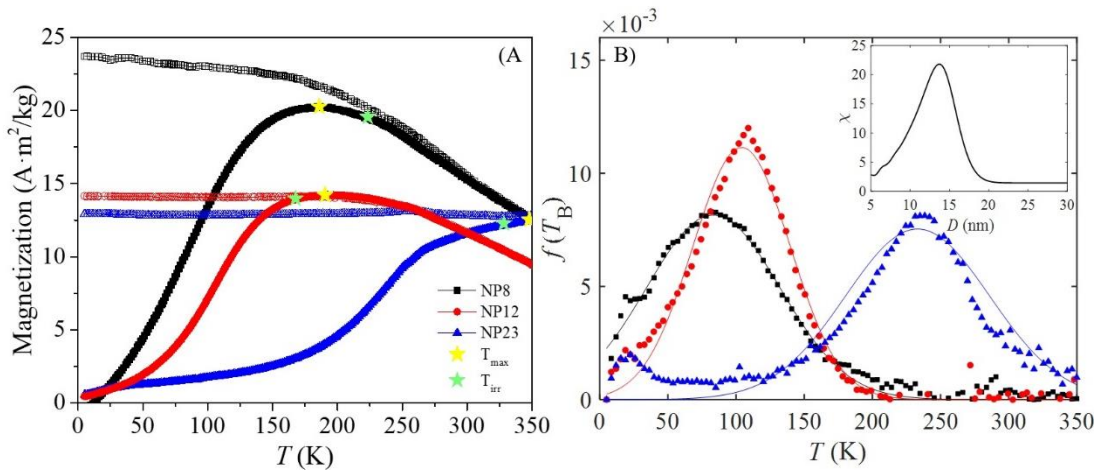


Figure 5. A) ZFC-FC curves for particles NP8 (black), NP12 (red) and NP23 (blue), obtained under a magnetic field of 5 mT. T_{max} (yellow star) and T_{irr} (green star) are indicated for the three samples; B) Distribution of blocking temperatures; Inset: Calculated magnetic susceptibility as a function of the size. The legend is common to both graphs.

3.2. Initial Magnetic Susceptibility

To estimate the size that would maximize the initial magnetic susceptibility, we may use Néel's model. The susceptibility of an ensemble of MNPs with randomly oriented easy axes can be calculated at temperature T according to equation (2) in ref. [36] for null frequency,

$$\chi(T) = \int_0^\infty \frac{2}{3} \frac{\mu_0 \rho^2 M_S^2}{K_{eff}} \left(\frac{K_{eff} V}{k_B T} + 1 \right) L(D, D_0, \sigma) dD \quad (6)$$

in which we have included the log-normal distribution function $L(D, D_0, \sigma)$

to account for the polydispersion of the particles size D . D_0 is the mean size, and σ is the standard deviation of the logarithm (see size analysis in the supplementary information file). We have used the parameters typical of magnetite particles (density $\rho = 5170 \text{ kg/m}^3$, $K_{\text{eff}} = 5 \times 10^4 \text{ J/m}^3$ and $M_S = 80 \text{ A}\cdot\text{m}^2/\text{kg}$), $\sigma = 0.01$, and $T = 300 \text{ K}$. The curve, plotted in the inset of Figure 5B, presents a maximum at $D_0 = 12 \text{ nm}$. The AC susceptibility measurements confirm this prediction, as shown in Table 1.

Table 1. Saturation magnetization M_S , blocking temperature T_B , maximum temperature T_{max} , effective anisotropy constant K_{eff} , and real and imaginary components of the initial susceptibility (dimensionless), χ' and χ'' , respectively.

Particle Sample	M_S ($\text{A}\cdot\text{m}^2/\text{kg Fe}_3\text{O}_4$)	T_B (K)	T_{max} (K)	T_{irr} (K)	K_{eff} (J/m^3)	χ'	χ''
NP8	79	87.1	182.6	128.6	$8.8\cdot 10^4$	12.85	0.15
NP12	75	101.3	186.8	178.5	$3.8\cdot 10^4$	18.48	0.01
NP23	83	224.9	>350	342.8	$1.2\cdot 10^4$	8.03	0.87

Due to the inductive character of the magnetic sensor, the signal grows with the excitation frequency ($\Delta Z \propto \nu$, see equation (2)). Then, higher frequencies would, in principle, benefit the detection of the MNPs. This idea makes it interesting to analyze the behavior of the susceptibility in the sensor working frequency range (10-200 MHz). To account for the influence of the frequency ν , equation (6) can be modified as follows:

$$\chi(\nu, T) = \int_0^\infty \frac{2}{3} \frac{\mu_0 \rho^2 M_S^2}{K_{\text{eff}}} \left(\frac{K_{\text{eff}} V / (k_B T)}{1 + i 2\pi \nu \exp(K_{\text{eff}} V / k_B T)} + 1 \right) L(D, D_0, \sigma) dD \quad (7)$$

The solution of equation (7) was numerically computed for the three types of particles by a trapezoidal method, using the size parameters given from the TEM histograms (see supplementary information S1), and M_S and K_{eff} from DC magnetization measurements (Table 1). The results are shown in Figure 6, where the dashed vertical lines delimit the working frequency range of the inductive sensor. In this scope, NP12 presents the highest and NP23 the lowest susceptibility values.

These calculations can be used to explain the sensor signal from the various particles. As we can see from equations (2) and (3), the signal S is proportional to the susceptibility with a multiplying factor that includes the MNPs mass (through ψ) and ν , so plotting $S/(m\nu)$ (Figure 7) versus ν should give the same type of curves as the simulations of Figure 6 (we

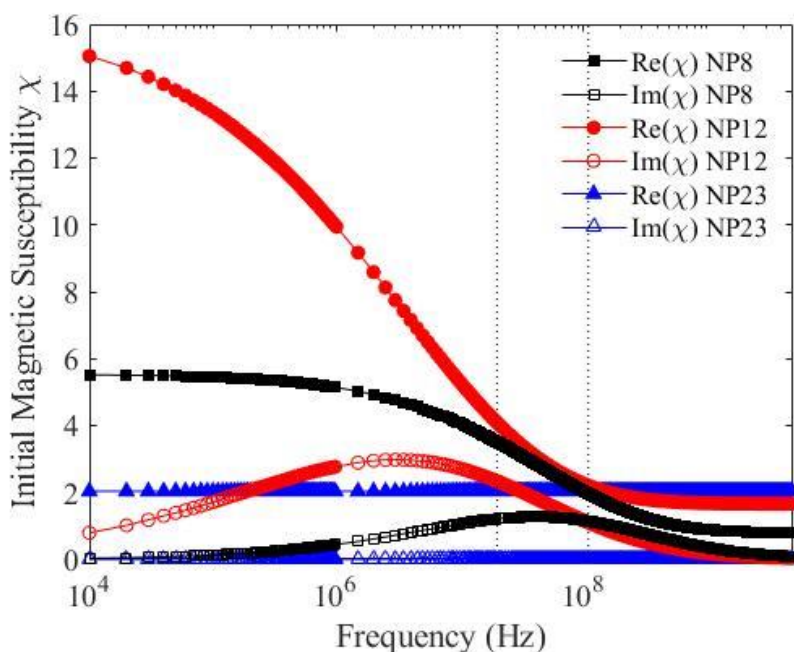


Figure 6. Computed frequency evolution of the initial susceptibility for samples NP8 (black), NP12 (red) and NP23 (blue).

must recall that the real part of S is proportional to χ' and the real part of S to χ'' .) We can observe effectively the similarities of the curves in the range of common frequencies (20-110 MHz): (i) The real part of the signal, which is related to χ'' , is much smaller than the imaginary component and barely changes (oscillations are attributable to noise;) (ii) The imaginary part of the signal decreases with the frequency, NP12 showing the largest and NP23 the smallest values. This allows us to confirm that, on equal terms of composition, mass, and coating, the initial susceptibility is a decisive parameter for detection. Given that the maximum susceptibility is achieved for the critical volume for superparamagnetism, this seems to be also optimal for inductive detection.

3.1. Nanoparticles as Labels

It is important to note that in the previous sections the particles were studied before biofunctionalization. This process is essential to capture the bioreceptor conjugated with its magnetic label at the test line. The superficial modification of this step involves activation of the carboxylic groups of the DMSA outer layer, which can imply some agglomeration of the particles. This, in turn, affects the number of particles that attach to each protein and, in consequence, the signal of the magnetic LFA through parameter ψ in (2).

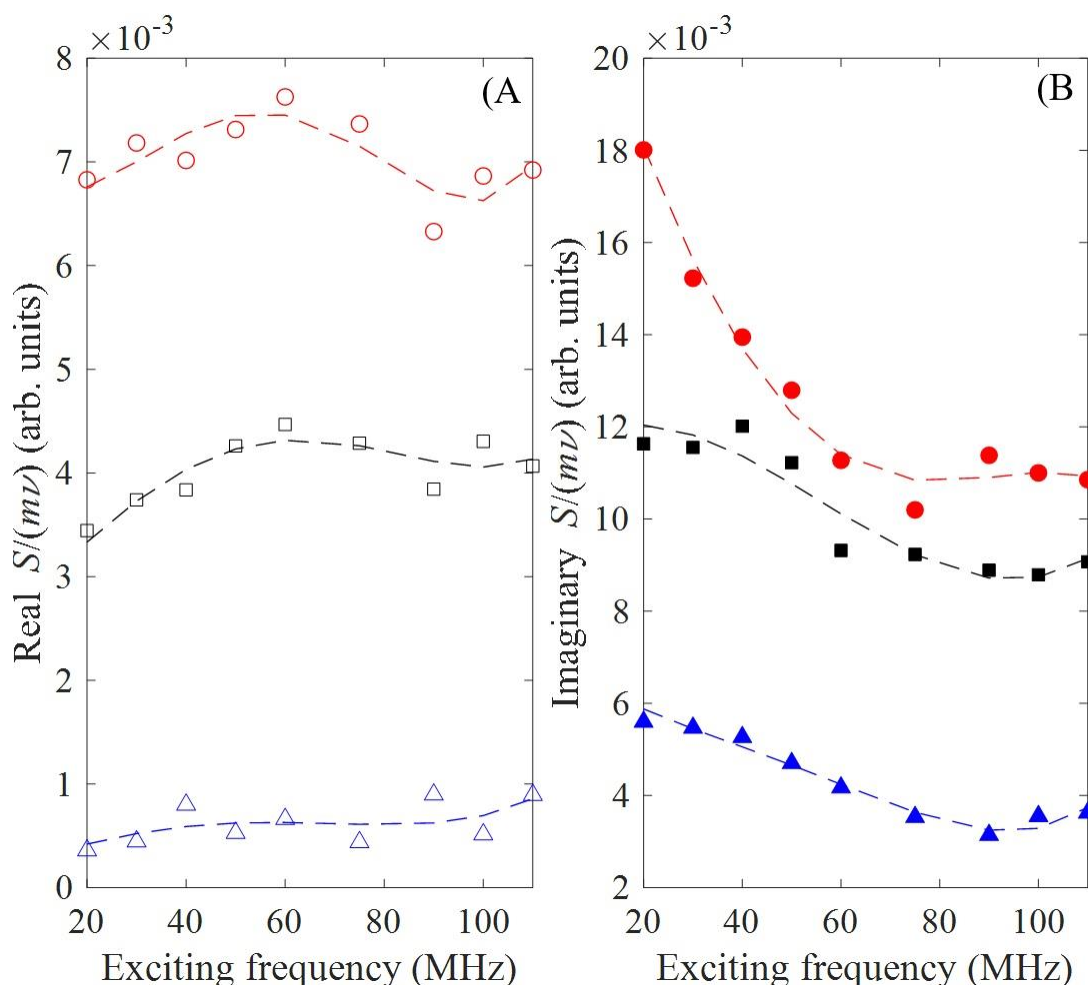


Figure 7. Real (A) and imaginary (B) components of the sensor signal divided by the measuring frequency corresponding to samples NP8 (black), NP12 (red) and NP23 (blue). The units of the vertical axes are $\Omega \cdot \text{mm}/(\text{mg} \cdot \text{MHz})$. The dashed lines are a guide to the eye.

To study this effect in the nitrocellulose strips, we tested NP8, NP12, and NP23 after functionalization. For comparison, all the processes have also been performed on NP12 after six months of settling (named sample NP12A.)

To analyze the agglomeration of particles caused by the biofunctionalization or other reasons, we measured their size by TEM and compared it to the DLS results. Table 2 displays the hydrodynamic size before (D_{DLS}^{BB}) and after (D_{DLS}^{AB}) biofunctionalization with their corresponding polydispersity index PDI (this dimensionless parameter is used in DLS to describe the width of the size distribution; values smaller than 0.05 are associated with highly monodisperse standards, while values above 0.7 correspond to broad size distributions,) and the mean TEM diameter D_0 . For NP12 and NP23 the difference between D_0 and D_{DLS}^{BB}

is only 10-15 %, typical for the diffuse layer and surfactant around the particles [43]. It indicates that these are stable suspensions of single particles. On the other hand, for NP8 and NP12A, the difference is substantial, evidencing agglomeration. After the biofunctionalization, the size of NP8 and NP12 remains almost constant. Its small increase is due to the protein, whose size is around 5 nm [44]. On the contrary, the size increase produced by the addition of neutravidin in NP23 and NP12A is much larger, indicating the post-functionalization agglomeration of the particles.

We conclude that there are three ways of agglomeration (schematized in Figure 8): (i) The smallest particles, NP8, agglomerate in the process of transferring them to water by DMSA coating; (ii) The intermediate-sized particles, NP12, agglomerate only after long storage, as in NP12A; (iii) The largest particles, NP23, agglomerate after neutravidin attachment. This could be caused by cross-linking effects due to the activation of the $-NH_2$ groups of the neutravidin. For the bioconjugation, we used a fixed neutravidin concentration per particle volume. Given that the surface area per unit volume is smaller in the larger particles, the amount of neutravidin per surface area is more significant, and could result in interparticle bridging through their $-COOH$ groups.

Table 2. Mean particle diameter by TEM D_0 and its standard deviation σ ; hydrodynamic diameter before biofunctionalization D_{DLS}^{BB} and after biofunctionalization D_{DLS}^{AB} , and their corresponding PDI values.

Particle Sample	D_0 (nm)	σ (nm)	D_{DLS}^{BB} (nm)	PDI	D_{DLS}^{AB} (nm)	PDI
NP8	7.6	0.15	94	0.36	106	0.20
NP12	11.6	0.08	22	0.20	34	0.26
NP12A			134	0.39	260	0.28
NP23	22.6	0.11	44	0.35	100	0.33

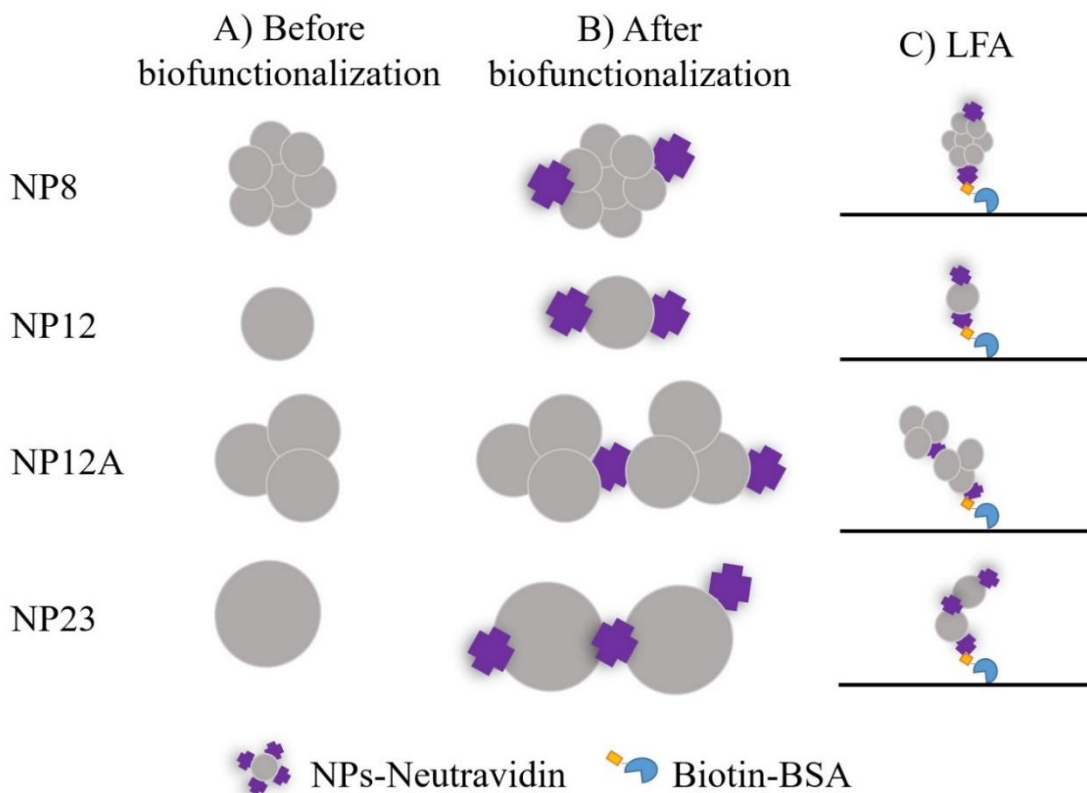


Figure 8. Schematic representation of the MNPs agglomeration (A) before and (B) after the functionalization with neutravidin, and (C) immobilized on the strip.

Figure 9 shows the magnetic sensor signal of the LFA run with different nanotags. In it, we observe that, despite NP12 having the largest magnetic susceptibility, the performance in the LFA is better for NP8 and NP23. Finally, NP12A has the best signal at all frequencies. The explanation may be agglomeration effects, as mentioned above. The number of nanotags per protein is minimum for NP12, while we will have a situation with few particles in the case of NP12A and NP23 and many more for NP8. As the number of anchoring biotin units immobilized in the test line is the same for the four cases, the signal would necessarily be smaller for NP12 than NP8 and NP23.

On the other hand, for the same agglomerate size, the mass of NP23 is larger, and this balances the smaller signal per unit mass. As a result, the signals recorded for NP23 are as large as those for NP8. Finally, NP12A encompasses both advantages, the highest magnetic susceptibility plus agglomeration, yielding the best signal at all frequencies.

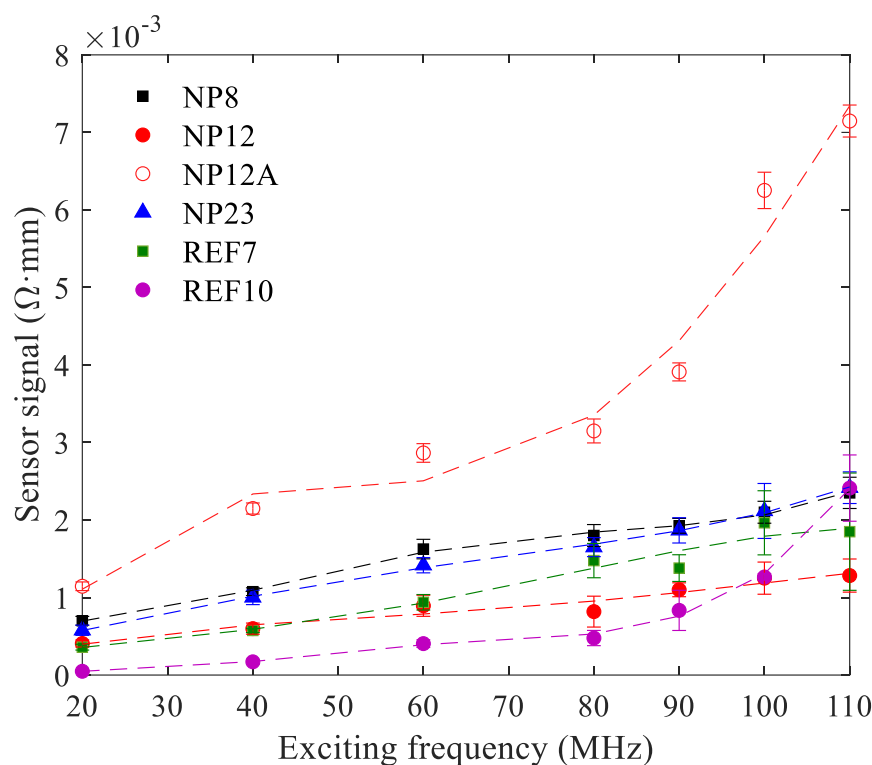


Figure 9. Magnetic signal obtained in the sensor at different frequencies for LFA with the three series of particles. The error bars show the standard deviation. The dashed lines serve as a guide to the eye.

Thus, particle agglomeration is crucial to enhance the performance of the magnetic LFA and can have an even greater influence than MNP permeability and saturation magnetization. As long as the agglomerates are small enough to flow through the membrane pores, some agglomeration is beneficial for the detection of the MNPs [45]. As a consequence, further development should include the controlled agglomeration or encapsulation of 12 nm sized nanoparticles, which will optimize simultaneously ψ and χ in equation (2).

To evaluate the practical implications of these results, we have also performed neutravidin-biotin LFA with nanoparticles that had been used in other biological assays (Figure 9 shows these results.) Specifically, REF7 was used for histamine levels determination in red wine by LFA, achieving results that agreed with the much more complex high-performance liquid chromatography [19]. Such sample consisted of 7 nm iron oxide MNPs forming agglomerates of 90 nm. The curve in Figure 9 corresponding to REF7 (green squares) was obtained with a concentration of neutravidin of 1 mg/mL, following the same protocol as for NP8, NP12, NP23 and NP12A. We can see in Figure 9 that MNPs with a size of 12 nm and agglomerations of 200 nm, like NP12A, promise to improve histamine detection by LFA. We also show the results for REF10,

a commercial sample of 10 nm-sized iron oxide MNPs, which formed agglomerates of 75 nm after bioconjugation. Such particles were used for prostate-specific antigen quantification (the neutravidin-MNP complexes were conjugated to a biotinylated antibody) in the range of clinical interest and the measurement achieving sensitivity limits of detection comparable to ELISA and a resolution of 50 pg of PSA [27]. The curve corresponding to REF10 in Figure 9 (magenta circles) was obtained with a concentration of neutravidin of 3 mg/mL. For NP12A, the magnetic sensor resolution in MNPs detection (as defined in equation (4)) is the same as that of REF10, $R = 0.58 \mu\text{g}$ (Figure 3). Therefore, the LFA detection could be improved up to 10 times by using 12 nm particles with controlled agglomeration, as long as the particles are properly functionalized, which is a critical step in this kind of tests.

4. Conclusions

Lateral flow assays for the detection of clinical and environmental analytes have significant advantages compared to more sophisticated techniques in terms of speed, cost, and portability. To further extend their use, we aimed to improve their sensitivity with magnetic materials and detection. For this study, we incorporated magnetic iron oxide particles as tags that can be quantified by an inductive sensor. We analyzed the influence of particle size and agglomeration on the LFA magnetic readings.

Superparamagnetism of the particles is crucial for high initial permeability at the working frequencies. However, larger particles increase both the magnetic permeability and the saturation magnetization. As a consequence, the optimal size for LFA is the critical threshold for superparamagnetism. For iron oxide, this is about 12 nm. Once this is optimized, the agglomeration of the particles before running the LFA has an enormous positive influence on the inductive measurement because it increases the magnetic moment captured at the test line. The larger the magnetic moment per biomolecule (in this case, per biotin), the larger the sensitivity of the assay. Nevertheless, this cannot be achieved by increasing the particle size, because that would eliminate the superparamagnetic behavior. The way to achieve this is to agglomerate particles with the adequate critical superparamagnetic size. Then, we conclude that 12 nm particles agglomerated in bigger particles of 200 to 300 nm give the best results in inductively-read magnetic LFA.

Declaration of Competing Interest

The authors declare that they have no conflict of interest.

Acknowledgments

This research was funded by the Spanish Ministry of Economy and Competitiveness under grants MAT2017-88148-R and MAT2017-84959-C2-1-R; the Council of Gijón-IUTA under grant SV-19-GIJÓN-1-25; and the Principality of Asturias under project IDI/2018/000185. A. Moyano and M. Salvador thanks University of Oviedo and the Principality of Asturias for their pre-doctoral grants.

References

- [1] P. Brangel, A. Sobarzo, C. Parolo, B.S. Miller, P.D. Howes, S. Gelkop, J.J. Lutwama, J.M. Dye, R.A. McKendry, L. Lobel, M.M. Stevens, A Serological Point-of-Care Test for the Detection of IgG Antibodies against Ebola Virus in Human Survivors, *ACS Nano*. 12 (2018) 63–73.
https://doi.org/10.1021/ACSNANO.7B07021/SUPPL_FILE/NN7B07021_SI_001.PDF.
- [2] R. Ranjan, S.D. Narnaware, K. Nath, R.K. Sawal, N. V. Patil, Rapid diagnosis of tuberculosis in dromedary camel (*Camelus dromedarius*) using lateral flow assay-based kit, *Trop. Anim. Health Prod.* 50 (2018) 907–910. <https://doi.org/10.1007/S11250-017-1502-6/FIGURES/2>.
- [3] W. Ren, S.I. Mohammed, S. Wereley, J. Irudayaraj, Magnetic Focus Lateral Flow Sensor for Detection of Cervical Cancer Biomarkers, *Anal. Chem.* 91 (2019) 2876–2884.
<https://pubs.acs.org/doi/full/10.1021/acs.analchem.8b04848> (accessed September 16, 2021).
- [4] D. Zhang, L. Huang, B. Liu, H. Ni, L. Sun, E. Su, H. Chen, Z. Gu, X. Zhao, Quantitative and ultrasensitive detection of multiplex cardiac biomarkers in lateral flow assay with core-shell SERS nanotags, *Biosens. Bioelectron.* 106 (2018) 204–211.
<https://doi.org/10.1016/J.BIOS.2018.01.062>.
- [5] M. Magiati, V.M. Myridaki, T.K. Christopoulos, D.P. Kalogianni, Lateral flow test for meat authentication with visual detection, *Food Chem.* 274 (2019) 803–807.
<https://doi.org/10.1016/J.FOODCHEM.2018.09.063>.
- [6] S.C. Razo, V.G. Panferov, I. V. Safenkova, Y.A. Varitsev, A. V. Zherdev, B.B. Dzantiev, Double-enhanced lateral flow immunoassay for potato virus X based on a combination of magnetic and gold nanoparticles, *Anal. Chim. Acta.* 1007 (2018) 50–60. <https://doi.org/10.1016/J.ACA.2017.12.023>.
- [7] D. Wang, J. Zhu, Z. Zhang, Q. Zhang, W. Zhang, L. Yu, J. Jiang, X. Chen, X. Wang, P. Li, Simultaneous Lateral Flow Immunoassay for

- Multi-Class Chemical Contaminants in Maize and Peanut with One-Stop Sample Preparation, *Toxins* 2019, Vol. 11, Page 56. 11 (2019) 56. <https://doi.org/10.3390/TOXINS11010056>.
- [8] M. Khater, A. de la Escosura-Muñiz, A. Merkoçi, Biosensors for plant pathogen detection, *Biosens. Bioelectron.* 93 (2017) 72–86. <https://doi.org/10.1016/J.BIOS.2016.09.091>.
- [9] J. Singh, S. Sharma, S. Nara, Evaluation of gold nanoparticle based lateral flow assays for diagnosis of enterobacteriaceae members in food and water, *Food Chem.* 170 (2015) 470–483. <https://doi.org/10.1016/J.FOODCHEM.2014.08.092>.
- [10] S.E.F. Melanson, M.J. Tanasijevic, P. Jarolim, Cardiac troponin assays: A view from the clinical chemistry laboratory, *Circulation.* 116 (2007). <https://doi.org/10.1161/CIRCULATIONAHA.107.722975>.
- [11] Y. He, S. Zhang, X. Zhang, M. Baloda, A.S. Gurung, H. Xu, X. Zhang, G. Liu, Ultrasensitive nucleic acid biosensor based on enzyme–gold nanoparticle dual label and lateral flow strip biosensor, *Biosens. Bioelectron.* 26 (2011) 2018–2024. <https://doi.org/10.1016/J.BIOS.2010.08.079>.
- [12] D.H. Choi, S.K. Lee, Y.K. Oh, B.W. Bae, S.D. Lee, S. Kim, Y.B. Shin, M.G. Kim, A dual gold nanoparticle conjugate-based lateral flow assay (LFA) method for the analysis of troponin I, *Biosens. Bioelectron.* 25 (2010) 1999–2002. <https://doi.org/10.1016/J.BIOS.2010.01.019>.
- [13] N.M. Rodriguez, W.S. Wong, L. Liu, R. Dewar, C.M. Klapperich, A fully integrated paperfluidic molecular diagnostic chip for the extraction, amplification, and detection of nucleic acids from clinical samples, *Lab Chip.* 16 (2016) 753–763. <https://doi.org/10.1039/C5LC01392E>.
- [14] A. Beninato, V. Sinatra, G. Tosto, M.E. Castagna, S. Petralia, S. Conoci, S. Baglio, Inductive integrated biosensor with extended operative range for detection of magnetic beads for magnetic immunoassay, *IEEE Trans. Instrum. Meas.* 66 (2016) 348–359. <https://doi.org/10.1109/TIM.2016.2619000>.
- [15] M.O. Rodríguez, L.B. Covián, A.C. García, M.C. Blanco-López, Silver and gold enhancement methods for lateral flow immunoassays, *Talanta.* 148 (2016) 272–278. <https://doi.org/10.1016/J.TALANTA.2015.10.068>.
- [16] K.M.M. Koczula, A. Gallotta, P. Estrela, K.M.M. Koczula, A. Gallotta, Lateral flow assays, *Essays Biochem.* 60 (2016) 111–120. <https://doi.org/10.1042/EBC20150012>.
- [17] M.A. Mansfield, The Use of Nitrocellulose Membranes in Lateral-Flow Assays, *Drugs Abus.* (2005) 71–85. https://doi.org/10.1007/978-1-59259-951-6_4.
- [18] G. Ruiz-Vega, M. Kitsara, M.A. Pellitero, E. Baldrich, F.J. del Campo, Electrochemical Lateral Flow Devices: Towards Rapid Immunomagnetic Assays, *ChemElectroChem.* 4 (2017) 880–889. <https://doi.org/10.1002/CELC.201600902>.
- [19] A. Moyano, M. Salvador, J.C. Martínez-García, V. Socoliuc, L.

- Vékás, D. Peddis, M.A. Alvarez, M. Fernández, M. Rivas, M.C. Blanco-López, Magnetic immunochromatographic test for histamine detection in wine, *Anal. Bioanal. Chem.* 2019 41125. 411 (2019) 6615–6624. <https://doi.org/10.1007/S00216-019-02031-6>.
- [20] A. Moyano, E. Serrano-Pertierra, M. Salvador, J.C. Martínez-García, M. Rivas, M.C. Blanco-López, Magnetic lateral flow immunoassays, *Diagnostics*. 10 (2020) 288. <https://doi.org/10.3390/diagnostics10050288>.
- [21] C.R. Tamanaha, S.P. Mulvaney, J.C. Rife, L.J. Whitman, *Magnetic labeling, detection, and system integration*, Elsevier, 2008.
- [22] V.G. Panferov, I. V. Safenkova, A. V. Zherdev, B.B. Dzantiev, Setting up the cut-off level of a sensitive barcode lateral flow assay with magnetic nanoparticles, *Talanta*. 164 (2017) 69–76. <https://doi.org/10.1016/j.talanta.2016.11.025>.
- [23] K. Aguilar-Arteaga, J.A. Rodríguez, E. Barrado, Magnetic solids in analytical chemistry: A review, *Anal. Chim. Acta.* 674 (2010) 157–165. <https://doi.org/10.1016/J.ACA.2010.06.043>.
- [24] X. Zhao, Y. Shi, Y. Cai, S. Mou, Cetyltrimethylammonium bromide-coated magnetic nanoparticles for the preconcentration of phenolic compounds from environmental water samples, *Environ. Sci. Technol.* 42 (2008) 1201–1206. https://doi.org/10.1021/ES071817W/SUPPL_FILE/ES071817W-FILE002.PDF.
- [25] D. Quesada-González, A. Merkoçi, Nanoparticle-based lateral flow biosensors, *Biosens. Bioelectron.* 73 47–63. <http://dx.doi.org/10.1016/j.bios.2015.05.050> (accessed September 6, 2021).
- [26] D. Lago-Cachón, M. Rivas, J.C. Martínez-García, J.A. García, Cu impedance-based detection of superparamagnetic nanoparticles, *Nanotechnology*. 24 (2013) 245501. <https://doi.org/10.1088/0957-4484/24/24/245501>.
- [27] D. Lago-Cachón, M. Oliveira-Rodríguez, M. Rivas, M.C. Blanco-López, J.C. Martínez-García, A. Moyano, M. Salvador, J.A. García, Scanning Magneto-Inductive Sensor for Quantitative Assay of Prostate-Specific Antigen, *IEEE Magn. Lett.* 8 (2017). <https://doi.org/10.1109/LMAG.2017.2702108>.
- [28] L.M. Bronstein, X. Huang, J. Retrum, A. Schmucker, M. Pink, B.D. Stein, B. Dragnea, Influence of iron oleate complex structure on iron oxide nanoparticle formation, *Chem. Mater.* 19 (2007) 3624–3632. https://doi.org/10.1021/CM062948J/SUPPL_FILE/CM062948JSI20070423_032524.PDF.
- [29] G. Salas, C. Casado, F.J. Teran, R. Miranda, C.J. Serna, M.P. Morales, Controlled synthesis of uniform magnetite nanocrystals with high-quality properties for biomedical applications, *J. Mater. Chem.* 22 (2012) 21065–21075. <https://doi.org/10.1039/C2JM34402E>.
- [30] R. Mejías, L. Gutiérrez, G. Salas, S. Pérez-Yagüe, T.M. Zotes, F.J. Lázaro, M.P. Morales, D.F. Barber, Long term biotransformation

- and toxicity of dimercaptosuccinic acid-coated magnetic nanoparticles support their use in biomedical applications, *J. Control. Release.* 171 (2013) 225–233. <https://doi.org/10.1016/J.JCONREL.2013.07.019>.
- [31] T.T. Le, P. Chang, D.J. Benton, J.W. McCauley, M. Iqbal, A.E.G. Cass, Dual Recognition Element Lateral Flow Assay Toward Multiplex Strain Specific Influenza Virus Detection, *Anal. Chem.* 89 (2017) 6781–6786. https://doi.org/10.1021/ACS.ANALCHEM.7B01149/SUPPL_FILE/AC7B01149_SI_001.PDF.
- [32] Z. Fang, W. Wu, X. Lu, L. Zeng, Lateral flow biosensor for DNA extraction-free detection of salmonella based on aptamer mediated strand displacement amplification, *Biosens. Bioelectron.* 56 (2014) 192–197. <https://doi.org/10.1016/J.BIOS.2014.01.015>.
- [33] K. V. Serebrennikova, J. V. Samsonova, A.P. Osipov, Enhancement of the Sensitivity of a Lateral Flow Immunoassay by Using the Biotin–Streptavidin System, *Moscow Univ. Chem. Bull.* 2018 733. 73 (2018) 131–134. <https://doi.org/10.3103/S0027131418030070>.
- [34] A. Ruiz, G. Salas, M. Calero, Y. Hernández, A. Villanueva, F. Herranz, S. Veintemillas-Verdaguer, E. Martínez, D.F. Barber, M.P. Morales, Short-chain PEG molecules strongly bound to magnetic nanoparticle for MRI long circulating agents, *Acta Biomater.* 9 (2013) 6421–6430. <https://doi.org/10.1016/J.ACTBIO.2012.12.032>.
- [35] C.P. Bean, J.D. Livingston, Superparamagnetism, *J. Appl. Phys.* 30 (1959) S120–S129. <https://doi.org/10.1063/1.2185850>.
- [36] R. Egli, Magnetic susceptibility measurements as a function of temperature and frequency I: Inversion theory, *Geophys. J. Int.* 177 (2009) 395–420. https://doi.org/10.1111/J.1365-246X.2009.04081.X/2/M_177-2-395-EQ075.JPEG.
- [37] H. Zhang, D. Zeng, Z. Liu, The law of approach to saturation in ferromagnets originating from the magnetocrystalline anisotropy, *J. Magn. Magn. Mater.* 322 (2010) 2375–2380. <https://doi.org/10.1016/j.jmmm.2010.02.040>.
- [38] R.M. Cornell, U. Schwertmann, *The Iron Oxides*, Wiley, 2003. <https://doi.org/10.1002/3527602097>.
- [39] D. Peddis, M. V. Mansilla, S. Mørup, C. Cannas, A. Musinu, G. Piccaluga, F. D’Orazio, F. Lucari, D. Fiorani, Spin-Canting and Magnetic Anisotropy in Ultrasmall CoFe₂O₄ Nanoparticles, *J. Phys. Chem. B.* 112 (2008) 8507–8513. <https://doi.org/10.1021/JP8016634>.
- [40] M.F. Hansen, S. Mørup, Estimation of blocking temperatures from ZFC/FC curves, *J. Magn. Magn. Mater.* 203 (1999) 214–216. [https://doi.org/10.1016/S0304-8853\(99\)00238-3](https://doi.org/10.1016/S0304-8853(99)00238-3).
- [41] M. Knobel, W.C. Nunes, L.M. Socolovsky, E. De Biasi, J.M. Vargas, J.C. Denardin, Superparamagnetism and other magnetic features in granular materials: A review on ideal and real systems, *J. Nanosci. Nanotechnol.* 8 (2008) 2836–2857.

- <https://doi.org/10.1166/jnn.2008.15348>.
- [42] J.H. Lee, J.T. Jang, J.S. Choi, S.H. Moon, S.H. Noh, J.W. Kim, J.G. Kim, I.S. Kim, K.I. Park, J. Cheon, Exchange-coupled magnetic nanoparticles for efficient heat induction, *Nat. Nanotechnol.* 2011 67. 6 (2011) 418–422. <https://doi.org/10.1038/nnano.2011.95>.
- [43] R.D. Boyd, S.K. Pichaimuthu, A. Cuenat, New approach to inter-technique comparisons for nanoparticle size measurements; using atomic force microscopy, nanoparticle tracking analysis and dynamic light scattering, *Colloids Surfaces A Physicochem. Eng. Asp.* 387 (2011) 35–42. <https://doi.org/10.1016/J.COLSURFA.2011.07.020>.
- [44] C. Rosano, P. Arosio, M. Bolognesi, The X-ray three-dimensional structure of avidin, *Biomol. Eng.* 16 (1999) 5–12. [https://doi.org/10.1016/S1050-3862\(99\)00047-9](https://doi.org/10.1016/S1050-3862(99)00047-9).
- [45] Y. Wang, H. Xu, M. Wei, H. Gu, Q. Xu, W. Zhu, Study of superparamagnetic nanoparticles as labels in the quantitative lateral flow immunoassay, *Mater. Sci. Eng. C.* 29 (2009) 714–718. <https://doi.org/10.1016/j.msec.2009.01.011>.

SUPPLEMENTARY INFORMATION

S1. Size Distribution Analysis

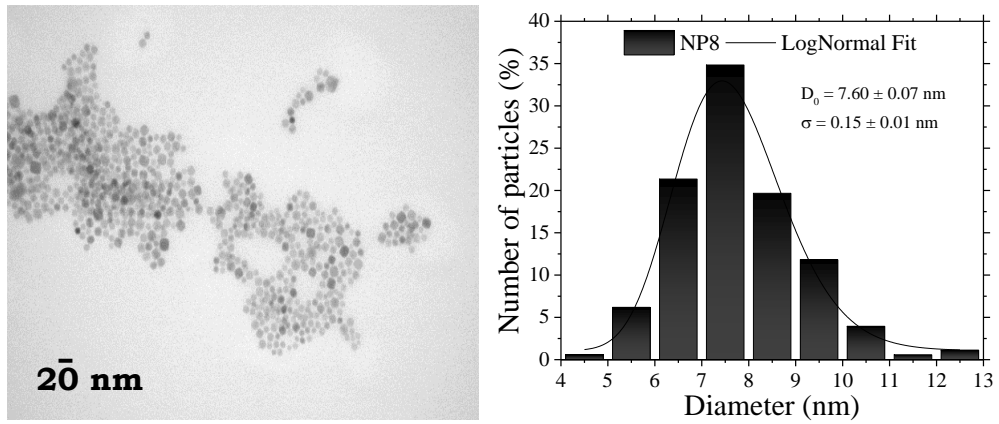


Figure S10. TEM image and size distribution histogram of sample NP8.

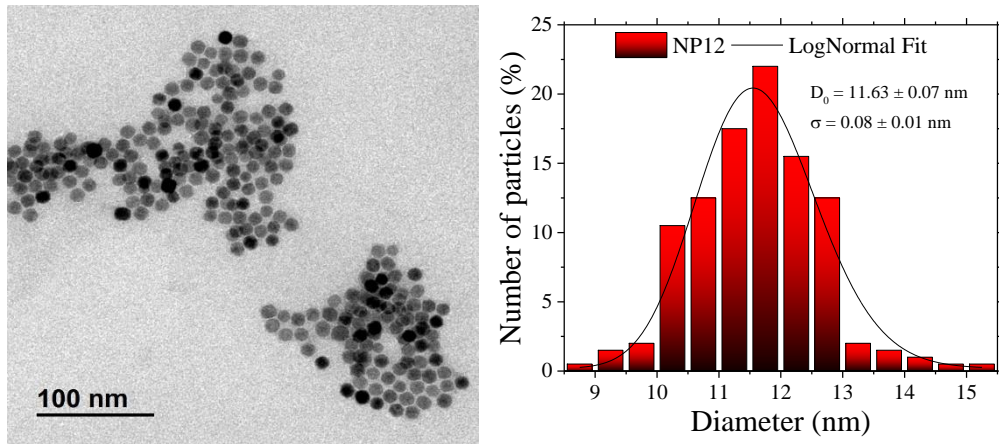


Figure S11. TEM image and size distribution histogram of sample NP12.

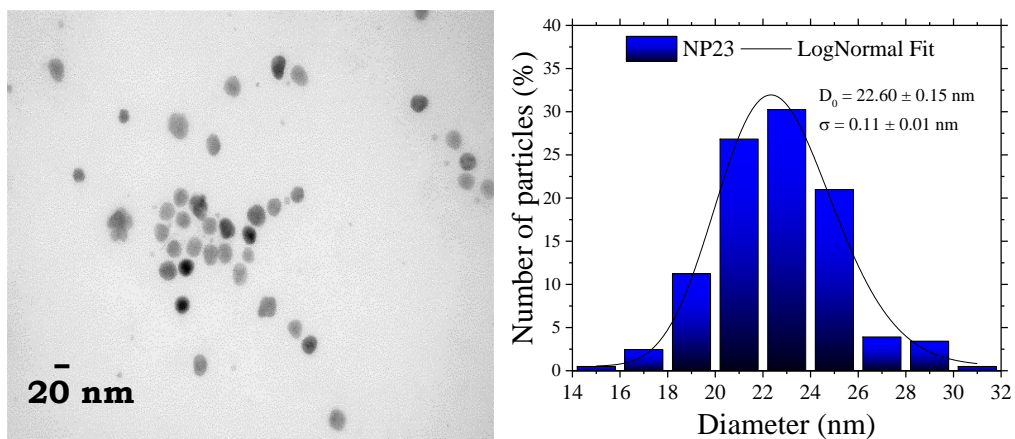


Figure S12. TEM image and size distribution histogram of sample NP23.

S2. Surface chemistry and nature of the iron oxide nanoparticles

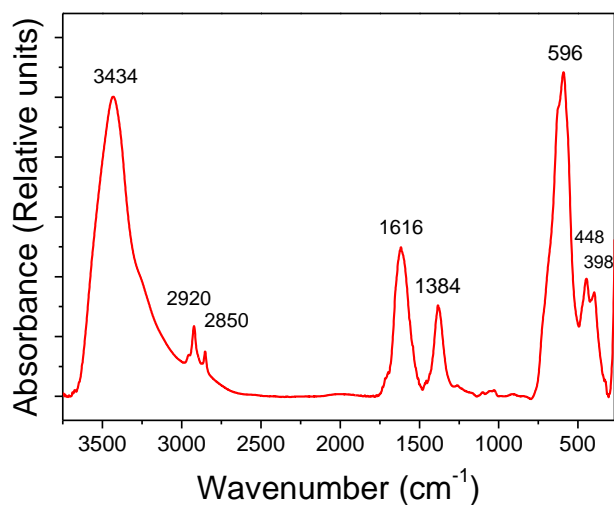


Figure S13. Infrared spectrum of sample NP8.

Figure S4 shows, as an example, the IR spectrum of sample NP8, which confirms the presence of the DMSA coating. It also shows a certain degree of oxidation from magnetite to maghemite. The infrared band at 3434 cm⁻¹ is due to the stretching band vibration of H₂O molecules. The absorption band at 1616 cm⁻¹ is due to the C=O bond vibration from the DMSA. Furthermore, the IR band at 1384 cm⁻¹ is attributed to the C-H bending vibration. In the low frequency region, bands at 596 cm⁻¹, 448 cm⁻¹, and 398 cm⁻¹ are attributable to iron oxide. The former is attributed to magnetite, and 448 and 398 cm⁻¹ bands suggest a partial oxidation of the particles, since they are typical from maghemite.

Section III - Chapter 3

Magnetic Nanoclusters Increase the Sensitivity of Lateral Flow Immunoassays for Protein Detection: Application to Pneumolysin in Urine as a Biomarker for *Streptococcus Pneumoniae*

Introduction and motivation

The previous chapter showed that the values to improve the signal in an inductive sensor are the labels' initial magnetic susceptibility and the volume of magnetic material per analyte unit. Regarding magnetic susceptibility, it is maximized with nanoparticles at the superparamagnetic limit, which is around 12 nm for iron ferrites. Regarding the magnetic mass, it is convenient to agglomerate these nanoparticles in clusters around 200 nm.

To validate these data in a real application, magnetic clusters (MNCs) were used as nanolabels. The nanocomposites are made up of 10 nm magnetite nanoparticles gathered in a polyacrylic acid matrix, forming individual agglomerates of about 85 nm. In addition, there is also some binding among these clusters, so their final effective size is around 200 nm. These particles resulted from a collaboration with Dr. Rodica Turcu and Dr. Alexander Bunge, from the National Institute for Research and Development of Isotopic and Molecular Technologies in Romania.

Pneumolysin is one of the most important virulence protein factors produced by *Streptococcus pneumoniae*, responsible for pneumococcal pneumonia. It is recognized as an essential biomarker for diagnosis in urine samples. Pneumonia is the infectious disease that causes the most deaths globally, especially among children under five years and adults over 65 years, most of them in low- and middle-income countries. Furthermore, most of these deaths are preventable. Diagnostic of pneumonia, and particularly determination of its etiology, is still a clinical challenge. Either appropriate samples are difficult or risky to obtain, or the diagnostic tests take too long. In most cases, antibiotics are prescribed without determining the actual agent of the disease (which specific bacteria or virus), so that they may be useless and even harmful. Therefore, a rapid diagnostic test with high sensitivity and specificity in

handy samples like urine will help overcome the current drawbacks such as false-negative and time-consuming cultures and the indiscriminate use of antibiotics.

This chapter presents the development of a lateral flow immunoassay for detecting pneumolysin using MNCs as labels. Dual calibrations are obtained by taking advantage of the magnetic and optical signals of the MNCs in the sandwich-type immunoassay developed. This allows the quantification with both a mobile phone camera and the inductive sensor. The MNCs magnetic character was used to pre-concentrate the samples and relocate the particles in the strip once the tests were done. The goal of preconcentration is to detect concentrations below the sensitivity range of the method. It is a straightforward procedure that allowed us to reduce by more than 30 times the amount of PLY. On the other hand, relocating the samples allowed us to increase the inductive signal by 20%. The results are promising and open a path for further improvement.

Below are the full details of this investigation.

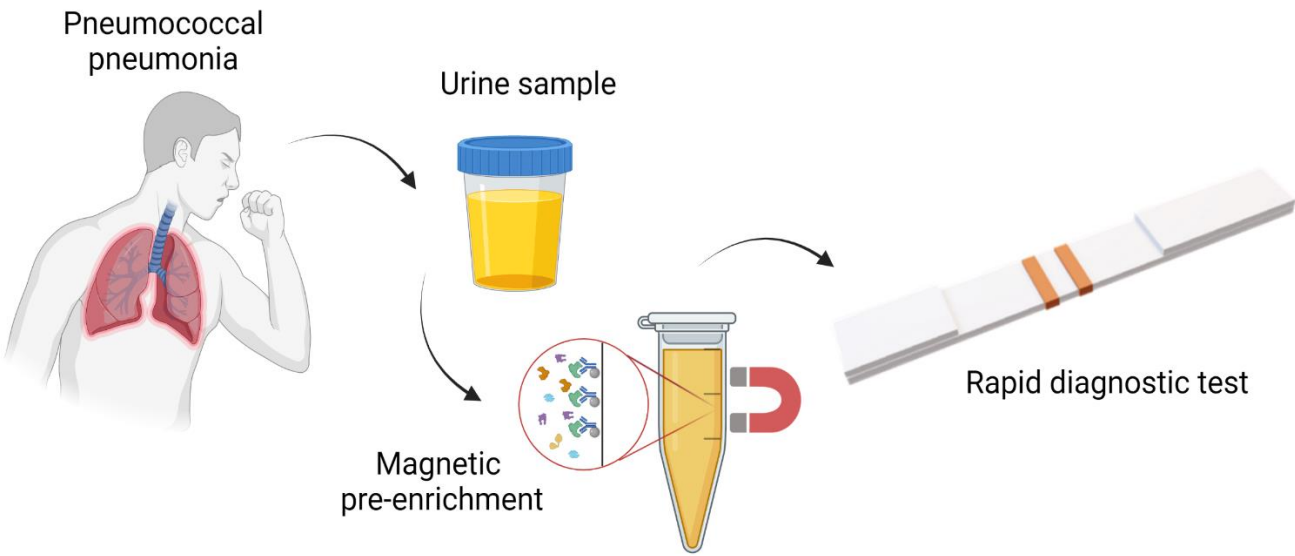
Scientific article (in preparation)

Magnetic Nanoclusters Increase the Sensitivity of Lateral Flow Immunoassays for Protein Detection: Application to Pneumolysin in Urine as a Biomarker for *Streptococcus Pneumoniae*

This work has been published in:

Cite as:

GRAPHICAL ABSTRACT



Magnetic Nanoclusters Increase the Sensitivity of Lateral Flow Immunoassays for Protein Detection: Application to Pneumolysin in Urine as a Biomarker for *Streptococcus Pneumoniae*

María Salvador^{1,2}, José Luis Marqués-Fernández¹, Alexander Bunge³, José Carlos Martínez-García¹, Rodica Turcu³, Davide Peddis^{2,4}, María del Mar García-Suárez⁵, María Dolores Cima-Cabal⁵, Montserrat Rivas¹

¹*Department of Physics & IUTA, University of Oviedo, Campus de Viesques, 33203 Gijón, Spain*

²*Institute of Structure of Matter – National Research Council (CNR), 00016 Monterotondo Scalo (RM), Rome, Italy*

³*National Institute for Research and Development of Isotopic and Molecular Technologies, 400293 Cluj-Napoca, Romania*

⁴*Department of Chemistry and Industrial Chemistry, Università degli Studi di Genova, 16146 Genova, Italy*

⁵*Escuela Superior de Ingeniería y Tecnología (ESIT), Universidad Internacional de la Rioja, UNIR. 26006 Logroño, Spain*

Abstract

Lateral flow immunoassays for detecting biomarkers in body fluids are simple, quick, inexpensive, point-of-care tests widely used in disease surveillance, for instance, during the coronavirus disease 2019 (COVID - 19) pandemic. Improvements in sensitivity would increase their utility in healthcare, food safety, and environmental control. Recently, biofunctional magnetic nanoclusters have been used to selectively label target proteins, which allows their detection and quantification with a magneto-inductive sensor. This type of detector is easily integrated with the lateral flow immunoassay format. Pneumolysin is a cholesterol-dependent cytolysin and one of the most important protein virulence factor of pneumonia produced by *Streptococcus pneumoniae*. It is recognized as an important biomarker for diagnosis in urine samples. Pneumonia is the infectious disease that causes the most deaths globally, especially among children under five years and adults over 65 years, most of them in low- and middle-income countries. There especially, a rapid

diagnostic urine test for pneumococcal pneumonia with high sensitivity and specificity would be helpful in primary care. In this work, lateral flow immunoassay with magnetic nanoclusters conjugated to anti-pneumolysin antibodies was combined with two strategies to increase the technique's performance: First, magnetic concentration of the protein before the immunoassay followed by quantification by means of a mobile telephone camera and the inductive sensor resulted in detection limits as low as 0.57 ng (telephone camera) and 0.24 ng (inductive sensor) of pneumolysin per milliliter. Second, magnetic relocation of the particles within the test strip after the immunoassay was completed increased the detected signal by 20%. Such results obtained with portable devices are promising when compared to non-portable conventional pneumolysin detection techniques like enzyme-linked immunosorbent assay. Combination and optimization of these approaches would have excellent application in point-of-care biodetection to reduce antibiotic misuse, hospitalizations, and deaths from community-acquired pneumonia.

Keywords: Lateral flow immunoassays, pneumococcal pneumonia, COVID-19, magnetic nanoparticles, magnetic separation, inductive sensor.

1. Introduction

Pneumonia is the leading cause of death from infectious diseases globally [1]. Moreover, its high incidence places it, along with other lower respiratory diseases, as the third overall global cause of mortality, surpassed only by ischemic heart and cerebrovascular diseases [2]. Pneumonia incidence is most significant at the extremes of age. People at risk are the elderly (> 65 years old), especially those with comorbidities, and children (< 5 years old), for whom it is the leading cause of mortality after the neonatal period. This is especially concerning because most pneumonia deaths should be preventable [3]. Even when it is not fatal, it increases the risk of death for an extended period after its onset [4]. A growing aging population and an increase in comorbidities [5] make this prospect even worse, with considerable implications for healthcare systems worldwide [6].

Identification of the etiologic agent of pneumonia is essential to guide therapy (avoiding antibiotics over-prescription) and prevention and control strategies: Bacteria, viruses, and fungi can all cause pneumonia

[7]. *Streptococcus pneumoniae* (pneumococcus) remains the leading pathogen responsible for most community-acquired pneumonia and other respiratory and systemic infections such as meningitis [8]. Pneumonia is currently the most common co-infection in COVID-19 patients, which likely contributes significantly to morbidity and mortality [9, 10].

Usually, the diagnosis of pneumococcal pneumonia is based on gram stain and sputum or blood cultures. Unfortunately, appropriate samples of the former are difficult to obtain, especially from pediatric patients, and the latter has a surprisingly poor yield [11]. Polymerase chain reaction (PCR) technology can be applied to detect the bacteria [12]. However, it requires sophisticated equipment and DNA kits that are likely unaffordable for primary health care centers and poorly resourced locations worldwide. Another option is the commercial lateral flow test Binax Now® for the detection of pneumococcal polysaccharide C in urine. However, it has been reported to have low sensitivity in adults, probably associated with the serotype changes and their polysaccharide C variability [13], and it is not helpful in children if they have had a prior bronchopulmonary disease or if they have been vaccinated [14, 15]. Therefore, the current challenge in pneumonia diagnosis, mainly but not exclusively in children, is a rapid diagnostic test with high sensitivity and specificity in handy samples like urine. Alone, or in combination with others, it would enable precise diagnosis and prompt treatment, reduction in hospitalization, avoidance of empirical antibiotic prescriptions and increasing antibiotic resistance, and, especially in less-developed countries, prevention of fatal outcomes.

Pneumolysin (PLY) is a cholesterol-dependent cytolysin recognized as one of the most important protein virulence factor of *S. pneumoniae* [16]. Its role in pneumococcal infection has been extensively studied: Mutant bacteria lacking PLY expression prove its relevant function in the infection [17]. Hence, PLY is an important target, both from a diagnostic and a therapeutic perspective [18].

Lateral flow immunoassays (LFAs) are bio-testing methods with many advantages for point-of-care (POC) applications, such as minimal manipulation, quickness, portability, easy use, and low cost. Its introduction to the general market occurred in the early 1980s with the home pregnancy test [19], and the COVID-19 pandemic has made them

more familiar. Besides these applications, they have been successfully used to detect other targets in different types of specimens [20, 21].

LFAs depend on capillary action and biorecognition. A strip of nitrocellulose guides the liquid sample by capillarity and the target molecule is selectively trapped at a test line by an immunological reaction. The biomolecule is labeled with nanoparticles to make it detectable. These nanoparticles (gold or latex) give a color signal that provides a yes/no (presence/absence) response. Such a qualitative result is sufficient for many applications; however, many others need quantitative results for cancer diagnosis and prognosis, serological information, or comparison against toxin thresholds. The quantification of the analyte can be accomplished by optical transducers based on image analysis or reflectance. However, optical methods are sensitive to interference from the ambient light, humidity, and staining or aging of the paper strip, which frequently cause difficulties in calibration and reproducibility [21, 22]. Additionally, only nanoparticles at the membrane surface contribute significantly to the signal [23].

Magnetic nanoparticles have been used before as efficient labels in LFAs [24]. They can be easily tailored in terms of size and surface and magnetic properties. Magnetic sensors can detect them without interference from the biological sample or the paper. More interestingly, these magnetic properties can be used for external manipulation, pre-concentration, or separation of the target analyte from the sample matrix. These strategies can improve the sensitivity of the LFAs enormously [25, 26].

Our research group has developed a detection method using superparamagnetic nanoparticles and an inductive sensor, which does not compromise the advantages of the LFAs. It is based on an excitation-detection planar coil that avoids the need for additional excitation coils or bulky components [27, 28]. It is an affordable system that can be easily miniaturized in a POC device. Previous studies have shown that the magnetic labels' crucial properties are their initial magnetic susceptibility and the mass retained in the test line [29]. From this point of view, clusters of magnetic nanoparticles are advantageous over isolated particles.

For this work, we have developed a LFA to detect PLY with biofunctional

magnetic nanoclusters (MNCs) conjugated to an anti-PLY antibody. The polyol solvothermal synthesis method was optimized for reproducible and scalable production, yielding MNCs with large initial magnetic susceptibility and high magnetic moment. A considerable improvement of the LFA's sensitivity was achieved thanks to the multifunctionality of the MNCs: First, magnetic preconcentration and relocation decrease the detection limit. Second, MNCs enable dual detection: optical (the test line has a brownish color) and magnetic (detectable, for example, with an inductive sensor).

2. Materials and methods

2.1. Chemicals and reagents

Sodium polyacrylate (molecular weight \approx 2100), $\text{FeCl}_3 \cdot 6\text{H}_2\text{O}$, anti-mouse IgG, 1-ethyl-3-[3-di-methylaminopropyl] carbodiimide (EDC), bovine serum albumin (BSA), N-hydroxysuccinimide (NHS), 2-(N-morpholino) ethanesulfonic acid (MES), and Tween20 were purchased from Sigma-Aldrich. Diethylene glycol 99% and ethylene glycol 99% were obtained from Alfa Aesar and S.C. Simex SRL, respectively. Ethanol pure was acquired from Chemical Company S.A.

Recombinant pneumolysin and both mouse anti-pneumolysin monoclonal antibodies (PLY-4 used as capture antibody and PLY-7 as detection antibody), were produced as previously described [30, 31].

For the lateral flow strips, the backing cards (HF000MC100) and the glass fiber membrane (GFCP001000) used as sample pad were purchased from Merck Life Science. The nitrocellulose membranes (UniSart CN95) were provided by Sartorius, Spain, and the absorbent pads (CF5) by Cytiva Europe GmbH, Spain.

2.2. Magnetic nanoclusters synthesis and characterization

A mixture of ethylene glycol (20 mL) and diethylene glycol (40 mL) was used to suspend/dissolve sodium acetate (6 g) and sodium polyacrylate (6 g). $\text{FeCl}_3 \cdot 6\text{H}_2\text{O}$ (2.17 g) was dissolved in diethylene glycol (20 mL). After stirring for 10 min at room temperature, the iron chloride solution was added to the suspension/solution of acetate and polyacrylate, stirred well for another 10 min, and transferred into a Teflon-lined autoclave (200 mL

capacity). The autoclave was heated to 200°C for 15.5 h and cooled naturally. The magnetite clusters were rinsed into a beaker with ethanol, magnetically separated, and washed two times with ethanol and three times with water before their re-suspension in water. The concentration of magnetic clusters was 22 mg/g suspension.

The size and shape of the nanoclusters were examined by scanning transmission electron microscopy (STEM) and high-resolution transmission electron microscopy (HRTEM). STEM images were acquired with a Hitachi HD2700 equipped with a cold field emission gun and a dual energy-dispersive X-ray system (X-Max N100TLE silicon drift detector) from Oxford Instruments. For the analysis, a suspension of the samples was previously sonicated (< 10 s) with a UP100H ultrasound finger and deposited by the droplet method on a 400-mesh copper grid coated with a thin carbon layer. The nominal operating voltage was 200 kV. HRTEM images were obtained with a JEOL JEM-2100 200 kV.

The analysis of the surface chemical composition of the clusters was done by X-ray photoelectron spectroscopy (XPS) using a SPECS XPS spectrometer equipped with a dual-anode Al/Mg X-ray source, a PHOIBOS 150 2D CCD hemispherical energy analyzer, and a multi-channel detector with vacuum maintained at 1.3×10^{-10} kPa. The Al K α X-ray source (1486.6 eV) operated at 200 W was used for the XPS investigations. XPS survey spectra were recorded at 30 eV pass energy, 0.5 eV per step. The high-resolution spectra for individual elements were recorded by accumulating multiple scans at 30 eV pass energy and 0.1 eV per step.

DC-magnetization measurements were performed using a vibrating sample magnetometer (Cyrogenic Ltd.). Zero field cooling (ZFC) and field cooling (FC) curves were performed using a Quantum Design SQUID magnetometer. Zero- field-cooled and field-cooled magnetization measurements were carried out by cooling the sample from room temperature to 5 K in zero magnetic field; then a static magnetic field of 2.5 mT was applied. MZFC was measured during warming up from 5 to 300 K, whereas MFC was recorded during the subsequent cooling. The magnetization values were referenced to the mass of iron oxide measured by thermogravimetric analysis.

The assessment of the MNCs as reporters in the inductive sensor was

done by depositing some droplets of known mass onto a 10 mm × 2 mm blotting paper, left to dry for at least 12 h. The performance of the MNCs was evaluated by the sensor sensitivity (Σ) defined as for magnetoimpedance sensors. For a fixed frequency and type of particles, Σ is defined as the relative percentage increase of the impedance (Z) per unit mass of particles (m). For Z with and Z_0 without particles in the inductive sensor:

$$\Sigma = \frac{1}{m} \frac{Z - Z_0}{Z_0} \cdot 100 \quad (1)$$

The resolution of the sensor (R) is defined as the smallest change in mass to be resolved, where σ_{base} is the noise as the standard deviation of the signal over time when measuring a blank, and ΔZ is $Z - Z_0$:

$$R = \frac{m\sigma_{base}}{\Delta Z} \quad (2)$$

2.3. Bioconjugation of the magnetic nanoclusters

In the immunoassay, a mouse monoclonal antibody (PLY7) against PLY was used as a selective detection antibody attached to the MNCs. For this bonding, the polyacrylic's carboxylic groups at the MNCs surface were activated using carbodiimide chemistry, as depicted in Figure 1a: 5 μ L of the MNCs, previously sonicated for 5 min, were mixed with 100 μ L of EDC (3.5 mg/mL in MES 50 mM, pH 6.00) and 100 μ L of NHS (3.5 mg/mL in MES 50 mM, pH 6.00). The mixture was sonicated for 10 min. Then, 71 μ L of the antibody (0.6 mg/mL) was added and left 4 h in a refrigerated ultrasonic bath while mechanically agitated. After the conjugation, the residual activated carboxyl groups were blocked by adding 107 μ L of the blocking solution (1% BSA in phosphate buffered saline (PBS) 1 mM, pH 7.4) and sonicating for 1 h. Then, the mixture was centrifuged at 7000 rpm for 5 min, and 380 μ L of the supernatant discarded. The same amount of freshly prepared buffer (PBS 1 mM, pH 7.4) was used to resuspend the pellet.

The hydrodynamic size distribution and average ζ -potential before and after the conjugation process were obtained by dynamic light scattering (DLS) measurements performed in a Malvern Instruments Zetasizer Nano SZ equipped with a solid-state He-Ne laser (wavelength 633 nm).

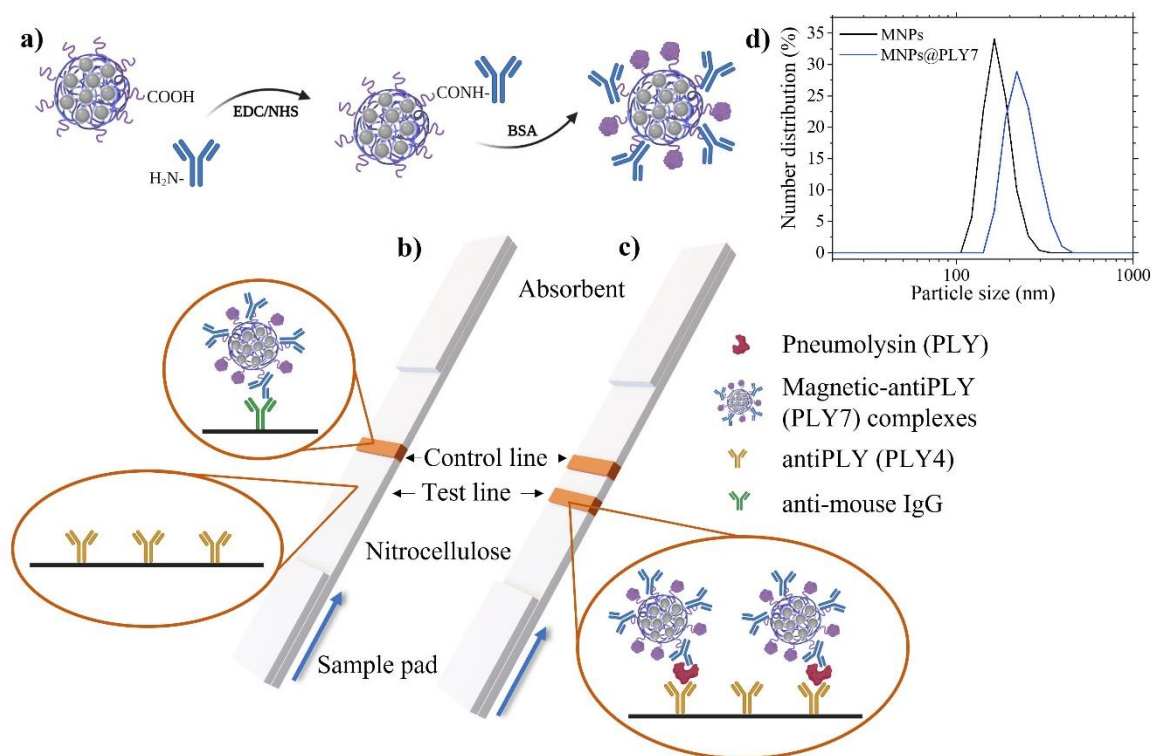


Figure 1. a) Schematic illustration of the MNCs biofunctionalization with anti-pneumolysin antibody PLY7 via EDC/NHS chemistry. b) Scheme of the lateral flow immunoassay, where specific antibodies against pneumolysin PLY4 (test line) and anti-mouse IgG antibodies (control line) are immobilized on the membrane. The blue arrow indicates the flow direction. In a blank sample, only the control line is visible. c) Lateral flow assay for a sample containing PLY, which forms a complex with the MNCs-PLY7 and is captured at the test line by the PLY4 antibodies. d) Hydrodynamic size distribution profile of the MNCs before (black) and after (blue) the bioconjugation with the PLY7 antibody.

2.4. Preparation of the immuno-strips

For the LFA strip assembly, the nitrocellulose membrane was attached to an adhesive backing card. To create the test and control lines (see Figure 1), the capture antibody (mouse monoclonal PLY4) and the anti-mouse IgG, respectively, both at a concentration of 1 mg/mL, were printed using a reagent dispenser. The latter consists of an automatic micropipette coupled with a micropositioner programmed to synchronize the micropipette dispensation with its motion. This printing method enables the deposition across the membrane at a rate of 0.1 $\mu\text{L}/\text{mm}$. The initial attraction of the antibodies to the nitrocellulose involves the interaction between the carboxyl groups in the former and the nitro group

dipoles in the latter. Adsorption is further enhanced by the interaction between the nitrocellulose and hydrophobic domains within the protein. Thus, the antibodies are immobilized in the membrane strip.

After drying, the sample pad (which enables a controlled transfer of the sample to the membrane) and the absorbent pad (which acts as a wick and prevents backflow) were placed onto the backing card with an overlap of 2 mm with the membrane. Finally, single 5 mm wide strips were cut with a guillotine (MS Yosan 30).

PLY standard solutions at concentrations of 13, 22, 30, 40, 60, 80, 120, 360, and 720 ng/mL were prepared by diluting a PLY stock solution in the sample buffer (PBS 1 mM, pH 7.4). To obtain the sample solution, which has a final total volume of 100 μ L, these standards were mixed with 20 μ L of the MNCs-PLY7 conjugates and freshly prepared running buffer (RB), containing 0.5% Tween20 in PBS (1 mM, pH 7.4).

The LFAs were then carried out in dipstick format by vertically introducing the sample pad in the solution, which then flowed upwards, driven by capillary action. The performance of the LFAs relies on a sandwich format in which the detection antibody PLY7 and the MNCs form a complex with the target analyte if it is present. These complexes

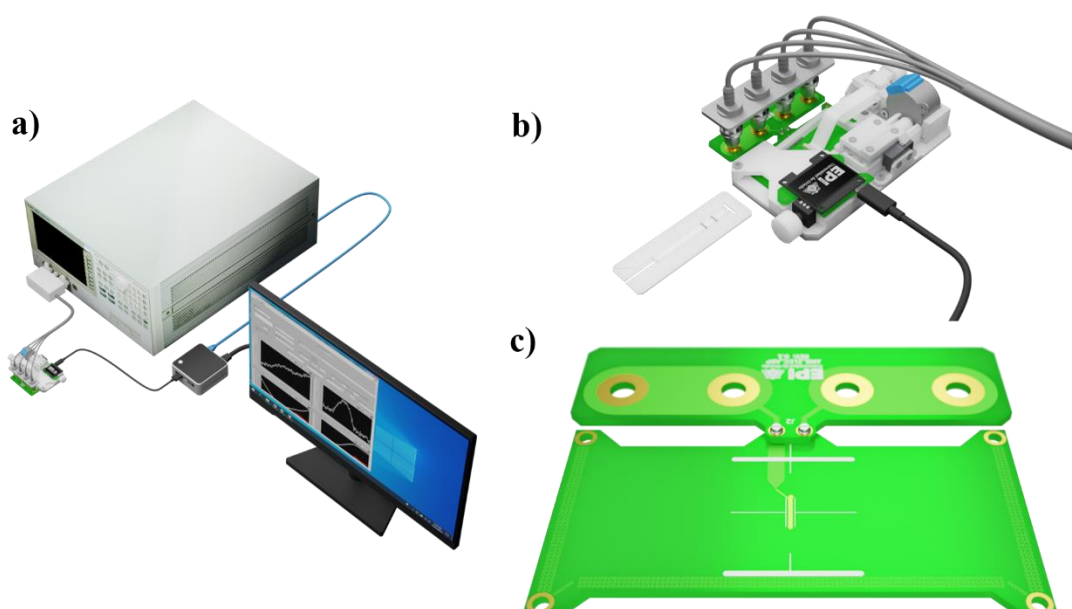


Figure 2. a) Schematic representation of the sensing system showing the impedance analyzer, the micropositioner, and the personal computer used to control both. b) Image of the sensing device, which comprises the planar inductor, the LFAs holder, and the micropositioner. c) Detailed image of the planar inductor specifically designed to encompass the entire width of the LFAs during scanning.

get trapped by the capture antibody at the test line, making it visible. The remaining sample will continue flowing all the way through the membrane, facing the control line, up to the absorbent (see Figure 1b and c for a detailed schematic). All the assays were performed in triplicate.

2.5. Quantification of the immunoassays

To provide a quantitative signal for the test line, two different methods were used. First, the optical signal was evaluated by taking photos of the LFAs strips with a mobile “smartphone” camera (Leica, 20 megapixels monochrome, 12 megapixels RGB, f/1.6). The intensity of the test line was analyzed using ImageJ software and integrated across the width of the test line. The images are converted to black and white, and then, the intensity is given in terms of a gray scale. Second, the signal from the test lines were quantified by a home-made inductive sensor specially adapted for scanning LFA strips (see Figure 2). It consists of a planar inductor whose impedance magnitude and phase are continuously measured with a precision impedance analyzer (Agilent 4294A, 16048G test leads, 500 mV/20 MHz) while the LFA strip is micropositioned in steps of 0.1 mm. The high magnetic permeability of the particles induces an impedance increase during the scan. This peak is integrated over position to account for all the particles present in the test line, no matter how they are distributed. The signal obtained has units $\mu\Omega\cdot\text{mm}$, coming from the cumulative integral of the impedance (micro-ohms) across the width of the test line scanned (millimeters). Previous studies [32] have demonstrated that this change in the impedance is directly proportional to the number of superparamagnetic nanoparticles present in the test line, allowing determination of the analyte concentration.

2.6. Magnetic pre-concentration

An initial 80 μL PLY standard solution of 13 ng/mL was prepared and further diluted by the addition of freshly prepared RB to obtain concentrations ranging from 6.5 down to 0.81 ng/mL. Then 20 μL of the PLY7-MNCs conjugates were added to the low-concentration solutions, shook, and left to sit for 15 min. During this time, the immunorecognition of the analyte by the MNCs-PLY7 takes place.

We used the simplest pre-concentration method possible: An Eppendorf tube was placed vertically on a NdFeB permanent magnet (N45, nickel-

plated, S-70-35-N, Supermagnete); the magnetic field gradient was on the order of 64 mT/mm as measured by a Hall probe (FW Bell, Model 4048) for another 15 min to attract the PLY-labeled MNCs to the bottom. Part of the supernatant was then removed up to obtain a final total volume of 100 μ L of concentrated sample. Such a solution was sonicated for 5 min and the LFA test carried out. This process is depicted in Figure 3a.

2.7. Magnetic relocation

Although magneto-inductive sensing is a form of non-contact, remote detection, the signal from the particles that are closer to the inductor is more intense. Hence, it is helpful to relocate the particles within the volume of the membrane towards the surface that faces the inductor.

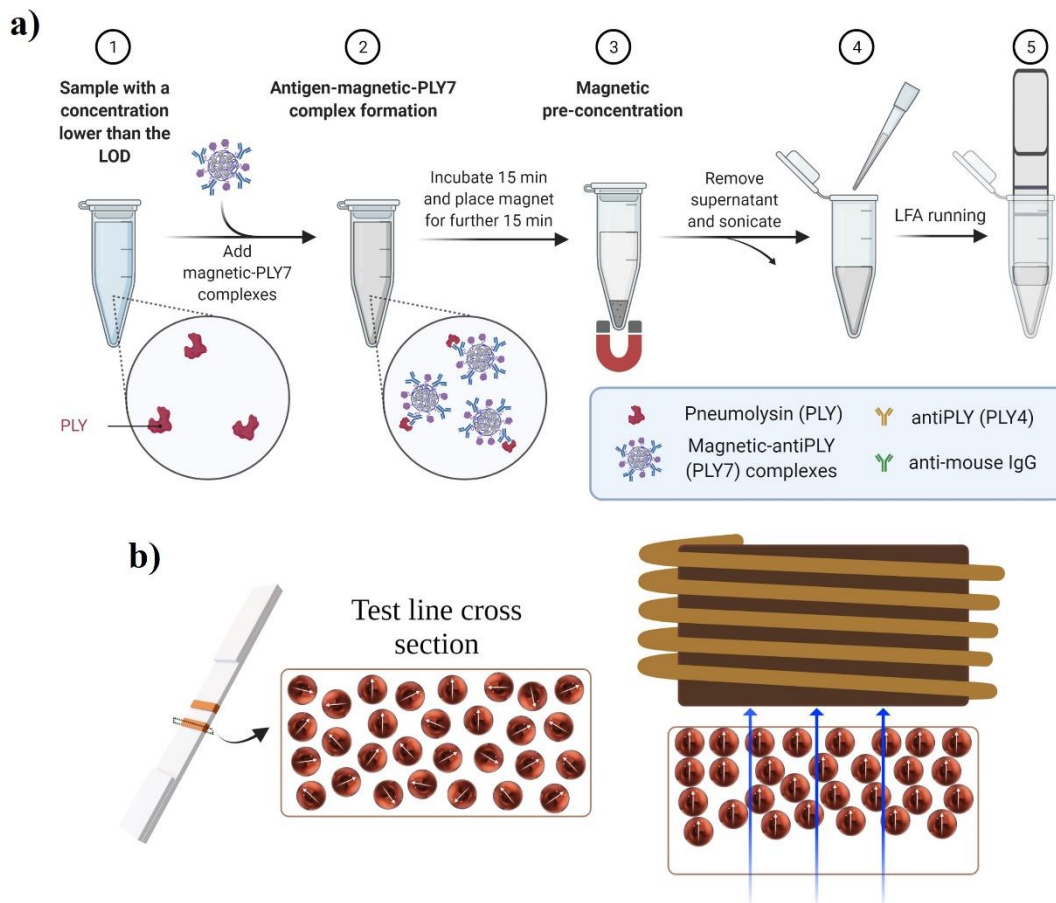


Figure 3. a) Schematic illustration of the magnetic pre-concentration procedure. b) Schematic illustration of the MNCs distributed within the membrane before (left) and after (right) of the relocation process. The blue arrows indicate the magnetic gradient direction.

Three different LFA strips were subjected to magnetic relocation after being run as described in section 2.4. A magnetic field gradient was applied perpendicular to the test line to demonstrate that the particles

can be relocated within the membrane (see Figure 3b). For this purpose, 10 μL of RB was deposited on the test line and placed on one of the poles of an electromagnet. For 2 h, a direct current generated a magnetic field gradient of 0.32 mT/mm, as measured by a Hall probe (FW Bell, Model 4048). After the magnetic relocation, the signal of the LFAs was once again evaluated with the inductive sensor.

3. Results and discussion

3.1. Characterization of the magnetic clusters

Magnetite clusters were synthesized by a well known solvothermal method using a polyol process [33]. Sodium polyacrylate was used as coating because the resulting clusters are relatively stable in suspension and display many carboxylate groups on the surface, which can be further functionalized. The size of the clusters was optimized to be below 100 nm using the ratio between the two solvents ethylene glycol and

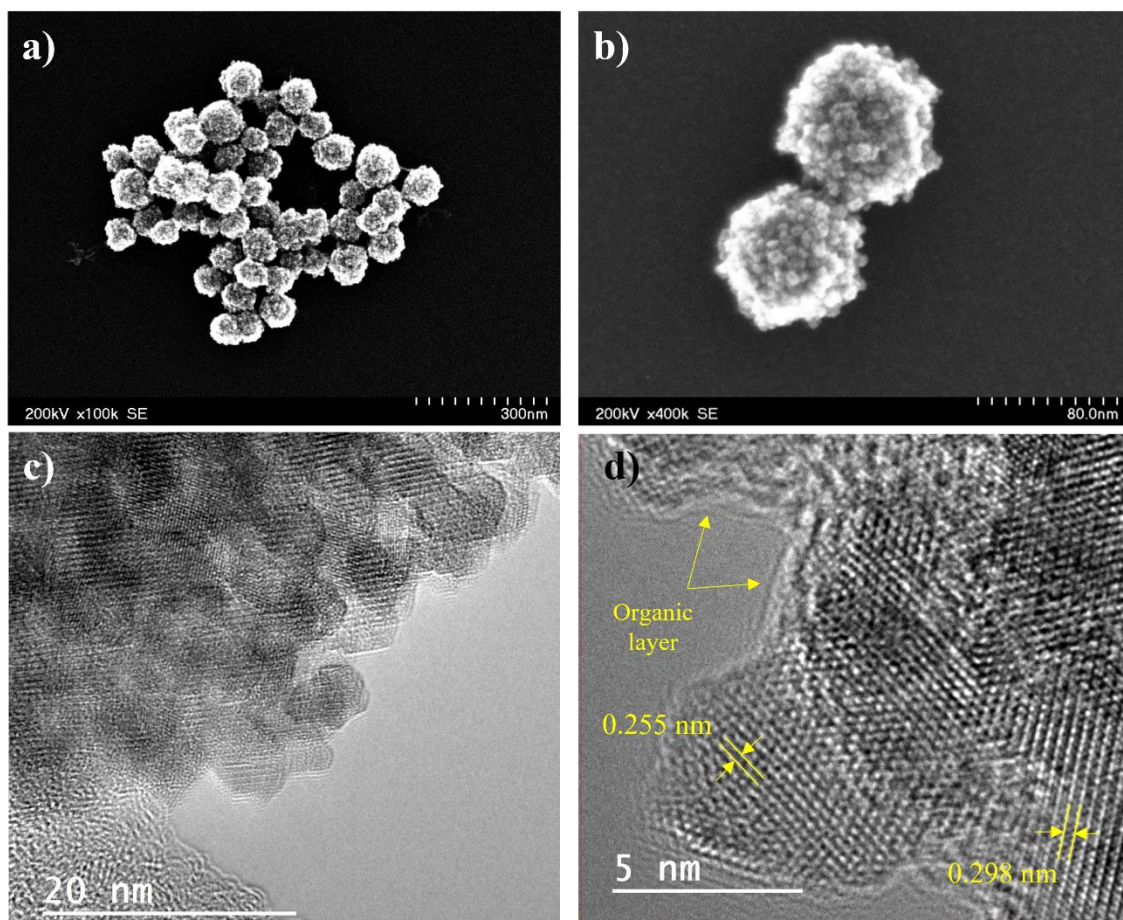


Figure 4. a) b) STEM images of magnetic clusters. c) HRTEM image of the magnetic nanoclusters with the organic layer at their surface. d) HRTEM image with the interplanar distance corresponding to the family of crystalline planes (220) and (311).

diethylene glycol. STEM images (see Figure 4a and b) confirm the formation of almost spherical magnetic clusters with a narrow size distribution with a mean size of 89 ± 1 nm and a standard deviation of 0.09 ± 0.01 nm.

HRTEM images in Figure 4c and d show the individual particles that make up the nanoclusters, with sizes that range from 4 nm to 7 nm. MNCs consist of a combination of individual agglomerated particles (attached by weak interactions of the polymeric coating) and aggregates (individual particles that share a surface). In Figure 4d, various particles appear trapped by an amorphous layer that corresponds to the organic polyacrylic acid on their surface. The interplanar crystal distances measured from the adjacent lattice fringes using a fast Fourier transform (FFT) are 0.298 nm, 0.255 nm, 0.220 nm, and 0.155 nm, which correspond to the planes with Miller indexes (220), (311), (400), and (440), respectively. These values agree with the standard card JCPDS N° 19-0629 for magnetite.

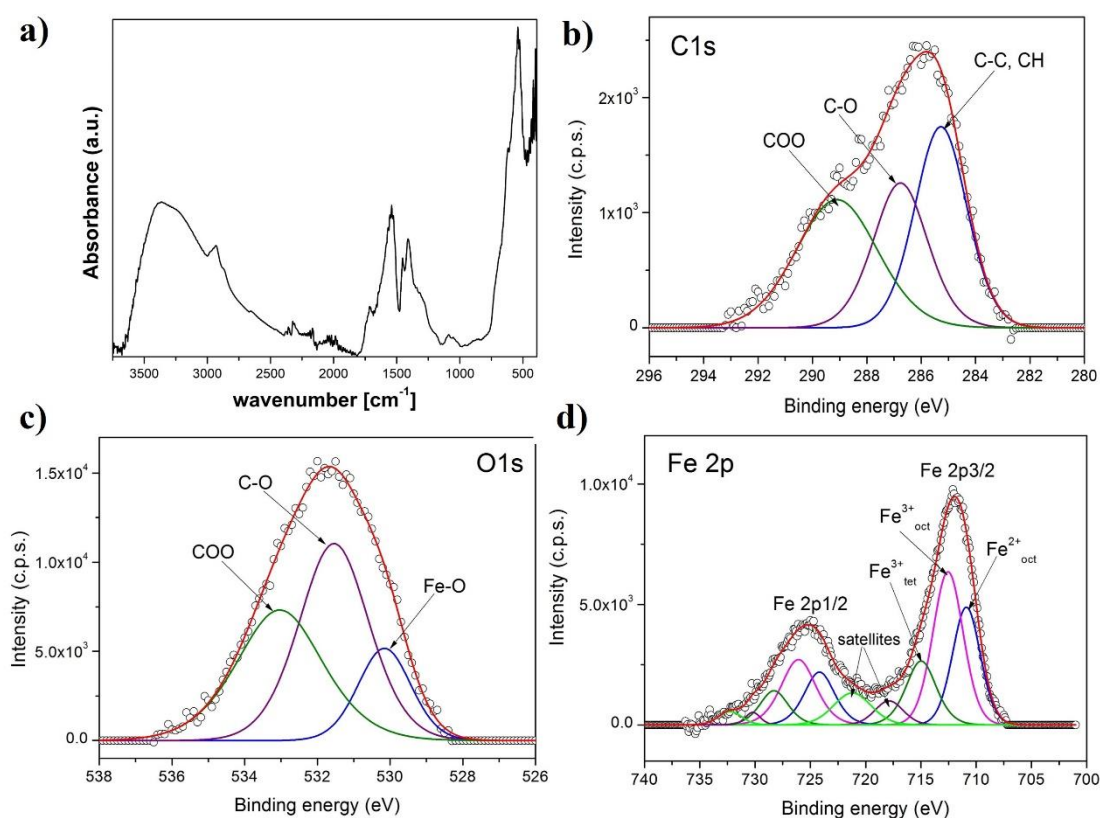


Figure 5. a) FTIR spectrum of the magnetic nanoclusters coated with polyacrylic acid. b) The high resolution XPS spectra of C 1s, c) O 1s, and d) Fe 2p core-levels for the clusters coated with polyacrylic acid.

Figure 5a shows the Fourier transform infrared (FTIR) spectrum of the nanoclusters. A band at 540 cm^{-1} is due to Fe-O stretching, which can be ascribed to the spinel iron oxides. The peak at 1092 cm^{-1} stems from $\nu(\text{C} - \text{O})$, from ethylene glycol bound to the clusters. Bands at 1414 cm^{-1} and 1540 cm^{-1} are indicative of carboxylate groups ($\nu(\text{C}=\text{O})$), both from polyacrylate as well as acetate bound to the surface. The bands at 2867 cm^{-1} and 2930 cm^{-1} are generic $\nu(\text{C}-\text{H})$ from the coating. Both surface-bound Fe-OH and carboxylic acid as well as hydroxyl groups (from ethylene glycol) give rise to the broad band between 3000 cm^{-1} and 3500 cm^{-1} ($\nu(\text{O}-\text{H})$).

XPS analysis was used to demonstrate the successful preparation of magnetic clusters coated with polyacrylic acid. The high resolution XPS spectra of C 1s, O 1s, and Fe 2p core-levels for the magnetic clusters are shown in Figure 5b, c, and d, respectively. The spectra have been deconvoluted into components so as to obtain the best fit. The C 1s spectrum contains three components ascribed to C-C, CH groups (285 eV), COO (289.1 eV) from polyacrylic acid, and C-O (286.6 eV) from ethylene glycol, which is also present on the surface of the nanoclusters. The oxygen spectrum in Figure 5c exhibits three components assigned to the oxygen atoms from the carboxyl group COO of the polyacrylic acid (533 eV), from C-O (531.5 eV) from the ethylene glycol, and from Fe-O in the magnetite (530 eV). The Fe 2p spectrum is made up of the doublet Fe 2p- $3/2$ and Fe 2p- $1/2$. The best fit for the Fe 2p spectrum in Figure 5d contains the components corresponding to Fe^{3+} and Fe^{2+} ions and their corresponding satellites. From the Fe^{3+} and Fe^{2+} 2p peaks, an $\text{Fe}^{3+}/\text{Fe}^{2+}$ atomic ratio of 2 was obtained. This result confirms that the cluster contains magnetite nanoparticles. The surface chemical composition (atomic concentrations) of the magnetic clusters calculated from high resolution XPS spectra has values of 26.6%, 48.5%, and 24.9% for C, O and Fe, respectively. These results demonstrate the successful preparation of magnetite nanoclusters coated with polyacrylic acid.

Field dependence of the magnetization of the MNCs sample at 300 K (Figure 6a) is not completely reversible, as shown in the inset (i.e., $H_C = 2.7\text{ mT}$, $M_r/M_S = 0.09$) suggesting the presence of constituent particles that are blocked at this temperature. This is confirmed by the ZFC-FC curves (see Figure 6b), where no irreversibility region is observed in all the explored temperature range [34]. This behavior can be ascribed to the presence of strong interparticle interactions confirmed by the

flatness of the FC curve. Therefore, in each MNC, densely packed superparamagnetic and blocked particles coexist.

Regardless, the coercivity (width of the magnetization loop) and hysteresis loss (area of the loop) are small, and the initial susceptibility (slope of the magnetization curve near zero field) is high, with a value of 28 (dimensionless, SI units). The saturation magnetization (M_S) of the MNCs referenced to the magnetite mass was calculated by fitting the experimental data to the law of approach to saturation [35], yielding a value of $60 \pm 2 \text{ A}\cdot\text{m}^2/\text{kg}$.

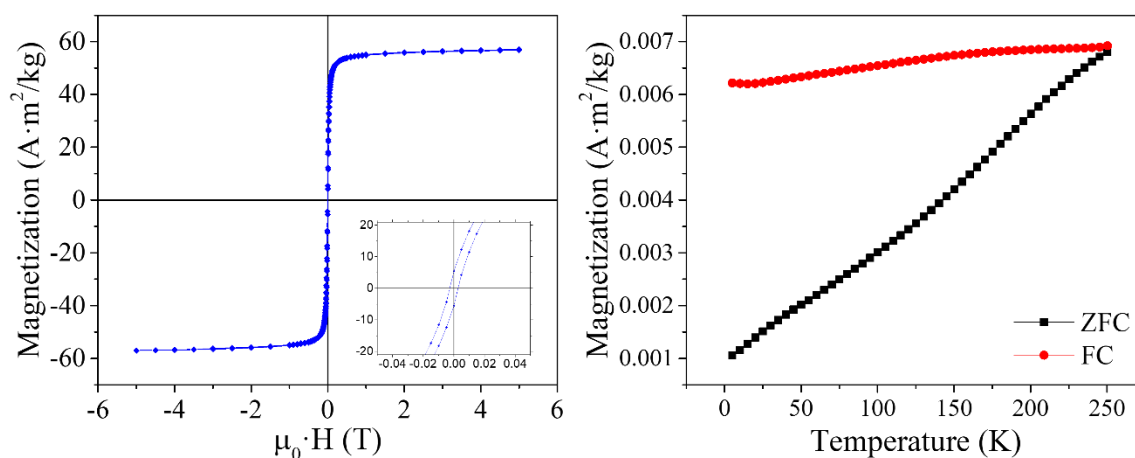


Figure 6. a) Hysteresis loop of a powdered sample of the MNCs at 300 K. Inset: magnification of the curve at low fields. b) ZFC-FC curves under a field of 2.5 mT.

The performance of the MNCs for this detection technique was evaluated by the sensitivity Σ , as defined in equation (1). A significant Σ value of 3000% per microgram of sample was obtained, which is due to the high initial χ . Finally, a resolution of 70 ng was achieved with the MNCs. Previous studies on inductive biosensing [29] have identified the high initial magnetic susceptibility at the threshold of superparamagnetic sizes as one of the main variables that affect the sensitivity and the resolution of inductive sensing. The MNCs in this work outperform all our previous results [29].

3.2. Bioconjugation of the clusters

The conjugation was confirmed by DLS (see Figure 1d). This technique allows the comparison between the nanoparticle hydrodynamic sizes before and after the reaction. The hydrodynamic diameter of the MNCs before the conjugation was 210 nm (PDI 0.3). Comparison of this result

with the value obtained by STEM, which gave a mean cluster size of 85 nm, indicates some agglomeration among the clusters. Agglomeration can have a positive impact on the detection because it increases the magnetic moment per biomolecule [36]. After conjugation, the new hydrodynamic size increased up to 237 nm (PDI 0.1). Taking in consideration the typical size of 10 nm for IgG type antibodies [37], this increase indicates the success of such attachment.

ζ -potential was used to assess the stability of the nanoclusters and the MNCs-PLY7 complexes. The values obtained were -35 mV and -29 mV for the bare clusters and the MNCs-PLY7 complexes, respectively. These values are typical of sufficiently strong electrostatic repulsions to provide colloidal stability of the particle solution [38].

3.3. Lateral flow strips reading-out

Once the tests were run and dried overnight, their optical and magnetic signals were measured and analyzed. Figure 7a shows the test lines of all the LFAs for one of the three series, where the PLY concentration increases from left to right. As can be seen, the test line intensity increases in this direction, in the usual way for a sandwich format immunoassay. Figure 7b shows the LFA with 120 ng/mL and its magnetic and optical signals. The two peaks in the records correspond to the MNCs present, at the test line (left) and control line (right), respectively. The optical (blue) and magnetic (black) calibration curves are presented in the inset of Figure 7c. Both signals increase with the PLY concentration up to saturation, which is reached when no more immobilized PLY4 antibody is available for binding the PLY-PLY7-MNC conjugate at the test line. Figure 7c shows the linear range of these calibration curves, with the fitting parameters of the experimental data. The magnetic signal shows a better correlation factor. Following the Eurachem Guidelines [39], the limit of detection (LOD) and the limit of quantification (LOQ) were calculated with σ_{blank} , the standard deviation of the concentration obtained for more than 10 independent measurements of the blank, as:

$$\begin{aligned} \text{LOD} &= 3.3 \cdot \sigma_{\text{blank}} \\ \text{LOQ} &= 10 \cdot \sigma_{\text{blank}} \end{aligned} \tag{3}$$

The former is the lowest analyte concentration that can be reliably

distinguished from the blank, whereas the latter is the lowest concentration at which the quantifying method performance is acceptable. Hence, a LOD of 6.3 ng/mL for the magnetic method and 10.8 ng/mL for the optical method are found. The LOQ were 19.0 ng/mL and 32.7 ng/mL for the inductive and optical signals, respectively. Both values and the superior correlation confirm the better performance of the inductive sensing platform.

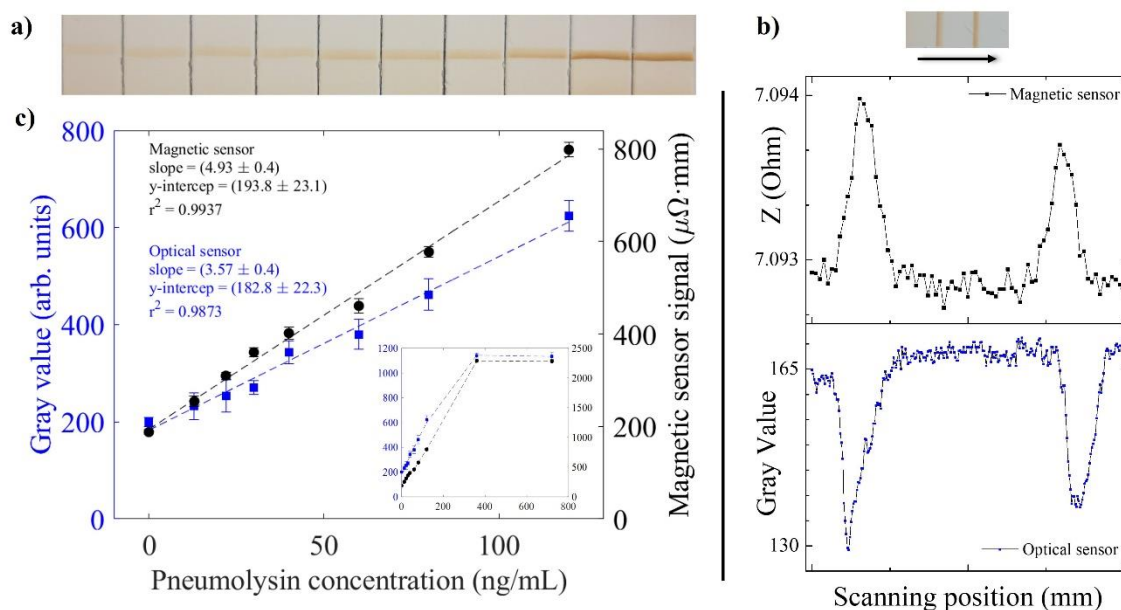


Figure 7. a) Image of the test lines of some LFAs covering the calibration range of PLY. The PLY concentration increases from left to right. b) LFA with 120 ng/mL of PLY and its magnetic (black) and optical (blue) signals obtained when scanning in the direction of the arrow: The left peak corresponds to the test line and the right one to the control line. c) Calibration curves for the optical (blue) and inductive signals obtained in the linear range of PLY concentration. Inset: Calibration curves for all PLY concentrations tested. Both graphs show the mean value, and the error bars represent their standard deviation.

3.4. Magnetic pre-concentration

The efficiency of the magnetic pre-concentration was evaluated as follows. Starting from a sample with an initial concentration of 13 ng of PLY per milliliter, various samples with different dilutions were obtained by adding RB. The same amount of liquid was removed after pre-concentration to assess the recovery of the analyte. The samples were measured in LFAs at the beginning and end of the whole process to see if the signals remained the same, within the margins of error, for both the optical and the inductive methods. Figure 8a shows the signal recovery

percentage calculated as the ratios between the signals before and after the process. The average signal recovery percentages are $98 \pm 3 \%$ and $94 \pm 3 \%$ for the inductive and optical methods, respectively. These figures suggest that this procedure recovers all the analyte.

To evaluate the new figures of merit of the technique due to magnetic pre-concentration, we represent on the vertical axis of Figure 8b the obtained signal multiplied by a concentration factor f that considers the relationship between the volumes during the process. This factor, which is defined as $f = V_f/V_i$, where V_f and V_i are the final and initial volumes of the sample, respectively, allows us to relate the signal obtained with the magnetic and optical method to the value of the actual concentration analyzed. The calibration curves with their fitting parameters are shown in Figure 8b. The LODs have now values of 0.2 ng/mL and 0.6 ng/mL for the inductive and optical systems, respectively. However, the new LOQs decrease to 0.7 ng/mL for the inductive sensor and 1.7 ng/mL for the optical one. This means that taking advantage of the magnetic pre-concentration, with both methodologies, it is possible to clearly improve the sensitivity of the system. Further improvement can be expected if the drag force is optimized by a specifically designed array of permanent magnets, as proved in [40]. These new figures of merit are achieved thanks to the magnetic character of the labels used.

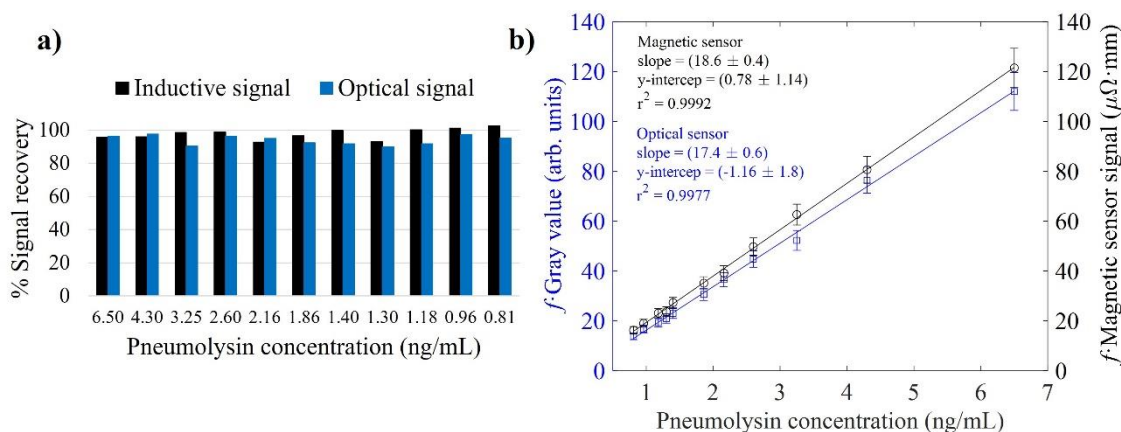


Figure 8. a) Signal recovery percentage for the optical (blue) and inductive (black) sensor. b) Calibration curves obtained for the optical and the inductive sensors with the preconcentration values. The error bars are calculated as the sum of the standard deviations of the linear regression of the calibration curve together with the error in the pipetting of each dilution volume.

It is remarkable that the optical evaluation of the LFAs performed with just a mobile phone shows excellent LOD and LOQ thanks to the

magnetic pre-concentration. These results show promise for diagnostic testing in harsh or locations with few resources. The inductive sensor gives more precise and reliable quantitative results: The staining or aging of the supporting nitrocellulose membrane does not interfere with the magnetic signal, nor does the ambient light. Consequently, the reproducibility of the inductive measurement technique allows storage and reuse of the calibration data for further sample evaluation.

3.5. Magnetic relocation

Magnetic relocation was explored as a way to further increase the sensitivity of the technique. Once the LFAs were run, a magnetic field gradient was applied at the test line to relocate the MNCs closer to the sensing region for LFAs with 6.5 ng/mL, 40 ng/mL, and 60 ng/mL of PLY resulting in an increase in the signals of 18%, 20%, and 28%, respectively.

This technique deserves further investigation. There are different bonds present with different binding energies, which could determine which one breaks: the bond between the capture antibody and the membrane, between the capture antibody and the antigen, and between the particles and the detection antibody. Although the former seems most likely, its confirmation requires further studies. The characteristics of the nanoparticles are key. For example, high magnetization and susceptibility are determining factors in their response to the applied relocation field gradient. It will also be worth studying the efficiency of the relocation in terms of the intensity of the magnetic gradient and time. Nevertheless, these preliminary results show the potential of magnetic relocation to further improve the LOD within an integrated device.

4. Conclusions

Pneumolysin quantification was developed via a combination of magnetic labeling in a lateral flow immunoassay and an inductive sensor. Spherical iron oxide nanoclusters with mean sizes of 88 nm were synthesized by a polyol method. Their capping with polycrylic acid enabled their biofunctionalization for the specific recognition of pneumolysin. The magnetic immunoassay was then calibrated with standard PLY solutions. The read-out of the test lines was dual: magnetic (by inductive sensing) and optical (by image analysis with a phone camera). The inductive reader yielded the larger linear range and better

correlation factor, limit of detection, and limit of quantification. Still, the figures of merit of the mobile phone method were remarkable taking into account the availability of such a device. More interestingly, the magnetic character of the clusters allowed us to considerably improve these figures of merit: the magnetic pre-concentration of diluted samples recovered 100% of the analyte and set new LODs at 0.2 ng/mL and 0.6 ng/mL for the inductive and optical sensors, respectively. Additionally, the magnetic relocation of the particles within the membrane further increased the signal of the LFAs by 20%.

The system has great potential for pneumococcal pneumonia diagnosis in harsh environments using just a mobile phone camera. The magneto-inductive sensor allows further increase in the sensitivity of the method. In any case, both approaches overcome the current drawbacks in etiological diagnosis, such as false-negative cultures, detrimental and inconclusive X-rays, especially in children, and the indiscriminate use of antibiotics.

5. Acknowledgments

This work was partially funded by the Spanish Ministry of Economy and Competitiveness under projects MAT2017-84959-C2-1-R and the Principality of Asturias (Spain) under project IDI/2018/000185. M. Salvador was supported by a “Severo Ochoa” fellowship (Consejería de Educación y Cultura del Gobierno del Principado de Asturias, grant BP19-141). She also thanks the University of Oviedo, the Ministry of Education, Culture and Sport, and Banco Santander for grant CEI15-24. J.L. Marqués was supported by the University Technological Institute of Asturias (IUTA) under grant SV-20-GIJÓN-1-22.

The authors would like to acknowledge the technical support provided by the Scientific and Technical Service of the University of Oviedo and R.B. Goldfarb (NIST) and J.A. Blanco (University of Oviedo) for fruitful discussions.

Some figures of this work were created with BioRender.com.

References

- [1] J. Ferreira-Coimbra, C. Sarda, J. Rello, Burden of Community-

- Acquired Pneumonia and Unmet Clinical Needs, *Adv. Ther.* 37 (2020) 1302–1318. <https://doi.org/10.1007/s12325-020-01248-7>.
- [2] A. Torres, C. Cillóniz, F. Blasi, J.D. Chalmers, J. Gaillat, N. Dartois, H.J. Schmitt, T. Welte, Burden of pneumococcal community-acquired pneumonia in adults across Europe: A literature review, *Respir. Med.* 137 (2018) 6–13. <https://doi.org/10.1016/j.rmed.2018.02.007>.
- [3] H.J. Zar, S.A. Madhi, S.J. Aston, S.B. Gordon, Pneumonia in low and middle income countries: Progress and challenges, *Thorax*. 68 (2013) 1052–1056. <https://doi.org/10.1136/thoraxjnl-2013-204247>.
- [4] C. Guertler, B. Wirz, M. Christ-Crain, W. Zimmerli, B. Mueller, P. Schuetz, Inflammatory responses predict long-term mortality risk in community-acquired pneumonia, *Eur. Respir. J.* 37 (2011) 1439–1446. <https://doi.org/10.1183/09031936.00121510>.
- [5] M.J. Divo, C.H. Martinez, D.M. Mannino, Ageing and the epidemiology of multimorbidity, *Eur. Respir. J.* 44 (2014) 1055–1068. <https://doi.org/10.1183/09031936.00059814>.
- [6] T. Welte, A. Torres, D. Nathwani, Clinical and economic burden of community-acquired pneumonia among adults in Europe, *Thorax*. 67 (2012) 71–79. <https://doi.org/10.1136/thx.2009.129502>.
- [7] C. Cilloniz, I. Martin-Loeches, C. Garcia-Vidal, A.S. Jose, A. Torres, Microbial Etiology of Pneumonia: Epidemiology, Diagnosis and Resistance Patterns, *Int. J. Mol. Sci.* 2016, Vol. 17, Page 2120. 17 (2016) 2120. <https://doi.org/10.3390/IJMS17122120>.
- [8] R.A. Hirst, A. Kadioglu, C. O’Callaghan, P.W. Andrew, The role of pneumolysin in pneumococcal pneumonia and meningitis, *Clin. Exp. Immunol.* 138 (2004) 195–201. <https://doi.org/10.1111/j.1365-2249.2004.02611.x>.
- [9] D. Cucchiari, J.M. Pericàs, J. Riera, R. Gumucio, E.C. Md, D. Nicolàs, Pneumococcal superinfection in COVID-19 patients: A series of 5 cases, *Med. Clin. (Barc)*. 155 (2020) 502–505. <https://doi.org/10.1016/j.medcli.2020.05.022>.
- [10] C. Pal, P. Przydzial, O. Chika-Nwosuh, S. Shah, P. Patel, N. Madan, Streptococcus pneumoniae Coinfection in COVID-19: A Series of Three Cases, *Case Rep. Pulmonol.* 2020 (2020). <https://doi.org/10.1155/2020/8849068>.
- [11] L.A. Mandell, Community-acquired pneumonia: An overview, *Postgrad. Med.* 127 (2015) 607–615. <https://doi.org/10.1080/00325481.2015.1074030>.
- [12] D.A. Tavares, S. Handem, R.J. Carvalho, A.C. Paulo, H. de Lencastre, J. Hinds, R. Sá-Leão, Identification of Streptococcus pneumoniae by a real-time PCR assay targeting SP2020, *Sci. Rep.*

9 (2019) 1–11. <https://doi.org/10.1038/s41598-019-39791-1>.

- [13] J. Molina, A. González-Gamarra, L. Ginel, M.E. Peláez, J.L. Juez, A. Artuñedo, G. Aldana, E. Quesada, J.J. Cabré, A. Gómez, M. Linares, M.T. Marín, P.Y. Sanchez, L. Núñez, J. González, E. Mascarós, J. López, A. Cano, J. Herrero, M.C. Serra, E. Cimas, M. Pedrol, J.V. Alfaro, F. Martín-Torres, I. Cifuentes, C. Méndez, D. Ocaña, Cappric study—characterization of community-acquired pneumonia in spanish adults managed in primary care settings, *Microorganisms*. 9 (2021) 1–11. <https://doi.org/10.3390/microorganisms9030508>.
- [14] R.A. Adegbola, S.K. Obaro, E. Biney, B.M. Greenwood, Evaluation of binax now Streptococcus pneumoniae urinary antigen test in children in a community with a high carriage rate of pneumococcus, *Pediatr. Infect. Dis. J.* 20 (2001) 718–719. <https://doi.org/10.1097/00006454-200107000-00018>.
- [15] D. Navarro, L. García-Maset, C. Gimeno, A. Escribano, J. García-De-Lomas, Performance of the binax NOW Streptococcus pneumoniae urinary antigen assay for diagnosis of pneumonia in children with underlying pulmonary diseases in the absence of acute pneumococcal infection, *J. Clin. Microbiol.* 42 (2004) 4853–4855. <https://doi.org/10.1128/JCM.42.10.4853-4855.2004>.
- [16] D.R. Neill, T.J. Mitchell, A. Kadioglu, Pneumolysin, in: *Streptococcus Pneumoniae Mol. Mech. Host-Pathogen Interact.*, Elsevier Inc., 2015: pp. 257–275. <https://doi.org/10.1016/B978-0-12-410530-0.00014-4>.
- [17] A.T. Nishimoto, J.W. Rosch, E.I. Tuomanen, Pneumolysin: Pathogenesis and Therapeutic Target, *Front. Microbiol.* 0 (2020) 1543. <https://doi.org/10.3389/FMICB.2020.01543>.
- [18] M.D.M. García-Suárez, M.D. Cima-Cabal, R. Villaverde, E. Espinosa, M. Falguera, J.R. De Los Toyos, F. Vazquez, F.J. Méndez, Performance of a pneumolysin enzyme-linked immunosorbent assay for diagnosis of pneumococcal infections, *J. Clin. Microbiol.* 45 (2007) 3549–3554. <https://doi.org/10.1128/JCM.01030-07>.
- [19] J.H.W. Leuvering, P.J.H.M. Thal, M. Van der Waart, A.H.W.M. Schuurs, A sol particle agglutination assay for human chorionic gonadotrophin, *J. Immunol. Methods.* 45 (1981) 183–194. [https://doi.org/10.1016/0022-1759\(81\)90212-X](https://doi.org/10.1016/0022-1759(81)90212-X).
- [20] Y. Huang, T. Xu, W. Wang, Y. Wen, K. Li, L. Qian, X. Zhang, G. Liu, Lateral flow biosensors based on the use of micro- and nanomaterials: a review on recent developments, *Microchim. Acta.* 187 (2020) 1–25. <https://doi.org/10.1007/s00604-019-3822-x>.
- [21] X. Huang, Z.P. Aguilar, H. Xu, W. Lai, Y. Xiong, Membrane-based lateral flow immunochromatographic strip with nanoparticles as reporters for detection: A review, *Biosens. Bioelectron.* 75 (2015)

- 166–180. <https://doi.org/10.1016/j.bios.2015.08.032>.
- [22] S. Dutta, Point of care sensing and biosensing using ambient light sensor of smartphone: Critical review, *TrAC - Trends Anal. Chem.* 110 (2019) 393–400. <https://doi.org/10.1016/j.trac.2018.11.014>.
- [23] P. Chun, Colloidal Gold and Other Labels for Lateral Flow Immunoassays, *Lateral Flow Immunoass.* (2009) 1–19. https://doi.org/10.1007/978-1-59745-240-3_5.
- [24] A. Moyano, E. Serrano-Pertierra, M. Salvador, J.C. Martínez-García, M. Rivas, M.C. Blanco-López, Magnetic lateral flow immunoassays, *Diagnostics*. 10 (2020) 288. <https://doi.org/10.3390/diagnostics10050288>.
- [25] V.G. Panferov, I. V. Safenkova, A. V. Zherdev, B.B. Dzantiev, Setting up the cut-off level of a sensitive barcode lateral flow assay with magnetic nanoparticles, *Talanta*. 164 (2017) 69–76. <https://doi.org/10.1016/j.talanta.2016.11.025>.
- [26] Z. Huang, S. Hu, Y. Xiong, H. Wei, H. Xu, H. Duan, W. Lai, Application and development of superparamagnetic nanoparticles in sample pretreatment and immunochromatographic assay, 2019. <https://doi.org/10.1016/j.trac.2019.03.004> (accessed March 24, 2021).
- [27] D. Lago-Cachón, M. Rivas, J.C. Martínez-García, M. Oliveira-Rodríguez, M.C. Blanco-López, J.A. García, High frequency lateral flow affinity assay using superparamagnetic nanoparticles, *J. Magn. Magn. Mater.* 423 (2017) 436–440. <https://doi.org/10.1016/j.jmmm.2016.09.106>.
- [28] M. Rivas, D. Lago-Cachón, J.C. Martínez-García, J.A. García, A.J. Calleja, Eddy-current sensing of superparamagnetic nanoparticles with spiral-like copper circuits, *Sensors Actuators A Phys.* 216 (2014) 123–127. <https://doi.org/10.1016/J.SNA.2014.05.023>.
- [29] M. Salvador, Á. Gallo-Cordova, A. Moyano, J.C. Martínez-García, M.C. Blanco-López, M. Puerto Morales, M. Rivas, Improved magnetic lateral flow assays with optimized nanotags for point-of-use inductive biosensing, *Analyst*. 145 (2020) 5905–5914. <https://doi.org/10.1039/d0an00849d>.
- [30] M.D. Cima-Cabal, F. Vázquez, J.R. De Los Toyos, F.J. Méndez, Rapid and reliable identification of *Streptococcus pneumoniae* isolates by pneumolysin-mediated agglutination, *J. Clin. Microbiol.* 37 (1999) 1964–1966. <https://doi.org/10.1128/jcm.37.6.1964-1966.1999>.
- [31] J.R. De Los Toyos, F.J. Méndez, J.F. Aparicio, F. Vázquez, M.D.M.G. Suárez, A. Fleites, C. Hardisson, P.J. Morgan, P.W. Andrew, T.J. Mitchell, Functional analysis of pneumolysin by use of monoclonal antibodies, *Infect. Immun.* 64 (1996) 480–484. <https://doi.org/10.1128/iai.64.2.480-484.1996>.

- [32] D. Lago-Cachón, M. Oliveira-Rodríguez, M. Rivas, M.C. Blanco-López, J.C. Martínez-García, A. Moyano, M. Salvador, J.A. García, Scanning Magneto-Inductive Sensor for Quantitative Assay of Prostate-Specific Antigen, *IEEE Magn. Lett.* 8 (2017). <https://doi.org/10.1109/LMAG.2017.2702108>.
- [33] A. Bunge, A.S. Porav, G. Borodi, T. Radu, A. Pîrnău, C. Berghian-Grosan, R. Turcu, Correlation between synthesis parameters and properties of magnetite clusters prepared by solvothermal polyol method, *J. Mater. Sci.* 54 (2019) 2853–2875. <https://doi.org/10.1007/s10853-018-3030-9>.
- [34] D. Peddis, P.E. Jönsson, S. Laureti, G. Varvaro, Magnetic interactions: A tool to modify the magnetic properties of materials based on nanoparticles, in: *Front. Nanosci.*, Elsevier, 2014: pp. 129–188. <https://doi.org/10.1016/B978-0-08-098353-0.00004-X>.
- [35] H. Zhang, D. Zeng, Z. Liu, The law of approach to saturation in ferromagnets originating from the magnetocrystalline anisotropy, *J. Magn. Mater.* 322 (2010) 2375–2380. <https://doi.org/10.1016/j.jmmm.2010.02.040>.
- [36] Y. Wang, H. Xu, M. Wei, H. Gu, Q. Xu, W. Zhu, Study of superparamagnetic nanoparticles as labels in the quantitative lateral flow immunoassay, *Mater. Sci. Eng. C.* 29 (2009) 714–718. <https://doi.org/10.1016/j.msec.2009.01.011>.
- [37] N.G. Welch, J.A. Scoble, B.W. Muir, P.J. Pigram, Orientation and characterization of immobilized antibodies for improved immunoassays (Review), *Biointerphases.* 12 (2017) 02D301. <https://doi.org/10.1116/1.4978435>.
- [38] J.D. Clogston, A.K. Patri, Zeta potential measurement., *Methods Mol. Biol.* 697 (2011) 63–70. https://doi.org/10.1007/978-1-60327-198-1_6.
- [39] B. Magnusson, U. Örnemark, eds., *Eurachem Guide: The Fitness for Purpose of Analytical Methods - A Laboratory Guide to Method Validation and Related Topics.*, <Http://Eurachem.Org/Images/Stories/Guides/Pdf/Valid.Pdf>, (Accessed: 11.05.13). (2014). www.eurachem.org. (accessed July 17, 2021).
- [40] A. Omelyanchik, G. Lamura, D. Peddis, F. Canepa, Optimization of a NdFeB permanent magnet configuration for in-vivo drug delivery experiments, *J. Magn. Mater.* 522 (2021) 167491. <https://doi.org/10.1016/J.JMMM.2020.167491>.

Section III - Chapter 4

MagCOVID: Development of a Rapid Magnetic Serological Test for COVID-19

Introduction and motivation

MNCs showed promising results for the detection of pneumolysin in the last chapter. A significant initial magnetic susceptibility, ideal agglomeration to increase the magnetic volume per biomolecule, and capability to preconcentrate the samples made them ideal nanolabels.

The LFAs advantages are even more pronounced in a crisis like the ongoing coronavirus disease 2019 (COVID-19). A serological test detects the antibodies generated by the presence of a pathogen, e.g., the severe acute respiratory syndrome coronavirus 2 (SARS-CoV-2). In the current situation, there is still the need to be precautious to avoid other outbreaks. Thus, these kinds of tests can help monitoring the immune response of the population and detecting asymptomatic and undiagnosed infections.

In this chapter, the same MNCs are used to prove the feasibility of a serological magnetic lateral flow immunoassay. The IgG antibody is selected as a biomarker to control the immune response during an infection or on its onset.

The IEEE Magnetics Society has funded this work by its Seed Funding Program, which is devoted to students, rewards collaboration among institutions. MagCOVID is an international project coordinated by the author of this thesis and involving the University of Oviedo (Spain), the University of Brasilia (Brazil), the University of Pavia (Italy), and the National Institute for Research and Development of Isotopic and Molecular Technologies (Romania).

The preliminary results of the investigation are detailed below.

Unpublished work

MagCOVID: Development of a Rapid Magnetic Serological Test for COVID- 19

M. Salvador¹, J.L. Marqués¹, F. Brero², F. G. da Silva³,
A. Bunge⁴, J.C. Martínez-García¹, M. Mariani², A.
Lascialfari², R. Turcu⁴, V. Pilati⁵, C. Kern⁵, F. Orsini⁶, J.
Depeyrot³ and M. Rivas¹

¹Department of Physics & IUTA, University of Oviedo, Gijón (Spain)

²Department of Physics & INFN, University of Pavia (Italy)

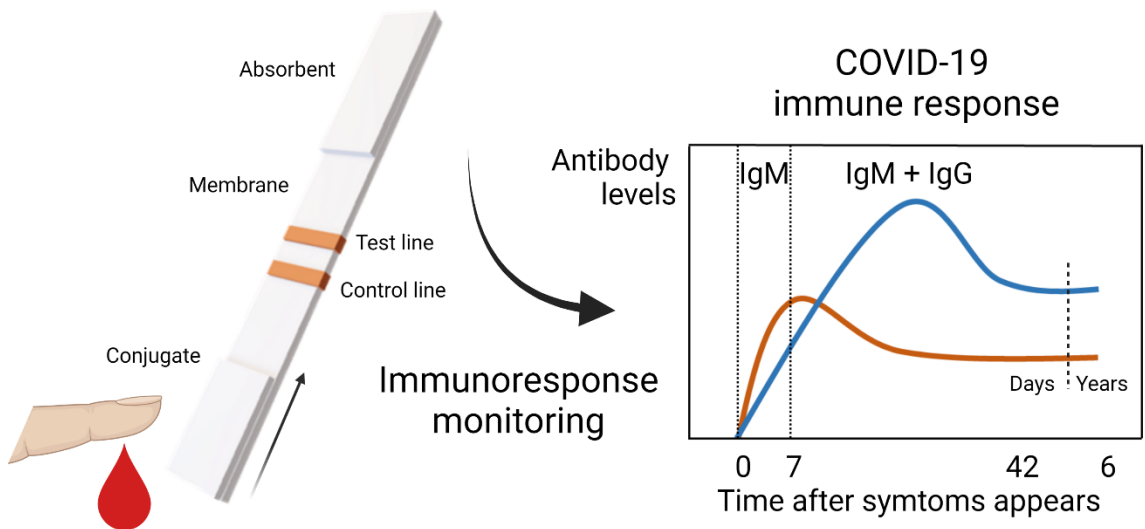
³Institute of Physics, Universidade de Brasilia (Brazil)

*⁴National Institute for Research and Development of Isotopic and
Molecular Technologies (Romania)*

*⁵Laboratory for Environmental and Applied Nanoscience, Universidade
de Brasilia (Brazil)*

⁶Department of Physics, University of Milan (Italy)

GRAPHICAL ABSTRACT



1. Introduction

The coronavirus disease 2019 (COVID-19) pandemic has hit and drastically changed the world during the last months. Since the outbreak in Wuhan (China), it has spread uncontrollably throughout the planet thanks to its high transmission rate. The severe consequences reveal the necessity of new diagnostic tools and procedures to reduce the impact of future emergencies. Development in genome sequence allowed for detection of the virus by the polymerase chain reaction (PCR), considered the gold standard technique. However, the procedure needs expensive reagents (e.g., specific primers and probes), sophisticated equipment, specialized personnel, and time [1]. We cannot afford to lose time in a critical situation.

Lateral flow immunoassays (LFA), better known as “rapid tests,” are paper build tests used to detect analytes via microfluidics and biorecognition. So far, their most spread use was the home pregnancy test. Thanks to their ability to produce sensitive, cost-efficient, and quick results, LFAs have also been developed to detect the SARS-CoV-2 by recognizing different parts, i.e., spike (S) or nucleocapsid (N) protein (see Figure 1). The important thing is that they were able to soften the impact on our health systems. Nowadays, rapid vaccine development has allowed us to recover our daily life partially. However, we cannot afford another outbreak, so monitoring the immune response of the population can guide public health interventions and help in the design of new vaccines [2]. LFAs can be again ideal candidates for that purpose.

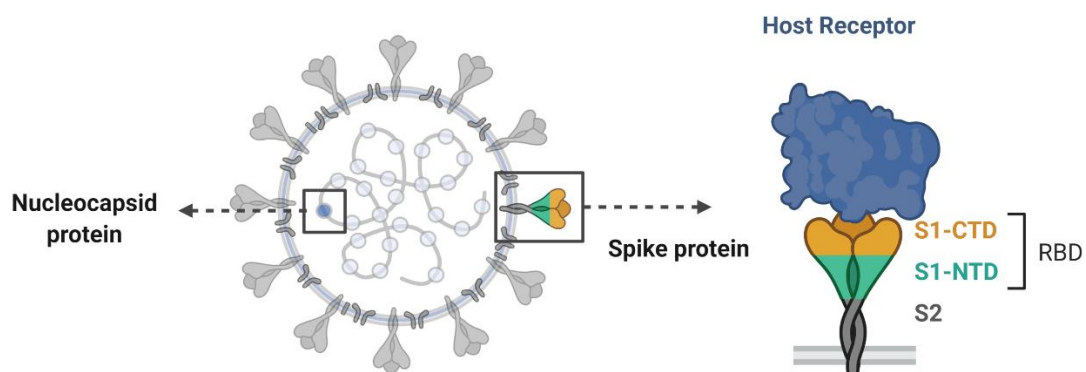


Figure 1. Schematic diagram of SARS-CoV-2 virus structure, with an enlarged spike protein showing its different parts and how it enters the cells.

Serological tests are designed to detect the presence of antibodies

against a given pathogen. Different classes of antibodies (immunoglobulin proteins) are involved in the antibody immune response, which are characterized by their functions, distributions, and half-life [3]. IgM is usually the first to be expressed while IgG starts appearing later because they mature for better affinity. The evolution of these two main antibody classes just after the infection, which is determined by the RNA increase, is schematized in Figure 2.

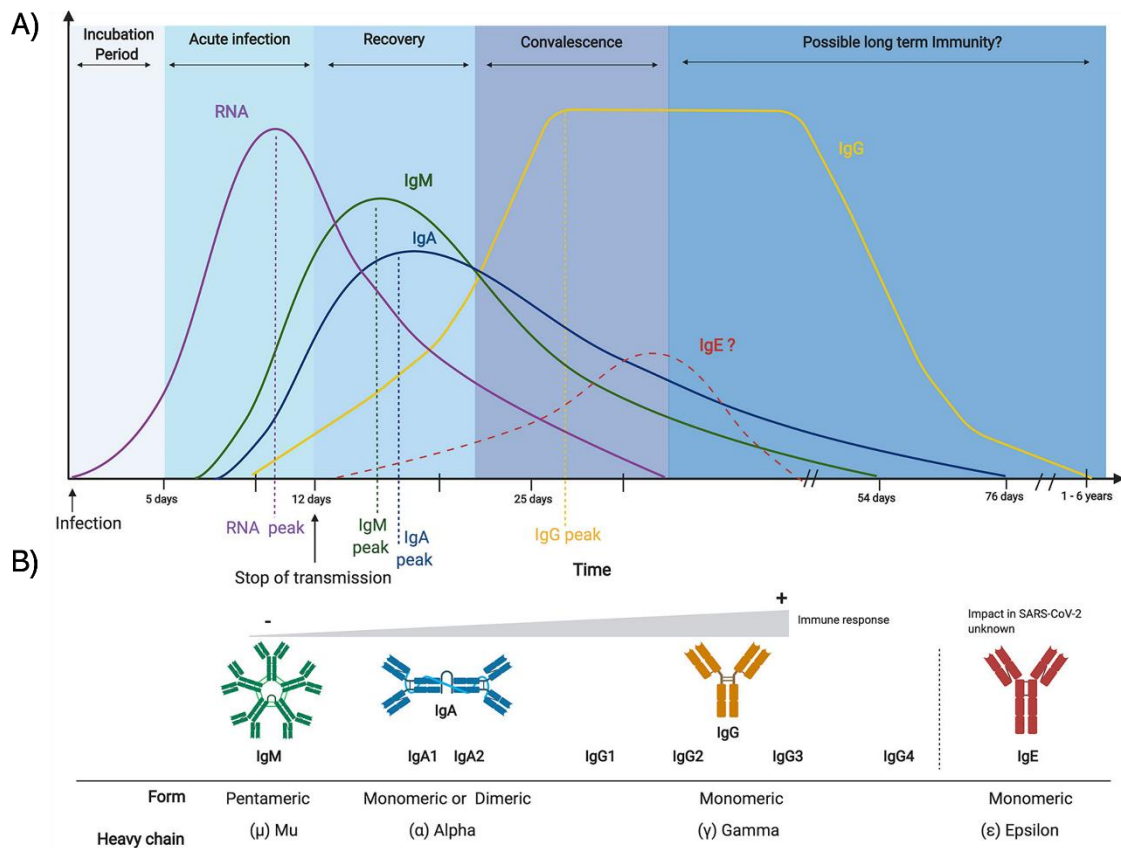


Figure 2. A) The approximate timeline of each isotype in relation to the viral RNA. B) Schematic representation of each antibody isotype. Obtained from [3].

After the infection with the SARS-CoV-2, the immune response includes the generation of these classes of antibodies against the N and S. There are also antibodies generated against the receptor-binding domain in the protein S (anti-S-RBD) that can block the virus-receptor interaction (see Figure 1). Therefore, those antibodies are called neutralizing antibodies. In case of any re-infection, all of them will specifically recognize the *intruder* and efficiently fight it.

Vaccines work in a similar way: they introduce an inoffensive pathogen or part of it, to train the immune system to create these antibodies without suffering the most harmful effects [4]. Most of the

SARS- CoV- 2 vaccines, which were developed with an unprecedented pace, rely on the viral protein S [5]. Thus, those injected with the jab will start producing antibodies against this protein.

In this work, we developed a serological test based on the LFA technology to detect human IgG antibodies against the S-RBD protein using magnetic nanoclusters (MNCs) as labels. Its design has a slightly different configuration than the standard sandwich immunoassay. In this case, the antigen is the S-RBD fragment, which will form the test line. Then, the patient's sample will flow by capillarity, and the anti-S-RBD antibodies will get trapped at the test line. Now, we need to label those antibodies to make them visible. To do so, the MNCs are bioconjugated with an anti-human IgG antibody (see Figure 3A). Commercially, these antibodies are known as secondary antibodies: they bind to the primary antibody aiding in the detection.

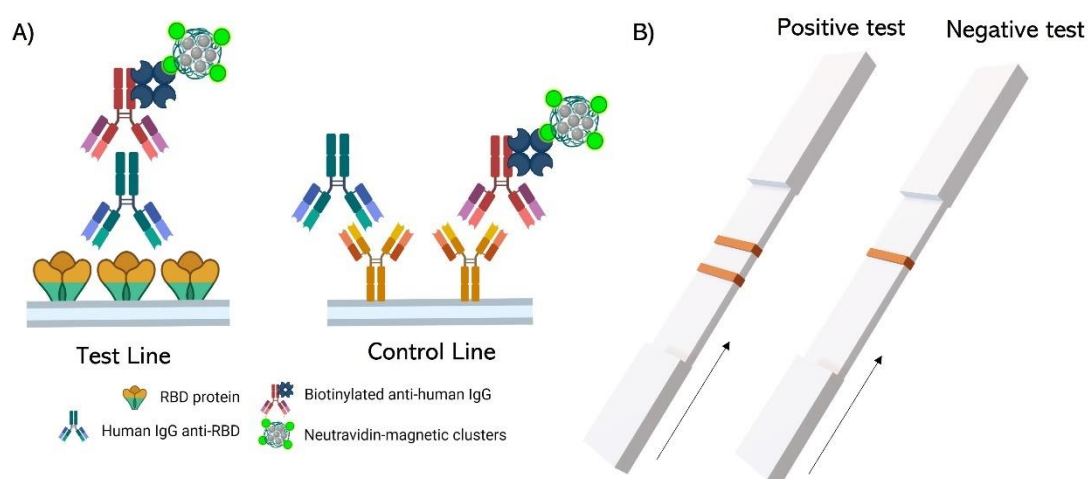


Figure 3. A) Design of the test and control lines. B) Representation of a positive and negative test.

In consequence, if the patient has IgG antibodies, two lines appear in the LFA, showing a positive result. On the contrary, if there are no IgG antibodies, only the control line will be visible in the test (see Figure 3).

2. Materials and methods

2.1. Chemicals and reagents

Anti-mouse IgG, 1-ethyl-3-[3-di-methylaminopropyl] carbodiimide (EDC), N-hydroxysuccinimide (NHS), biotin-conjugated bovine serum albumin (BBSA), and Tween20 were purchased from Sigma-Aldrich.

Neutravidin protein and mouse anti-human IgG (H+L) secondary antibody (biotin) were obtained from Thermo Fischer Scientific (USA). SARS-CoV-2 (COVID-19) S protein RBD His Tag and human IgG1 anti-SARS-CoV-2 Spike RBD neutralizing antibody (AS35) were purchased from ACROBiosystems.

For the lateral flow strips, the backing cards (HF000MC100) and the glass fiber membrane (GF001000) used as sample pads were purchased from Merck Life Science. The nitrocellulose membranes (UniSart CN95) were provided by Sartorius, Spain, and the absorbent pads (CF5) by Cytiva Europe GmbH, Spain.

2.2. Bioconjugation of the nanoparticles

In the immunoassay, neutravidin is attached to the MNCs. For this bonding, the polyacrylic's carboxylic groups at the MNCs surface were activated using carbodiimide chemistry, as depicted in Figure 4: 5 μL of the MNCs, previously sonicated for 5 min, were mixed with 100 μL of EDC (1.5 mg/mL in PBS 1 mM, pH 7.4) and 100 μL of NHS (1.5 mg/mL in PBS 1 mM, pH 7.4). The mixture was sonicated for 10 min. Then, 100 μL of a neutravidin solution with different concentrations (1, 1.5, 2, and 3 mg/mL) was added and left 4 h in a refrigerated ultrasonic bath while mechanically agitated. The mixture was centrifuged at 7000 rpm for 15 min. finally, 300 μL of the supernatant were discarded and the pellet resuspended in fresh PBS (1mM, pH 7.4).

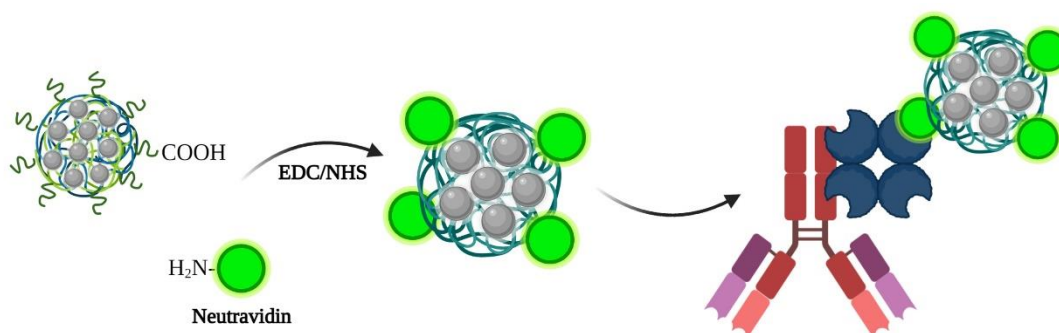


Figure 4. Schematic representation of the bioconjugation process of the MNCs.

2.3. Preparation of the immunoassays

The first step to assemble the LFA strip is to attach the nitrocellulose membrane to an adhesive backing card. To test the neutravidin concentration, only a test line of BBSA (2 mg/mL) is necessary. However, for the immunoassay, both the test and control lines need to be present.

For the former, the RBD segment of the S protein, while in the latter, the anti-mouse IgG control antibody, both at a concentration of 1 mg/mL. In all cases, the lines are printed using a reagent dispenser. The reagent dispenser consists of an automatic micropipette coupled with a micropositioner that has been programmed to synchronize the dispensation with the motion. This printing method enables the deposition across the membrane at a rate of 0.1 $\mu\text{L}/\text{mm}$.

After drying for 12 h, the sample pad (which enables a controlled sample transfer to the membrane) and the absorbent pad (which acts as a wick and prevents backflow) were placed onto the backing card with an overlap of 2 mm with the membrane. Finally, single 5 mm wide strips were cut with a guillotine.

2.4. Running of the tests

The LFAs were then carried out in dipstick format by vertically introducing the sample pad in the solution, which flowed upwards driven by capillary forces. The configuration of the LFA is slightly different from a conventional sandwich assay, so it must be run in two steps. In the first one, the sample flows, and if there are any IgG antibodies present, they will get trapped in the test line. The second is the signal development, based on the retention of the anti-IgG-MNCs complexes. In both cases, the remaining sample will continue flowing through the membrane, facing the control line up to the absorbent.

Considering 100 μL as the final volume for each of these two steps, the corresponding RB is added in consequence. Then, for a blank test (negative sample), there is only one step consisting of a sample of 20 μL of the MNPs@N and 2.5 μL of anti-IgG. On the contrary, for a positive test, the first step is to run a sample containing different volumes of the human IgG. Then, the strip is left to dry for one hour. Finally, to develop the signal, the same solution as with the blank test is added. The tests are left to drive overnight for their visual investigation.

3. Results and discussion

3.1. Optimization of the bioconjugation

Biorecognition in the proposed LFA is based on binding a biotinylated antibody against IgG. To label it, we bind the MNCs to neutravidin. Therefore, the first step is optimizing the amount of protein that

completely covers the MNCs surface.

Different concentrations of neutravidin were used. To confirm the bioconjugation, MNCs were tested in a strip with a BBSA line. If the MNCs are properly bioconjugated with neutravidin, they will be retained in the test line. Figure 5A shows the different strips obtained with the concentrations used of neutravidin. As can be seen, the best signal is obtained with a concentration of 2 mg / mL. In lower concentrations than this, almost no signal is appreciated, while in larger ones, the agglomerates formed. Their sizes do not allow the sample to flow and mostly remain at the beginning of the membrane. Therefore, the optimized concentration for the immunoassay is 2 mg/mL of neutravidin.

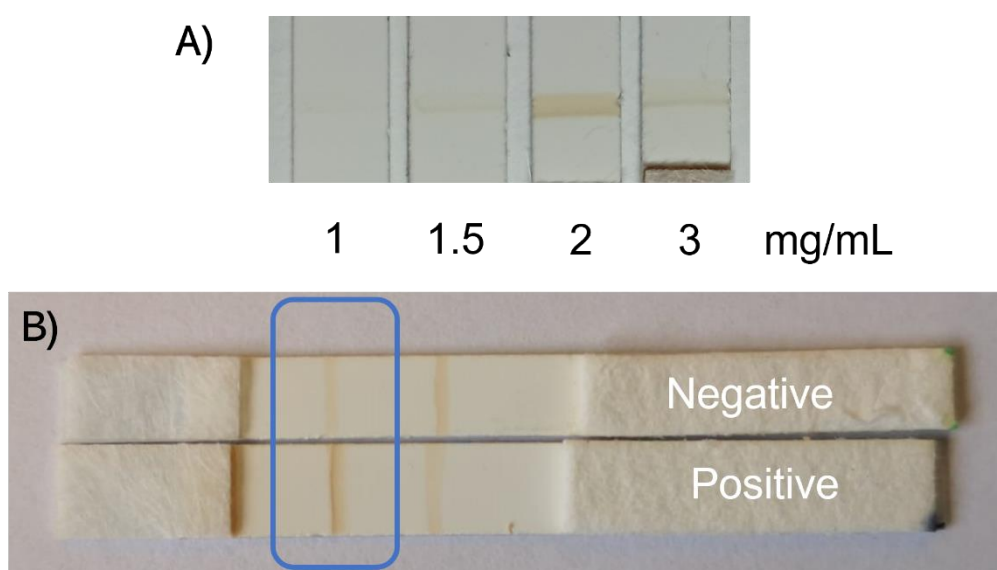


Figure 5. A) LFA with the different neutravidin concentrations tested. B) Negative and positive LFA for IgG.

3.2. Immunoassay development

The immunoassay to detect the IgG generated during the infection or by the vaccines slightly differs from the typical sandwich one. The antigen (S-RBD) is printed as the test line. During the first step, the sample flows by capillarity and if the IgG is present, it will get trapped by the antigen. Then, the second step consists of the color development, for which the anti-human IgG-MNCs complex will be retained at the test line thanks to the recognition of the IgG.

Figure 5B shows the LFA strips for a negative and a positive result. There is a clear increase in the intensity of the test line between both, indicating the satisfactory detection of the IgG trapped there. The

concentration of the positive test is 5 $\mu\text{g}/\text{mL}$. The average peak concentration of the IgG antibody is around 17 $\mu\text{g}/\text{mL}$. The detection of less amount of antibody than the peak concentration indicates that the design of the test might accomplish the detection within the relevant concentration range.

4. Conclusions

A lateral flow immunoassay for detection of IgG antibody against SARS-CoV-2 has been developed. The labels are iron-based magnetic nanoclusters coated with polyacrylic acid that enables their biofunctionalization. By means of a secondary antibody, we have detected an anti-S-RBD IgG antibody concentration as low as 5 $\mu\text{g}/\text{mL}$. This concentration is in the clinical region of interest, ensuring a good sensibility for monitoring the evolution of the immune response either just after the vaccine or on the infection onset and end.

5. Future work

Thanks to the color the MNPSs provide, the detection of the IgG is visual. The difference in the intensity of the test line indicates the presence of the analyte. Further development of the immunoassay will consist of the optimization of the bioconjugation process. This will improve the test in two different ways. First, by decreasing the unspecific signal obtained in the test line for a negative test (no IgG present). Secondly, by optimizing the recognition capabilities of the anti-human IgG-MNCs complex. All together will allow moving from a qualitative response to a quantitative one. These MNCs have shown excellent results in the inductive sensing of other biomolecules. Additionally, we would like to test other particles with different compositions. By changing the elements of the particles, we can tune the magnetic properties of the particles, which will enhance the signal in the sensor.

There is also the option to use other membranes for the immunoassay. The anti-human IgG-MNCs complex is extensive. If the agglomeration during the bioconjugation is not fine controlled, it could not be able to flow. Pore sizes within the membrane are not controlled. The membranes are then characterized by the time a fluid (usually water) takes to travel 4 cm. If the time is considerable, it is assumed that the pores are small and the other way around. We could take advantage of a more significant pore sizes distribution in the membrane to avoid problems in the sample

flowing even when there is more agglomeration.

Finally, the detection and quantification of the IgM class antibodies will be attempted. In this case, the bigger size of this antibody will require modifications again in the bioconjugation process. Even more so, membranes with bigger pore sizes will favor the flowing of the sample.

6. Acknowledgments

The authors are very grateful to the IEEE Magnetic Society for funding the MagCOVID project under their Seed Funding Program. It is an honor to be the leading head in a project only for students and post-docs.

References

- [1] B. Singh, B. Datta, A. Ashish, G. Dutta, A comprehensive review on current COVID-19 detection methods: From lab care to point of care diagnosis, *Sensors Int.* 2 (2021) 100119. <https://doi.org/10.1016/J.SINTL.2021.100119>.
- [2] B. Isho, K.T. Abe, M. Zuo, A.J. Jamal, B. Rathod, J.H. Wang, Z. Li, G. Chao, O.L. Rojas, Y.M. Bang, A. Pu, N. Christie-Holmes, C. Gervais, D. Ceccarelli, P. Samavarchi-Tehrani, F. Guvenc, P. Budyłowski, A. Li, A. Paterson, Y.F. Yun, L.M. Marin, L. Caldwell, J.L. Wrana, K. Colwill, F. Sicheri, S. Mubareka, S.D. Gray-Owen, S.J. Drews, W.L. Siqueira, M. Barrios-Rodiles, M. Ostrowski, J.M. Rini, Y. Durocher, A.J. McGeer, J.L. Gommerman, A.C. Gingras, Persistence of serum and saliva antibody responses to SARS-CoV-2 spike antigens in COVID-19 patients, *Sci. Immunol.* 5 (2020). <https://doi.org/10.1126/sciimmunol.abe5511>.
- [3] Y. Galipeau, M. Greig, G. Liu, M. Driedger, M.A. Langlois, Humoral Responses and Serological Assays in SARS-CoV-2 Infections, *Front. Immunol.* 11 (2020) 3382. <https://doi.org/10.3389/fimmu.2020.610688>.
- [4] A. Iwasaki, S.B. Omer, Why and How Vaccines Work, *Cell.* 183 (2020) 290–295. <https://doi.org/10.1016/J.CELL.2020.09.040>.
- [5] F.X. Heinz, K. Stiasny, Distinguishing features of current COVID-19 vaccines: knowns and unknowns of antigen presentation and modes of action, *Npj Vaccines.* 6 (2021) 1–13. <https://doi.org/10.1038/s41541-021-00369-6>.

SECTION IV

CONCLUSIONS
AND FUTURE
PERSPECTIVES

I. Conclusions

In this doctoral thesis, different magnetic nanoparticles have been studied and characterized for their use in modern biomedicine, in general, and as detection labels in lateral flow assays, in particular. For this purpose, different magnetic nanoparticles have been synthesized by various routes and characterized physiochemically, structurally, superficially and magnetically. These characteristics are then correlated with their performance as contrast agents in nuclear magnetic resonance and heat mediators in magnetic hyperthermia and, above all, as biosensing tags. In this way, its characterization, focused on its detection in an inductive sensor, has made it possible to determine the parameters that optimize their application in lateral flow immunoassays. With this information, two LFAs have been successfully developed, one to determine the presence of SARS-CoV-2 antibodies and the other to quantify the levels of the pneumococcal pneumonia biomarker.

The conclusions derived from this doctoral thesis were presented within the corresponding chapters in section III and are summarized below:

1. We have used MNPs synthesized by co-precipitation with a double layer of fatty acids to determine their applicability in three of the most promising applications of nanoparticles in biomedicine.
 - i. The double layer of fatty acids made it possible to obtain hydrophilic nanoparticles (stable in water) with functional chemical groups on their external surface.
 - ii. The electronic images of the nanoparticles showed inorganic cores with sizes around 10 nm, but with a wide distribution. The magnetic characterization demonstrated the superparamagnetic behaviour of the NPs at room temperature and the predominant presence of interactions of dipolar origin (demagnetizing).
 - iii. The three types of particles showed an adequate heat release for their use in magnetic hyperthermia, highlighting the values obtained for the sample stabilized with oleic acid.
 - iv. The three types of particles exceeded the relaxation values of Endorem®, the standard commercial contrast agent for this purpose. Significantly, the myristic acid stabilized sample showed a value that doubles the relaxivity of Endorem®.

- v. It was shown that MNPs could be used as labels in magnetic lateral flow assays. The one stabilized with lauric acid reports the best results from the three nanoparticles thanks to its agglomeration in the functionalization process and its high initial permeability.
2. Magnetic nanoparticles with sizes between 5 nm and 23 nm have been synthesized. Its physical-chemical and magnetic characterization has allowed determining the essential characteristics for its use as labels in inductive biosensing.
- i. A thermal decomposition route was used to better control their size with a narrow distribution. A ligand exchange was carried out to replace the oleic acid with dimercaptosuccinic acid (DMSA) to use the MNPs in aqueous media. This small organic molecule also has functional chemical groups to anchor other biomolecules to the MNPs surface.
 - ii. The magnetic characterization of the MNPs and their calibration in the inductive sensor allowed us to establish a direct correlation between the initial magnetic susceptibility and the obtained signal, as long as they have a superparamagnetic size. For iron-based MNPs, this size is around 12 nm.
 - iii. The bioconjugation process allows the recognition biomolecule to bind to the surface of the MNP, which is a crucial step to capture the analyte. The MNP agglomeration during this process increased the number of particles that bind to each biomolecule, which amplifies its signal. However, this agglomeration must be controlled to allow a good calibration and avoid excessive sizes that could prevent a correct sample flow through the membrane. The ideal agglomerate size is around 200 nm.
3. An LFA has been developed to detect and quantify a molecule of clinical interest, the pneumolysin. Its presence in urine allows diagnosing pneumonia of pneumococcal origin. For this, magnetic clusters with an average size of 88 nm consisting of individual magnetite nanoparticles around 10 nm have been used. They are

assembled during the synthesis within a polyacrylic acid network.

- i. The structural and surface characterization of the nanoclusters confirmed the formation of magnetite nanoparticles and the polyacrylic acid coating, providing functional chemical groups for bioconjugation.
 - ii. The magnetic characterization of the clusters showed that the extraordinarily high signal in the inductive sensor is due to its high initial magnetic susceptibility.
 - iii. The LFA was developed in a sandwich format. The MNPs allowed a dual detection of the test line: On the one hand, by ImageJ analysis of the photographic images taken with a mobile phone. On the other, by quantifying the MNPs with the inductive sensor. The results indicated that the latter provides a broader linear measurement region, a better correlation factor in the linear fit, and a lower detection limit (6.3 ng / mL and 10.8 ng / mL for the magnetic and optical method, respectively).
 - iv. Magnetic pre-concentration and relocation were helpful tools that clearly reduced the detection limits and increased the signal in the inductive sensor. The new detection limits, including the pre-concentration technique, were only 0.2 ng/mL and 0.6 ng/mL for the magnetic and optical methods. These values are excellent and especially relevant for a portable quantifying device. When writing this thesis, we have found no precedents in the literature.
 - v. Preliminary studies of magnetic relocation of the particles were done to displace the MNPs in the test line closer to the sensitive area. This procedure further increased the signal by 20% the signal, demonstrating its potential and the interest of future research.
4. An LFA was developed that visually detects IgG antibodies generated by SARS-CoV-2 infection. The minimum concentration visually detected is around 5 $\mu\text{g/mL}$, which is within the range of clinical interest to monitor the immune response.
- i. In this case, we have developed a test that does not follow the typical configuration of a sandwich-type test. It is carried out

in two stages, as in a competitive one. Regardless, the signal is directly proportional to the antibody concentration in the test line, as in a sandwich format. This format will allow for a future multiplex assay to detect different antibodies.

- ii. The chosen antigen is a fragment of the spike protein of the SARS-CoV-2 virus, which can be helpful determine the response generated by current RNA vaccines that use this protein.
- iii. The formation of the MNPs-biotinylated antibody anti-human IgG complex is a critical step. The proportion of reagents must be optimized to avoid the agglomeration that prevents correct flow in the second stage of the assay.

In summary, MNPs allow a dual quantification (optical and magnetic) in lateral flow magnetic tests in which they are used as labels. In addition, the MNPs characteristics significantly influence the quantifying ability of the tests. To improve the sensitivity, MNPs must have a high initial susceptibility and show a certain degree of organization in clusters of controlled size. In this way, a portable method was developed to quantify biomolecules with high sensitivity for real clinical interest applications. In the method, MNPs stand out for their twofold functionality: they are both analyte concentrators (or separators) and detection reporters.

II. Conclusiones

En esta tesis doctoral se han estudiado y caracterizado diferentes nanopartículas magnéticas para su uso en biomedicina moderna, en general, y como marcas de detección en ensayos de flujo lateral, en particular. Para ello, se ha dispuesto de nanopartículas sintetizadas por diferentes rutas y que se han caracterizado fisicoquímica, estructural, superficial y magnéticamente. De esta forma, se correlacionan dichas características con su habilidad como agentes de contraste en resonancia magnética nuclear y mediadores de calor en hipertermia magnética y, sobre todo, como marcas de biodetección. De esta forma, su caracterización, enfocada a su detección en un sensor inductivo, ha permitido determinar los parámetros que optimizan su aplicación en inmunoensayos de flujo lateral. Con estos datos, se han podido desarrollar con éxito dos LFA, uno para determinar la presencia de anticuerpos de SARS-CoV-2 y otro para cuantificar los niveles del biomarcador de neumonía neumocócica.

Las conclusiones derivadas de la presente tesis doctoral se han presentado en la sección III de la misma en sus correspondientes capítulos, y se sintetizan a continuación:

1. Hemos utilizado nanopartículas magnéticas (MNPs) sintetizadas mediante coprecipitación con una doble capa de ácidos grasos para determinar su aplicabilidad en tres de las aplicaciones más prometedoras de las nanopartículas en medicina.
 - i. La doble capa de los ácidos grasos permitió obtener nanopartículas hidrofílicas (estables en agua) que además presentan grupos químicos funcionales en su superficie más externa.
 - ii. Las imágenes electrónicas de las nanopartículas mostraron núcleos inorgánicos con tamaños en torno a los 10 nm, pero con gran amplitud en su distribución. La caracterización magnética demostró el comportamiento súperparamagnético de las NPs a temperatura ambiente y la presencia predominante de interacciones de origen dipolar (desimanadora).
 - iii. Se ha demostrado que los tres tipos de partículas presentan una liberación de calor adecuada para su uso en hipertermia

magnética, destacando los valores obtenidos para la muestra estabilizada con ácido oleico.

- iv. Se ha demostrado que los tres tipos de partículas superan los valores de relajación de Endorem®, el referente comercial para tal fin. Especialmente, la muestra estabilizada con ácido mirístico presenta un valor que dobla la relaxividad de Endorem®.
 - v. Se ha demostrado que las MNPs pueden usarse como marcas en los ensayos de flujo lateral magnético. De las tres, la estabilizada con ácido láurico reporta los mejores resultados gracias a su aglomeración en el proceso de funcionalización y a su alta permeabilidad inicial.
2. Se han sintetizado nanopartículas magnéticas con tamaños entre 5 y 23 nm. Su caracterización físico-química y magnética ha permitido determinar las características más importantes para su uso como marcas en biodetección inductiva.
- i. Para la obtención de las partículas se utilizó una ruta de descomposición térmica ya que permite un mayor control de su tamaño con una distribución estrecha. Para utilizarlas en medios acuosos, se ha realizado un intercambio de ligandos que sustituye el ácido oleico por ácido dimercaptosuccínico (DMSA). Esta pequeña molécula orgánica dispone además de grupos químicos funcionales para anclar otras biomoléculas a la superficie de las partículas.
 - ii. La caracterización magnética y la calibración en el sensor inductivo de las MNPs permitió establecer una correlación directa entre la susceptibilidad magnética inicial de las mismas y la señal obtenida, siempre y cuando tengan un tamaño superparamagnético. Para MNPs basadas en hierro, este tamaño es entorno a los 12 nm.
 - iii. El proceso de bioconjugación permite unir la biomolécula de reconocimiento a la superficie de la MNP, lo que es un paso crucial para capturar el analito. La aglomeración de las MNPs durante este proceso aumenta el número de partículas que se unen a cada biomolécula, lo que amplifica la señal correspondiente a la misma. Sin embargo, dicha aglomeración debe de ser controlada para permitir una

buena calibración y evitar tamaños excesivos que puedan impedir un flujo correcto de la muestra por la membrana. El tamaño ideal de aglomerado está en torno a los 200 nm.

3. Se ha desarrollado un LFA para la detección y cuantificación de una molécula de interés clínico real, la neumolisina, proteína cuya presencia en orina indica neumonía neumocócica. Para ello, se han utilizado clústeres magnéticos con un tamaño medio de 88 nm y formados por nanopartículas individuales de magnetita en torno a los 10 nm. Su aglomeración se lleva a cabo durante la síntesis, en la que las nanopartículas individuales quedan dentro de una red de ácido poliacrílico, formando los nanoclústeres.
 - i. La caracterización estructural y superficial de los nanoclústeres confirmó la formación de nanopartículas de magnetita y la presencia del ácido poliacrílico, que permite su bioconjugación.
 - ii. La caracterización magnética de los clústeres demostró que la señal extraordinariamente elevada en el sensor inductivo se debe a su gran susceptibilidad magnética inicial.
 - iii. El LFA se desarrolló en formato sándwich. Las MNPs permitieron una cuantificación dual de la línea de test. Por un lado, se utilizó un análisis mediante ImageJ de las imágenes fotográficas tomadas con un teléfono móvil y, por otro, la cuantificación de las MNPs en el sensor inductivo. Los resultados indicaron que este último proporciona una región lineal de medida más amplia, un mejor factor de correlación en el ajuste lineal y un límite de detección más bajo (6.3 ng/mL y 10.8 ng/mL para el método magnético y el óptico, respectivamente).
 - iv. Se demostró que la pre-concentración y la recolocación magnéticas son herramientas útiles que permiten reducir claramente los límites de detección y aumentar la señal en el sensor inductivo. Los nuevos límites de detección incluyendo la técnica de pre-concentración son de solo 0.2 ng/mL y 0.6 ng/mL, para el método magnético y el óptico, respectivamente. Estos valores son excelentes y especialmente relevantes teniendo en cuenta que se trata de un dispositivo portátil y cuantificador. En el momento de

escribir esta tesis no hemos encontrado precedentes en la literatura.

- v. Se realizaron estudios preliminares de recolocación magnética de las partículas en la línea de test para favorecer su aproximación al área sensible. Con ello se logró un 20% adicional de la señal, lo que demuestra el potencial de esta técnica y el interés de una investigación futura.
4. Se desarrolló un LFA que detecta visualmente los anticuerpos IgG generados por la infección por SARS-CoV-2. La concentración mínima detectada de forma visual está en torno a los 5 $\mu\text{g}/\text{mL}$ lo que se encuentra dentro del rango de interés clínico para monitorizar la respuesta inmune.
- i. En este caso, hemos desarrollado un test que no sigue la configuración típica de un ensayo tipo sándwich, sino que se realiza en dos etapas, como en uno competitivo. Sin embargo, la señal es directamente proporcional a la concentración de anticuerpos en la línea de test, como en un formato sándwich. Esta conformación permite realizar un ensayo multiplex para detectar diferentes anticuerpos.
 - ii. El antígeno elegido es un fragmento de la proteína de espícula del virus SARS-CoV-2 que podría ayudar en la determinación de la respuesta generada por las vacunas de RNA actuales, que utilizan dicha proteína.
 - iii. La formación del complejo MNPs-anticuerpo biotinilado anti-IgG humano es una etapa clave en la que hay que optimizar la proporción de reactivos para evitar la aglomeración de los clústeres que impiden el flujo correcto en la segunda etapa del ensayo.

En resumen, las MNPs permiten una cuantificación dual (óptica y magnética) de los ensayos de magnéticos de flujo lateral en los que se utilizan como marcas. Sus características tienen una gran influencia en la habilidad cuantificadora que otorgan a estos tests. Para la mejora de la sensibilidad, las MNPs deben de tener una alta susceptibilidad inicial y mostrar cierto grado de organización en clústeres de tamaño controlado. De esta forma, se ha desarrollado un método portátil que permite

cuantificar con una elevada sensibilidad biomoléculas con un interés clínico real, y en el que las MNPs destacan además por su funcionalidad dual: son tanto preconcentradores del analito (o separadores) como mediadores de la detección.

III. Conclusioni

In questa tesi di dottorato, sono state studiate e caratterizzate diverse nanoparticelle magnetiche con lo scopo di ottimizzare le loro proprietà per applicazioni in biomedicina ed in particolare come etichette di rilevamento nei saggi a flusso laterale. In quest'ottica sono stati utilizzati diversi metodi per la sintesi di nanoparticelle magnetiche e sui materiali ottenuti è stata effettuata una accurata caratterizzazione morfologica, chimico-fisica e magnetica. Queste caratteristiche sono poi correlate alle loro prestazioni come agenti di contrasto nella risonanza magnetica nucleare, come mediatori del calore nell'ipertermia magnetica e, soprattutto, come marcatori di biosensori. In particolare, un accurato studio sulla rilevazione delle nanoparticelle magnetiche, in un sensore induttivo, ha permesso di determinare i parametri che ottimizzano la loro applicazione negli immunodosaggi a flusso laterale. Con queste informazioni, sono stati sviluppati con successo due LFA, uno per determinare la presenza di anticorpi SARS-CoV-2 e l'altro per quantificare i livelli del biomarcatore della polmonite pneumococcica.

Le conclusioni tratte da questa tesi di dottorato sono state presentate nei corrispondenti capitoli della sezione III, e sono riassunte di seguito:

1. Abbiamo utilizzato nanoparticelle magnetiche sintetizzate mediante coprecipitazione con un doppio strato di acidi grassi per determinare la loro applicabilità in tre delle applicazioni più promettenti delle nanoparticelle in biomedicina.
 - i. Il doppio strato di acidi grassi ha permesso di ottenere nanoparticelle idrofiliche (stabili in acqua) con gruppi chimici funzionali sulla loro superficie esterna.
 - ii. Le immagini di microscopia elettronica in trasmissione delle nanoparticelle hanno mostrato nuclei inorganici con dimensioni intorno ai 10 nm, ma con un'ampia distribuzione. La caratterizzazione magnetica ha dimostrato il comportamento superparamagnetico delle nanoparticelle a temperatura ambiente e la presenza predominante di interazioni di origine dipolare (i.e., interazioni demagnetizzanti).
 - iii. I tre tipi di particelle hanno mostrato un adeguato rilascio di calore per il loro utilizzo in ipertermia magnetica,

evidenziando i valori ottenuti per il campione stabilizzato con acido oleico.

- iv. I tre tipi di particelle hanno superato i valori di rilassamento di Endorem®, il mezzo di contrasto commerciale standard per questo scopo. Significativamente, il campione stabilizzato con acido miristico ha mostrato un valore che raddoppia la rilassività di Endorem®.
- v. È stato dimostrato che queste nanoparticelle magnetiche possono essere utilizzati come etichette nei saggi di flusso laterale magnetico. Il campione di nanoparticelle stabilizzate con acido laurico ha mostrato i risultati più promettenti grazie alla sua agglomerazione nel processo di funzionalizzazione e alla sua elevata permeabilità iniziale.

2. Sono state sintetizzate nanoparticelle magnetiche con dimensioni comprese tra 5 nm e 23 nm. La caratterizzazione chimico-fisica e magnetica dei materiali ha consentito di determinarne le caratteristiche essenziali per il loro utilizzo come label nel biorilevamento induttivo.

- i. Per ottenere le particelle è stata utilizzata una via di decomposizione termica per consentire un maggiore controllo della loro dimensione con una distribuzione ristretta. È stato effettuato uno scambio di ligandi per sostituire l'acido oleico con acido dimercaptosuccinico (DMSA) per utilizzare gli MNP in mezzi acquosi. Questa piccola molecola organica ha anche gruppi chimici funzionali per ancorare altre biomolecole alla superficie delle nanoparticelle magnetiche.
- ii. La caratterizzazione magnetica delle nanoparticelle e la loro calibrazione nel sensore induttivo hanno permesso di stabilire una correlazione diretta tra la suscettività magnetica iniziale e il segnale ottenuto, purché di dimensione superparamagnetica. Per le nanoparticelle magnetiche a base di ferro, questa dimensione è di circa 12 nm.
- iii. Il processo di bioconiugazione consente alla biomolecola di riconoscimento di legarsi alla superficie delle nanoparticelle, passaggio cruciale per catturare l'analita. L'agglomerato di

nanoparticelle magnetiche durante questo processo ha aumentato il numero di particelle che si legano a ciascuna biomolecola, il che ne amplifica il segnale. Tuttavia, questo agglomerato deve essere controllato per consentire una buona calibrazione ed evitare dimensioni eccessive che potrebbero impedire un corretto flusso del campione attraverso la membrana. La dimensione ideale dell'agglomerato è di circa 200 nm.

3. È stato sviluppato un LFA per rilevare e quantificare una molecola di reale interesse clinico, la pneumolisina. La presenza di questa proteina nelle urine indica polmonite pneumococcica. Per questo sono stati utilizzati cluster magnetici con una dimensione media di circa 90 nm costituiti da singole nanoparticelle di magnetite di circa 10 nm. Il loro agglomerato avviene durante la sintesi, in cui le singole nanoparticelle rimangono all'interno di una rete di acido poliacrilico, formando i nanocluster.
 - i. La caratterizzazione strutturale e superficiale dei nanocluster ha confermato la formazione di nanoparticelle di magnetite e la presenza di acido poliacrilico, che ne consente la bioconiugazione.
 - ii. La caratterizzazione magnetica dei cluster ha mostrato che il segnale straordinariamente alto nel sensore induttivo è dovuto alla sua elevata suscettibilità magnetica iniziale.
 - iii. L'LFA è stato sviluppato in un formato sandwich. Le nanoparticelle magnetiche hanno consentito una doppia quantificazione della linea di test. Da un lato è stata utilizzata un'analisi ImageJ delle immagini fotografiche scattate con un telefono cellulare. Dall'altro, la quantificazione delle nanoparticelle magnetiche con il sensore induttivo. I risultati hanno indicato che quest'ultimo fornisce una regione di misurazione lineare più ampia, un migliore fattore di correlazione nell'adattamento lineare e un limite di rilevamento inferiore (6,3 ng/mL e 10,8 ng/mL rispettivamente per il metodo magnetico e ottico).
 - iv. La pre-concentrazione magnetica e la ricollocazione delle nanoparticelle magnetiche sono stati strumenti utili che riducono chiaramente i limiti di rilevamento e aumentano il

segnale nel sensore induttivo. I nuovi limiti di rilevamento, inclusa la tecnica di pre-concentrazione, erano 0,2 ng/mL e 0,6 ng/mL per i metodi magnetici e ottici. Questi valori sono ottimi e soprattutto rilevanti considerando che si tratta di un quantificatore portatile. Nello scrivere questa tesi, non abbiamo trovato precedenti in letteratura.

- v. Sono stati condotti studi preliminari sulla ricollocazione magnetica delle particelle per avvicinare le nanoparticelle magnetiche nella linea di prova all'area sensibile. Questa procedura ha aumentato del 20% il segnale, dimostrando le sue potenzialità e l'interesse per la ricerca futura.
4. È stato sviluppato un LFA che rileva visivamente gli anticorpi IgG generati dall'infezione da SARS-CoV-2. La concentrazione minima rilevata visivamente è di circa 5 µg/mL, che rientra nell'intervallo di interesse clinico per monitorare la risposta immunitaria.
- i. In questo caso abbiamo sviluppato un test che non segue la configurazione tipica di un test di tipo sandwich. Si svolge in due fasi, come in una competitiva. Tuttavia, il segnale è direttamente proporzionale alla concentrazione di anticorpi nella linea del test, come in un formato sandwich. Questa conformazione consente a un test multiplex di rilevare diversi anticorpi.
 - ii. L'antigene scelto è un frammento della proteina spike del virus SARS-CoV-2. Questa scelta potrebbe aiutare a determinare la risposta generata dagli attuali vaccini a RNA che utilizzano questa proteina.
 - iii. La formazione del complesso MNPs-anticorpo biotinilato anti-IgG umane è un passaggio critico. La proporzione dei reagenti deve essere ottimizzata per evitare l'agglomerazione che impedisce il corretto flusso nella seconda fase del dosaggio.

In sintesi, e come conclusione finale, è stato dimostrato che le nanoparticelle magnetiche consentono una doppia quantificazione (ottica e magnetica) nei test magnetici a flusso laterale in cui vengono utilizzate come marcatori. Inoltre, le caratteristiche delle nanoparticelle

magnetiche influenzano significativamente la capacità di quantificazione dei test. Per migliorare la sensibilità, le nanoparticelle magnetiche devono avere un'elevata suscettibilità iniziale e mostrare un certo grado di organizzazione in cluster di dimensioni controllate. In questo modo, è stato sviluppato un metodo portatile per quantificare le biomolecole con elevata sensibilità per applicazioni di reale interesse clinico. Nel metodo proposto, le nanoparticelle magnetiche si distinguono per la loro doppia funzionalità: sono sia mediatori di segnale che concentratori (o separatori) di analiti.

IV. Future perspectives

This thesis has demonstrated the potential of magnetic nanoparticles as detection labels in lateral flow immunoassays and their many advantages. However, there is still much work that can be done to develop the method's full potential in its three main aspects: the lateral flow strips, the magnetic nanoparticles, and the sensor. These possible lines of research are pointed out in the following lines.

1. Lateral flow strips

- i. The membranes that make up the lateral flow strips have a pore size distribution that determines the maximum size of the fluid sample constituents. Membranes with larger pores can be considered that allow the flow of larger particles with a larger magnetic moment.
- ii. One of the disadvantages of working with membranes with larger pores is that they reduce the interaction time between the labelled analyte and the antibody deposited on the test line. A magnetic field can be applied in the area close to the test line to hold the molecules and then release them, so increasing the reaction time.
- iii. Multiplex assays should be developed in which more than one analyte can be evaluated in different test lines of the same assay strip. This strategy provides more information to enable a more precise diagnosis.

2. Magnetic nanoparticles

- i. Development of protocols that allow the controlled agglomeration of nanoparticles and the agglomerates size. Different combinations of large individual nanoparticles (within the superparamagnetic limit) in small clusters or vice versa could be tested in the sensor to increase the sensitivity.
- ii. Vary the composition of the magnetic nanoparticles. The chemical elements in the magnetic nanoparticles determine their magnetic properties. Different ferrites could be tested on the sensor to optimize the magnetic susceptibility. For example, manganese ferrites have a smaller magnetic anisotropy than magnetite, which increases the initial

susceptibility. Synthesis routes to adjust their size and assemble them in superparamagnetic nanoclusters with suitable polymeric coatings need to be elaborated.

- iii. Study of the influence of the MNP easy axis orientation. A small field applied during the synthesis of MNPs can cause them to grow together and oriented. This conformation could provide a more significant signal in the sensor due to the MNPs cooperative behaviour.
- iv. Study of the influence of the MNPs shape. Specific configurations, such as nanodisks or nanowires, have different magnetic properties due to their geometric shape, such as larger magnetic susceptibility.
- v. The pre-concentration process can be improved by developing a platform that allows applying a controlled field gradient in a large fluid volume.
- vi. Improvements in the magnetic relocation process are required, studying parameters such as the time and the amplitude of the applied field gradient. It would also be interesting to study the strength of the bond between the capture antibody or biomolecule and the labelled analyte to confirm how specifically the relocation occurs.

3. Sensor

- i. Study of different electronics to reduce the measuring device size and cost. In this way, a portable POCT device could be obtained.
- ii. Incorporation in the POCT device of elements allows introducing the advantages of MNPs, such as pre-concentration or magnetic relocation before measuring.

In short, the excellent results obtained in this thesis and the method's versatility promise great future developments in which a POCT device based on LFA with MNPS can meet societal needs, especially in times of crisis and emergencies.

SCIENTIFIC
PRODUCTION

In this section, the scientific production of the doctoral student during the development of the thesis is gathered.

Scientific articles presented in the thesis

Table 1. Information on the scientific journals in which the articles presented in this thesis have been published.

Journal	Year	Impact Factor	Journal Rank	Field	Status
Journal of Nanoscience and Nanotechnology	2019	1.134	Q3	Materials Science	Published
Nanomaterials	*	4.921	Q1	Applied Physics	*Submitted
The analyst	2020	4.616	Q1	Analytical Chemistry	Published
IEEE Access	*	3.367	Q2	Materials Science	*Submitted

Other scientific articles published

- **Microemulsion synthesis of superparamagnetic nanoparticles for bioapplications.** María Salvador, Gemma Gutiérrez, Sara Noriega, Amanda Moyano, María Carmen Blanco-López, María Matos. International Journal of Molecular Sciences 2021, 22(1):427. <https://doi.org/10.3390/ijms22010427>
- **Electrodecoration and characterization of superparamagnetic iron oxide nanoparticles with bioactive synergistic nanocopper: magnetic hyperthermia-induced ionic release for anti-biofilm action.** Verdiana Marchianò, María Salvador, Amanda Moyano, S. Yáñez, Yolanda Piñeiro, José Rivas, José C. Martínez-García, Davide Peddis, María C. Blanco-López, Montserrat Rivas, Nicola Cioffi, Nicoletta Ditaranto. Antibiotics 2021, 10(2), 119; <https://doi.org/10.3390/antibiotics10020119>
- **Magnetic lateral flow immunoassay for small extracellular vesicles quantification. Application to colorectal cancer biomarker detection.** Amanda Moyano, Esther Serrano-Pertierra, José María Duque, Virginia Ramos, Estefanía Teruel-Barandiarán, María Teresa Fernández-Sánchez, María Salvador, José Carlos Martínez-García, Luis Sánchez, Luis García-Flórez, Montserrat

Rivas, María del Carmen Blanco-López. *Sensors* 2021, 21(11), 3756; <https://doi.org/10.3390/s21113756>

- **From the astro to the nano scale: Downsizing the planets, upsizing the molecules.** María Salvador, David Lago-Cachón, Pietro Calandra, Andrea Malito, Davide Peddis. Vol. 99, No. S1, A29 (2021). <https://doi.org/10.1478/AAPP.99S1A29>
- **Carbon-coated superparamagnetic nanoflowers for biosensors based on lateral flow immunoassays.** A. Moyano, E. Serrano-Pertierra, M. Salvador, J.C. Martínez-García, Y. Piñeiro, S. Yañez-Vilar, Manuel González-Gómez, J. Rivas, M. Rivas, M. C. Blanco-López. *Biosensors* 2020, 10(8), 80. <https://doi.org/10.3390/bios10080080>
- **Extracellular Vesicles: Current Analytical Techniques for Detection and Quantification.** Esther Serrano-Pertierra, Myriam Oliveira-Rodríguez, María Matos, Gemma Gutiérrez, María Salvador, Montserrat Rivas, María Carmen Blanco-López. *Biomolecules* 2020, 10(6), 824. <https://doi.org/10.3390/biom10060824>
- **Magnetic Lateral Flow Immunoassays.** Amanda Moyano, Esther Serrano-Pertierra, María Salvador, José Carlos Martínez-García, Montserrat Rivas, M. Carmen Blanco-López. *Diagnostics* 2020, 10(5), 288; <https://doi.org/10.3390/diagnostics10050288>
- **Magnetic immunochromatographic test for histamine detection in wine.** Amanda Moyano, María Salvador, José C. Martínez-García, Vlad Socoliuc, Ladislau Vékás, Davide Peddis, Miguel A. Alvarez, María Fernández, Montserrat Rivas, M. Carmen Blanco-López. *Analytical and Bioanalytical Chemistry*, 411: 6615. 2019. <https://doi.org/10.1007/s00216-019-02031-6>
- **Detectar ciguatoxina antes de que llegue a nuestra mesa: un nuevo reto para el bionálisis.** María Salvador, Amanda Moyano, José Carlos Martínez, María Teresa Fernández-Sánchez, Antonello Novelli, María Cezón, Jose Luis Suárez, Montserrat Rivas, Carmen Blanco-López. *Revista Alimentaria. Ediciones y Publicaciones Alimentarias*, S.A. Mayo 2019.
- **Co-doped MnFe₂O₄ nanoparticles: magnetic anisotropy and interparticle interactions.** Bagher Aslibeiki, Parviz Kameli, Hadi Salamati, Giorgio Concas, María Salvador Fernández, Alessandro

Talone, Giuseppe Muscas, Davide Peddis. Beilstein Journal of Nanotechnology, 10, 856–865. March 2019. <https://doi.org/10.3762/bjnano.10.86>

- **Experimental Protocols for Measuring Properties of Nanoparticles Dispersed in Fluids.** Alexander Omelyanchik, Valeria Rodionova, Davide Peddis, Gaspare Varvaro, Sara Laureti, María Salvador, Ana Mrakovic, Vladan Kusigerski, Erzsébet Illés, Nikola Knezevic. 2018 IEEE 8th International Conference Nanomaterials: Application & Properties (NAP), Zatoka, Ukraine, 2018, pp. 1-5. <https://doi.org/10.1109/NAP.2018.8915059>
- **Scanning Magneto-Inductive Sensor for Quantitative Assay of Prostate-Specific Antigen.** David Lago-Cachón, Myriam Oliveira-Rodríguez, Montserrat Rivas, María C. Blanco-López, José-C. Martínez-García, Amanda Moyano, María Salvador, José A. Gracia. IEEE Magnetics Letters, Volume 8, June 2017. <https://doi.org/10.1109/LMAG.2017.2702108>

Participation in congresses

- *Poster communication*

A rapid magnetic serological test for COVID-19. M. Salvador, J.L. Marqués, F. Brero, F. G. da Silva, A. Bunge, J.C. Martínez-García, M. Mariani, A. Lascialfari, R. Turcu, V. Pilati, C. Kern, F. Orsini, J. Depeyrot and M. Rivas.

Joint MMM-INTERMAG, 10th – 14th January 2022, ONLINE.

- *Oral communication*

Nanolabel optimization for the development of a magnetic immunoserological test for COVID-19. M. Salvador, J. Marqués, F. Brero, F. G. da Silva, J.C. Martínez-García, M. Mariani, A. Lascialfari, V. Pilati, C. Kern, F. Orsini, J. Depeyrot and M. Rivas

5th Young Researchers in Magnetism – Annual meeting CEMAG - IEEE Magnetic Society Spanish Chapter, 10th – 12th November 2021, Girona, Spain.

- *Poster communication*

Magnetic Particles' Size and Clustering Effects for Improved Magnetic Lateral Flow Assays. María Salvador; Álvaro Gallo-Cordova,

Amanda Moyano, J. Carlos Martínez-García, M. Puerto Morales, Montserrat Rivas

XXVII National Congress SCI, 14th – 23rd September 2021, ONLINE.

- *Poster Communication*

Magnetic versus Plasmonic Nanotags for Histamine Biodetection in Wine. María Salvador, Amanda Moyano, J.C. Martínez-García, Vlad Socoliuc, Ladislau Vékás, Davide Peddis, María Fernández, M.C. Blanco-López, Montserrat Rivas.

7th Italian Conference on Magnetism. ONLINE, 11th-12th February 2021

- *Oral Communication*

Optimizing Size Nanoparticle and Agglomeration on Magnetic Nanotags for Lateral Flow Immunoassays. M. Salvador, A. Gallo-Córdova, A. Moyano, J.C. Martínez-García, M.C. Blanco-López, M.P. Morales, M. Rivas.

JEMS 2020 Conference, ONLINE, 7th – 11th December 2020.

- *Poster Communication*

Size and Clustering Nanoparticle Effects on Inductive Biosensing for Improved Magnetic Lateral Flow Assays. María Salvador, Álvaro Gallo-Cordova, Amanda Moyano, J. Carlos Martínez-García, M. Puerto Morales, Montserrat Rivas.

3rd Spanish Conference on Biomedical Applications of Nanomaterials (SBAN). ONLINE, 3rd September 2020.

- *Oral Communication*

Nanoparticle Effects on Magnetic Lateral Flow Assays: Size and Clustering for Improved Inductive Biosensing. M. Salvador, A. Gallo-Córdova, A. Moyano, J.C. Martínez-García, M.C. Blanco-López, M.P. Morales, M. Rivas.

Around the clock, around the globe. IEEE Magnetic Society. ONLINE, 27th August 2020.

- *Oral Communication*

Size Nanoparticle and Agglomeration Effects on Magnetic Lateral Flow Immunoassays. M. Salvador, A. Gallo-Córdova, A. Moyano, J.C. Martínez-García, M.C. Blanco-López, M.P. Morales, M. Rivas.

2nd Nanomaterials Applied to Life Sciences (NALS), 29th – 31st January 2020, Madrid, Spain.

- *Poster Communication*

Tuning the initial magnetic susceptibility by means of chemical composition in spinel ferrites nanoparticles for paper-supported biosensing. M. Salvador, O. Arriortua, A. Moyano, J.C. Martínez-García, M. Insausti, M.C. Blanco-López, M. Rivas.

2nd Nanomaterials Applied to Life Sciences (NALS), 29th – 31st January 2020, Madrid, Spain.

- *Oral Communication*

Improving Magnetic Lateral Flow Immunoassays by a Magnetic Field Gradient. María Salvador, Álvaro Gallo-Córdova, Amanda Moyano, J.C. Martínez-García, M. Carmen Blanco-López, M. Puerto Morales, Montserrat Rivas.

9th International Conference on Nanomaterials: Applications & Properties, 15 - 20 September 2019, Odesa, Ukraine.

- *Oral Communication*

Spinel Ferrite Nanoparticles as Magnetic Labels in Lateral Flow Immunoassays. M. Salvador, O. Arriortua, A. Moyano, J.C. Martínez-García, M.C. Blanco-López, M. Insausti, M. Rivas.

3rd International Baltic Conference on Magnetism, 18 - 22 August 2019, Kaliningrad, Russia. (Best Student Oral Presentation Award)

- *Oral Communication*

Fatty-acid stabilised superparamagnetic nanoparticles to understand the reading-out of paper-based immunoassays. M. Salvador, A. Moyano, J.C. Martínez-García, M.C. Blanco-López, V. Socoliuc, L. Vékas, D. Peddis, M. Rivas.

10th International Conference on Fine Particle Magnetism. 27th – 31st May 2019. Gijón. Spain.

- *Poster Communication*

Enhancement of magnetic lateral flow immunoassays signal by means of a magnetic field gradient. M. Salvador, A. Moyano, J.C. Martínez-García, M.C. Blanco-López, V. Socoliuc, L. Vékas, D. Peddis, M.P. Morales, M. Rivas.

10th International Conference on Fine Particle Magnetism. 27th – 31st May 2019. Gijón. Spain.

- *Poster Communication*

Superparamagnetic nanoparticles for rapid bioanalysis in magnetic lateral flow immunoassays. M. Salvador, A. Moyano, J. C. Martínez-García, Vlad Socoliuc, Ladislau Vékás, Davide Peddis, María Fernández, M. Rivas, M.C. Blanco-López.

6th Italian Conference on Magnetism. Jan 30th – Feb 1st, 2019. Italy

- *Oral Communication*

A magnetic field gradient to enhance the signal in magnetic lateral flow immunoassays. M. Salvador, A. Moyano, J. C. Martínez-García, M.C. Blanco-López, M. Puerto Morales, M. Rivas.

Young Researchers in Magnetism - Spanish Magnetism Club and Spanish Chapter of the IEEE Magnetic Society Meeting. 29th – 30th November 2018 Gijón

- *Oral Communication*

Biodetection of histamine in wine: magnetic versus plasmonic labels. M. Salvador, A. Moyano, J. C. Martínez-García, Vlad Socoliuc, Ladislau Vékás, Davide Peddis, María Fernández, M. Rivas, M.C. Blanco-López.

25th International Symposium on Metastable, Amorphous and Nanostructured Materials (ISMANAM 2018). 2nd – 6th July 2018

- *Poster Communication*

Enhancement of magnetic lateral flow immunoassays by means of a magnetic field gradient. M. Salvador, A. Moyano, J. C. Martínez-García, M.C. Blanco-López, M. Puerto Morales, M. Rivas.

8th Early-Stage Researchers Workshop in Nanoscience. IMDEA Nanoscience. Madrid, Spain. 13 and 14 June 2018. (Best Student Poster Presentation Award)

- *Invited oral communication*

When a problem meets its solution: Superparamagnetic Lateral Flow Immunoassay for Cancer Screening. M. Salvador, L.J. G. Flórez, J. C. Martínez-García, A. Moyano, M.C. Blanco-López, M. Rivas.

1st Nanomaterials Applied to Life Sciences. 12th – 15th December 2017, Gijón, (Spain).

- *Poster Communication*

Superparamagnetic Iron Oxide Nanoparticles with Extraordinary Properties for Biodetection. María Salvador, Amanda Moyano, J.C. Martínez-García, Vlad Socoliuc, Ladislau Vékás, Montserrat Rivas, Davide Peddis.

1st Nanomaterials Applied to Life Sciences. 12th – 15th December 2017, Gijón, (Spain)

- *Oral communication*

Quantification of troponin by superparamagnetic lateral flow immunoassay. M. Salvador, A. Moyano, M. Rivas, J. C. Martínez-García, M. Oliveira-Rodríguez, C. Blanco-López.

X Biotech Annual Congress (Federación Española de Biotecnólogos). 13th – 15th July 2016, Gijón, (Spain).

Related training activities

- European School on Magnetism: Fundamentals of Magnetism. ONLINE. 28th September – 2nd October 2020.
- IEEE Magnetics Society Summer School. Virginia Commonwealth University, Richmond, VA, USA. 2nd – 8th July 2019.
- 1st NanoBioAp School: Nanoparticles for Bioapplications. Llanes, Asturias. 23rd – 25th May 2019.
- 4th Italian School on Magnetism: Advanced magnetic materials and devices for biomedical applications, Torino, Italy. 21st – 25th May 2018.

LITERATURE

- [1] K.J. Land, D.I. Boeras, X.-S. Chen, A.R. Ramsay, R.W. Peeling, REASSURED diagnostics to inform disease control strategies, strengthen health systems and improve patient outcomes, *Nat. Microbiol.* 2018 41. 4 (2018) 46–54. <https://doi.org/10.1038/s41564-018-0295-3>.
- [2] P. Estrela, N. Bhalla, P. Jolly, N. Formisano, P. Estrela, Introduction to biosensors, *Essays Biochem.* 60 (2016) 1–8. <https://doi.org/10.1042/EBC20150001>.
- [3] V. Naresh, N. Lee, A Review on Biosensors and Recent Development of Nanostructured Materials-Enabled Biosensors, *Sensors* 2021, Vol. 21, Page 1109. 21 (2021) 1109. <https://doi.org/10.3390/S21041109>.
- [4] R. Etzioni, N. Urban, S. Ramsey, M. McIntosh, S. Schwartz, B. Reid, J. Radich, G. Anderson, L. Hartwell, The case for early detection, *Nat. Rev. Cancer* 2003 34. 3 (2003) 243–252. <https://doi.org/10.1038/nrc1041>.
- [5] P.K. Drain, E.P. Hyle, F. Noubary, K.A. Freedberg, D. Wilson, W.R. Bishai, W. Rodriguez, I. V. Bassett, Diagnostic point-of-care tests in resource-limited settings, *Lancet Infect. Dis.* 14 (2014) 239–249. [https://doi.org/10.1016/S1473-3099\(13\)70250-0](https://doi.org/10.1016/S1473-3099(13)70250-0).
- [6] P.B. Luppa, C. Müller, A. Schlichtiger, H. Schlebusch, Point-of-care testing (POCT): Current techniques and future perspectives, *TrAC Trends Anal. Chem.* 30 (2011) 887–898. <https://doi.org/10.1016/J.TRAC.2011.01.019>.
- [7] H. Chen, K. Liu, Z. Li, P. Wang, Point of care testing for infectious diseases, *Clin. Chim. Acta.* 493 (2019) 138–147. <https://doi.org/10.1016/J.CCA.2019.03.008>.
- [8] M.U. Ahmed, M.M. Hossain, M. Safavieh, Y.L. Wong, I.A. Rahman, M. Zourob, E. Tamiya, Toward the development of smart and low cost point-of-care biosensors based on screen printed electrodes, <Http://Dx.Doi.Org/10.3109/07388551.2014.992387>. 36 (2015) 495–505. <https://doi.org/10.3109/07388551.2014.992387>.
- [9] S. Smith, J.G. Korvink, D. Mager, K. Land, The potential of paper-based diagnostics to meet the ASSURED criteria, *RSC Adv.* 8 (2018) 34012–34034. <https://doi.org/10.1039/C8RA06132G>.
- [10] S. Nishat, A.T. Jafry, A.W. Martinez, F.R. Awan, Paper-based microfluidics: Simplified fabrication and assay methods, *Sensors Actuators B Chem.* 336 (2021) 129681. <https://doi.org/10.1016/J.SNB.2021.129681>.
- [11] A.S. John, C.P. Price, Existing and Emerging Technologies for Point-of-Care Testing, *Clin. Biochem. Rev.* 35 (2014) 155. </pmc/articles/PMC4204237/> (accessed September 6, 2021).
- [12] N. Jiang, R. Ahmed, M. Damayantharan, B. Ünal, H. Butt, A.K.

- Yetisen, Lateral and Vertical Flow Assays for Point-of-Care Diagnostics, *Adv. Healthc. Mater.* 8 (2019) 1900244. <https://doi.org/10.1002/ADHM.201900244>.
- [13] P. Chen, M. Gates-Hollingsworth, S. Pandit, A. Park, D. Montgomery, D. AuCoin, J. Gu, F. Zenhausern, Paper-based Vertical Flow Immunoassay (VFI) for detection of bio-threat pathogens, *Talanta*. 191 (2019) 81–88. <https://doi.org/10.1016/J.TALANTA.2018.08.043>.
- [14] D.E.W. Patabadige, S. Jia, J. Sibbitts, J. Sadeghi, K. Sellens, C.T. Culbertson, Micro Total Analysis Systems: Fundamental Advances and Applications, *Anal. Chem.* 88 (2015) 320–338. <https://doi.org/10.1021/ACS.ANALCHEM.5B04310>.
- [15] V.A.O.P. da Silva, R.C. de Freitas, P.R. de Oliveira, R.C. Moreira, L.H. Marcolino-Júnior, M.F. Bergamini, W.K.T. Coltro, B.C. Janegitz, Microfluidic paper-based device integrated with smartphone for point-of-use colorimetric monitoring of water quality index, *Measurement*. 164 (2020) 108085. <https://doi.org/10.1016/J.MEASUREMENT.2020.108085>.
- [16] B. O'Farrell, Evolution in Lateral Flow-Based Immunoassay Systems, *Lateral Flow Immunoass.* (2009) 1–33. https://doi.org/10.1007/978-1-59745-240-3_1.
- [17] J.H.W. Leuvering, P.J.H.M. Thal, M. Van der Waart, A.H.W.M. Schuurs, A sol particle agglutination assay for human chorionic gonadotrophin, *J. Immunol. Methods*. 45 (1981) 183–194. [https://doi.org/10.1016/0022-1759\(81\)90212-X](https://doi.org/10.1016/0022-1759(81)90212-X).
- [18] A. S, A short history, principles, and types of ELISA, and our laboratory experience with peptide/protein analyses using ELISA, *Peptides*. 72 (2015) 4–15. <https://doi.org/10.1016/J.PEPTIDES.2015.04.012>.
- [19] M.A. Mansfield, The Use of Nitrocellulose Membranes in Lateral-Flow Assays, *Drugs Abus.* (2005) 71–85. https://doi.org/10.1007/978-1-59259-951-6_4.
- [20] L. Anfossi, F. Di Nardo, S. Cavallera, C. Giovannoli, C. Baggiani, Multiplex Lateral Flow Immunoassay: An Overview of Strategies towards High-throughput Point-of-Need Testing, *Biosens.* 2019, Vol. 9, Page 2. 9 (2018) 2. <https://doi.org/10.3390/BIOS9010002>.
- [21] T.-T. Tsai, T.-H. Huang, N.Y.-J. Ho, Y.-P. Chen, C.-A. Chen, C.-F. Chen, Development of a multiplex and sensitive lateral flow immunoassay for the diagnosis of periprosthetic joint infection, *Sci. Reports* 2019 9. 9 (2019) 1–8. <https://doi.org/10.1038/s41598-019-52051-6>.
- [22] D. Zhang, L. Huang, B. Liu, H. Ni, L. Sun, E. Su, H. Chen, Z. Gu, X. Zhao, Quantitative and ultrasensitive detection of multiplex cardiac biomarkers in lateral flow assay with core-shell SERS

- nanotags, *Biosens. Bioelectron.* 106 (2018) 204–211. <https://doi.org/10.1016/J.BIOS.2018.01.062>.
- [23] Y. Zhao, H. Wang, P. Zhang, C. Sun, X. Wang, X. Wang, R. Yang, C. Wang, L. Zhou, Rapid multiplex detection of 10 foodborne pathogens with an up-converting phosphor technology-based 10-channel lateral flow assay, *Sci. Reports* 2016 61. 6 (2016) 1–8. <https://doi.org/10.1038/srep21342>.
- [24] J. Li, J. Macdonald, Multiplexed lateral flow biosensors: Technological advances for radically improving point-of-care diagnoses, *Biosens. Bioelectron.* 83 (2016) 177–192. <https://doi.org/10.1016/J.BIOS.2016.04.021>.
- [25] Y. Wu, Y. Zhou, Y. Leng, W. Lai, X. Huang, Y. Xiong, Emerging design strategies for constructing multiplex lateral flow test strip sensors, *Biosens. Bioelectron.* 157 (2020) 112168. <https://doi.org/10.1016/J.BIOS.2020.112168>.
- [26] E. Liddell, *Antibodies, Immunoass. Handb.* (2013) 245–265. <https://doi.org/10.1016/B978-0-08-097037-0.00017-8>.
- [27] M. Moser, O. Leo, Key concepts in immunology, *Vaccine.* 28 (2010) C2–C13. <https://doi.org/10.1016/J.VACCINE.2010.07.022>.
- [28] E.O. Saphire, R.L. Stanfield, M.D. Max Crispin, P.W.H.I. Parren, P.M. Rudd, R.A. Dwek, D.R. Burton, I.A. Wilson, Contrasting IgG Structures Reveal Extreme Asymmetry and Flexibility, *J. Mol. Biol.* 319 (2002) 9–18. [https://doi.org/10.1016/S0022-2836\(02\)00244-9](https://doi.org/10.1016/S0022-2836(02)00244-9).
- [29] N.S. Lipman, L.R. Jackson, L.J. Trudel, F. Weis-Garcia, Monoclonal Versus Polyclonal Antibodies: Distinguishing Characteristics, Applications, and Information Resources, *ILAR J.* 46 (2005) 258–268. <https://doi.org/10.1093/ILAR.46.3.258>.
- [30] M.C. Brown, *Antibodies: Key to a Robust Lateral Flow Immunoassay, Lateral Flow Immunoass.* (2009) 1–16. https://doi.org/10.1007/978-1-59745-240-3_4.
- [31] R. Peltomaa, R. Barderas, E. Benito-Peña, M.C. Moreno-Bondi, Recombinant antibodies and their use for food immunoanalysis, *Anal. Bioanal. Chem.* 2021. (2021) 1–25. <https://doi.org/10.1007/S00216-021-03619-7>.
- [32] P. Büscher, Nucleic acid lateral flow tests for molecular diagnosis: an update, <Http://Dx.DoI.Org/10.1517/17530059.2011.542143>. 5 (2011) 85–89. <https://doi.org/10.1517/17530059.2011.542143>.
- [33] T.P.D. Andrade, D. V Lightner, Development of a method for the detection of infectious myonecrosis virus by reverse-transcription loop-mediated isothermal amplification and nucleic acid lateral flow hybrid assay, *J. Fish Dis.* 32 (2009) 911–924. <https://doi.org/10.1111/J.1365-2761.2009.01072.X>.

- [34] L. Jiang, R. Gu, X. Li, D. Mu, Simple and rapid detection *Aspergillus fumigatus* by loop-mediated isothermal amplification coupled with lateral flow biosensor assay, *J. Appl. Microbiol.* (2021). <https://doi.org/10.1111/JAM.15092>.
- [35] S. Pecchia, D. Da Lio, Development of a rapid PCR-Nucleic Acid Lateral Flow Immunoassay (PCR-NALFIA) based on rDNA IGS sequence analysis for the detection of *Macrophomina phaseolina* in soil, *J. Microbiol. Methods.* 151 (2018) 118–128. <https://doi.org/10.1016/J.MIMET.2018.06.010>.
- [36] M.B.T. Fogaça, A.K. Bhunia, L. Lopes-Luz, E.P.R.P. de Almeida, J.D.G. Vieira, S. Bühner-Sékula, Antibody- and nucleic acid-based lateral flow immunoassay for *Listeria monocytogenes* detection, *Anal. Bioanal. Chem.* 2021 41316. 413 (2021) 4161–4180. <https://doi.org/10.1007/S00216-021-03402-8>.
- [37] M. Jauset-Rubio, M.S. El-Shahawi, A.S. Bashammakh, A.O. Alyoubi, C.K. O'Sullivan, Advances in aptamers-based lateral flow assays, *TrAC Trends Anal. Chem.* 97 (2017) 385–398. <https://doi.org/10.1016/J.TRAC.2017.10.010>.
- [38] E. Zavyalova, A. Kopylov, DNA aptamer-based molecular nanoconstructions and nanodevices for diagnostics and therapy, *Nanostructures Eng. Cells, Tissues Organs From Des. to Appl.* (2018) 249–290. <https://doi.org/10.1016/B978-0-12-813665-2.00007-7>.
- [39] R. Reid, B. Chatterjee, S.J. Das, S. Ghosh, T.K. Sharma, Application of aptamers as molecular recognition elements in lateral flow assays, *Anal. Biochem.* 593 (2020) 113574. <https://doi.org/10.1016/J.AB.2020.113574>.
- [40] P. Chun, Colloidal Gold and Other Labels for Lateral Flow Immunoassays, *Lateral Flow Immunoass.* (2009) 1–19. https://doi.org/10.1007/978-1-59745-240-3_5.
- [41] K.M.M. Koczula, A. Gallotta, P. Estrela, K.M.M. Koczula, A. Gallotta, Lateral flow assays, *Essays Biochem.* 60 (2016) 111–120. <https://doi.org/10.1042/EBC20150012>.
- [42] X. Huang, Z.P. Aguilar, H. Xu, W. Lai, Y. Xiong, Membrane-based lateral flow immunochromatographic strip with nanoparticles as reporters for detection: A review, *Biosens. Bioelectron.* 75 (2015) 166–180. <https://doi.org/10.1016/j.bios.2015.08.032>.
- [43] L.C. Waters, R.W. Counts, A. Palausky, R.A. Jenkins, Colorimetric strip tests: a comparison of visual and reflectometric measurements for quantitative applications, *J. Hazard. Mater.* 43 (1995) 1–12. [https://doi.org/10.1016/0304-3894\(95\)00022-M](https://doi.org/10.1016/0304-3894(95)00022-M).
- [44] E. Calucho, C. Parolo, L. Rivas, R. Álvarez-Diduk, A. Merkoçi, Nanoparticle-based lateral flow assays, *Compr. Anal. Chem.* 89 (2020) 313–359. <https://doi.org/10.1016/BS.COAC.2020.04.011>.

- [45] V.T. Nguyen, S. Song, S. Park, C. Joo, Recent advances in high-sensitivity detection methods for paper-based lateral-flow assay, *Biosens. Bioelectron.* 152 (2020) 112015. <https://doi.org/10.1016/J.BIOS.2020.112015>.
- [46] K. Faulstich, R. Gruler, M. Eberhard, D. Lentzsch, K. Haberstroh, Handheld and Portable Reader Devices for Lateral Flow Immunoassays, *Lateral Flow Immunoass.* (2009) 1–27. https://doi.org/10.1007/978-1-59745-240-3_9.
- [47] F. Di Nardo, M. Chiarello, S. Cavalera, C. Baggiani, L. Anfossi, Ten Years of Lateral Flow Immunoassay Technique Applications: Trends, Challenges and Future Perspectives, *Sensors* 2021, Vol. 21, Page 5185. 21 (2021) 5185. <https://doi.org/10.3390/S21155185>.
- [48] J. Yang, K. Wang, H. Xu, W. Yan, Q. Jin, D. Cui, Detection platforms for point-of-care testing based on colorimetric, luminescent and magnetic assays: A review, *Talanta.* 202 (2019) 96–110. <https://doi.org/10.1016/J.TALANTA.2019.04.054>.
- [49] D. Quesada-González, A. Merkoçi, Nanoparticle-based lateral flow biosensors, *Biosens. Bioelectron.* 73 47–63. <http://dx.doi.org/10.1016/j.bios.2015.05.050> (accessed September 6, 2021).
- [50] S. Thobhani, S. Attree, R. Boyd, N. Kumarswami, J. Noble, M. Szymanski, R.A. Porter, Bioconjugation and characterisation of gold colloid-labelled proteins, *J. Immunol. Methods.* 356 (2010) 60–69. <https://doi.org/10.1016/J.JIM.2010.02.007>.
- [51] E.M. Linares, L.T. Kubota, J. Michaelis, S. Thalhammer, Enhancement of the detection limit for lateral flow immunoassays: Evaluation and comparison of bioconjugates, *J. Immunol. Methods.* 375 (2012) 264–270. <https://doi.org/10.1016/J.JIM.2011.11.003>.
- [52] D. Bera, L. Qian, T.-K. Tseng, P.H. Holloway, Quantum Dots and Their Multimodal Applications: A Review, *Mater.* 2010, Vol. 3, Pages 2260-2345. 3 (2010) 2260–2345. <https://doi.org/10.3390/MA3042260>.
- [53] A. Foubert, N. V. Beloglazova, A. Gordienko, M.D. Tessier, E. Drijvers, Z. Hens, S. De Saeger, Development of a Rainbow Lateral Flow Immunoassay for the Simultaneous Detection of Four Mycotoxins, *J. Agric. Food Chem.* 65 (2016) 7121–7130. <https://doi.org/10.1021/ACS.JAFC.6B04157>.
- [54] C.T. Matea, T. Mocan, F. Tabaran, T. Pop, O. Mosteanu, C. Puia, C. Iancu, L. Mocan, Quantum dots in imaging, drug delivery and sensor applications, *Int. J. Nanomedicine.* 12 (2017) 5421–5431. <https://doi.org/10.2147/IJN.S138624>.
- [55] S. Wilhelm, Perspectives for Upconverting Nanoparticles, *ACS Nano.* 11 (2017) 10644–10653. <https://doi.org/10.1021/ACSNANO.7B07120>.

- [56] R.S. Niedbala, H. Feindt, K. Kardos, T. Vail, J. Burton, B. Bielska, S. Li, D. Milunic, P. Bourdelle, R. Vallejo, Detection of Analytes by Immunoassay Using Up-Converting Phosphor Technology, *Anal. Biochem.* 293 (2001) 22–30. <https://doi.org/10.1006/ABIO.2001.5105>.
- [57] J. Langer, D.J. de Aberasturi, J. Aizpurua, R.A. Alvarez-Puebla, B. Augu  , J.J. Baumberg, G.C. Bazan, S.E.J. Bell, A. Boisen, A.G. Brolo, J. Choo, D. Cialla-May, V. Deckert, L. Fabris, K. Faulds, F.J.G. de Abajo, R. Goodacre, D. Graham, A.J. Haes, C.L. Haynes, C. Huck, T. Itoh, M. K  ll, J. Kneipp, N.A. Kotov, H. Kuang, E.C. Le Ru, H.K. Lee, J.-F. Li, X.Y. Ling, S.A. Maier, T. Mayerh  fer, M. Moskovits, K. Murakoshi, J.-M. Nam, S. Nie, Y. Ozaki, I. Pastoriza-Santos, J. Perez-Juste, J. Popp, A. Pucci, S. Reich, B. Ren, G.C. Schatz, T. Shegai, S. Schl  cker, L.-L. Tay, K.G. Thomas, Z.-Q. Tian, R.P. Van Duyne, T. Vo-Dinh, Y. Wang, K.A. Willets, C. Xu, H. Xu, Y. Xu, Y.S. Yamamoto, B. Zhao, L.M. Liz-Marz  n, Present and Future of Surface-Enhanced Raman Scattering, *ACS Nano*. 14 (2019) 28–117. <https://doi.org/10.1021/ACSNANO.9B04224>.
- [58] P. Mao, C. Liu, G. Favraud, Q. Chen, M. Han, A. Fratilocchi, S. Zhang, Broadband single molecule SERS detection designed by warped optical spaces, *Nat. Commun.* 2018 91. 9 (2018) 1–8. <https://doi.org/10.1038/s41467-018-07869-5>.
- [59] B. Khlebtsov, N. Khlebtsov, Surface-Enhanced Raman Scattering-Based Lateral-Flow Immunoassay, *Nanomater.* 2020, Vol. 10, Page 2228. 10 (2020) 2228. <https://doi.org/10.3390/NANO10112228>.
- [60] D. Calabria, M.M. Calabretta, M. Zangheri, E. Marchegiani, I. Trozzi, M. Guardigli, E. Michelini, F. Di Nardo, L. Anfossi, C. Baggiani, M. Mirasoli, Recent Advancements in Enzyme-Based Lateral Flow Immunoassays, *Sensors* 2021, Vol. 21, Page 3358. 21 (2021) 3358. <https://doi.org/10.3390/S21103358>.
- [61] A. Perju, N. Wongkaew, Integrating high-performing electrochemical transducers in lateral flow assay, *Anal. Bioanal. Chem.* 2021 41322. 413 (2021) 5535–5549. <https://doi.org/10.1007/S00216-021-03301-Y>.
- [62] Z. Huang, S. Hu, Y. Xiong, H. Wei, H. Xu, H. Duan, W. Lai, Application and development of superparamagnetic nanoparticles in sample pretreatment and immunochromatographic assay, 2019. <https://doi.org/10.1016/j.trac.2019.03.004> (accessed March 24, 2021).
- [63] Y. Liu, L. Zhan, Z. Qin, J. Sackrison, J.C. Bischof, Ultrasensitive and Highly Specific Lateral Flow Assays for Point-of-Care Diagnosis, *ACS Nano*. 15 (2021) 3593–3611. <https://doi.org/10.1021/ACSNANO.0C10035>.
- [64] W. Ren, S.I. Mohammed, S. Wereley, J. Irudayaraj, Magnetic Focus Lateral Flow Sensor for Detection of Cervical Cancer Biomarkers,

- Anal. Chem. 91 (2019) 2876–2884. <https://pubs.acs.org/doi/full/10.1021/acs.analchem.8b04848> (accessed September 16, 2021).
- [65] A. Moyano, M. Salvador, J.C. Martínez-García, V. Socoliuc, L. Vékás, D. Peddis, M.A. Alvarez, M. Fernández, M. Rivas, M.C. Blanco-López, Magnetic immunochromatographic test for histamine detection in wine, *Anal. Bioanal. Chem.* 2019 41125. 411 (2019) 6615–6624. <https://doi.org/10.1007/S00216-019-02031-6>.
- [66] H. Wei, Y. Hu, J. Wang, X. Gao, X. Qian, M. Tang, Superparamagnetic iron oxide nanoparticles: Cytotoxicity, metabolism, and cellular behavior in biomedicine applications, *Int. J. Nanomedicine.* 16 (2021) 6097–6113. <https://doi.org/10.2147/IJN.S321984>.
- [67] T.K. Jain, M.K. Reddy, M.A. Morales, D.L. Leslie-Pelecky, V. Labhasetwar, Biodistribution, Clearance, and Biocompatibility of Iron Oxide Magnetic Nanoparticles in Rats, *Mol. Pharm.* 5 (2008) 316–327. <https://doi.org/10.1021/MP7001285>.
- [68] C.P. Bean, J.D. Livingston, Superparamagnetism, *J. Appl. Phys.* 30 (1959) S120–S129. <https://doi.org/10.1063/1.2185850>.
- [69] V. Schaller, G. Wahnström, A. Sanz-Velasco, P. Enoksson, C. Johansson, Monte Carlo simulation of magnetic multi-core nanoparticles, *J. Magn. Magn. Mater.* 321 (2009) 1400–1403. <https://doi.org/10.1016/J.JMMM.2009.02.047>.
- [70] M. Knobel, W.C. Nunes, L.M. Socolovsky, E. De Biasi, J.M. Vargas, J.C. Denardin, Superparamagnetism and other magnetic features in granular materials: A review on ideal and real systems, *J. Nanosci. Nanotechnol.* 8 (2008) 2836–2857. <https://doi.org/10.1166/jnn.2008.15348>.
- [71] R.W. Chantrell, J. Popplewell, S.W. Charles, Measurements of particle size distribution parameters in ferrofluids, *IEEE Trans. Magn.* 14 (1978) 975–977. <https://doi.org/10.1109/TMAG.1978.1059918>.
- [72] D.X. Chen, A. Sanchez, E. Taboada, A. Roig, N. Sun, H.C. Gu, Size determination of superparamagnetic nanoparticles from magnetization curve, *J. Appl. Phys.* 105 (2009) 083924. <https://doi.org/10.1063/1.3117512>.
- [73] M. Unni, A.M. Uhl, S. Savliwala, B.H. Savitzky, R. Dhavalikar, N. Garraud, D.P. Arnold, L.F. Kourkoutis, J.S. Andrew, C. Rinaldi, Thermal Decomposition Synthesis of Iron Oxide Nanoparticles with Diminished Magnetic Dead Layer by Controlled Addition of Oxygen, *ACS Nano.* 11 (2017) 2284–2303. <https://pubs.acs.org/doi/abs/10.1021/acsnano.7b00609> (accessed March 4, 2021).

- [74] R.D. Zysler, E. De Biasi, C.A. Ramos, D. Fiorani, H. Romero, Surface and Interparticle Effects in Amorphous Magnetic Nanoparticles, in: Springer, Boston, MA, 2005: pp. 239–261. https://doi.org/10.1007/0-387-26018-8_8.
- [75] E.C. Stoner, E.P. Wohlfarth, A mechanism of magnetic hysteresis in heterogeneous alloys, *Philos. Trans. R. Soc. London. Ser. A, Math. Phys. Sci.* 240 (1948) 599–642. <https://doi.org/10.1098/RSTA.1948.0007>.
- [76] X. Batlle, A. Labarta, Finite-size effects in fine particles: magnetic and transport properties, *J. Phys. D. Appl. Phys.* 35 (2002) R15. <https://doi.org/10.1088/0022-3727/35/6/201>.
- [77] D. Fiorani, D. Peddis, Understanding dynamics of interacting magnetic nanoparticles: from the weak interaction regime to the collective superspin glass state, *J. Phys. Conf. Ser.* 521 (2014) 012006. <https://doi.org/10.1088/1742-6596/521/1/012006>.
- [78] K.L. Livesey, S. Ruta, N.R. Anderson, D. Baldomir, R.W. Chantrell, D. Serantes, Beyond the blocking model to fit nanoparticle ZFC/FC magnetisation curves, *Sci. Reports* 2018 81. 8 (2018) 1–9. <https://doi.org/10.1038/s41598-018-29501-8>.
- [79] G.T. Landi, F.R. Arantes, D.R. Cornejo, A.F. Bakuzis, I. Andreu, E. Natividad, AC susceptibility as a tool to probe the dipolar interaction in magnetic nanoparticles, *J. Magn. Magn. Mater.* 421 (2017) 138–151. <https://doi.org/10.1016/j.jmmm.2016.08.011>.
- [80] A.C. Bohorquez, C. Rinaldi, In situ evaluation of nanoparticle-protein interactions by dynamic magnetic susceptibility measurements, *Part. Part. Syst. Charact.* 31 (2014) 561–570. <https://doi.org/10.1002/ppsc.201300296>.
- [81] H. Remmer, E. Roeben, A.M. Schmidt, M. Schilling, F. Ludwig, Dynamics of magnetic nanoparticles in viscoelastic media, *J. Magn. Magn. Mater.* 427 (2017) 331–335. <https://doi.org/10.1016/J.JMMM.2016.10.075>.
- [82] S.A. Majetich, M. Sachan, Magnetostatic interactions in magnetic nanoparticle assemblies: Energy, time and length scales, *J. Phys. D. Appl. Phys.* 39 (2006) R407. <https://doi.org/10.1088/0022-3727/39/21/R02>.
- [83] L. Gutiérrez, L. De La Cueva, M. Moros, E. Mazarío, S. De Bernardo, J.M. De La Fuente, M.P. Morales, G. Salas, Aggregation effects on the magnetic properties of iron oxide colloids, *Nanotechnology*. 30 (2019) 112001. <https://doi.org/10.1088/1361-6528/aafbff>.
- [84] D. Peddis, P.E. Jönsson, S. Laureti, G. Varvaro, Magnetic interactions: A tool to modify the magnetic properties of materials based on nanoparticles, in: *Front. Nanosci.*, Elsevier, 2014: pp. 129–188. <https://doi.org/10.1016/B978-0-08-098353-0.00004-X>.

- [85] S. Mørup, M.F. Hansen, C. Frandsen, Magnetic nanoparticles, in: *Compr. Nanosci. Nanotechnol.*, Academic Press, 2019: pp. 89–140. <https://doi.org/10.1016/B978-0-12-803581-8.11338-4>.
- [86] F.G. Silva, J. Depeyrot, Y.L. Raikher, V.I. Stepanov, I.S. Poperechny, R. Aquino, G. Ballon, J. Geshev, E. Dubois, R. Perzynski, Exchange-bias and magnetic anisotropy fields in core-shell ferrite nanoparticles, *Sci. Reports* 2021 111. 11 (2021) 1–10. <https://doi.org/10.1038/s41598-021-84843-0>.
- [87] J.A. De Toro, M. Vasilakaki, S.S. Lee, M.S. Andersson, P.S. Normile, N. Yaacoub, P. Murray, E.H. Sánchez, P. Muñoz, D. Peddis, R. Mathieu, K. Liu, J. Geshev, K.N. Trohidou, J. Nogués, Remanence plots as a probe of spin disorder in magnetic nanoparticles, *Chem. Mater.* 29 (2017) 8258–8268. <https://doi.org/10.1021/acs.chemmater.7b02522>.
- [88] R. Cicheler, A. Harres, K.D. Sossmeier, J.E. Schmidt, J. Geshev, Magnetic interactions in exchange-coupled yet unbiased IrMn/NiCu bilayers, *J. Phys. Condens. Matter.* 25 (2013) 426001. <https://doi.org/10.1088/0953-8984/25/42/426001>.
- [89] E.P. Wohlfarth, Relations between different modes of acquisition of the remanent magnetization of ferromagnetic particles, *American Institute of Physics AIP*, n.d. <https://doi.org/10.1063/1.1723232>.
- [90] P.E. Kelly, K. O'Grady, P.L. Mayo, R.W. Chantrell, Switching mechanisms in cobalt-phosphorus thin films, *IEEE Trans. Magn.* 25 (1989) 3881–3883. <https://doi.org/10.1109/20.42466>.
- [91] S. Laureti, G. Varvaro, A.M. Testa, D. Fiorani, E. Agostinelli, G. Piccaluga, A. Musinu, A. Ardu, D. Peddis, Magnetic interactions in silica coated nanoporous assemblies of CoFe₂O₄ nanoparticles with cubic magnetic anisotropy, *Nanotechnology.* 21 (2010) 315701. <https://doi.org/10.1088/0957-4484/21/31/315701>.
- [92] D. Bobo, K.J. Robinson, J. Islam, K.J. Thurecht, S.R. Corrie, Nanoparticle-Based Medicines: A Review of FDA-Approved Materials and Clinical Trials to Date, 33 (2016) 2373–2387. <https://link.springer.com/article/10.1007/s11095-016-1958-5> (accessed September 20, 2021).
- [93] A.G. Niculescu, C. Chircov, A.M. Grumezescu, Magnetite nanoparticles: Synthesis methods – A comparative review, *Methods.* (2021). <https://doi.org/10.1016/J.YMETH.2021.04.018>.
- [94] T.D. Schladt, K. Schneider, H. Schild, W. Tremel, Synthesis and bio-functionalization of magnetic nanoparticles for medical diagnosis and treatment, *Dalt. Trans.* 40 (2011) 6315–6343. <https://doi.org/10.1039/c0dt00689k>.
- [95] V.K. LaMer, R.H. Dinegar, Theory, Production and Mechanism of Formation of Monodispersed Hydrosols, *J. Am. Chem. Soc.* 72 (2002) 4847–4854. <https://doi.org/10.1021/JA01167A001>.

- [96] P. Tartaj, S. Veintemillas-Verdaguer, T. Gonzalez-Carreño, C.J. Serna, Preparation of magnetic nanoparticles for applications in biomedicine, in: *Magn. Nanoparticles Biosensing Med.*, Cambridge University Press, 2019: pp. 52–67. <https://doi.org/10.1017/9781139381222.003>.
- [97] R. Massart, Preparation of Aqueous Magnetic Liquids in Alkaline and Acidic Media, *IEEE Trans. Magn.* 17 (1981) 1247–1248. <https://doi.org/10.1109/TMAG.1981.1061188>.
- [98] S.S. Staniland, A. Rawlings, J. Bramble, J. Tolosa, O. Wilson, J.C. García-Martínez, C. Binns, Novel methods for the synthesis of magnetic nanoparticles, in: *Front. Nanosci.*, Elsevier Ltd, 2014: pp. 85–128. <https://doi.org/10.1016/B978-0-08-098353-0.00003-8>.
- [99] N. Bhattarai, S. Khanal, J.J. Velazquez-Salazar, M. Jose-Yacamán, Advanced electron microscopy in the study of multimetallic nanoparticles, in: *Adv. Transm. Electron Microsc. Appl. to Nanomater.*, Springer, Cham, 2015: pp. 59–92. https://doi.org/10.1007/978-3-319-15177-9_3.
- [100] B. Michen, C. Geers, D. Vanhecke, C. Endes, B. Rothen-Rutishauser, S. Balog, A. Petri-Fink, Avoiding drying-artifacts in transmission electron microscopy: Characterizing the size and colloidal state of nanoparticles, *Sci. Reports* 2015 51. 5 (2015) 1–7. <https://doi.org/10.1038/srep09793>.
- [101] P. Lemal, C. Geers, B. Rothen-Rutishauser, M. Lattuada, A. Petri-Fink, Measuring the heating power of magnetic nanoparticles: an overview of currently used methods, *Mater. Today Proc.* 4 (2017) S107–S117. <https://doi.org/10.1016/J.MATPR.2017.09.175>.
- [102] P.C. Lin, S. Lin, P.C. Wang, R. Sridhar, Techniques for physicochemical characterization of nanomaterials, *Biotechnol. Adv.* 32 (2014) 711–726. <https://doi.org/10.1016/j.biotechadv.2013.11.006>.
- [103] S.P. Schwaminger, D. Bauer, P. Fraga-García, F.E. Wagner, S. Berensmeier, Oxidation of magnetite nanoparticles: impact on surface and crystal properties, *CrystEngComm.* 19 (2017) 246–255. <https://doi.org/10.1039/C6CE02421A>.
- [104] U. Holzwarth, N. Gibson, The Scherrer equation versus the “Debye-Scherrer equation,” *Nat. Nanotechnol.* 2011 69. 6 (2011) 534–534. <https://doi.org/10.1038/nnano.2011.145>.
- [105] J. Stetefeld, S.A. McKenna, T.R. Patel, Dynamic light scattering: a practical guide and applications in biomedical sciences, *Biophys. Rev.* 8 (2016) 409–427. <https://doi.org/10.1007/S12551-016-0218-6/TABLES/3>.
- [106] M. Jones, Dynamic light scattering, (n.d.). https://en.wikipedia.org/wiki/Dynamic_light_scattering (accessed October 15, 2021).

- [107] I. V Gmshinski, S.A. Khotimchenko, V.O. Popov, B.B. Dzantiev, A. V Zherdev, V.F. Demin, Y.P. Buzulukov, *Nanomaterials and nanotechnologies: methods of analysis and control*, *Russ. Chem. Rev.* 82 (2013) 48–76. <https://doi.org/10.1070/rc2013v082n01abeh004329>.
- [108] R.K. Dumas, T. Hogan, *Recent Advances in SQUID Magnetometry*, *Magn. Meas. Tech. Mater. Character.* (2021) 39–62. https://doi.org/10.1007/978-3-030-70443-8_3.
- [109] R0oland, VSM, Wikimedia Commons. (n.d.). https://commons.wikimedia.org/wiki/File:VSM_en.svg (accessed October 13, 2021).
- [110] D. Murzin, D.J. Mapps, K. Levada, V. Belyaev, A. Omelyanchik, L. Panina, V. Rodionova, *Ultrasensitive Magnetic Field Sensors for Biomedical Applications*, *Sensors* 2020, Vol. 20, Page 1569. 20 (2020) 1569. <https://doi.org/10.3390/S20061569>.
- [111] J.-W. Liao, H.-W. Zhang, C.-H. Lai, *Magnetic Nanomaterials for Data Storage*, *Magn. Nanomater. - Fundam. Synth. Appl.* (2017) 439–472. <https://doi.org/10.1002/9783527803255.CH14>.
- [112] Q. Zhang, E. Uchaker, S.L. Candelaria, G. Cao, *Nanomaterials for energy conversion and storage*, *Chem. Soc. Rev.* 42 (2013) 3127–3171. <https://doi.org/10.1039/c3cs00009e>.
- [113] T. Wang, S. Ai, Y. Zhou, Z. Luo, C. Dai, Y. Yang, J. Zhang, H. Huang, S. Luo, L. Luo, *Adsorption of agricultural wastewater contaminated with antibiotics, pesticides and toxic metals by functionalized magnetic nanoparticles*, *J. Environ. Chem. Eng.* 6 (2018) 6468–6478. <https://doi.org/10.1016/j.jece.2018.10.014>.
- [114] M.A. Mohamed, A.E.M.A. Mohamed, K.A. Abd-Elsalam, *Magnetic Nanoparticles in Plant Protection: Promises and Risks*, in: *Nanotechnol. Life Sci.*, Springer, Cham, 2019: pp. 225–246. https://doi.org/10.1007/978-3-030-16439-3_12.
- [115] F. Mustafa, S. Andreescu, *Nanotechnology-based approaches for food sensing and packaging applications*, *RSC Adv.* 10 (2020) 19309–19336. <https://doi.org/10.1039/D0RA01084G>.
- [116] A. Ríos, M. Zougagh, M. Bouri, *Magnetic (nano)materials as an useful tool for sample preparation in analytical methods. A review*, *Anal. Methods.* 5 (2013) 4558–4573. <https://doi.org/10.1039/c3ay40306h>.
- [117] S.P. Schwaminger, P. Fraga-García, M. Eigenfeld, T.M. Becker, S. Berensmeier, *Magnetic Separation in Bioprocessing Beyond the Analytical Scale: From Biotechnology to the Food Industry*, *Front. Bioeng. Biotechnol.* 0 (2019) 233. <https://doi.org/10.3389/FBIOE.2019.00233>.
- [118] D. Baragaño, J. Alonso, J.R. Gallego, M.C. Lobo, M. Gil-Díaz,

- Magnetite nanoparticles for the remediation of soils co-contaminated with As and PAHs, *Chem. Eng. J.* 399 (2020) 125809. <https://doi.org/10.1016/J.CEJ.2020.125809>.
- [119] J.D. Navratil, M.T. Shing Tsair, Magnetic separation of iron and heavy metals from water, *Water Sci. Technol.* 47 (2003) 29–32. <https://doi.org/10.2166/WST.2003.0009>.
- [120] O. V. Kharissova, H.V.R. Dias, B.I. Kharisov, Magnetic adsorbents based on micro- and nano-structured materials, *RSC Adv.* 5 (2014) 6695–6719. <https://doi.org/10.1039/C4RA11423J>.
- [121] R.A. Bohara, N.D. Thorat, S.H. Pawar, Role of functionalization: strategies to explore potential nano-bio applications of magnetic nanoparticles, *RSC Adv.* 6 (2016) 43989–44012. <https://doi.org/10.1039/C6RA02129H>.
- [122] K. Wu, D. Su, J. Liu, R. Saha, J.-P. Wang, Magnetic nanoparticles in nanomedicine: a review of recent advances, *Nanotechnology.* 30 (2019) 502003. <https://doi.org/10.1088/1361-6528/AB4241>.
- [123] A. Sandhu, P. Southern, S.C. de Freitas, S. Knudde, F.A. Cardoso, P.P. Freitas, G. V. Kurlyandskaya, Sensing Magnetic Nanoparticles, in: *Magn. Nanoparticles Biosensing Med.*, Cambridge University Press, 2019: pp. 172–227. <https://doi.org/10.1017/9781139381222.007>.
- [124] T.A.P. Rocha-Santos, Sensors and biosensors based on magnetic nanoparticles, *TrAC Trends Anal. Chem.* 62 (2014) 28–36. <https://doi.org/10.1016/J.TRAC.2014.06.016>.
- [125] D. Issadore, Y.I. Park, H. Shao, C. Min, K. Lee, M. Liong, R. Weissleder, H. Lee, Magnetic sensing technology for molecular analyses, *Lab Chip.* 14 (2014) 2385–2397. <https://pubs.rsc.org/en/content/articlehtml/2014/lc/c4lc00314d> (accessed March 4, 2021).
- [126] D. Alcantara, S. Lopez, M.L. García-Martin, D. Pozo, Iron oxide nanoparticles as magnetic relaxation switching (MRSw) sensors: Current applications in nanomedicine, *Nanomedicine Nanotechnology, Biol. Med.* 12 (2016) 1253–1262. <https://doi.org/10.1016/j.nano.2016.01.005>.
- [127] Y. Xianyu, Q. Wang, Y. Chen, Magnetic particles-enabled biosensors for point-of-care testing, *TrAC - Trends Anal. Chem.* 106 (2018) 213–224. <https://doi.org/10.1016/j.trac.2018.07.010>.
- [128] J. Zhao, Z. Wang, Y. Chen, D. Peng, Y. Xianyu, Horseradish peroxidase-catalyzed formation of polydopamine for ultra-sensitive magnetic relaxation sensing of aflatoxin B1, *J. Hazard. Mater.* 419 (2021) 126403. <https://doi.org/10.1016/J.JHAZMAT.2021.126403>.
- [129] C. Kaittanis, S.A. Naser, J.M. Perez, One-step, nanoparticle-

- mediated bacterial detection with magnetic relaxation, *Nano Lett.* 7 (2007) 380–383. <https://doi.org/10.1021/nl062553z>.
- [130] K. Enpuku, Y. Tsujita, K. Nakamura, T. Sasayama, T. Yoshida, Biosensing utilizing magnetic markers and superconducting quantum interference devices, *Supercond. Sci. Technol.* 30 (2017) 053002. <https://doi.org/10.1088/1361-6668/aa5fce>.
- [131] Y.-T. Chen, A.G. Kolhatkar, O. Zenasni, S. Xu, T.R. Lee, Biosensing Using Magnetic Particle Detection Techniques, *Sensors* 2017, Vol. 17, Page 2300. 17 (2017) 2300. <https://doi.org/10.3390/S17102300>.
- [132] A.K. Bhuiya, M. Asai, H. Watanabe, T. Hirata, Y. Higuchi, T. Yoshida, K. Enpuku, Characterization of magnetic markers and sensors for liquid-phase immunoassays using brownian relaxation, *IEEE Trans. Magn.* 48 (2012) 2838–2841. <https://doi.org/10.1109/TMAG.2012.2194137>.
- [133] N.L. Adolphi, K.S. Butler, D.M. Lovato, T.E. Tessier, J.E. Trujillo, H.J. Hathaway, D.L. Fegan, T.C. Monson, T.E. Stevens, D.L. Huber, J. Ramu, M.L. Milne, S.A. Altobelli, H.C. Bryant, R.S. Larson, E.R. Flynn, Imaging of Her2-targeted magnetic nanoparticles for breast cancer detection: comparison of SQUID-detected magnetic relaxometry and MRI, *Contrast Media Mol. Imaging.* 7 (2012) 308–319. <https://doi.org/10.1002/CMMI.499>.
- [134] L.M. Wang, T.W. Yang, C.Y. Wang, D. Shen, J.M. Chen, K.L. Chen, S.H. Liao, Magnetic Nanoparticle Images and Assaying Biomarkers via the Magnetic Relaxation of Biofunctionalized Nanoparticles Associated with Biotargets, *IEEE Sens. J.* 19 (2019) 9004–9009. <https://doi.org/10.1109/JSEN.2018.2884893>.
- [135] B. Cao, K. Wang, H. Xu, Q. Qin, J. Yang, W. Zheng, Q. Jin, D. Cui, Development of magnetic sensor technologies for point-of-care testing: Fundamentals, methodologies and applications, *Sensors Actuators A Phys.* 312 (2020) 112130. <https://doi.org/10.1016/J.SNA.2020.112130>.
- [136] A. Rajan, N.K. Sahu, Review on magnetic nanoparticle-mediated hyperthermia for cancer therapy, *J. Nanoparticle Res.* 2020 2211. 22 (2020) 1–25. <https://doi.org/10.1007/S11051-020-05045-9>.
- [137] D. Chang, M. Lim, J.A.C.M. Goos, R. Qiao, Y.Y. Ng, F.M. Mansfeld, M. Jackson, T.P. Davis, M. Kavallaris, Biologically Targeted Magnetic Hyperthermia: Potential and Limitations, *Front. Pharmacol.* 0 (2018) 831. <https://doi.org/10.3389/FPHAR.2018.00831>.
- [138] E.A. Périgo, G. Hemery, O. Sandre, D. Ortega, E. Garaio, F. Plazaola, F.J. Teran, Fundamentals and advances in magnetic hyperthermia, *Appl. Phys. Rev.* 2 (2015) 041302. <https://doi.org/10.1063/1.4935688>.

- [139] D. Ortega, Q.A. Pankhurst, Magnetic hyperthermia, in: 2012: pp. 60–88. <https://doi.org/10.1039/9781849734844-00060>.
- [140] I. Andreu, E. Natividad, Accuracy of available methods for quantifying the heat power generation of nanoparticles for magnetic hyperthermia, <Http://Dx.Doi.Org/10.3109/02656736.2013.826825>. 29 (2013) 739–751. <https://doi.org/10.3109/02656736.2013.826825>.
- [141] I. Conde-Leboran, D. Baldomir, C. Martinez-Boubeta, O. Chubykalo-Fesenko, M. del P. Morales, G. Salas, D. Cabrera, J. Camarero, F.J. Teran, D. Serantes, A Single Picture Explains Diversity of Hyperthermia Response of Magnetic Nanoparticles, *J. Phys. Chem. C.* 119 (2015) 15698–15706. <https://doi.org/10.1021/ACS.JPCC.5B02555>.
- [142] H. Gavilán, S.K. Avugadda, T. Fernández-Cabada, N. Soni, M. Cassani, B.T. Mai, R. Chantrell, T. Pellegrino, Magnetic nanoparticles and clusters for magnetic hyperthermia: optimizing their heat performance and developing combinatorial therapies to tackle cancer, *Chem. Soc. Rev.* 50 (2021) 11614–11667. <https://doi.org/10.1039/d1cs00427a>.
- [143] W.J. Atkinson, I.A. Brezovich, D.P. Chakraborty, Usable Frequencies in Hyperthermia with Thermal Seeds, *IEEE Trans. Biomed. Eng.* BME-31 (1984) 70–75. <https://doi.org/10.1109/TBME.1984.325372>.
- [144] G. Salas, S. Veintemillas-Verdaguer, M. del P. Morales, Relationship between physico-chemical properties of magnetic fluids and their heating capacity, <Http://Dx.Doi.Org/10.3109/02656736.2013.826824>. 29 (2013) 768–776. <https://doi.org/10.3109/02656736.2013.826824>.
- [145] R. Di Corato, A. Espinosa, L. Lartigue, M. Tharaud, S. Chat, T. Pellegrino, C. Ménager, F. Gazeau, C. Wilhelm, Magnetic hyperthermia efficiency in the cellular environment for different nanoparticle designs, *Biomaterials.* 35 (2014) 6400–6411. <https://doi.org/10.1016/J.BIOMATERIALS.2014.04.036>.
- [146] S. Caspani, R. Magalhães, J.P. Araújo, C.T. Sousa, Magnetic Nanomaterials as Contrast Agents for MRI, *Mater.* 2020, Vol. 13, Page 2586. 13 (2020) 2586. <https://doi.org/10.3390/MA13112586>.
- [147] N. Lee, T. Hyeon, Designed synthesis of uniformly sized iron oxide nanoparticles for efficient magnetic resonance imaging contrast agents, *Chem. Soc. Rev.* 41 (2012) 2575–2589. <https://doi.org/10.1039/c1cs15248c>.
- [148] J. Estelrich, M.J. Sánchez-Martín, M.A. Busquets, Nanoparticles in magnetic resonance imaging: from simple to dual contrast agents, *Int. J. Nanomedicine.* 10 (2015) 1727–1741.

<https://doi.org/10.2147/IJN.S76501>.

- [149] M. Rogosnitzky, S. Branch, Gadolinium-based contrast agent toxicity: a review of known and proposed mechanisms, *BioMetals*. 29 (2016) 365–376. <https://doi.org/10.1007/S10534-016-9931-7/TABLES/2>.
- [150] Q.A. Pankhurst, N.T.K. Thanh, S.K. Jones, J. Dobson, Progress in applications of magnetic nanoparticles in biomedicine, *J. Phys. D. Appl. Phys.* 42 (2009) 224001. <https://doi.org/10.1088/0022-3727/42/22/224001>.
- [151] Z. Zhou, R. Bai, J. Munasinghe, Z. Shen, L. Nie, X. Chen, T1–T2 Dual-Modal Magnetic Resonance Imaging: From Molecular Basis to Contrast Agents, *ACS Nano*. 11 (2017) 5227–5232. <https://doi.org/10.1021/ACSNANO.7B03075>.
- [152] H. Wei, O.T. Bruns, M.G. Kaul, E.C. Hansen, M. Barch, A. Wiśniowska, O. Chen, Y. Chen, N. Li, S. Okada, J.M. Cordero, M. Heine, C.T. Farrar, D.M. Montana, G. Adam, H. Ittrich, A. Jasanoff, P. Nielsen, M.G. Bawendi, Exceedingly small iron oxide nanoparticles as positive MRI contrast agents, *Proc. Natl. Acad. Sci.* 114 (2017) 2325–2330. <https://doi.org/10.1073/PNAS.1620145114>.
- [153] T.-H. Shin, Y. Choi, S. Kim, J. Cheon, Recent advances in magnetic nanoparticle-based multi-modal imaging, *Chem. Soc. Rev.* 44 (2015) 4501–4516. <https://doi.org/10.1039/C4CS00345D>.
- [154] Wahajuddin, S. Arora, Superparamagnetic iron oxide nanoparticles: magnetic nanoplatforms as drug carriers, *Int. J. Nanomedicine*. 7 (2012) 3445–3471. <https://doi.org/10.2147/IJN.S30320>.
- [155] B. Gleich, J. Weizenecker, Tomographic imaging using the nonlinear response of magnetic particles, *Nat.* 2005 4357046. 435 (2005) 1214–1217. <https://doi.org/10.1038/nature03808>.
- [156] E.U. Saritas, P.W. Goodwill, L.R. Croft, J.J. Konkle, K. Lu, B. Zheng, S.M. Conolly, Magnetic particle imaging (MPI) for NMR and MRI researchers, *J. Magn. Reson.* 229 (2013) 116–126. <https://doi.org/10.1016/j.jmr.2012.11.029>.
- [157] L.M. Bauer, S.F. Situ, M.A. Griswold, A.C.S. Samia, Magnetic Particle Imaging Tracers: State-of-the-Art and Future Directions, *J. Phys. Chem. Lett.* 6 (2015) 2509–2517. <https://doi.org/10.1021/ACS.JPCLETT.5B00610>.
- [158] L.C. Wu, Y. Zhang, G. Steinberg, H. Qu, S. Huang, M. Cheng, T. Bliss, F. Du, J. Rao, G. Song, L. Pisani, T. Doyle, S. Conolly, K. Krishnan, G. Grant, M. Wintermark, A Review of Magnetic Particle Imaging and Perspectives on Neuroimaging, *Am. J. Neuroradiol.* 40 (2019) 206–212. <https://doi.org/10.3174/AJNR.A5896>.

- [159] H. Kratz, M. Taupitz, A.A. de Schellenberger, O. Kosch, D. Eberbeck, S. Wagner, L. Trahms, B. Hamm, J. Schnorr, Novel magnetic multicore nanoparticles designed for MPI and other biomedical applications: From synthesis to first in vivo studies, *PLoS One.* 13 (2018) e0190214. <https://doi.org/10.1371/JOURNAL.PONE.0190214>.
- [160] B. Gleich, J. Borgert, J. Weizenecker, Magnetic Particle Imaging (MPI), *Medicamundi.* 50 (2018) 115–133. <https://doi.org/10.1016/B978-0-08-101925-2.00004-8>.
- [161] L. Yan, X. Chen, Nanomaterials for Drug Delivery, in: *Nanocrystalline Mater. Their Synth. Relationships Appl.*, Elsevier, 2013: pp. 221–268. <https://doi.org/10.1016/B978-0-12-407796-6.00007-5>.
- [162] R. Singh, J.W. Lillard, Nanoparticle-based targeted drug delivery, *Exp. Mol. Pathol.* 86 (2009) 215–223. <https://doi.org/10.1016/j.yexmp.2008.12.004>.
- [163] S. Kralj, T. Potrc, P. Kocbek, S. Marchesan, D. Makovec, Design and Fabrication of Magnetically Responsive Nanocarriers for Drug Delivery, *Curr. Med. Chem.* 24 (2016) 454–469. <https://doi.org/10.2174/0929867323666160813211736>.
- [164] M.J. Mitchell, M.M. Billingsley, R.M. Haley, M.E. Wechsler, N.A. Peppas, R. Langer, Engineering precision nanoparticles for drug delivery, *Nat. Rev. Drug Discov.* 20 (2020) 101–124. <https://doi.org/10.1038/s41573-020-0090-8>.
- [165] K.M. El-Say, H.S. El-Sawy, Polymeric nanoparticles: Promising platform for drug delivery, *Int. J. Pharm.* 528 (2017) 675–691. <https://doi.org/10.1016/J.IJPHARM.2017.06.052>.
- [166] G. Béalle, L. Lartigue, C. Wilhelm, J. Ravaux, F. Gazeau, R. Podor, D. Carrière, C. Ménager, Surface decoration of cationic vesicles with superparamagnetic iron oxide nanoparticles: a model system for triggered release under moderate temperature conditions, *Phys. Chem. Chem. Phys.* 16 (2014) 4077–4081. <https://doi.org/10.1039/C3CP54484B>.
- [167] P.M. Price, W.E. Mahmoud, A.A. Al-Ghamdi, L.M. Bronstein, Magnetic Drug Delivery: Where the Field Is Going, *Front. Chem.* 0 (2018) 619. <https://doi.org/10.3389/FCHEM.2018.00619>.
- [168] E. Amstad, M. Textor, E. Reimhult, Stabilization and functionalization of iron oxide nanoparticles for biomedical applications, *Nanoscale.* 3 (2011) 2819–2843. <https://doi.org/10.1039/C1NR10173K>.
- [169] J. Salafranca, J. Gazquez, N. Pérez, A. Labarta, S.T. Pantelides, S.J. Pennycook, X. Batlle, M. Varela, Surfactant organic molecules restore magnetism in metal-oxide nanoparticle surfaces, *Nano Lett.* 12 (2012) 2499–2503. <https://doi.org/10.1021/nl300665z>.

- [170] S. Moraes Silva, R. Tavallaie, L. Sandiford, R.D. Tilley, J.J. Gooding, Gold coated magnetic nanoparticles: from preparation to surface modification for analytical and biomedical applications, *Chem. Commun.* 52 (2016) 7528–7540. <https://doi.org/10.1039/C6CC03225G>.
- [171] M.E. Fortes Brollo, P. Hernández Flores, L. Gutiérrez, C. Johansson, D.F. Barber, M.D.P. Morales, Magnetic properties of nanoparticles as a function of their spatial distribution on liposomes and cells, *Phys. Chem. Chem. Phys.* 20 (2018) 17829–17838. <https://doi.org/10.1039/C8CP03016B>.
- [172] Z. Chen, C. Wu, Z. Zhang, W. Wu, X. Wang, Z. Yu, Synthesis, functionalization, and nanomedical applications of functional magnetic nanoparticles, *Chinese Chem. Lett.* 29 (2018) 1601–1608. <https://doi.org/10.1016/J.CCLET.2018.08.007>.
- [173] R.C. Popescu, E. Andronescu, B.S. Vasile, Recent advances in magnetite nanoparticle functionalization for nanomedicine, *Nanomaterials.* 9 (2019) 1791. <https://doi.org/10.3390/nano9121791>.
- [174] A. Cernat, A. Florea, I. Rus, F. Truta, A.-M. Dragan, C. Cristea, M. Tertis, Applications of magnetic hybrid nanomaterials in Biomedicine, *Biopolym. Nanomater.* (2021) 639–675. <https://doi.org/10.1016/B978-0-12-824364-0.00014-9>.
- [175] M. Vasilakaki, N. Ntallis, N. Yaacoub, G. Muscas, D. Peddis, K.N. Trohidou, Optimising the magnetic performance of Co ferrite nanoparticles via organic ligand capping, *Nanoscale.* 10 (2018) 21244–21253. <https://doi.org/10.1039/C8NR04566F>.
- [176] M. Barrow, A. Taylor, P. Murray, M.J. Rosseinsky, D.J. Adams, Design considerations for the synthesis of polymer coated iron oxide nanoparticles for stem cell labelling and tracking using MRI, *Chem. Soc. Rev.* 44 (2015) 6733–6748. <https://doi.org/10.1039/c5cs00331h>.
- [177] S. Laurent, D. Forge, M. Port, A. Roch, C. Robic, L. Vander Elst, R.N. Muller, Magnetic Iron Oxide Nanoparticles: Synthesis, Stabilization, Vectorization, Physicochemical Characterizations, and Biological Applications, *Chem. Rev.* 108 (2008) 2064–2110. <https://doi.org/10.1021/CR068445E>.
- [178] A. Friedman, S. Claypool, R. Liu, The Smart Targeting of Nanoparticles, *Curr. Pharm. Des.* 19 (2013) 6315–6329. <https://doi.org/10.2174/13816128113199990375>.
- [179] N.G. Welch, J.A. Scoble, B.W. Muir, P.J. Pigram, Orientation and characterization of immobilized antibodies for improved immunoassays (Review), *Biointerphases.* 12 (2017) 02D301. <https://doi.org/10.1116/1.4978435>.
- [180] R.A. Sperling, W.J. Parak, Surface modification, functionalization

and bioconjugation of colloidal Inorganic nanoparticles, *Philos. Trans. R. Soc. A Math. Phys. Eng. Sci.* 368 (2010) 1333–1383. <https://doi.org/10.1098/rsta.2009.0273>.

- [181] K. V. Serebrennikova, J. V. Samsonova, A.P. Osipov, Enhancement of the Sensitivity of a Lateral Flow Immunoassay by Using the Biotin–Streptavidin System, *Moscow Univ. Chem. Bull.* 73 (2018) 131–134. <https://doi.org/10.3103/S0027131418030070>.
- [182] D. Lago-Cachón, M. Oliveira-Rodríguez, M. Rivas, M.C. Blanco-López, J.C. Martínez-García, A. Moyano, M. Salvador, J.A. García, Scanning Magneto-Inductive Sensor for Quantitative Assay of Prostate-Specific Antigen, *IEEE Magn. Lett.* 8 (2017). <https://doi.org/10.1109/LMAG.2017.2702108>.

It was at the height of his accomplishments as chancellor of the German empire that Otto von Bismarck asked his great commanding general Helmuth von Moltke what could possibly be left for them to do.

“After such events,” Bismarck said, “is there anything left worth experiencing?”

Moltke’s response: “Yes, Your Excellency, watching a tree grow.”

